

https://dspace.org/

A computational tool for two-dimensional, external-compression, supersonic inlet design and analysis

Baloyi, Boitshoko Tessa Cybna

2021

https://hdl.handle.net/10539/33377

Downloaded from a DSpace repository. https://dspace.org/

A Computational Tool for Two-Dimensional, External-Compression, Supersonic Inlet Design and Analysis

Boitshoko Tessa Cybna Baloyi

A dissertation submitted to the Faculty of Engineering and the Built Environment, University of the Witwatersrand, Johannesburg, in fulfilment of the requirements for the degree of Master of Science in Engineering.

Johannesburg, September 2021

Declaration

I declare that this dissertation is my own, unaided work, except where otherwise acknowledged. It is being submitted for the degree of Master of Science in Engineering in the University of the Witwatersrand, Johannesburg. It has not been submitted before for any degree or examination at any other university.

Signed this 27th day of September 2021



Acknowledgements

I have received a great deal of assistance and support throughout this study. I would like to thank the people without whom I would not have been able to complete this research.

I want to thank the Council for Scientific and Industrial Research (CSIR) for funding my studies through a Masters Studentship. I would also like to thank Dr David Maclucas from the CSIR for mentoring me, providing his knowledge and expertise, and ensuring that I always stayed on track.

I want to thank my supervisor, Dr Randall Paton (University of the Witwatersrand), and co-supervisor, Dr Nico Wilke (University of Pretoria), for their guidance and support. Their knowledge and expertise steered me through this research.

I want to thank my family for the unconditional love and support they have shown me through this research. I want to give a special thank you to my mother, Belitha Baloyi, for the endless sacrifices that she makes for my brothers and I. She has played an instrumental role in me being where I am today. Words cannot begin to describe how much I love and appreciate her.

This work was made possible by an allocation of resources (programme number MECH0847) at the Centre for High-Performance Computing, a part of the South African National Integrated Cyberinfrastructure System.

Abstract

A shape optimisation tool to design and analyse two-dimensional (2D), external-compression, supersonic inlets developed. The tool provides the user with an inlet geometry based on user-defined inputs. The tool also provides the user with the performance parameters of the generated inlet. The performance parameters include the total pressure recovery and the mass flow ratio of the inlet when it is operating in the critical mode. Furthermore, the user is provided with the Mach number of the airflow at the aerodynamic interface plane (AIP) to ensure that it does not exceed the combustion chamber blow-off limit.

The theory of inviscid compressible flow was the starting point in developing the tool. Inviscid compressible flow calculations were used to generate inlet geometries that were optimised for maximum total pressure recovery and mass flow ratio. The assumption of inviscid flow is not always applicable to real-world compressible flows. Therefore, the effects of viscosity on the supersonic inlet flow fields and performance parameters were investigated with a detailed computational fluid dynamics (CFD) model.

The CFD model was developed in both the 2D and three-dimensional (3D) space. The 2D CFD model provided reasonable approximations of the 2D, external-compression, supersonic inlet flow field and captured the essential flow features. However, the 3D CFD model produced results that were in better agreement with experimental data compared to the results that were produced by the 2D CFD model. The accuracy of the 3D CFD model has a high computational cost and requires too much time to design, mesh, and run a simulation. The computational cost is greatly reduced in the 2D CFD model. Therefore, the 2D CFD model was used to analyse the air flowing through the generated supersonic inlets.

The CFD analyses showed that viscous flow phenomena, such as boundary layer development, shock-wave/boundary-layer interactions and boundary layer separation, are frequently occurring phenomena in supersonic inlet flow fields. Furthermore, viscous flow phenomena cause a difference between the optimised supersonic inlet performance parameters computed by inviscid flow calculations and the performance parameters obtained from viscous CFD analyses.

A sensitivity study was performed to investigate how changing the user-defined inputs varies the impact of viscous flow phenomena on the total pressure recovery and mass flow ratios of the inlets generated by the tool. The data obtained from the sensitivity study were used to develop a method to apply viscous corrections to the supersonic inlet performance parameters. The viscous corrections provide the user with an improved approximation of the supersonic inlet performance parameters. They also provide the user with an improved understanding of the quality of the air that the inlet supplies to the combustion chamber.

Contents

Declaration i

Acknowledgements ii

Abstract iii

Contents v

List of Figures xi

List of Tables xvii

List of Symbols xix

List of Acronyms xxi

1 Introduction 1

1.1 Background 1

1.2 Motivation 2

1.3 Problem Statement 3

1.4 Existing Supersonic Inlet Design and Analysis Tools 3

2 Objectives 9

3 Methodology 10

4 Literature Survey 12

4.1 The Theory of Supersonic Inlet Design and Analysis 12

4.1.1 Introduction 12

4.1.2 Supersonic Inlet Geometric Structure 12

4.1.3 Supersonic Inlet Flow Field Analyses 14

4.1.3.1 Inviscid Flow Analyses 14

4.1.3.1.1 The Theory of Inviscid Compressible Flow 15

4.1.3.1.2 Inviscid Flow Analysis at the Free-Stream Station 17

4.1.3.1.3 Inviscid Flow Analysis on the Fore-Body 21

4.1.3.1.4 Inviscid Flow Analysis at the Normal Shock Wave 25

4.1.3.1.5 Inviscid Flow Analysis in the Internal Diffuser 25

4.1.3.1.6 Inviscid Flow Analysis at the Cowl Lip 27

4.1.3.2 Viscous Flow Field Analysis 29

4.1.3.2.1 Boundary Layer Theory 29

4.1.3.2.2 Implications of Viscous Effects on Supersonic Inlet Flow Fields 31

4.1.3.3 Supersonic Inlet Modes of Operation 36

4.1.3.4 Supersonic Inlet Performance Parameters 37

4.1.3.4.1 Total Pressure Recovery 38

4.1.3.4.2 Mass Flow Ratio 38

4.1.3.4.3 Drag 40

4.2 Optimisation Theory . . . 41
4.3 Curve Theory . . . 44
4.3.1 Curve Fitting . . . 44
4.3.2 Curvature . . . 47
4.4 Design of Experiments . . . 48
4.5 Surrogate Modelling . . . 50

5 The Development of IADAM **54**

5.1 Introduction . . . 54
5.2 Geometric Structure . . . 55
5.3 Flow Analysis . . . 57
5.4 Shape Optimisation Algorithms . . . 59
5.4.1 Fore-Body . . . 59
5.4.2 Internal Diffuser . . . 62
5.4.2.1 Cowl Lip . . . 63
5.4.2.2 Cowl Interior . . . 65
5.4.2.3 Cowl Exterior . . . 68
5.4.2.4 Internal Diffuser Bottom Surface . . . 70
5.5 Multi-Start Optimisation Study . . . 72
5.6 Conclusion . . . 77

6 Investigation and Implementation of Viscous Effects on IADAM **78**

6.1 Introduction . . . 78
6.2 Computational Fluid Dynamics . . . 79

6.2.1 Domain Specification . . . 79
6.2.2 Mesh Specification . . . 81
6.2.3 Physics Models . . . 84
6.2.4 Boundary Conditions . . . 86
6.2.5 Reference Values and Initial Conditions . . . 88
6.2.6 Solver . . . 90
6.2.7 Results and Discussion . . . 90
6.2.8 Validation . . . 96
6.2.8.1 Validation Study Introduction . . . 96
6.2.8.2 Validation Study Results and Discussion . . . 97
6.2.8.3 Validation Study Conclusion . . . 103
6.3 Sensitivity Study . . . 104
6.3.1 Sensitivity Study Design Space . . . 104
6.3.2 Sensitivity Study Execution . . . 108
6.3.3 Results and Discussion . . . 111
6.3.3.1 The Variation of E_{P_R}, with changes in H, M_∞, M_{AIP}, n and h_{cap} . . . 111
6.3.3.2 The Variation of E_{m_R}, with changes in H, M_∞, M_{AIP}, n and h_{cap} . . . 120
6.4 Viscous Corrections . . . 123
6.4.1 Viscous Correction Response Surface Formulation . . . 123
6.4.2 Total Pressure Recovery Response Surface Formulation . . . 124
6.4.3 Mass Flow Ratio Response Surface Formulation . . . 125

6.4.4 AIP Mach Number Response Surface Formulation 125
6.4.5 Mach Number Contour Plot 126
6.5 Conclusion 127

7 Viscous Correction Verification **128**
7.1 Introduction 128
7.2 Methodology 128
7.3 Results and Discussion 129
7.4 Conclusion 133

8 Summary and Conclusion **134**

9 Recommendations **136**

Bibliography **139**

A The Two-Dimensional, External-Compression, Supersonic Inlet Design and Analysis Tool **144**

B Oblique and Normal Shock Wave Theory Equations **145**

C CFD Validation **147**
C.1 Introduction 147
C.2 2D CFD Simulation of the Supersonic Inlet Flow Field 148
C.2.1 Domain Specification 148
C.2.2 Mesh Specification 149
C.2.3 Physics Models 153

C.2.4 Boundary Conditions . . . 154
C.2.5 Reference Values and Initial Conditions . . . 157
C.2.6 Solver . . . 158
C.2.7 Results and Discussion . . . 159
C.3 3D CFD Simulation of the Supersonic Inlet Flow Field . . . 163
C.3.1 Domain Specification . . . 163
C.3.2 Mesh Specification . . . 164
C.3.3 Physics Models . . . 165
C.3.4 Boundary Conditions . . . 167
C.3.5 Reference Values and Initial Conditions . . . 167
C.3.6 Solver . . . 167
C.3.7 Results and Discussion . . . 167
C.4 Conclusion . . . 171

D A Survey of Two-Dimensional, External-Compression, Supersonic Inlet Geometries **173**

E Sensitivity Study Digital Appendix **176**

F Images of Two-Dimensional, External-Compression, Supersonic Inlets on Aircraft **179**

List of Figures

1.1 The Meteor Missile 1

1.2 A ramjet 2

1.3 A 2D, external-compression, supersonic inlet 3

1.4 External-compression supersonic inlets available in SUPIN 6

3.1 A conceptual framework of the present research 11

4.1 The components of a 2D, external-compression, supersonic inlet 13

4.2 A Boundary layer diverter and a boundary layer bleed 14

4.3 The stations on a supersonic inlet where inviscid flow analyses are performed 15

4.4 The variation of temperature with altitude 20

4.5 The variation of pressure with altitude 20

4.6 The variation of density with altitude 20

4.7 An oblique shock wave 21

4.8 A graphical representation of the $\theta - \beta - M$ relation with $\gamma = 1.4$ 22

4.9 The intersection of two left-running shock waves 24

4.10 A normal shock wave 25

4.11 Quasi-1D flow 26

4.12 Unstarted flow in a contracting duct 27

4.13 A detached bow shock wave in front of a blunt body 28

4.14 The development of a boundary layer over a flat plate 29

4.15 The characteristics of a weak oblique shock-wave/boundary-layer interaction . 32

4.16 The characteristics of a strong oblique shock-wave/boundary-layer interaction 33

4.17 The interaction of a weak normal shock wave with a laminar boundary layer . 33

4.18 The interaction of a stronger normal shock wave with a laminar boundary layer 34

4.19 The interaction of a strong normal shock wave with a laminar boundary layer 34

4.20 The interaction of a weak normal shock wave with a turbulent boundary layer 35

4.21 Supersonic inlet modes of operation 36

4.22 Oblique shock wave reflection 37

4.23 The stream tube area and the inlet capture area 39

4.24 The performance characteristic curve for a supersonic inlet 39

4.25 A NURBS curve 47

4.26 The variables used to compute the curvature on a point of a curve 48

4.27 CCD sampling for two design variables 50

5.1 The geometric structure of the inlets generated by IADAM 55

5.2 Noteworthy fore-body design features and dimensions 56

5.3 Cowl lip profiles 56

5.4 Noteworthy internal diffuser coordinates and dimensions 57

5.5 Fore-body shape optimisation objective function flow chart 60

5.6 Mach number contours of an inlet at different modes of operation 64

5.7 Cowl interior shape optimisation objective function flow chart 66

5.8 Cowl interior design features and dimensions 67

5.9 Cowl exterior design features and dimensions 69

5.10 IDBS design features and dimensions 70

5.11 The geometric profiles of 100 inlets generated during the multi-start optimisation study 75

5.12 The percentage errors relative to h_{cap} for the geometric profiles of the inlets generated during the multi-start optimisation study 76

6.1 A 2D, external-compression, supersonic inlet generated by IADAM 79

6.2 The 2D CFD model domain with boundary conditions 80

6.3 The P_R distribution at the AIP for various 2D mesh cell sizes 81

6.4 The 2D CFD model computational mesh 82

6.5 The mesh metrics of the 2D CFD model computational mesh 83

6.6 A Mach number contour plot of the supersonic inlet flow field 91

6.7 The M_{AIP} distribution 91

6.8 The complex shock wave patterns occurring in the viscous flow adjacent to the fore-body surface 93

6.9 The bow shock wave ahead of the cowl lip 94

6.10 The P_R distribution at the AIP 96

6.11 A photograph of the validation inlet installed in a wind tunnel 97

6.12 The Mach number contour plots of the air flowing through the validation inlet 98

6.13 Flow visualisation images of the shock/boundary-layer interaction documented during a wind-tunnel experiment 98

6.14 A comparison of the static pressure distributions produced by the 2D CFD model, the 3D CFD model and the experimental data 99

6.15 A comparison of the P_R distribution at the AIP produced by the 2D CFD model, the 3D CFD model and a wind-tunnel experiment 101

6.16 Sensitivity study sample points 110

6.17 The Mach number contour plot of inlet model 1 111

6.18 The variation of E_{P_R}, with changes in H, M_∞, M_{AIP}, n and h_{cap} 112

6.19 The P_R distribution for inlet model 1 at the AIP 113

6.20 The Mach number contour plots of inlet models 1 and 10 114

6.21 The Mach number contour plots of inlet models 1 and 2 114

6.22 The Mach number contour plots of inlet models 12 and 13 115

6.23 The Mach number contour plots of inlet models 2 and 6 116

6.24 The P_R distribution for inlet models 2 and 6 at the AIP 117

6.25 The Mach number contour plots of inlet models 6 and 32 118

6.26 The relationship between altitude and the ratio of the Reynolds number at a specific altitude to the Reynolds number at sea level 119

6.27 The P_R distribution for inlet models 6 and 32 at the AIP 119

6.28 The Mach number contour plots of inlet models 2 and 28 120

6.29 The variation of E_{m_R}, with changes in H, M_∞, M_{AIP}, n and h_{cap} 121

6.30 A visual representation of the response surfaces representing the P_R at a specific point on the AIP 125

6.31 A visual representation of the response surfaces representing the M_{AIP} at a specific point on the AIP 126

7.1 The Mach number contour plots of verification inlet 1 and 2 130

7.2 A comparison of the P_R distributions obtained from CFD and RBF 131

7.3 A comparison of the M_{AIP} distributions obtained from CFD and RBF 133

C.1 A photograph of the inlet installed in the wind tunnel 147

C.2 The geometry of a 2D, external-compression, supersonic inlet 148

C.3 The 2D CFD domain with boundary conditions 149

C.4 The P_R distribution at the AIP for various 2D mesh cell sizes 150

C.5 The 2D CFD computational mesh 151

C.6 The mesh metrics of the 2D CFD model computational mesh 152

C.7 The 2D CFD validation Mach number contour plot 159

C.8 Flow visualisation images of the shock/boundary-layer interaction documented during a wind-tunnel experiment 160

C.9 A comparison of the static pressure distributions produced by the 2D CFD model and the experimental data 161

C.10 A comparison of the P_R distribution at the AIP produced by the 2D CFD model and a wind-tunnel experiment 162

C.11 The 3D CFD domain with boundary conditions 164

C.12 The 3D CFD computational mesh 165

C.13 The mesh metrics of the 3D CFD model computational mesh 166

C.14 The 3D CFD validation Mach number contour plot 168

C.15 A comparison of the static pressure distributions produced by the 3D CFD model and experimental data 168

C.16 A comparison of the total pressure recovery distribution at the AIP produced by the 3D CFD model and experimental data 170

D.1 Survey model 1 174

D.2 Survey Model 2 174

D.3 Survey Model 3 174

D.4 Survey Model 4 175

D.5 Survey model 5 175

F.1 The Meteor Missile 179

F.2 The GQM-163 Coyote Missile 179

F.3 The XB-70 Valkyrie 180

F.4 The Boeing F-15 181

F.5 The Concord 181

List of Tables

4.1 Descriptions of the supersonic inlet flow analyses stations 15

4.2 Temperature gradients with respect to geopotential altitude for the standard atmosphere model 19

4.3 Radial basis functions 52

5.1 The user-defined inputs used by IADAM to generate inlets for the multi-start optimisation study 73

5.2 The ranges over which random initial approximations were generated for the fore-body shape optimisation algorithm multi-start optimisation study 73

5.3 The ranges over which random initial approximations were generated for the cowl interior shape optimisation algorithm multi-start optimisation study . . 73

5.4 The ranges over which random initial approximations were generated for the cowl exterior shape optimisation algorithm multi-start optimisation study . . 74

5.5 The ranges over which random initial approximations were generated for the IDBS shape optimisation algorithm multi-start optimisation study 74

5.6 Statistical data of the percentage errors relative to h_cap for the geometric profiles of the inlets generated during the multi-start optimisation study . . . 76

6.1 The errors between P_R distribution curves for various 2D mesh cell sizes . . . 82

6.2 The size of the 2D CFD model computational mesh 82

6.3 The 2D CFD model physics models 85

6.4 The 2D CFD model free-stream boundary conditions 86

6.5 The 2D CFD model pressure outlet boundary condition 87

6.6 The 2D CFD model reference values 88

6.7 The 2D CFD model initial conditions 89

6.8 Sensitivity study design space 105

6.9 The remaining user-defined inputs which were not investigated during the sensitivity study but are still required to generate inlets 106

6.10 Sensitivity study sample points 108

7.1 The user-defined inputs used to generate verification inlets 1 and 2 129

7.2 A comparison between the mass flow ratios obtained from CFD and RBF . . 132

C.1 The errors between P_R distribution curves for various 2D mesh cell sizes . . . 150

C.2 The size of the 2D CFD computational mesh 150

C.3 The physics models 153

C.4 The free-stream boundary conditions 155

C.5 The pressure outlet boundary conditions 156

C.6 The reference values 157

C.7 The initial conditions 158

C.8 The size of the 3D CFD model computational mesh 164

D.1 The dimensions of 2D, external-compression, supersonic inlets from several studies 173

E.1 Sensitivity study results 177

List of Symbols

The units of quantities defined by a symbol are indicated in square brackets following the description of the symbol. Quantities with no indicated units may be assumed to be dimensionless.

A Flow area $[m^2]$.

E_{P_R} Total pressure recovery error[-].

E_{m_R} Mass flow ratio error[-].

H Geometric altitude $[m]$.

M Mach number [-].

$N_{i,q}(\mathbf{u})$ NURBS curve qth degree B-spline basis function [-].

P_i NURBS curve control points [-].

P_R Total pressure recovery[-].

R Specific gas constant $[J/(kg \cdot K)]$.

R_E Radius of the earth $[m]$.

R_e Reynolds number [-].

T Absolute temperature $[K]$.

Z Geopotential altitude $[m]$.

a Local speed of sound $[m/s]$.

g_o Standard acceleration due to gravity at sea level$[m/s^2]$.

h A characteristic linear dimension representing height $[m]$.

h_{cap} Supersonic inlet capture height $[m]$.

l A characteristic linear dimension representing length $[m]$.

$m_{_R}$ Mass flow ratio [-].

n The number of ramps on a 2D, external-compression, supersonic inlet fore-body [-].

p Absolute pressure $[Pa]$.

q NURBS curve degree [-].

t A characteristic linear dimension representing thickness $[m]$.

u NURBS curve parametric independent variable [-].

v Velocity $[m/s]$.

w_i NURBS curve control point weights [-].

w_j The weight of a radial basis function.

β Oblique shock wave angle [°].

γ Ratio of specific heats [-].

δ^* Boundary layer displacement thickness $[m]$.

δ Boundary layer thickness $[m]$.

ϵ Radial basis function shape parameter.

θ^* Boundary layer momentum thickness $[m]$.

θ Flow deflection angle [°].

κ Curvature $[m^{-1}]$.

ρ Density $[kg/m^3]$.

ϕ Radial basis function [-].

List of Acronyms

1D one-dimensional.

2D two-dimensional.

3D three-dimensional.

AIP aerodynamic interface plane.

CCD central composite design.

CFD computational fluid dynamics.

CIS cowl interior surface.

COBYLA Constrained Optimisation BY Linear Approximation.

CR centre rake.

CSIR Council for Scientific and Industrial Research.

DOE design of experiments.

FTIS fore-body and top interior surface.

IADAM inviscid analytical design and analysis method.

IDBS internal diffuser bottom surface.

IIP Inlet Installation Programme.

IPAC Inlet Performance Analysis Code.

LR left rake.

MOC method of characteristics.

NASA National Aeronautics and Space Administration.

NIDA NAWC Inlet Design and Analysis.

NURBS non-uniform rational basis spline.

RBF radial basis function.

RR right rake.

RSM response surface methodology.

SLSQP Sequential Least SQuares Programming.

SUPIN SUPersonic INlet design and analysis tool.

Chapter 1 Introduction

1.1 Background

There has been a growing interest in supersonic flight ever since the time of World War II, when rocket-propelled aircraft were being developed. Rocket-propelled aircraft are capable of high-speed flight; however, they must carry their own fuel and oxidiser. These contribute to the total mass carried by the aircraft and limit the payload that the vehicle can potentially carry. Air-breathing propulsion systems eliminate the need for a high-speed propulsion system to carry an onboard oxidiser. They use the atmospheric air captured by the propulsion system during flight to oxidise the fuel (Storm et al. 2007). There are different types of air-breathing propulsion systems. However, the focus of the present research is on ramjets. Ramjets are used to propel the high-speed Meteor missile illustrated in figure 1.1.

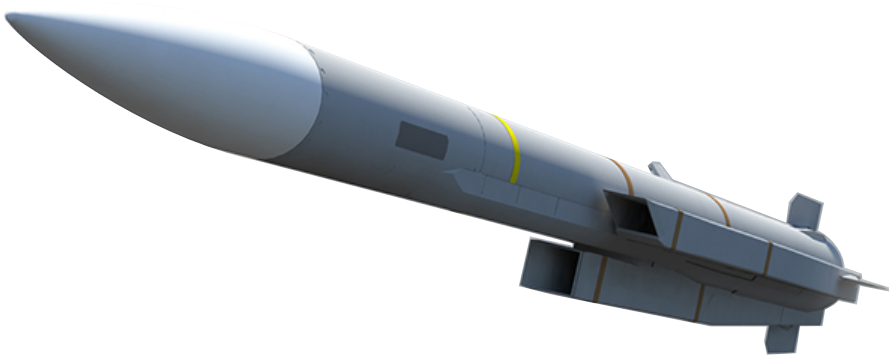


Figure 1.1: The Meteor Missile (Eshel 2017)

Ramjets are air-breathing propulsion systems that propel aircraft at supersonic speeds. The main components of a ramjet are illustrated in figure 1.2. Air is collected and compressed by the inlet diffuser, mixed with fuel and burnt in the combustion chamber, and the combustion products expand to a high velocity in the exhaust nozzle. The thrust generated by a ramjet is a reaction caused by the change in momentum of the air flowing through the ramjet. The

pressure difference across the ramjet also generates a pressure thrust. However, the pressure thrust is generally smaller than the momentum change thrust (Rathakrishnan 2010).

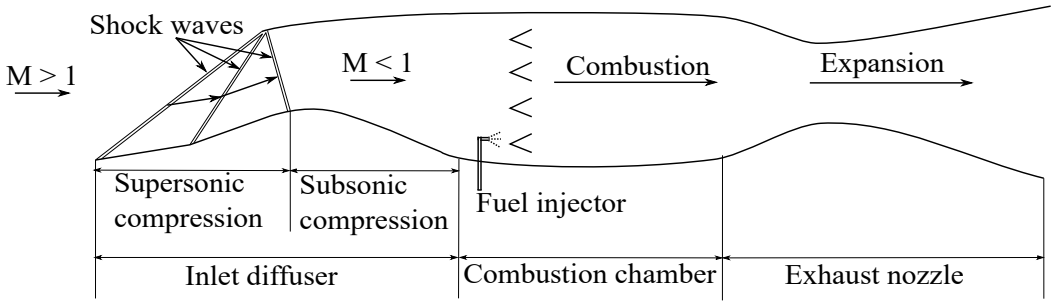


Figure 1.2: A ramjet

Ramjets are different from conventional jet engines because they do not use moving parts such as turbo-machinery to condition the captured air to favourable conditions for optimum combustion. The ramjet inlet diffuser is solely responsible for capturing the required air from the atmosphere, conditioning the air to conditions favourable to optimum combustion, and delivering the air to the combustion chamber. Combustion takes place subsonically. Therefore, the air supplied to the combustion chamber must be moving subsonically. The performance of the inlet diffuser is directly reflected in the overall engine performance. Therefore, the ramjet inlet diffuser is an essential part of the engine cycle (Faro 1965; Seddon and Goldsmith 1999). The ramjet inlet diffusers on the Meteor are clearly visible as the openings of the rectangular structures on the sides of the missile (Figure 1.1).

1.2 Motivation

The Council for Scientific and Industrial Research (CSIR) has become aware of a growing interest in redirecting the field of aeronautics to the research and development of commercial supersonic flight. As such, they have taken a particular interest in supersonic inlet design and analysis. The CSIR have the facilities to conduct supersonic inlet testing in their high-speed wind tunnel facility. However, they have identified the need for a supersonic inlet design and analysis capability that provides a good starting point to execute detailed supersonic inlet designs rapidly. Computational tools for supersonic inlet design and analysis already exist, as discussed in section 1.4. Unfortunately, they are not freely available to people outside of the institutions where they were developed. For the CSIR to remain competitive in this particular field, they have decided to develop a computational supersonic inlet design and analysis tool of their own.

1.3 Problem Statement

The research undertaken presents the development of a computational tool that can generate optimised geometric profiles of two-dimensional (2D), external-compression, supersonic inlets (Figure 1.3). The current research builds on work previously done by Baloyi (2017). Baloyi (2017) developed a shape optimisation algorithm to design and analyse optimised fore-body geometries for 2D, external-compression, supersonic inlets based on user-defined inputs. The algorithm performs its analyses using inviscid compressible flow relations such as those in NACA Report 1135 (Ames Research Staff 1953). Unfortunately, the mathematical formulation used to develop this algorithm sometimes fails to generate inlets with total pressure recoveries that ensure that the engines yield acceptable amounts of thrust. Furthermore, the effects of viscosity on the air flowing over the fore-bodies have not been considered.

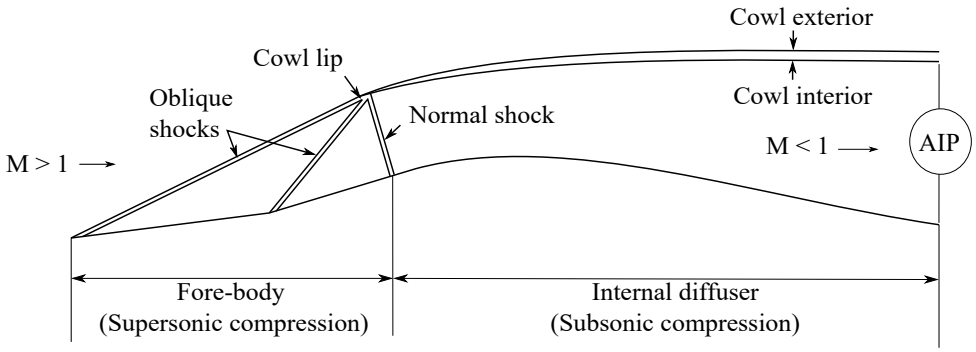


Figure 1.3: A 2D, external-compression, supersonic inlet

In the present work, the fore-body shape optimisation algorithm developed by Baloyi (2017) was modified to generate fore-body geometries with maximum total pressure recoveries. Additional algorithms were developed to complete the geometric profiles of 2D, external-compression, supersonic inlets by adding internal diffusers to the fore-bodies. Furthermore, the viscous effects on supersonic inlet flow fields were taken into account, and viscous corrections were applied to the supersonic inlet performance parameters.

1.4 Existing Supersonic Inlet Design and Analysis Tools

Supersonic inlet design and analysis has been a topic of research and development for over 70 years (Storm et al. 2007). Several studies have been dedicated to developing computer programmes that automate the design and analyses of inlets during this time. The theory of inviscid compressible flow documented in NACA Report 1135 formed a starting point in developing several supersonic inlet design and analysis tools (Ames Research Staff 1953).

Therefore, it is considered an acceptable starting point for the 2D, external-compression, supersonic inlet design and analysis tool developed in the present work. The tools documented by Barnhart (1997) and Sorensen (1965) are examples of tools that were developed based on the assumption of inviscid compressible flow. These tools are discussed in further detail in the following paragraphs.

The Inlet Performance Analysis Code (IPAC) is an inlet design and analysis tool developed by the National Aeronautics and Space Administration (NASA). It was developed to compute the total pressure recovery, mass flow and aerodynamic drag of common inlet designs. The analyses performed by IPAC can model the airflow in three types of inlet geometries, i.e. pitot, axisymmetric and 2D. IPAC uses the theory of inviscid compressible flow to perform its analyses, and viscous effects are not taken into account. The analyses performed by IPAC are useful in creating preliminary supersonic inlet designs (Barnhart 1997).

NASA also developed a Fortran IV computer program, which calculates the fluid properties of the flow fields on the fore-bodies of 2D, three-dimensional (3D) and axisymmetric supersonic inlets. The analyses performed by this programme are limited to smoothly contoured fore-bodies. The flow fields evaluated by this programme consist of oblique shock waves originating from the leading edge of the fore-bodies. The smoothly contoured fore-bodies generate an infinite number of infinitely weak oblique shock waves. The programme is slightly more sophisticated than IPAC in that it employs the method of characteristics (MOC) to perform its analyses on the described flow fields (Sorensen 1965). A 2D, isentropic, irrational and steady flow field can be mathematically represented by partial differential equations. MOC is a numerical technique used to solve these partial differential equations and calculate the fluid properties of a flow field that satisfies a set of boundary conditions. MOC is limited to solving compressible, inviscid, irrotational and supersonic flows in the 2D, 3D and axisymmetric spaces (Vos and Farokhi 2015). The Fortran IV computer program calculates the total pressure, Mach number, local flow angle and static pressure ratio at various points within the flow field. Similarly to IPAC, viscous effects are not taken into account (Sorensen 1965).

The use of simple inviscid compressible flow calculations permits IPAC and the Fortran IV programme mentioned above to perform rapid calculations resulting in quick turn-around times for inlet design assessments. However, the assumption of inviscid flow does not always apply to real-world compressible flows. Friction between the supersonic inlet surfaces and the air flowing through the supersonic inlets introduce viscous effects, which can significantly affect the supersonic inlet flow field. Similarly to IPAC and the Fortran IV program, the Level II Inlet Installation Programme (IIP) code, the NAWC Inlet Design and Analysis (NIDA) code and the SUPersonic INlet design and analysis tool (SUPIN) use low-fidelity inviscid compressible flow calculations to perform their analyses. However, they also make use of

empirical data from wind tunnel experiments to apply viscous corrections to their analyses. Level II IIP, NIDA and SUPIN are described in further detail in the following paragraphs.

The Grumman Aerospace Cooperation developed Level II IIP on behalf of the United States Air Force. The programme was developed to estimate the performance of a given military aircraft inlet based on total pressure recovery and drag. The code was developed by combining several existing computational tools and incorporating some new simple compressible flow calculations into the tool. Level II IIP accounts for viscous effects by means of a correlation between simple compressible flow phenomena and empirical data. Furthermore, the Level II IIP code assesses whether an inlet/engine/airframe integration study should be conducted for a given inlet. Level II IIP is the only tool discussed in the present section (Section 1.4) known to perform an integration assessment (Tindell and Tamplin 1983).

NIDA was developed at the United Technologies Research Center. Similarly to Level II IIP, supersonic inlets are designed using inviscid compressible flow principles. Furthermore, viscous corrections are applied using empirical data. The application of viscous corrections is achieved by separating the supersonic inlet flow field into two regions. The first is the region of supersonic flow that exists upstream of the inlet throat. The second is the region of subsonic flow in the internal diffuser located downstream of the inlet throat. Similarly to IPAC, the flow field in the first region is analysed using the inviscid compressible flow theory. NIDA is also similar to the Fortran IV program developed by NASA in that MOC is incorporated into the first region analysis. NIDA analyses the flow field in the second region using one-dimensional (1D) empirical correlations that take the normal shock-wave/boundary-interaction that occurs inside subsonic diffuser into account (Haas, Elmquist and Sobel 1993). This is similar to the manner in which Level II IIP applies viscous corrections.

SUPIN is the most recent supersonic inlet design and analysis tool developed by NASA. Similarly to Level II IIP and NIDA, it uses "low-fidelity aerodynamic analysis and design methods that are based on analytical, numerical and empirical methods". The performance of the inlets generated by SUPIN are determined by evaluating the mass flow rate, total pressure recovery and drag (Slater 2012).

SUPIN is slightly more sophisticated than the other tools developed by NASA because "it was developed to retain the capability of the various past tools while updating and documenting the coding and methods". SUPIN is capable of designing and analysing traditional inlet types, such as the 2D and axisymmetric inlets. Furthermore, it can also design and analyse newer inlet types, such as the streamline-traced inlets. The inlet types generated by SUPIN are illustrated in figure 1.4 (Slater 2012).

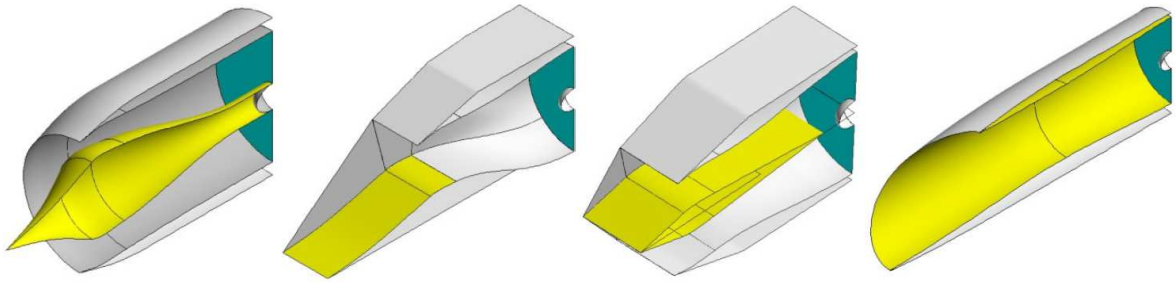


Figure 1.4: External-compression supersonic inlets available in SUPIN (left to right: axisymmetric outward-turning, two-dimensional single-duct, two-dimensional bifurcated-duct and the streamline-traced Busemann inlets) (Slater 2012)

The present work did not use wind tunnel data for viscous corrections like Level II IIP, NIDA and SUPIN. This is because the objective of the 2D, external-compression, supersonic inlet design and analysis tool developed in the present work is to generate supersonic inlets of various shapes, sizes and operating conditions based on user-defined inputs. A large amount of wind tunnel data would have been needed to apply viscous corrections to all the possible inlet configurations that the tool may generate. Too much time and money would have been spent designing, manufacturing, and testing the inlets used to gather the required data.

The advent of powerful computers has led to the increased use of computational fluid dynamics (CFD) methods to analyse the viscous flow in supersonic inlet flow fields. The increased fidelity provided by CFD methods requires greater complexity and time for the analyses. CFD was used in the present work to identify the viscous flow features that exist in supersonic inlet flow fields and study the severity of viscous effects on the performance parameters of the inlets generated by the tool.

CFD is popular with supersonic inlet design and analysis tools that incorporate design optimisation. The tools documented by Zha et al. (1996), Bourdeau et al. (1999) and Carrier et al. (2001) have been able to achieve better quality designs by combining supersonic inlet design tools with CFD solvers and incorporating them into an optimisation loop. This was done to obtain supersonic inlet geometries with the best aerodynamic performance.

Zha et al. (1996) introduced a strategy that combines an existing inlet design and analysis tool (i.e. NIDA) with a Navier-Stokes CFD analysis tool. NIDA is incorporated into an optimisation loop. The optimisation objective is to obtain a supersonic inlet design that has maximum total pressure recovery. The Navier-Stokes CFD analysis tool is used to "verify, select and filter the final design" (Zha et al. 1996).

Bourdeau et al. (1999) developed a method to design and analyse 3D, multi-ramp, mixed-compression, supersonic inlets with optimised performance parameters. The performance of the inlets is assessed based on the total pressure recoveries and mass flow ratios of the inlets. An optimiser and a flow solver are incorporated into an optimisation loop. The optimiser is an inlet design technique that generates inlet designs based on nine geometric parameters. The solver analyses the performances of the candidate inlets. The Reynolds Averaged Navier-Stokes solvers are the ideal solvers to use for this type of application. However, it would have been computationally expensive to run multiple 3D CFD analyses on all the candidate inlets. Therefore, a hybrid flow solver was developed. The solver is composed of an Euler solver and a 1D subsonic diffuser model. Similarly to Zha et al. (1996), the performance of the final inlet model was validated with a Reynolds Averaged Navier-Stokes solver.

Carrier et al. (2001) performed multi-criteria design optimisations for a 2D, mixed-compression, supersonic inlet. The criteria are a set of three inlet performance parameters at different stages of flight. The first, second and third design optimisation criteria are "the mass flow ratio during acceleration and the total pressure recovery during cruise and manoeuvrer", respectively. The multi-criteria design optimisations are performed to find the Pareto front. A Pareto front is a set of solutions generated by a multi-criteria design optimisation problem when it is impossible to optimise the solution for one criterion without sacrificing another criterion. The inlet geometries with the best shapes lie on the Pareto front. A single inlet geometry is selected based on the compromises that the user is willing to make. The approach used in this tool is more realistic compared to the approach used by the other tools discussed in the present section (Section 1.4). The performance of an inlet is not constant and will change during different stages of flight. This approach allows the user to take the performance of an inlet at different stages of flight into consideration when selecting an ideal inlet design

Computational tools for supersonic inlet design, analysis and optimisation already exist. Unfortunately, they are not freely available to people outside of the institutions where they were developed. This research aims to be a starting point in developing a supersonic inlet design and analysis tool for the CSIR. Some of the themes and methodologies used to develop already existing tools were applied to the present work. For instance, the theory of inviscid compressible flow was the starting point in developing the tool. Similarly to several tools such as IPAC, Level II IIP, NIDA, etc., the performance of the inlets generated by the tool developed in the present work are evaluated based on total pressure recovery. This is because it directly impacts the amount of thrust generated by the entire ramjet, as discussed in section 4.1.3.1.3. The concept used by Zha et al. (1996) to generate inlets that are optimised for maximum total pressure recovery was loosely applied in the present work. Design optimisation principles were incorporated into the tool to generate supersonic inlets that have been

optimised for maximum total pressure recovery. The computation of total pressure recovery in the optimisation loop was performed using inviscid flow calculations similar to the analyses performed in IPAC. CFD was used to study the effects of viscosity in supersonic inlet flow fields. The CFD results were used to apply viscous corrections to the performance parameters of the inlets generated by the tool.

Chapter 2 Objectives

The over-arching objective of the present work is to develop a computational tool to automatically design and analyse optimised geometric profiles of 2D, external-compression, supersonic inlets based on user-defined inputs. To achieve this, the objective is divided into the following aims:

1. Develop a low-fidelity shape optimisation tool to generate the geometric profiles of 2D, external-compression, supersonic inlets based on user-defined inputs using the theory of inviscid compressible flow as a starting point.
2. Increase the fidelity of the shape optimisation tool mentioned in the first aim by developing a detailed CFD model to investigate and implement the effects of viscosity on the inlets generated by the low-fidelity shape optimisation tool.
3. Verify the performance of the higher fidelity shape optimisation tool mentioned in the second aim.

Chapter 3 Methodology

A low-fidelity shape optimisation tool for generating the geometric profiles of 2D, external-compression, supersonic inlets based on user-defined inputs forms the starting point of the present work. It is developed based on the assumption of inviscid compressible flow (Section 4.1.3.1.1). Therefore, it will be referred to as inviscid analytical design and analysis method (IADAM). IADAM applies mathematical optimisation theory (Section 4.2) to generate geometric profiles that are optimised for maximum total pressure recovery and mass flow ratio. To achieve this, the fore-body shape optimisation algorithm is formulated as a mathematical optimisation problem that computes the ramp angles required to produce maximum total pressure recovery. This algorithm is a modification of the fore-body design and analysis algorithm developed by Baloyi (2017). The internal diffuser surfaces are constructed as smooth curves generated with a curve fitting model (Section 4.3.1). The algorithms generating the internal diffuser surfaces are formulated as mathematical optimisation problems that compute surfaces with minimum curvature.

A detailed CFD model is developed to study the impact of viscous flow phenomena on supersonic inlet flow fields. The impact of viscous flow on supersonic inlet flow fields may vary for inlets generated using different user-defined inputs. Therefore, a sensitivity study is performed to study how the user-defined inputs affect the impact of viscous flow phenomena on the supersonic inlet flow fields. The sample points for the sensitivity study are selected using a design of experiments (DOE) technique (Section 4.4). The data obtained from the sensitivity study are used to create off-line viscous corrections to the performance parameters of the inlets generated by the tool through the application of a surrogate model (Section4.5).

Figure 3.1 presents a conceptual framework of the steps taken during the present work to develop a shape optimisation tool for generating the geometric profiles of 2D, external-compression, supersonic inlets. The bold text in the descriptions highlight theories that are applied during each step. These theories are discussed in the literature survey, i.e. chapter 4

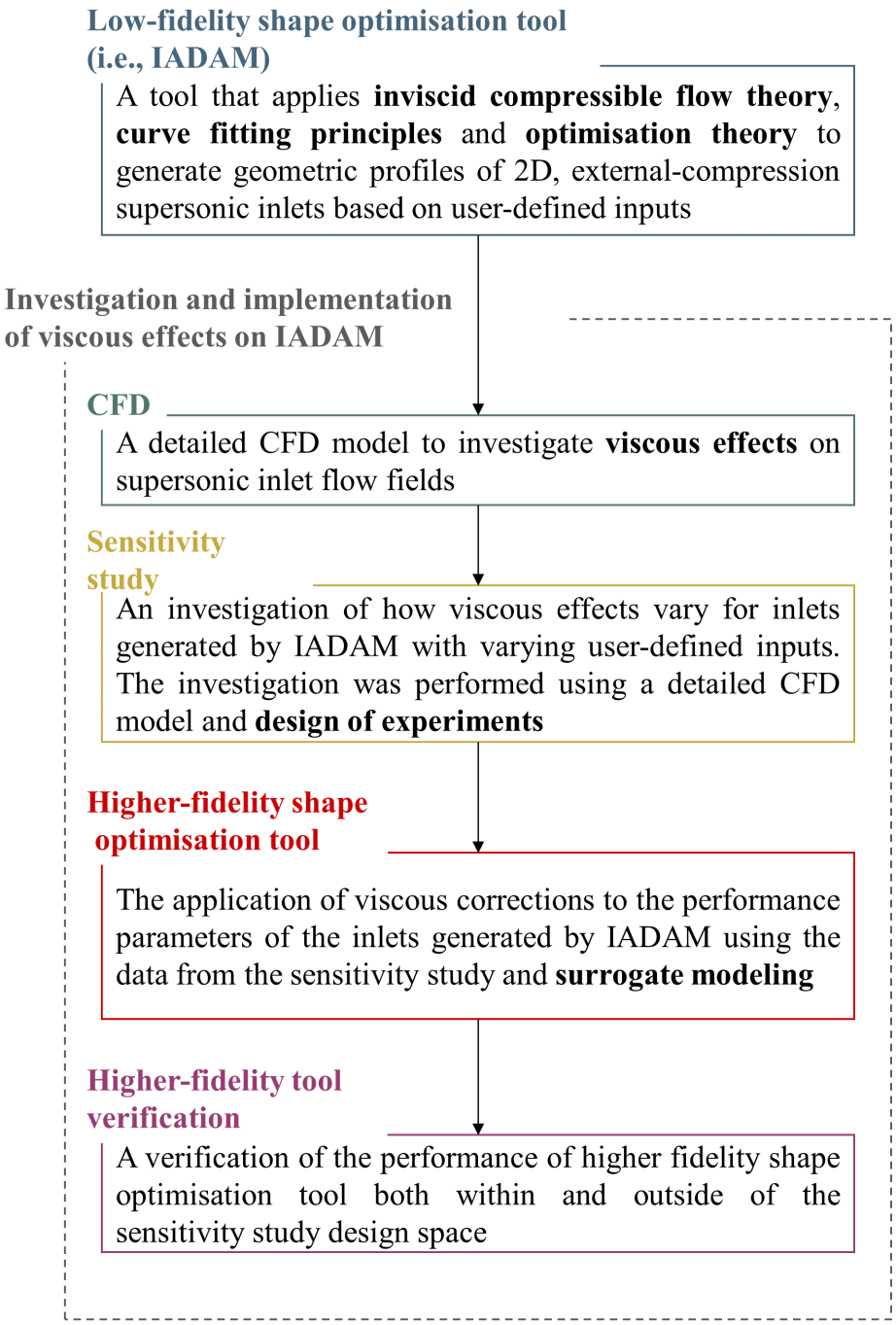


Figure 3.1: A conceptual framework of the present research

Chapter 4 Literature Survey

4.1 The Theory of Supersonic Inlet Design and Analysis

4.1.1 Introduction

A supersonic inlet is a jet engine component that is solely responsible for capturing the required amount of air from the atmosphere, conditioning the air to conditions favourable to optimum combustion and delivering the air to the combustion chamber (Faro 1965; Seddon and Goldsmith 1999). There are different types of supersonic inlets. Supersonic inlets are categorised based on flow structure dimension (i.e. axisymmetric, 2D and 3D), supersonic flow compression region (i.e. pitot, external-, internal- and mixed-compression) and installation location (i.e. fuselage-, side-, nose-, or top-mounted, etc.) (Seddon and Goldsmith 1999). Ideally, a supersonic inlet design and analysis tool should be capable of generating various types of inlets. However, this study will focus on isolated, 2D, external-compression, supersonic inlets. The addition of other inlet types is beyond the scope of this study but can be revisited in future work.

4.1.2 Supersonic Inlet Geometric Structure

The geometric structure of a 2D, external-compression, supersonic inlet is illustrated in figure 4.1. The main components of this type of inlet are the fore-body and the internal diffuser. The fore-body is a structure consisting of a single or multiple compression ramps. When supersonic air flows past the compression ramps, a series of oblique shock waves are generated. The oblique shock waves compress the captured airflow from the supersonic free-stream Mach number to a lower supersonic Mach number. The physics of oblique shock wave generation is explained in detail in section 4.1.3.1.3.

The airflow delivered to the combustion chamber must be moving subsonically. The deceleration of the captured air to a subsonic Mach number is achieved through a normal shock

wave. The normal shock wave in an external-compression inlet is typically located at the internal diffuser entry plane. The internal diffuser is a diverging duct. It is responsible for decelerating the subsonic air entering the internal diffuser to an even lower subsonic Mach number via area expansion. The physics of airflow acceleration/deceleration via area expansion/contraction is explained in more detail in section 4.1.3.1.5. The internal diffuser exit plane is referred to as the aerodynamic interface plane (AIP). The AIP is a plane between the inlet and the combustion chamber where measurements are taken. These measurements include the air distortion and the performance parameters of the inlet (Walsh et al. 1997).

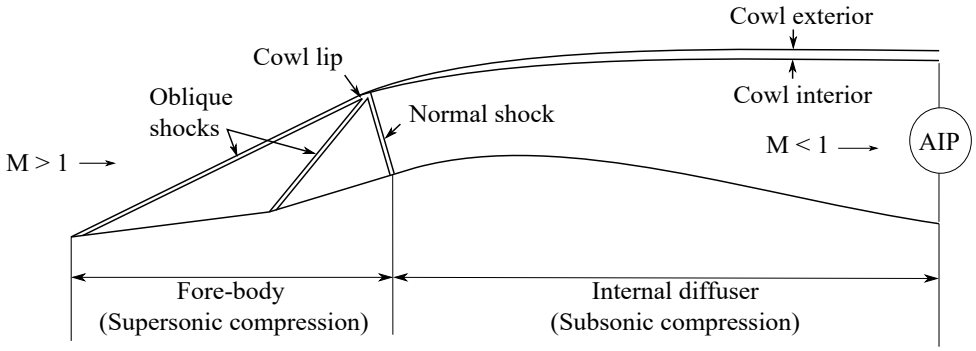


Figure 4.1: The components of a 2D, external-compression, supersonic inlet

Although the airflow downstream of the normal shock wave is already subsonic, it often needs to be decelerated to an even lower subsonic Mach number before entering the combustion chamber. This is because the combustion chambers used in ramjets have a maximum Mach number at which the air entering them must be moving. This Mach number is referred to as the 'blow-off limit'. The 'blow-off limit' is the Mach number at which the flame remains attached to the flame holders in the combustion chamber. According to Rathakrishnan (2010), Slater (2012) and Storm et al. (2007), the blow-off limit ranges between Mach 0.2 and Mach 0.5.

The airflow inside the internal diffuser is separated from the air outside of the supersonic inlet by means of a cowl. The cowl consists of a cowl interior, a cowl exterior and a cowl lip. The cowl interior is an internal diffuser surface. It is responsible for turning the air entering the internal diffuser from the direction of the fore-body to a direction appropriate for the combustion chamber. The cowl exterior is the external surface of the cowl.

The cowl lip is located at the point where the fore-body generated oblique shock waves converge. It is responsible for dividing the incoming airflow into an internal and external airflow. It can have a sharp or a blunt profile. A sharp cowl lip profile minimises pressure drag. However, it may be difficult to manufacture. Therefore, the cowl lip typically has a blunt profile. The advantage of a blunt lip is that it may reduce the pre-entry drag by delaying normal shock wave expulsion. (Faro 1965). A blunt cowl lip is a small blunt body

is a supersonic flow field. A curved bow shock wave forms when a blunt body moves through a supersonic flow. This is discussed in further detail in section 4.1.3.1.6.

Boundary layers develop on supersonic inlet surfaces. Boundary layer development is caused by friction between the supersonic inlet flow field and the inlet surfaces. Boundary layers and shock-wave/boundary-layer interactions have an undesirable effect on the performance of an inlet. This is discussed in more detail in section 4.1.3.2. Some supersonic inlets are equipped with a boundary layer diverter and/or a boundary layer bleed to prevent the boundary layer from a forward external surface (e.g. the fuselage, wing, fore-body, etc.) from entering the engine. A boundary layer diverter is a scoop between the inlet and the forward external surface. It allows the boundary layer on that surface to escape down a channel. A boundary layer bleed is a separate duct in the throat of the internal diffuser. It leads the boundary layer away from the internal diffuser. Figure 4.2 illustrates a boundary layer diverter and bleed on a 2D, external-compression, supersonic inlet (Seddon and Goldsmith 1999).

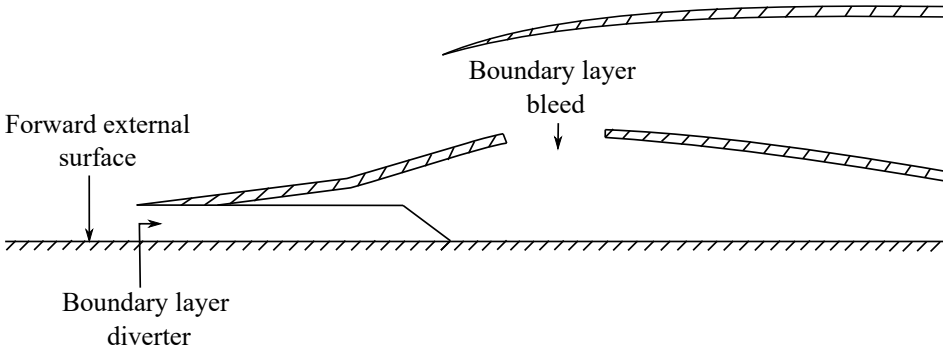


Figure 4.2: A Boundary layer diverter and a boundary layer bleed

4.1.3 Supersonic Inlet Flow Field Analyses

4.1.3.1 Inviscid Flow Analyses

The earliest contributors to the field of supersonic inlet design and analysis developed low-fidelity analytical methods that directly apply the theory of inviscid compressible flow to execute supersonic inlet designs and perform supersonic inlet flow field analyses (Seddon and Goldsmith 1999; Mahoney 1990). These methods were incorporated into computational tools such as IPAC, the Level II IIP code, NIDA, etc.

Inviscid flow analyses of the air flowing through a 2D, external-compression, supersonic inlet are performed at various stations. The stations at which low-fidelity inviscid flow analyses are typically performed are illustrated in figure 4.3. Furthermore, the station descriptions are tabulated in table 4.1.

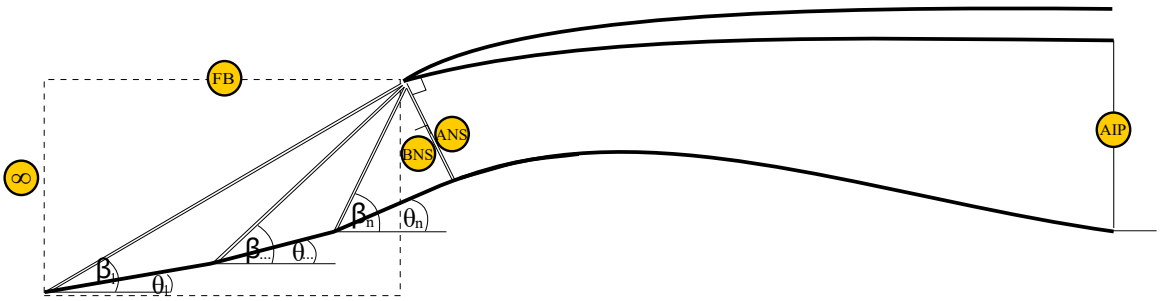


Figure 4.3: The stations on a supersonic inlet where inviscid flow analyses are performed

Table 4.1: Descriptions of the supersonic inlet flow analyses stations

Station	Description
∞	Free-stream flow
FB	The fore-body where external supersonic compression occurs
BNS	Just before the normal shock wave
ANS	Just after the normal shock wave
AIP	Aerodynamic interface plane

To perform inviscid flow analyses at the stations outlined in figure 4.3, the theory of inviscid compressible flow is briefly introduced in section 4.1.3.1.1. After that, the inviscid flow analyses performed at each station are explained in sections 4.1.3.1.2 through to 4.1.3.1.6.

4.1.3.1.1 The Theory of Inviscid Compressible Flow

The Ideal Gas Law A compressible fluid, or a gas, is a fluid that experiences changes in density when it is subjected to a pressure or temperature gradient. It consists of a collection of randomly moving particles (i.e. molecules, atoms, ions, electrons, etc.). An ideal gas is a theoretical gas in which the intermolecular forces between the gas molecules are assumed to be negligible, and the collisions between the molecules are assumed to be perfectly elastic. The relationship between the pressure, the temperature and the density of an ideal gas is referred to as the ideal gas law, as represented by equation 4.1 (Anderson 2010).

$$p = \rho RT \tag{4.1}$$

where:

p is the absolute pressure of the compressible fluid,
ρ is the density of the compressible fluid,
T is the absolute temperature of the compressible fluid and,
R is the specific gas constant of the compressible fluid.

The Local Speed of Sound When there is a disturbance in a fluid, it transfers energy to the fluid molecules adjacent to it. The energised fluid molecules collide with their neighbouring molecules and transfer the energy to these neighbouring molecules. This energy transfer pattern results in the propagation of energy in the form of an information-relaying sound wave. The speed that the sound wave propagates through a fluid is referred to as the local speed of sound. In an ideal gas, where there is no heat transfer and the entropy remains constant, the local speed of sound is computed using equation 4.2 (Anderson 2010).

$$a = \sqrt{\gamma RT} \tag{4.2}$$

where:

a is the local speed of sound of the compressible fluid,
γ is the ratio of specific heats for an ideal gas,
R is the specific gas constant of the compressible fluid and,
T is the absolute temperature of the compressible fluid.

It is common to normalise the local speed of a moving fluid with the local speed of sound. The normalised value is referred to as the Mach number, as represented by equation 4.3:

$$M = \frac{v}{a} \tag{4.3}$$

where:

M is the Mach number of the compressible fluid,
v is the local fluid velocity and,
a is the local speed of sound of the compressible fluid.

The Mach number is used to determine the degree of compressibility of the moving fluid. A general rule of thumb is that slower fluid flows (i.e. $M < 0.3$) are treated as incompressible. Conversely, faster fluid flows (i.e. $M > 0.3$) are treated as compressible (Anderson 2010).

When a fluid is moving at a Mach number greater than one, it is moving at a supersonic speed. Conversely, a fluid that is moving at a Mach number less than one is moving at a subsonic speed. When a fluid is moving at a Mach number of one, it is moving at a sonic speed (Anderson 2010).

The Isentropic Flow Relations The static fluid properties of a moving fluid are the properties observed when moving along with the fluid at the local fluid velocity. The stagnation fluid properties are defined as the fluid properties that a fluid would attain if it undergoes an isentropic process that brings the fluid to rest. An isentropic process is a process with no gain in entropy. For this to be true, the process must be adiabatic and reversible. It should be noted that the temperature of a fluid is independent of the process that the fluid undergoes

from one state to the other. It is only dependent on the initial and final states of the fluid (Anderson 2010).

The stagnation fluid properties provide a reference state because they remain constant throughout the flow field provided that all the processes that the fluid undergoes are isentropic. Equations 4.4, 4.5 and 4.6 define the relationships between static and stagnation values of temperature, pressure and density, respectively, of a compressible fluid moving at a specified Mach number. Subscript '0' represents stagnation fluid properties (Anderson 2010).

$$\frac{T_0}{T} = 1 + \frac{\gamma - 1}{2} M^2 \tag{4.4}$$

$$\frac{p_0}{p} = \left(1 + \frac{\gamma - 1}{2} M^2\right)^{\frac{\gamma}{\gamma - 1}} \tag{4.5}$$

$$\frac{\rho_0}{\rho} = \left(1 + \frac{\gamma - 1}{2} M^2\right)^{\frac{1}{\gamma - 1}} \tag{4.6}$$

The stagnation fluid properties are often referred to as the 'total' fluid properties. However, the definitions of these terms are not entirely identical. The stagnation fluid properties are measured at a stagnation point. The total fluid properties are stagnation fluid properties that are measured relative to an arbitrary datum level and take the effects of gravity into account. In the current context of compressible flow theory, the terms 'stagnation' and 'total' are considered synonymous and are often used interchangeably (Anderson 2010).

4.1.3.1.2 Inviscid Flow Analysis at the Free-Stream Station

The fluid properties of the captured free-stream airflow vary with altitude. Aircraft have specific cruising altitude ranges that they remain in during flight. The altitude range is influenced by several factors such as the type of aircraft, the aircraft payload, the type of engine used and the cruise speed. Commercial subsonic aircraft fly between altitudes of 30 000 ft (approximately 9 144 m) and 40 000 ft (approximately 12 192 m) (Storm et al. 2007).

Supersonic aircraft fly higher than subsonic aircraft. When an aircraft flies at a supersonic speed, a shock wave forms just upstream of the aircraft. Shock wave formation is discussed in more detail in section 4.1.3.1.3. The shock wave causes a sharp release of the pressure build-up. This is heard as a sonic boom. A sonic boom is a loud sound that is similar to the sound of an explosion. It can be startling to the people that hear it and cause some structural damage. Supersonic aircraft fly at higher altitudes to increase the distance that the shock wave must travel before it reaches the ground, and reduce the intensity of the sonic boom (Plotkin 1989). Flying at higher altitudes also reduces the drag experienced by an aircraft.

This is because the density of the air in the atmosphere decreases with an increase in altitude, as illustrated in figure 4.6. As a result, the lower density reduces the aircraft drag.

Ramjet- and scramjet-powered aircraft have achieved altitudes within the range of 40 000 ft (approximately 12 192 m) - 110 000 ft (approximately 33 528 m). Examples include the Concord, which flew at a maximum altitude of 60 000 ft (approximately 18 288 m) (Collard 1991); the Lockheed SR-71 Blackbird that has reached altitudes that exceed 80 000 ft (approximately 24 384 m) (Crickmore 2015); and the NASA X-43A that has reached an altitude of 110 000 ft (approximately 33 528 m) (Engelund et al. 2001; Storm et al. 2007). The standard atmosphere model is introduced to describe how the fluid properties of the air in the atmosphere vary with altitude.

The Standard Atmosphere Model The fluid properties of the free-stream air in the atmosphere vary with altitude. The standard atmosphere model is a commonly-used model that has been defined to predict the fluid properties of air at various altitudes. This model divides the atmosphere into several regions. Each region is assumed to have a constant temperature gradient with respect to geopotential altitude. The geopotential altitude is an adjustment to the geometric altitude that takes the variation of gravity with altitude into account. It is measured relative to the mean sea level of the earth (Phillips 2010). The geopotential and geometric altitudes are related as per equation 4.7.

$$Z = \frac{R_E H}{R_E + H} \tag{4.7}$$

where:

Z is the geopotential altitude,
H is the geometric altitude and,
R_E is the radius of the earth.

The temperature gradients in the different regions of the atmosphere are summarised in table 4.2. Subscript 'i' and 'i+1' refer to a value at the lower and upper bounds of a particular atmospheric region, respectively. The prime symbol, $'$, denotes the gradient of a particular value with respect to geopotential altitude. The temperature in each region is defined by the linear equation 4.8 (Phillips 2010):

$$T(Z) = T(Z_i) + T_i'(Z - Z_i) \tag{4.8}$$

The air pressure in each atmospheric region is calculated with equation 4.9 (Phillips 2010):

$$p(Z) = \begin{cases} p_i \exp\left[-\dfrac{g_o(Z - Z_i)}{RT_i} \right], & T_i' = 0 \\ p_i \left[\dfrac{T_i + T_i'(Z - Z_i)}{T_i} \right]^{\frac{-g_o}{RT_i'}}, & T_i' \neq 0 \end{cases} \tag{4.9}$$

where:

g_o is the standard acceleration due to gravity at sea level.

The density is calculated using the ideal gas law (i.e. equation 4.1). Based on the standard atmosphere model, the variations of free-stream temperature, pressure and density with altitude are illustrated in figures 4.4, 4.5 and 4.6, respectively.

The free-stream stagnation fluid properties are calculated using the isentropic flow relations presented in section 4.1.3.1.1. More specifically, the free-stream stagnation temperature, pressure and density are calculated using equations 4.4, 4.5 and 4.6, respectively. To calculate the stagnation fluid properties, the free-stream static fluid properties (computed using the standard atmosphere model) and the free-stream Mach number are required.

Table 4.2: Temperature gradients with respect to geopotential altitude for the standard atmosphere model (Phillips 2010)

Geopotential altitude range		Initial temperature	Temperature gradient
Z_i (m)	Z_{i+1} (m)	T_i (K)	T_i' (K/km)
0	11 000	288.150	-6.5
11 000	20 000	216.650	0.0
20 000	32 000	216.650	1.0
32 000	47 000	228.650	2.8
47 000	52 000	270.650	0.0
61 000	79 000	252.650	-4.0
79 000	90 000	180.650	0.0

The standard atmosphere is characterised by an absolute temperature of 288.15 K, an absolute pressure of 101325 Pa and a standard acceleration due to gravity of 9.806645 m/s^2 at sea level (Phillips 2010).

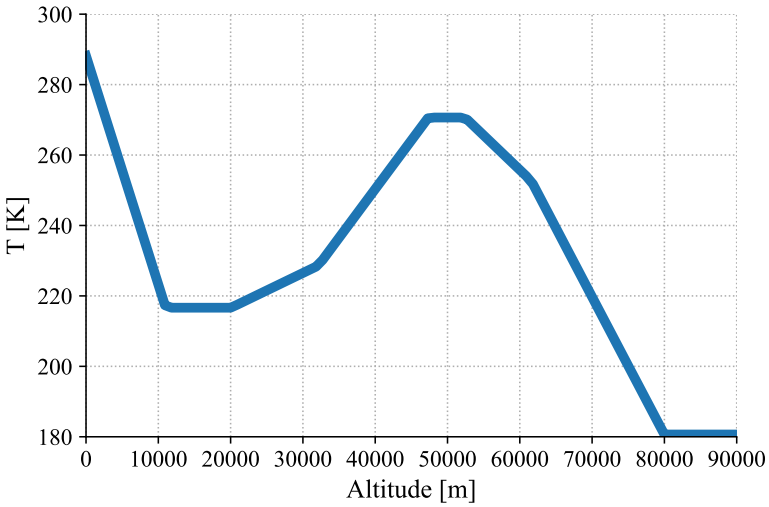


Figure 4.4: The variation of temperature with altitude

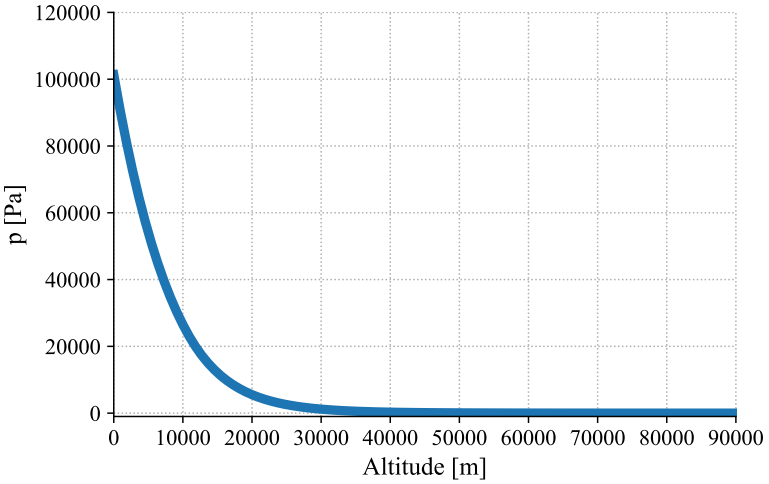


Figure 4.5: The variation of pressure with altitude

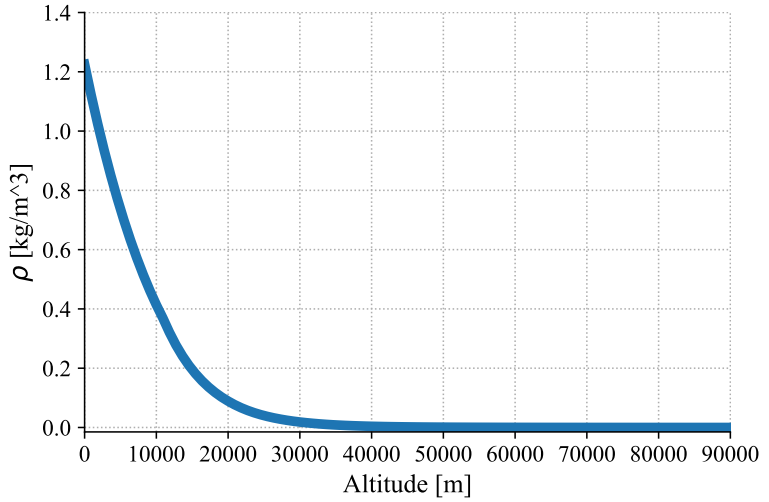


Figure 4.6: The variation of density with altitude

4.1.3.1.3 Inviscid Flow Analysis on the Fore-Body

The compression ramps on a fore-body are responsible for generating an oblique shock wave system to compress the captured airflow from the supersonic free-stream Mach number to a lower supersonic Mach number.. The theory of oblique shock waves explains how oblique shock waves are generated.

The Theory of Oblique Shock Waves An object moving through a fluid transmits information-relaying sound waves about the presence of the object to the fluid ahead of the object. When the object is moving at a supersonic speed, the speed at which information-relaying sound waves move through the fluid is slower than the speed at which the object is moving (Section 4.1.3.1.1). The sound waves cannot work their way upstream. Consequently, they pile up, coalesce and form a shock wave (Anderson 2010).

A shock wave is an extremely thin region across which flow properties discontinuously change. The change in fluid properties across a shock wave is adiabatic and irreversible. The Mach number across a shock wave decreases while the static pressure, density and temperature increase. The stagnation pressure and density across a shock wave decrease while the stagnation temperature remains unchanged (Anderson 2010).

Oblique shock waves are generated as a result of supersonic air flowing over a compression ramp. Consider supersonic air flowing over a wall, as illustrated in figure 4.7. The wall is turned upward at the corner through the deflection angle θ. This resembles the flow over a compression ramp on a fore-body.

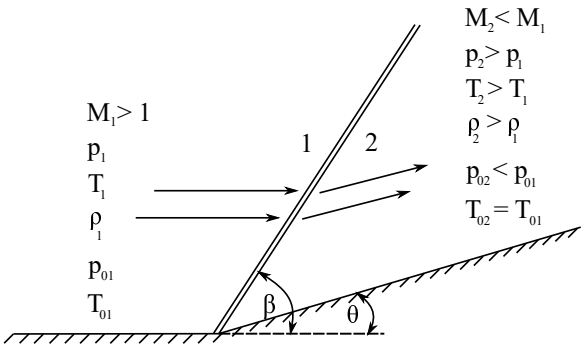


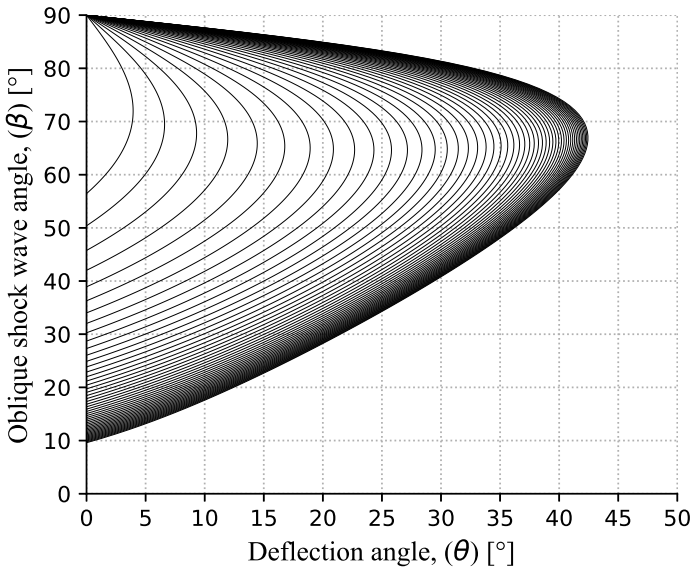
Figure 4.7: An oblique shock wave

The air flowing over the wall cannot flow into and out of the wall. Therefore, the component of velocity perpendicular to the wall is zero. The physical principle of mass conservation is that the amount of fluid entering a region must be equal to the amount of fluid leaving the

region plus the amount of fluid stored within the region. For this to be true, the air flowing over the wall must remain tangent to the wall. Therefore, the air is also deflected upward at the corner through the deflection angle θ. This upward deflection causes the flow to turn into itself. When supersonic flow is made to turn into itself, an oblique shock wave forms. The upstream flow cannot sense the presence of the corner. Therefore, the oblique shock wave discontinuously redirects the flow at the corner (Anderson 2010).

The angle between the oblique shock wave and the upstream flow direction, denoted by β, is referred to as the oblique shock wave angle. The relationship between the deflection angle, the oblique shock wave angle and the Mach number of the flow upstream of the corner is referred to as the $\theta-\beta-M$ relation, as represented by equation 4.10. Figure 4.8 is a graphical representation of equation 4.10 for upstream Mach numbers ranging from $M_1 = 1.2$ on the left to $M_1 = 10$ on the right (Anderson 2010).

$$\tan\theta = 2\cot\beta\frac{M_1^2\sin^2\beta - 1}{M_1^2(\gamma + \cos 2\beta) + 2} \tag{4.10}$$



,

Figure 4.8: A graphical representation of the $\theta - \beta - M$ relation with $\gamma = 1.4$

Based on figure 4.8, there is a maximum deflection angle θ_{max} for any given upstream Mach number. The maximum deflection angle represents the maximum value for which an attached straight oblique shock wave exists. Exceeding the maximum deflection angle will cause a curved detached shock wave to form ahead of the corner. The maximum deflection angle separates two oblique shock wave solutions for a given upstream Mach number. The large oblique shock wave angle is the strong shock solution, and the small oblique shock wave angle is the weak shock solution. The strong shock solution generates a subsonic downstream Mach

number flow, whereas the weak shock solution generates a lower supersonic downstream Mach number flow. The weak shock solution generally occurs in nature except in cases where the back pressure is high (Anderson 2010).

The equations used to calculate the fluid property changes across oblique shock waves are presented in appendix B. Equations B.1 through to B.6 are technically used to calculate the fluid properties across normal shock waves. However, a normal shock wave is an oblique shock wave with a deflection angle of 0° and a shock wave angle of 90°. Therefore, these equations can be used to compute the fluid properties of the air downstream of an oblique shock wave provided that the normal component of the oncoming Mach number, i.e. $M \sin \beta$, is used. In the case of Mach number, equation B.1 calculates the normal component of the Mach number just downstream of the oblique shock wave, i.e. $M_2 \sin(\beta - \theta)$. To obtain the value of M_2, the calculated value must be divided by the value of $\sin(\beta - \theta)$.

The Principle of Staged Compression The deceleration of the captured air from a supersonic to a subsonic Mach number is accomplished through a normal shock wave. If the performance of an inlet were solely reliant on this Mach number requirement, then a single normal shock wave would be enough for the inlet to perform its intended task. However, this is not the case. The total pressure loss of the air flowing through the inlet must be minimal. This is because a loss in total pressure results in a loss in the total internal energy of the flow field. This reduces the amount of internal energy available for the ramjet nozzle to convert to kinetic energy, thus decreasing the maximum speed of the air expelled by the nozzle. The thrust generated by a ramjet is a reaction caused by the change in momentum of the air flowing through the ramjet. Therefore, a decreased maximum exit speed results in decreased thrust (Seddon and Goldsmith 1999).

The total pressure loss across a normal shock wave increases non-linearly with an increase in the upstream Mach number. The total pressure loss across a normal shock wave with an upstream Mach number greater than Mach 1.5 can lead to inefficient thrust production. The principle of staged compression was introduced to minimise total pressure loss. It was formed on the basis that compressing air in stages through a series of oblique shock waves and subsequently by a normal shock wave significantly reduces the total pressure loss across an inlet. The amount by which the total pressure loss is reduced is dependent on several factors such as: the number of oblique shock waves, the Mach number of the air just upstream of the shock waves and the oblique shock wave angles. The oblique shock waves gradually decelerate the flow to a lower supersonic Mach number before the normal shock wave. Thus reducing the total pressure loss across the normal shock wave. The airflow also experiences total pressure loss across the oblique shock waves. However, the total pressure loss across

the weak oblique shock waves is considerably smaller than the total pressure loss across the normal shock wave (Seddon and Goldsmith 1999).

The greater the number of oblique shock waves, the lower the total pressure loss across the inlet. This is because the more oblique shock waves there are, the weaker the oblique shock waves need to be to achieve the necessary amount of deceleration before the normal shock wave. Furthermore, the more oblique shock waves there are, the more opportunities there are for the oblique shock waves to decelerate the flow to an even lower supersonic Mach number before the normal shock wave. The greatest total pressure loss occurs across the normal shock wave. Therefore, the lower the Mach number upstream of the normal shock wave, the lower the total pressure loss. The principle of staged compression can be extended to its limits to lead to the concept of isentropic compression. Isentropic compression is achieved using a smoothly contoured fore-body which generates an infinite number of infinitely weak oblique shock waves (Seddon and Goldsmith 1999).

Oblique Shock Wave Interaction A fore-body with multiple compression ramps has multiple oblique shock waves. Ideally, the oblique shock waves should converge at a single point, i.e. the cowl lip. This shock wave structure is preferred because it aims to ensure a maximum mass flow rate. Furthermore, this shock wave structure minimises the spillage and pre-entry drag, which are discussed in section 4.1.3.4.3. The interaction of an oblique shock wave system is illustrated in figure 4.9.

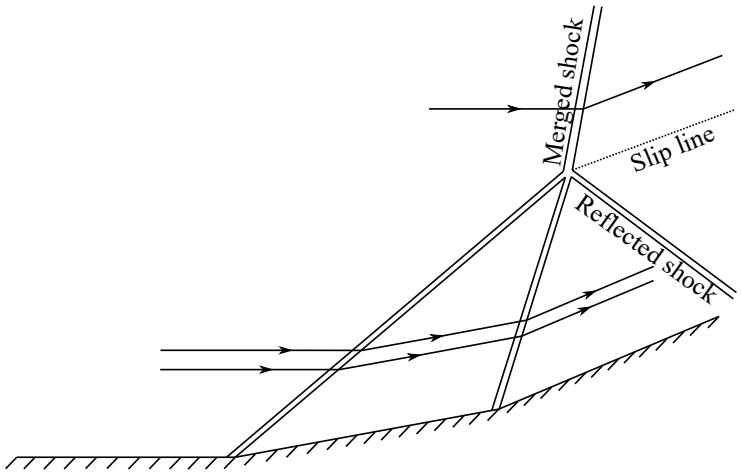


Figure 4.9: The intersection of two left-running shock waves

Based on figure 4.9, the converging oblique shock waves merge into a stronger shock wave. The merged shock wave has a different shock wave angle to the oblique shock waves. Therefore, the flow downstream of the merged shock wave moves in a different direction to the flow after the second oblique shock wave. The flow behind the merged shock wave is separated from

the flow behind the second oblique shock wave by a slip line. A reflected shock wave forms at the point of intersection. The purpose of the reflected shock wave is to adjust the flow such that the direction of flow in the regions separated by the slip line is the same. Shock wave reflection is not specular reflection as in the case of light. The reflected shock wave forms to satisfy the downstream conditions, such as a sudden change in direction (Anderson 2010).

4.1.3.1.4 Inviscid Flow Analysis at the Normal Shock Wave

Fore-bodies generate weak oblique shock waves, which decelerate the captured air from a higher supersonic Mach number to a lower supersonic Mach number. The air delivered to the combustion chamber must be subsonic. Decelerating the captured air to a subsonic Mach number is achieved through a normal shock wave located at the internal diffuser entry plane. A normal shock wave is an oblique shock wave with a deflection angle of 0° and a shock wave angle of 90°, as illustrated in figure 4.10. It is a strong oblique shock wave that occurs in instances where there is a high back pressure in the flow field (Anderson 2010). The equations used to calculate the changes in the fluid properties across normal shock waves are presented in appendix B.

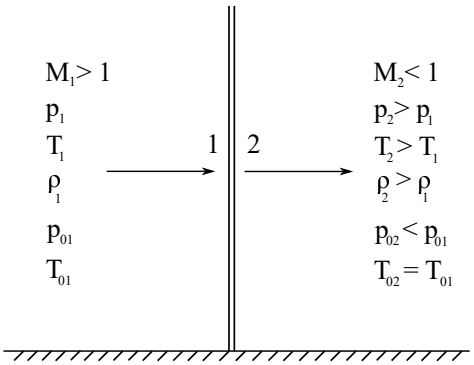


Figure 4.10: A normal shock wave

4.1.3.1.5 Inviscid Flow Analysis in the Internal Diffuser

The airflow downstream of the normal shock wave is subsonic. However, it often needs to be decelerated to an even lower Mach number (i.e. below the blow-off limit) before entering the combustion chamber. The internal diffuser is a diverging duct that decelerates the subsonic airflow just downstream of the normal shock wave to an appropriate Mach number for the combustion chamber. The theory of compressible flow through ducts explains how this is achieved.

The Theory of Compressible Flow Through Ducts Consider a compressible flow through a duct whereby the cross-sectional area of the duct changes as a function of x, as illustrated in figure 4.11. This flow field is technically 3D. However, the components of the flow field variables in the y and z directions may be neglected if the area variation is moderate and the flow field variables in the y and z directions are small relative to the x-component. Such a flow field is referred to as quasi-1D flow (Anderson 2010).

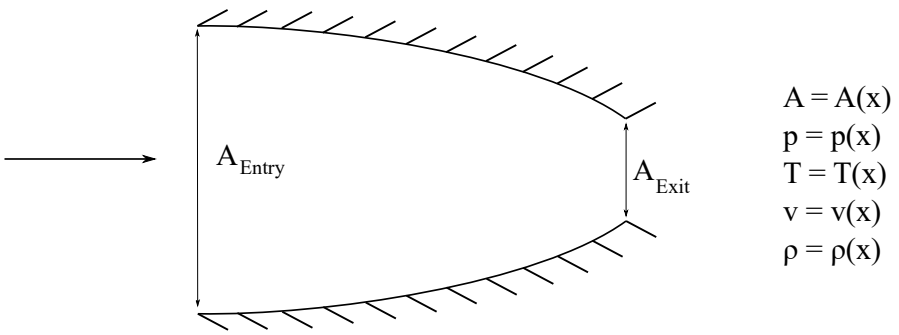


Figure 4.11: Quasi-1D flow

The integral forms of the continuity, momentum and energy equations have been used to obtain the governing equations for quasi-1D flow. One such governing equation is the Hugoniot area-velocity relation presented in equation 4.11 (Anderson 2010).

$$\frac{dA}{A} = (M^2 - 1)\frac{dv}{v} \tag{4.11}$$

Based on equation 4.11, the highest possible Mach number that subsonic flow can be isentropically accelerated to via area contraction is $M = 1$. Similarly, the lowest possible Mach number that supersonic flow can be isentropically decelerated to via area contraction is $M = 1$. This leads to another important relation in the study of quasi-1D flow: the area-Mach number relation, presented in equation 4.12 (Anderson 2010).

$$\left(\frac{A}{A^*}\right)^2 = \frac{1}{M^2}\left[\frac{2}{\gamma+1}\left(1 + \frac{\gamma-1}{2}M^2\right)\right]^{\frac{\gamma+1}{\gamma-1}} \tag{4.12}$$

Equation 4.12 indicates that the Mach number at any location in a duct is a function of the ratio of the local duct area, denoted by A, to the sonic throat area, denoted by A^*. The throat of a duct is the minimum area of the duct. The sonic throat area is the minimum duct area where sonic conditions exist. There are two Mach number solutions for a given area ratio. One is subsonic while the other is supersonic. The solution applicable to a specific case depends on the pressures at the entry and exit of the duct (Anderson 2010).

A stream of supersonic air flowing through a contracting duct can be isentropically reduced to sonic conditions at the exit of the duct. A contracting duct is said to be choked when the

airflow is sonic at the throat. If the contraction ratio (i.e. A_{exit}/A_{entry}) is smaller than that required to decelerate the flow to sonic conditions (Equation 4.12), supersonic flow would not be able to exist in the duct. A detached bow shock wave will form upstream of the duct entry to ensure that the flow entering the duct is subsonic. The subsonic air accelerates to sonic conditions at the exit as a result of the area contraction. Excess mass is spilled out. This type of flow is known as unstarted flow, as illustrated in figure 4.12 (Kantrowitz and Donaldson 1945).

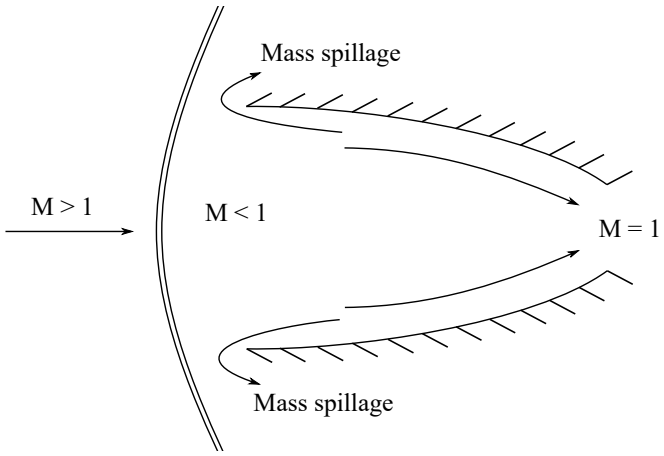


Figure 4.12: Unstarted flow in a contracting duct

A flow is started when the normal shock wave has been swallowed into the duct. Kantrowitz and Donaldson (1945) suggested that for the normal shock wave to be swallowed spontaneously into the duct, the contraction ratio must be greater than the Kantrowitz limit, as represented by equation 4.13.

$$\left(\frac{A_{exit}}{A_{entry}}\right)_{Kantrowitz} = \left[\frac{\gamma-1}{\gamma+1} + \frac{2}{(\gamma+1)M_e^2}\right]^{-\frac{1}{2}} \left[\frac{2\gamma}{\gamma+1} + \frac{\gamma-1}{(\gamma+1)M_e^2}\right]^{-\frac{1}{\gamma-1}} \tag{4.13}$$

4.1.3.1.6 Inviscid Flow Analysis at the Cowl Lip

The cowl lip is not officially a station at which flow analyses are performed. However, there are some aerodynamic flow features that may occur at the cowl lip. These flow features are discussed in the current section.

The cowl lip is located at the point where the fore-body generated oblique shock waves converge. It is responsible for dividing the incoming airflow into an internal and external airflow. It can have a sharp or a blunt profile. A sharp cowl lip may be difficult to manufacture. Therefore, the cowl lip typically has a blunt profile. A blunt cowl lip is a small blunt body in

a supersonic flow field. A curved bow shock wave forms when a blunt body moves through a supersonic flow. This is discussed in further detail in the following paragraphs.

Detached Bow Shock Wave in Front of a Blunt Body A curved bow shock wave forms on a blunt body when the blunt body moves through a compressible fluid at a supersonic speed. The high subsonic pressure behind the shock wave drives the shock wave upstream to a position some distance from the object, as illustrated in figure 4.13 (Anderson 2010).

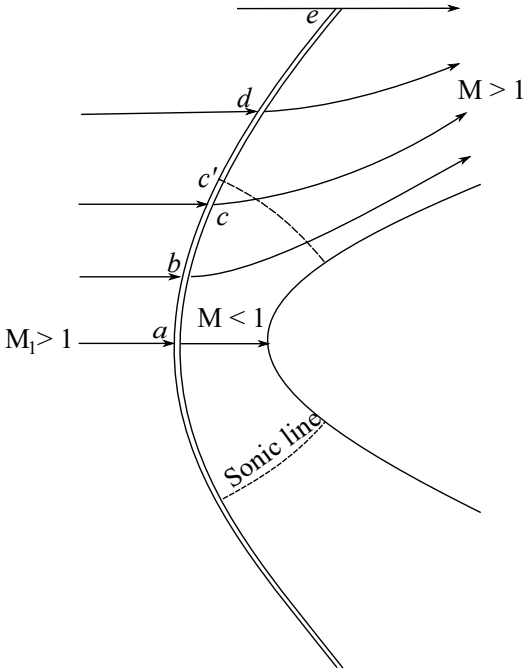


Figure 4.13: A detached bow shock wave in front of a blunt body

A detached bow shock wave is an instance in nature where all possible oblique shock wave solutions can be observed at once for a given upstream Mach number. All the possible oblique shock wave solutions are illustrated in figure 4.13 and explained as follows (Anderson 2010):

- Point a corresponds to a normal shock wave. The flow moving past this point is subsonic downstream of the shock wave.
- Point b corresponds to the strong oblique shock wave solution. Again, the flow moving past this point is subsonic downstream of the shock wave.
- The flow deflection increases further along the bow shock until point c. Point c corresponds to the maximum deflection angle.
- All the points from c' to e correspond to the weak oblique shock wave solution. The flow moving past these points is supersonic downstream of the shock wave.
- Point e corresponds to a Mach wave.

- The sonic line separates the subsonic and supersonic regions downstream of the curved bow shock wave.

4.1.3.2 Viscous Flow Field Analysis

The assumption of inviscid flow is not always applicable to real-world compressible flows. The interaction of a solid supersonic inlet surface and the air flowing through the inlet introduces a viscous boundary layer to the supersonic inlet flow field. The theory of viscous boundary layer flow is introduced in the present section. After that, the implications of boundary layer flow on a supersonic inlet flow field are discussed.

4.1.3.2.1 Boundary Layer Theory

Real supersonic inlet flow fields are solved by considering the flow as consisting of two independent components, i.e. a potential non-viscous flow region and a viscous boundary layer. A boundary layer is a thin region of flow adjacent to a surface where the flow is retarded by the influence of friction between the flow and the surface (Anderson 2010).

There are two main types of boundary layer flow, i.e. laminar and turbulent. The characteristics of the different types of boundary layer flow are demonstrated by considering the boundary layer development resulting from uniform free-stream flow over a flat plate, as illustrated in figure 4.14. The boundary layer that develops on the flat plate is initially laminar, starting from the leading edge. The laminar boundary layer flow is characterised by smooth and regular streamlines. The boundary layer then reaches a region where it becomes unstable and small regions of turbulence begin to emerge. This region is defined as the transition region. The flow within the transition region can sometimes exhibit the characterises of both laminar and turbulent boundary layer flows. The transition region ends when the boundary layer becomes completely turbulent. The turbulent boundary layer flow is characterised by streamlines that are highly irregular, random and tortuous (Anderson 2010).

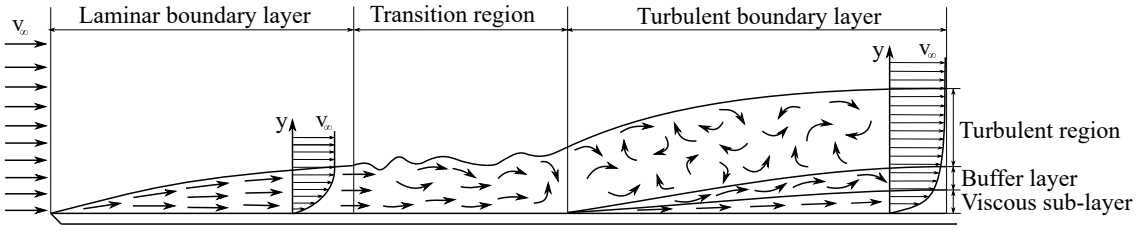


Figure 4.14: The development of a boundary layer over a flat plate

There are three different regions within the turbulent boundary layer that may be differentiated as a function of the perpendicular distance from the surface. These regions are referred to as the viscous sub-layer, the buffer layer and the turbulent region, as illustrated in figure 4.14. The viscous sub-layer is a thin layer of flow adjacent to the surface of the plate. The characteristics of the flow within the viscous sub-layer are similar to those of a laminar boundary layer. The buffer layer is right next to the viscous sub-layer. It is characterised by the emergence of small-scale turbulence. The region of flow right next to the buffer layer and extending to the free-stream flow is the fully turbulent region. The flow within this region is characterised by turbulent mixing (Incropera et al. 2007).

The fluid within a boundary layer is characterised by a velocity profile that is zero at the surface and increases to the free-stream velocity in the direction perpendicular to the surface (Anderson 2010). Both the laminar and turbulent boundary layer velocity profiles are illustrated in figure 4.14. The turbulent boundary layer velocity profile is relatively flat compared to the laminar boundary layer velocity profile. This is a consequence of the steep velocity gradient within the viscous sub-layer resulting from the mixing within the buffer layer and the turbulent region (Incropera et al. 2007).

The height above a surface required to reach 99% of the free-stream velocity is defined as the boundary layer thickness, denoted by δ. The boundary layer thickness is a function of: the distance from the leading edge of the surface; the pressure gradient across the surface; any heat transfer between the fluid and the surface; surface roughness; and the Reynolds number of the flow.

Uniform inviscid flow over a flat plate has a flat velocity profile. The velocity profile of the airflow within a boundary layer is not flat. It is zero at the surface and increases to the velocity of the mainstream flow in the direction perpendicular to the surface. This causes a velocity deficit to occur within the boundary layer. The mass flow rate of an airflow is a function of the air velocity. The velocity deficit within the boundary layer reduces the mass carrying capability of the airflow within the boundary layer. Therefore, resulting in a mass flow rate deficit within the boundary layer. To obtain the mass flow rate computed by inviscid flow calculations, the surface must be displaced a certain distance in the direction perpendicular to the surface. This distance is referred to as the displacement thickness, denoted by δ^*. The displacement thickness also represents the physical distance through which the non-viscous potential airflow is displaced outward due to the velocity decrease within the boundary layer. This gives rise to the concept of an 'effective surface'. The effective surface is the given surface plus the displacement thickness (Anderson 2010).

The momentum flow rate of an airflow is also a function of the air velocity. Due to the velocity deficit within the boundary layer, the momentum flow rate of the air within the boundary

layer is less than it would be if no boundary layer existed. As a result, the air flowing over a surface experiences a momentum deficit compared with that of inviscid potential flow. To obtain the momentum flow rate computed by inviscid flow calculations, the surface must be displaced a certain distance in the direction perpendicular to the surface. This distance is referred to as the momentum thickness, denoted by θ^* (Anderson 2010).

4.1.3.2.2 Implications of Viscous Effects on Supersonic Inlet Flow Fields

Viscous boundary layers affect a supersonic inlet flow field in several ways. The boundary layers cause a deficit in the mass and momentum flow rates of the inlets, as discussed previously. Furthermore, the boundary layers alter the effective supersonic inlet surfaces. This causes the fore-body compression ramp angles to appear larger to the captured airflow than they are in reality. As a result, the oblique shock wave angles differ from those computed by inviscid flow calculations (Section 4.1.3.1.3). The boundary layers also cause the effective cross-sectional areas of the internal diffuser to be smaller than they are in reality. As a result, the internal diffuser area expansion ratio is smaller than the real expansion ratio of the duct. Therefore, the Mach number of the air at the AIP could potentially be larger than that computed by inviscid flow calculations (Section 4.1.3.1.5).

Boundary Layer Separation The boundary layers in a supersonic inlet flow against an adverse pressure gradient. When this happens, the pressure reinforces the retarding viscous forces close to the surface. This causes the difference between the flow velocity close to the surface and the free-stream velocity to become even more pronounced. The result is an even greater boundary layer growth. If the boundary layer travels far enough against an adverse pressure gradient, the deceleration of the boundary layer will ultimately reverse the direction of the flow within the boundary layer. The boundary layer develops a point of inflection and separates from the surface. Boundary layer separation is characterised by the detachment of a boundary layer from the surface into a broader wake (Anderson 2010). Boundary layer separation is undesirable in supersonic inlet flow fields. This is because separated flow is characterised by high levels of distortion and total pressure loss. Supplying separated air to the combustion chamber will negatively affect the performance of the combustion chamber and, consequently, the performance of the engine as a whole (Seddon and Goldsmith 1999).

Shock-Wave/Boundary-Layer Interactions Shock-wave/boundary-layer interactions are frequently occurring phenomena in supersonic flows. The shock waves introduce an infinitely large adverse pressure gradient to the boundary layer on the surface. The strength of a shock wave impacts significantly on the characteristics of a shock-wave/boundary-layer interaction.

The shock wave strength is characterised by the total pressure ratio across a shock wave. The higher the total pressure ratio, the stronger the shock wave (Houghton and Carpenter 2003).

The interaction of the oblique shock waves and the boundary layer on the fore-body yields complex shock wave patterns. A weak oblique shock wave gradually thickens the boundary layer upstream of the compression ramp. The thickened boundary layer makes the sharp corner appear smoother to the air flowing over the ramp. A series of compression waves form on the thickened boundary layer and converge with the oblique shock wave at some distance above the ramp, as illustrated in figure 4.15 (Houghton and Carpenter 2003).

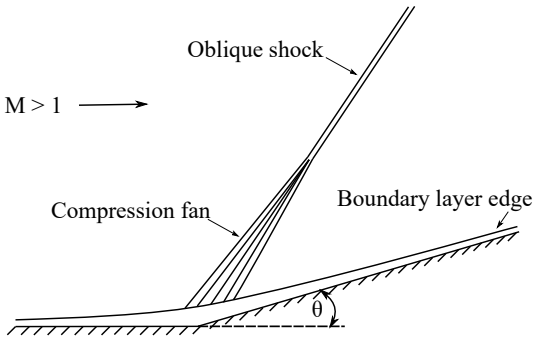


Figure 4.15: The characteristics of a weak oblique shock-wave/boundary-layer interaction

An oblique shock wave strengthens when the upstream Mach number increases or when the compression ramp angle increases. The interaction of a strong oblique shock wave with a boundary layer causes the boundary layer to separate from the surface and subsequently turn back and reattach to the surface at some downstream location. As a result, a separation bubble forms. The high pressure behind the shock wave feeds upstream through the subsonic portion of the boundary layer, causing the leading edge of the separation bubble to be upstream of the compression corner. The separation bubble turns the airflow upstream of the compression corner into itself, thus generating an oblique shock wave. A second oblique shock wave forms at the rear end of the separation bubble. Both the leading and rear shock waves merge into the resultant oblique shock wave generated by the compression ramp (Houghton and Carpenter 2003). The complex flow characteristics of a strong oblique shock-wave/boundary-layer interaction at a compression ramp are shown in figure 4.16. The interaction between the leading and rear oblique shock waves is similar to the interaction of two left-running shock waves, as illustrated in figure 4.9.

The interaction of the terminating normal shock wave and the boundary layers on the inlet surfaces also cause a complex shock wave structure. The complex shock wave structure can take on different forms depending on the strength of the normal shock wave and the type of boundary layer, i.e. laminar or turbulent.

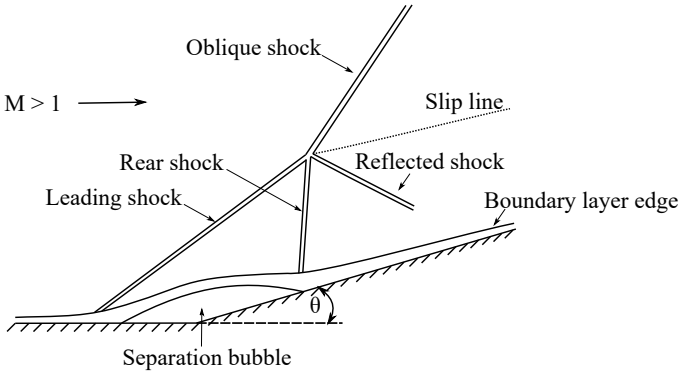


Figure 4.16: The characteristics of a strong oblique shock-wave/boundary-layer interaction

When a weak normal shock wave (i.e. a normal shock wave with an upstream Mach number just above one) interacts with a laminar boundary layer, the boundary layer ahead of the normal shock wave gradually thickens. The thickening of the boundary layer causes a series of compression waves to develop just upstream of the normal shock wave. The compression waves converge with the normal shock wave at some distance above the surface. The boundary layer begins to thin out immediately after the normal shock wave. This causes the air flowing over the thinning boundary layer to expand locally to a slightly supersonic speed again. This is followed by another near-normal shock wave that develops similarly to the initial normal shock wave. This process repeats several times until the flow settles at a subsonic Mach number, as illustrated in figure 4.17 (Houghton and Carpenter 2003).

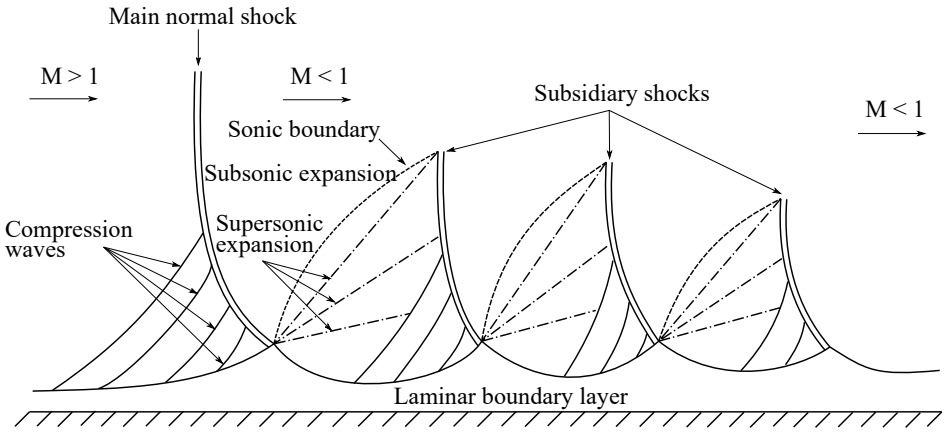


Figure 4.17: The interaction of a weak normal shock wave with a laminar boundary layer

The characteristics of the interaction between the normal shock wave and the laminar boundary layer change as the normal shock wave strengthens. The main normal shock wave becomes stronger than the subsidiary shock waves. The subsidiary shock waves occur less frequently until only one occurs, as illustrated in figure 4.18. This is expected because a stronger main normal shock wave will produce a lower subsonic Mach number behind it. This decreases the likelihood of the airflow behind the main normal shock wave expanding to supersonic speeds (Houghton and Carpenter 2003).

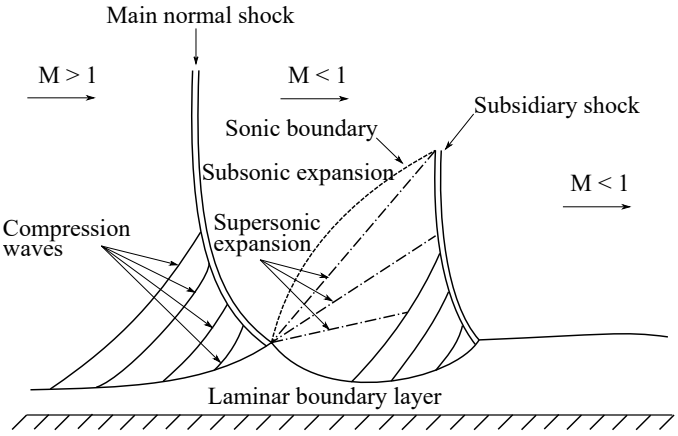


Figure 4.18: The interaction of a stronger normal shock wave with a laminar boundary layer

A further increase in the strength of a normal shock wave causes the rate of upstream boundary layer thickening to increase. The boundary layer separates from the surface, and subsequently turns back and reattaches to the surface at some downstream location. The high pressure behind the shock wave feeds upstream through the subsonic portion of the boundary layer, causing the point of separation to be slightly ahead of the normal shock wave (Anderson 2010). The separation bubble causes the oncoming supersonic flow to turn into itself, thus generating an oblique shock wave referred to as the leading shock. The leading shock eventually intersects the normal shock wave at a particular distance above the surface. The point of intersection is referred to as the bifurcation point. A second oblique shock wave, referred to as the trailing shock, is generated at the bifurcation point and propagates back toward the surface. It is generated to satisfy the compatibility of flow direction (Seddon and Goldsmith 1999). The characteristics of the interaction of a boundary layer with a strong normal shock wave are shown in figure 4.19. The shock wave structure illustrated in figure 4.19 is referred to as a lambda shock wave because it resembles the lowercase Greek letter lambda, i.e. 'λ'.

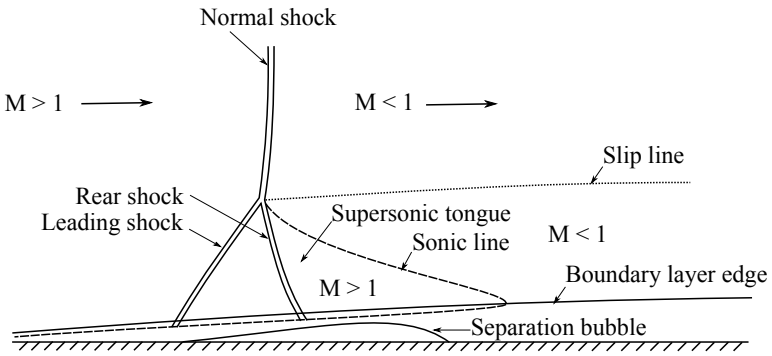


Figure 4.19: The interaction of a strong normal shock wave with a laminar boundary layer

The flow in a lambda shock wave is divided into three regions: the mainstream flow passing through the normal shock; an intermediate layer whereby the flow passes through the bifurcated shock system; and the viscous layer, including the boundary layer separation bubble. The downstream properties of the flow in the mainstream differ from the downstream properties of the flow in the intermediate layer. This is because the flow properties downstream of the mainstream normal shock result from the oncoming flow passing through a strong normal shock wave. In contrast, the flow properties downstream of the intermediate layer result from the oncoming flow passing through two weak oblique shock waves. The slip line is the boundary where the static pressure and flow direction of the mainstream and the intermediate layer match. The flow above the slip line is subsonic, whereas the flow below the slip line increases in velocity from the slip line to the edge of the boundary layer and may become supersonic. The flow downstream of the two weak oblique shock waves is supersonic due to the weak strength of the leading and rear shock waves. This results in the presence of a supersonic 'tongue' that extends downstream of the rear shock, as illustrated in figure 4.19 (Seddon and Goldsmith 1999).

Increasing the strength of a normal shock wave even further results in the occurrence of boundary layer separation without any subsequent reattachment. For flat plates, boundary layer separation generally occurs when the Mach number of the airflow upstream of the normal shock wave exceeds Mach 1.3 (Bordbar and Yao 2015; Seddon 1966; Slater 2012).

The interaction of a weak normal shock wave with a turbulent boundary layer differs from its interaction with a laminar boundary layer. The upstream thickening of the boundary layer is rapid, causing the compression waves to occur over a tiny localised region. The thinning of the laminar boundary layer behind the normal shock wave does not occur in turbulent boundary layers. Since the turbulent boundary layer does not thin out, there are no opportunities for the flow to expand to supersonic speeds. Therefore, the subsidiary normal shock waves do not develop, as illustrated in figure 4.20 (Houghton and Carpenter 2003).

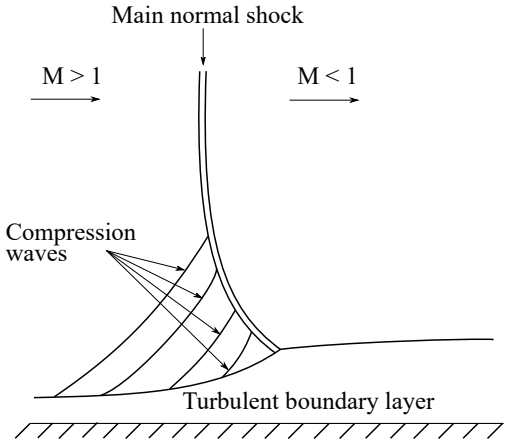
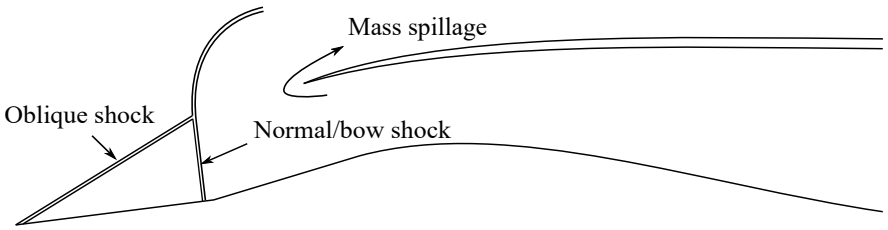


Figure 4.20: The interaction of a weak normal shock wave with a turbulent boundary layer

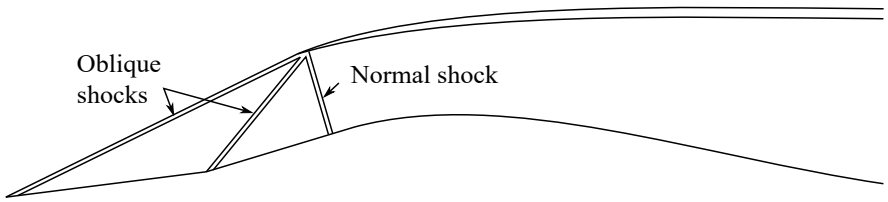
An increase in the strength of the normal shock wave causes the interaction between the normal shock wave and the turbulent boundary layer to resemble the structure illustrated in figure 4.19 (Houghton and Carpenter 2003).

4.1.3.3 Supersonic Inlet Modes of Operation

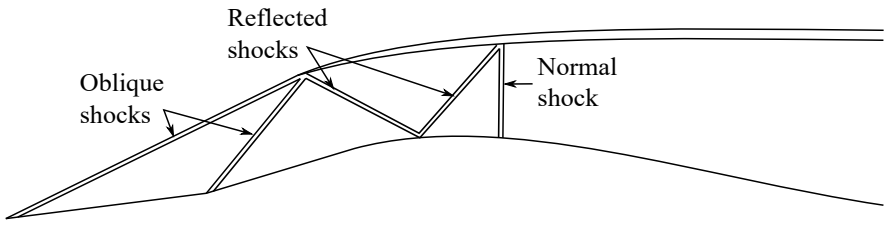
A supersonic inlet has three modes of operation that are characterised by the position of the normal shock wave, as illustrated in figure 4.21. When the normal shock wave is located ahead of the cowl lip (Figure 4.21a), the inlet is said to be operating in the sub-critical mode. This occurs when the amount of air supplied by the inlet is more than that required by the engine. The normal shock wave is expelled so that the excess air is removed. An inlet operating in this mode may experience an instability known as diffuser buzz, which is characterised by the oscillation of the shock wave system (Seddon and Goldsmith 1999).



(a) Sub-critical mode of operation



(b) Critical mode of operation



(c) Super-critical mode of operation

Figure 4.21: Supersonic inlet modes of operation

An inlet with a normal shock wave located precisely at the cowl lip, as illustrated in figure 4.21b, is said to be operating in the critical mode of operation. This occurs when the amount of air supplied by the inlet is the exact amount required for the engine to operate efficiently

(Seddon and Goldsmith 1999). The position of the cowl lip is not the most stable position for the normal shock wave to be located. Suppose the inlet experiences a disturbance during flight, such as a Mach number fluctuation. In that case, the position of the normal shock wave makes it easier for it to be expelled from the inlet and consequently experience diffuser buzz. External compression inlets are designed to operate in the critical mode.

The super-critical mode of operation occurs when the normal shock wave is positioned inside the internal diffuser (Figure 4.21c). When the amount of air supplied by the inlet is less than that required by the engine, the normal shock wave is swallowed into the internal diffuser. This is the most stable position for a normal shock wave to be located.

There may be some shock wave reflection that occurs inside an inlet operating in the super-critical mode. Shock wave reflection occurs when an oblique shock wave impinges on another solid surface. As in the case illustrated in figure 4.22, a horizontal supersonic compressible flow between two parallel walls experiences a sudden change in direction due to the presence of a corner on the bottom wall. The compressible flow is turned into itself. As a result, an oblique shock wave is generated. The upper wall remains parallel to the original flow direction, keeping the flow tangent to the wall parallel to the original flow direction. For the supersonic flow to exist in this space, another oblique shock wave must form where the incident oblique shock wave impinges on the upper wall. The function of the second oblique shock wave is to rotate the flow such that the flow near the upper wall remains tangent to it (Anderson 2010).

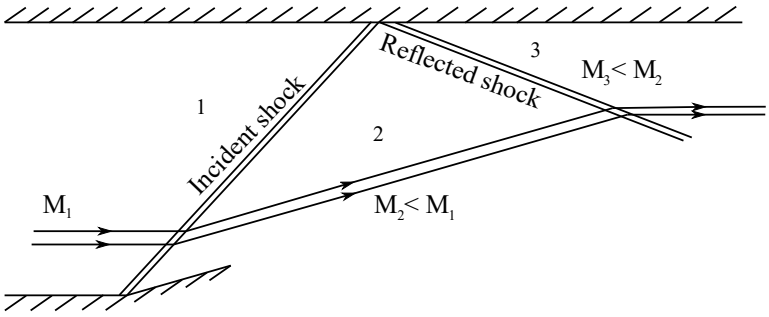


Figure 4.22: Oblique shock wave reflection

4.1.3.4 Supersonic Inlet Performance Parameters

The performance of a supersonic inlet is specified by parameters that describe the inlet capability and efficiency. The most common supersonic inlet performance parameters used are total pressure recovery, mass flow ratio and total inlet drag (Esterhuyse 1997; Faro 1965; Seddon and Goldsmith 1999; Slater 2012).

4.1.3.4.1 Total Pressure Recovery

The total pressure recovery of an inlet is the ratio between the total pressure of the air at the AIP to the total pressure of the air at free-stream conditions, as per equation 4.14.

$$P_{R} = \frac{p_{0,AIP}}{p_{0,\infty}} \tag{4.14}$$

where:

P_{R} is the total pressure recovery of the inlet,
$p_{0,AIP}$ is the total pressure at the AIP and,
$p_{0,\infty}$ is the total pressure of the free-stream airflow

The total pressure recovery directly influences the amount of thrust generated by an engine, as discussed in section 4.1.3.1.3. Therefore, the total pressure recovery across an inlet must be maximised to ensure optimum engine performance (Seddon and Goldsmith 1999).

Based on the theory of inviscid compressible flow, air experiences a loss in total pressure when it flows across a shock wave. The total pressure recovery across an oblique shock wave is calculated using equation 4.15. The total pressure upstream and downstream of the oblique shock wave are represented by subscripts '1' and '2', respectively. The total pressure recovery across a normal shock wave is calculated by substituting a shock wave angle of 90° into equation 4.15 (Ames Research Staff 1953).

$$\frac{p_{0,2}}{p_{0,1}} = \left[\frac{(\gamma+1)M_1^2\sin^2\beta}{(\gamma-1)M_1^2\sin^2\beta+2}\right]^{\frac{\gamma}{\gamma-1}}\left[\frac{\gamma+1}{2\gamma M_1^2\sin^2\beta-(\gamma-1)}\right]^{\frac{1}{\gamma-1}} \tag{4.15}$$

The fore-body of an inlet can generate several oblique shock waves. The total pressure recovery of the air flowing through the shock wave system is a product of all the total pressure recoveries across each individual shock wave (Anderson 2010).

The air flowing through an inlet also experiences a loss in total pressure due to viscous flow phenomena in real compressible flows. The total pressure loss is specifically due to the friction between the air and the inlet walls, shock-wave/boundary-layer interaction, and the turbulent mixing caused by boundary layer separation or near separation (Seddon and Goldsmith 1999).

4.1.3.4.2 Mass Flow Ratio

The mass flow ratio of an inlet is the ratio of the actual mass flow rate of the air captured by an inlet to the maximum possible mass flow rate that the inlet can support. The inlet capture

area limits the maximum possible mass flow rate. The mass flow ratio can be computed using equation 4.16 (Faro 1965).

$$m_{_R} = \frac{\dot{m}_{actual}}{\dot{m}_{maximum}} = \frac{\rho_\infty A_\infty v_\infty}{\rho_\infty A_{cap} v_\infty} \tag{4.16}$$

The capture area is a geometric feature of a supersonic inlet (Figure 4.23). The difference between the inlet capture area (A_{cap}) and the cross-sectional area of the stream-tube of the air that is actually captured by the inlet (A_∞) is illustrated in figure 4.23. The value of $m_{_R}$ is one when the inlet is operating in the critical and super-critical modes. However, it is less than unity when the inlet operates in the sub-critical mode (Faro 1965).

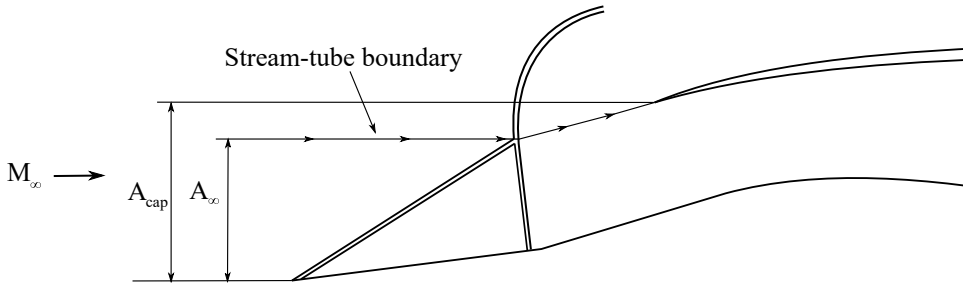


Figure 4.23: The stream tube area and the inlet capture area

The performance of a supersonic inlet is typically represented by a characteristic curve that illustrates the relationship between the inlet total pressure recovery and mass flow ratio. Such a curve is illustrated in figure 4.24. Figure 4.24 also illustrates the modes of operation that correspond to certain positions on the curve.

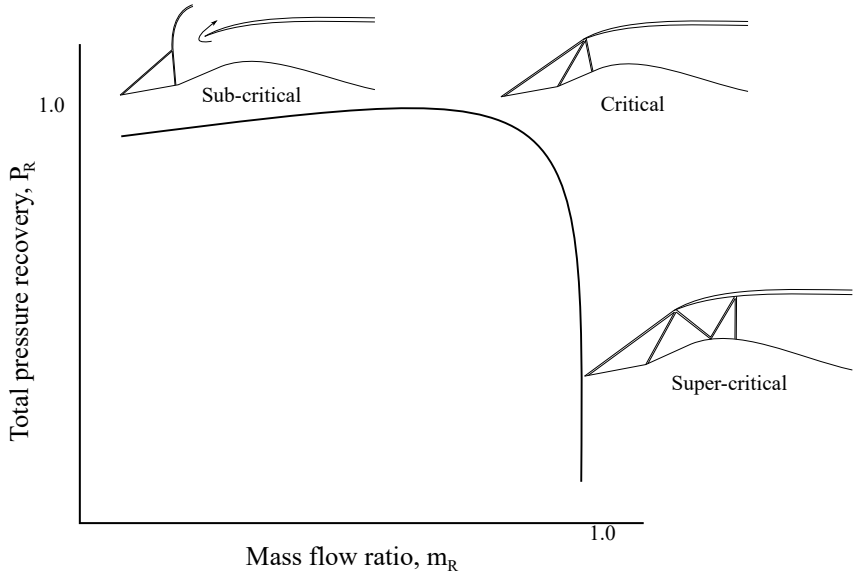


Figure 4.24: The performance characteristic curve for a supersonic inlet

4.1.3.4.3 Drag

The primary objective of any propulsion system is to generate thrust to propel an aircraft in a particular flight direction. Seddon and Goldsmith (1999) define the inlet drag as the resultant force opposing the flight direction. It is produced on the inlet system by the external and the internal flow fields.

The cowl wave drag is an external drag component. It is a pressure drag due to the frontal projected area of the cowl in relation to the capture stream-tube. The larger the cowl projected area, the greater the cowl wave drag. It should be noted that external-compression inlets are not recommended for flight Mach numbers above Mach 2.5. Flying at a Mach number higher than Mach 2.5 requires the fore-body to turn the air at a large angle to achieve the necessary amount of supersonic compression. The airflow typically has to be turned back to the direction of free-stream flow in the internal diffuser before it is delivered to the combustion chamber. Turning the flow back to the free-stream direction by a large angle will require a large cowl projected area. This can result in increased cowl wave drag (Esterhuyse 1997).

The other external drag components include the skin friction drag, the spillage drag, the pre-entry drag (or additive drag), and the boundary layer bleed and diverter drag. The skin friction drag is caused by the friction between the air and the cowl exterior. The spillage drag occurs when the normal shock wave is pushed out in front of the inlet resulting in air spilling out of the inlet, as illustrated in figures 4.12 and 4.21a. The pre-entry drag occurs when the inlet is operating at a Mach number below the design Mach number. An inlet operating at a Mach number below the design Mach number causes the oblique shock waves to be in front of the cowl lip. As a result, air is spilled out around the cowl lip. There is an unbounded stream-tube of air around the cowl lip. The pressure force of the unbounded stream-tube acts on the cowl external surface. This causes pre-entry drag to occur. The boundary layer diverter drag is caused by the wave pressure (static pressures behind the shock waves) and the skin friction drag on this component (Esterhuyse 1997; Seddon and Goldsmith 1999).

The internal drag is primarily caused by the boundary layer bleed. This is because the air flowing through the bleed loses momentum when it is turned away from the main flow and redirected to a bleed chamber. However, this is not a major drag contributing component (Esterhuyse 1997).

4.2 Optimisation Theory

Over the past 60 years, aerodynamic shape optimisation has become an essential part of aerodynamic design. Aerodynamic shape optimisation has many applications, including aircraft, internal pipe flows, wind turbines, etc. (Skinner and Zare-Behtash 2018). The theory of mathematical optimisation was applied in the present work to create shape optimisation algorithms that generate geometric profiles of 2D, external-compression, supersonic inlets. Mathematical optimisation is the science of computing the best solution to a well-defined mathematical problem. According to Snyman and Wilke (2018), mathematical optimisation is formally defined as the process of formulating and obtaining the solution of a constrained optimisation problem of the mathematical form presented in equation 4.17.

$$\underset{\text{w.r.t. } \mathbf{x}}{\text{minimize}}\ f(\mathbf{x}),\ \mathbf{x} = [x_1, x_2, ..., x_n]^T\ \in\ \mathbb{R}^n \tag{4.17}$$

subject to constraints:

$$g_j(\mathbf{x}) \leq 0,\ j = 1, 2, ..., m$$

$$h_k(\mathbf{x}) = 0,\ k = 1, 2, ..., r$$

The components x_i of $\mathbf{x} = [x_1, x_2, ..., x_n]^T$ are the design variables. The function $f(\mathbf{x})$ is the objective function. The constraint functions $g_j(\mathbf{x})$ and $h_k(\mathbf{x})$ represent inequality and equality constraint functions, respectively. The functions $f(\mathbf{x})$, $g_j(\mathbf{x})$ and $h_k(\mathbf{x})$ are scalar functions of the column vector $\mathbf{x}$ (Snyman and Wilke 2018).

The 2D, external-compression, supersonic inlet design and analysis tool was developed using the Python™ programming language. The Python™ SciPy module has a unified built-in function for optimising defined optimisation problems and was specifically chosen for this application. Python™ has other optimisation packages apart from the SciPy module. These include pyOpt, Mystic and NLopt. Beals and Govindarajan (2021) recently investigated the use pyOpt and found that it did not appear as though it was well maintained and did not install with current versions of NumPy. NumPy is a built-in Python™ module that consists of high-level mathematical functions to operate on large, multi-dimensional arrays and matrices.

Furthermore, Beals and Govindarajan (2021) found that NLopt and Mystic are fully functional packages and have the same algorithms as SciPy. The reason these packages and their algorithms were not included in the work done by Beals and Govindarajan (2021) was that the SciPy algorithms performed sufficiently well, such that other options were not needed. Based on the investigation conducted by Beals and Govindarajan (2021), pyOpt, Mystic and NLopt were not considered for the current work.

Several minimisation algorithms are available in the Python™ SciPy module. A minimisation algorithm is selected based on the type of mathematical model that needs to be optimised. The present research was focused on the algorithms that solve non-linear minimisation problems subject to bounds, equality constraints and inequality constraints. The algorithms available in Python™ to solve such problems are the Constrained Optimisation BY Linear Approximation (COBYLA), the Sequential Least SQuares Programming (SLSQP) and the *trust-constr* algorithms.

The COBYLA algorithm initially computes a candidate optimal solution by approximating the objective and constraint functions as linear models and solving a linear programming problem to obtain a candidate optimal solution. The candidate optimal solution is evaluated using the original objective and constraint functions. The results of the evaluation are used as a new data point in the optimisation space. The new data point improves the approximated linear programming problem. This process is done iteratively until the candidate optimal solution converges to a single optimal solution (Powell 1994).

The SLSQP algorithm is also an iterative method. The algorithm models the non-linear problem for a given candidate optimum solution as a quadratic programming sub-problem during each iteration. The sub-problem is solved, and the resulting solution is added to the optimisation space to improve the quadratic programming sub-problem approximations for the next iteration. The process continues until a local minimum of the non-linear problem is obtained. This minimum is the optimal solution (Kraft 1988).

The *trust-constr* algorithm alternates between two methods depending on the type of constraint. The algorithm uses the Byrd-Omojokun Trust-Region sequential quadratic programming method for equality constraints and changes to the trust-region interior-point method for inequality constraints. The methodologies implemented in the two methods are well described by Lalee, Nocedal and Plantenga (1998).

The selection of the minimisation algorithm used in the present work was guided by research studies performed by others in the aerodynamic shape optimisation space. The optimisation problems in other literature may not be identical to the optimisation problems in the current work. However, findings from further research helped to guide the selection of an appropriate minimisation algorithm.

Beals and Govindarajan (2021) performed a study to explore techniques that allow robust six-degree-of-freedom Unmanned Aircraft Systems (UAS) trim within the iterative rotorcraft sizing framework named HYDRA. The trim problem for over-actuated UAS configuration has an infinite number of trim solutions. Beals and Govindarajan (2021) used an optimisation-based approach because it allows designers to find a suitable local minimum solution of

the trim problem for an over-actuated UAS configuration. During this study, different off-the-shelf optimisers available in the Python™ programming language were considered. As mentioned previously, Python™ has other optimisation packages apart from Scipy, namely pyOpt, Mystic and NLopt. Beals and Govindarajan (2021) found Scipy to be the most suitable for reasons mentioned in the earlier paragraphs of the current section. Furthermore, the minimisation algorithms available in Scipy, namely COBYLA, SLSQP and *trust-constr*, were investigated to identify the best-suited minimisation algorithm.

Beals and Govindarajan (2021) excluded COBYLA during the earlier stages of the investigation. They found that it did not converge consistently for a simple two-degree-of-freedom problem. Therefore, it was not considered further. Furthermore, COBYLA was found to be inconvenient to implement because it does not explicitly accept equality constraints. It had to be tricked into accepting equality constraints by using two inequality constraints. COBYLA also does not explicitly accept bounds. Therefore, to use COBYLA, the bounds also had to be formulated as inequality constraints.

Beals and Govindarajan (2021) tested SLSQP and *trust-constr* for both four- and six-degree-of-freedom UAS trim problems. Both minimisation algorithms successfully solved for the same trim solutions. However, the SLSQP algorithm consistently found solutions at a faster rate than the *trust-constr* for both problems. More specifically, the SLSQP algorithm was found to converge up to 96% faster than the *trust-constr* algorithm. This was caused by the fact that the *trust-constr* algorithm computes the Hessian matrix for the constraint functions even though the Hessian is zero due to the linear constraints. The SLSQP algorithm does not compute second derivatives for problems with equality constraints only. Therefore, it was able to converge at a much faster rate. Beals and Govindarajan (2021) concluded that the SLSQP algorithm is the best suited for this application.

Several other studies have found the SLSQP algorithm to be well suited for aerodynamic shape optimisation problems. For instance, Wendorff, Botero and Alonso (2016) performed a study to compare the performance of different off-the-shelf Python™ optimisers' when applied to SUAVE, a conceptual aerospace vehicle design tool. The minimisation algorithms considered in this study were: Sparse Nonlinear OPTimiser (SNOPT), SLSQP, COBYLA and Augmented Lagrangian Particle Swarm Optimizer (ALPSO). SNOPT is a non-linear gradient-based optimisation algorithm. It is suitable for large problems subject to non-linear constraints. ALPSO is a population-based optimiser that finds global optima using a particle swarm method. The study performed by Wendorff, Botero and Alonso (2016) revealed that SNOPT and SLSQP yielded the best results, with SNOPT being slightly faster than SLSQP. The ALPSO algorithm found optimum solutions that were close to those obtained by SNOPT and SLSQP. However, the solutions were found at a slower rate. This was expected because ALPSO does not evaluate gradients. Furthermore, in this two-dimensional domain,

the gradient-based optimisers (i.e. SNOPT and SLSQP) do not get stuck in local minima. The COBYLA algorithm was found to converge to worse solutions at a slower rate compared to SNOPT and SLSQP. This was unexpected because COBYLA finds optimum solutions with a simplex method which should be robust. SNOPT is only accessible through the pyOpt module. As mentioned previously, the pyOpt module is not considered in the present study because a more recent study performed by Beals and Govindarajan (2021) found that it did not appear as though it was well maintained and did not install with current versions of NumPy. Therefore, the SLSQP algorithm was considered to be the next best alternative.

The work done by Fayez et al. (2021) is yet another example of an aerodynamic shape optimisation algorithm that uses the SLSQP minimisation algorithm. Other minimisation algorithms were also considered (i.e. COBYLA and *trust-constr*). However, the SLSQP was chosen as the initial driver to construct the optimisation problem. This is because SLSQP was believed to be well suited to solve optimisation problems subject to equality and inequality constraints. The SLSQP minimisation algorithm performed satisfactorily. However, it was concluded that other minimisation algorithms could be used in the future to further study the performance of different minimisation algorithms.

Although the optimisation problems discussed above are not identical to the shape optimisation problems explored in the present work, the literature does provide a good starting point in identifying a suitable minimisation algorithm. The approach used in the current work is similar to the approach taken by Fayez et al. (2021). SLSQP was chosen to solve the shape optimisation problems in the current work for two reasons. Firstly, it is well suited to solve non-linear optimisation problems subject to bounds, equality constraints and inequality constraints (similar to the shape optimisation problems in the current work). Secondly, the research performed by others has found the SLSQP to compute satisfactory optimisation solutions at a relatively faster rate than other minimisation algorithms. Therefore, the present work chose the SLSQP minimisation algorithm as an initial driver to construct the shape optimisation algorithms. However, other minimisation algorithms could be used in the future to further improve the 2D, external-compression, supersonic inlet design and analysis tool developed in the current work.

4.3 Curve Theory

4.3.1 Curve Fitting

Using a curve-fitting method, the 2D, external-compression, supersonic inlet design and analysis tool constructs the internal diffuser surfaces as smooth curves. Curve fitting refers to

the process of constructing curve functions that fit into a set of geometric data, such as data points and derivative vectors. Curve fitting falls into two broad categories, i.e. interpolation and approximation. The interpolation techniques are used to construct curves that satisfy the given set of geometric data exactly. The constructed curve passes through all the given data points and assumes the given derivatives at said points. The approximation techniques construct smooth curves that approximately satisfy the given set of geometric data. The curve does not go through all the data points exactly. Instead, it captures the "shape" of the provided data points (Piegl and Tiller 1997).

The 2D, external-compression, supersonic inlet design and analysis tool was developed using a curve fitting model to design the internal diffuser surfaces. There are three main criteria that the internal diffuser surfaces must meet for the design to be satisfactory:

1. the surfaces have to rotate the incoming airflow from the direction of the last fore-body ramp angle to a direction that is suitable for the combustion chamber;
2. the surfaces have to provide the area expansion required to diffuse the incoming airflow to the desired Mach number at the AIP and;
3. the surfaces have to be smooth and optimised for minimum curvature.

The choice to use smooth surfaces that have been optimised for minimum curvature was made for several reasons. The use of smooth surfaces can reduce the risk of momentum-driven boundary layer separation. Suppose an inlet operates in the super-critical mode of operation (Figure 4.21c). In that case, the smooth surfaces are designed to avoid shock wave reflection at the cowl lip and delay shock wave formation and reflection inside the internal diffuser. Avoiding shock waves inside the internal diffuser reduces the risk of additional total pressure loss caused by the reflected shock waves. Furthermore, it reduces the risk of additional shock-wave/boundary-layer interactions occurring inside the internal diffuser when an inlet operates super-critically.

The curve-fitting technique used does not need to find a curve function that exactly satisfies a set of geometric data. However, it needs to be flexible enough to approximate various internal diffuser surface shapes that meet the above criteria for different inlet configurations. For this reason, an approximation technique was considered to be more suitable for constructing the internal diffuser surfaces.

There are several curve fitting approximation models. The most popular models fall into two main categories, i.e. polynomials and splines. Multiple variations of the surfaces must be generated during the optimisation process to obtain the shapes that meet the above criteria. In this context, splines were preferred over polynomials for the following reasons (Hastie, Tibshirani and Friedman 2009):

1. Splines have greater flexibility when constructing curves. This is advantageous to the present study because the shapes of the curves used to generate the internal diffuser vary based on user-defined inputs.
2. The number of terms in a polynomial can grow quite large with an increase in the number of input variables used to construct the polynomial. This is a disadvantage to the present study because the number of input variables is dependent on the number of user-defined inputs. Eleven user-defined inputs are required by the tool to generate an inlet. Even for a lower order polynomial, the number of terms required to generate the internal diffuser surfaces can result in a computationally expensive curve generating process, especially when the process is repeatedly executed in an optimisation loop.
3. Lower degree splines can construct a curve similar to higher degree polynomials.
4. Polynomials can produce undesirable results at the boundaries. This can be detrimental to the internal diffuser design because the coordinate points and derivative vectors at the boundaries play a crucial role in meeting the internal diffuser criteria.

One of the most popular spline models is the non-uniform rational basis spline (NURBS) model. NURBS is a mathematical model for constructing curves and surfaces. The NURBS model can generate analytical shapes (i.e. cone sections and quadratic surfaces) and free-form shapes (i.e. cars, ships and aircraft) flexibly and precisely (Piegl and Tiller 1997). NURBS curves are used in computational tool SUPIN, discussed in section 1.4, to form smooth internal diffuser surfaces (Slater 2012).

A NURBS curve (Figure 4.25) is mainly defined by the weighted control points, the degree of the curve and the knot vector. As the name suggests, control points are a set of points that control the shape of the curve. Each control point has an associated number, referred to as the weight. The associated weights affect the influence that each control point has on the overall shape of the curve (Piegl and Tiller 1997).

The order of a NURBS curve is a number that determines the number of control points that influence a particular point on the curve. The order must be less than or equal to the total number of control points. The NURBS curve has a degree that is one less than the order (Piegl and Tiller 1997).

NURBS curves are parametric curves. This means that the functions that defined them, i.e. $C(\mathbf{u})$, are dependent on parameters, i.e. $\mathbf{u}$, that are not directly a part of the geometry. Several polynomials in the parametric space are joined together to generate a NURBS curve. Knots are values that determine how and where in the NURBS curve these polynomials start and stop. The knot vector is a collection of knots (Piegl and Tiller 1997).

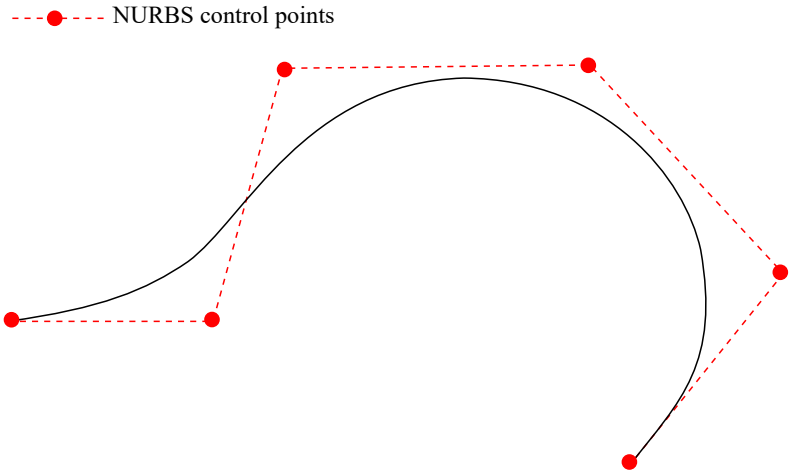


Figure 4.25: A NURBS curve

A q^th degree NURBS curve with m control points is defined by equation 4.18,

$$C(\mathbf{u}) = \frac{\sum_{i=0}^{m} N_{i,q}(\mathbf{u}) w_i P_i}{\sum_{i=0}^{m} N_{i,q}(\mathbf{u}) w_i} \tag{4.18}$$

where:

u is a parametric variable,
P_i are the control points,
w_i are the weights and,
$N_{i,q}(\mathbf{u})$ is the qth degree B-spline basis function.

The internal diffuser may take various forms depending on the user's subsonic diffuser flow field requirements. The NURBS model provides the flexibility and versatility needed to generate the multiple forms representative of the internal diffusers.

4.3.2 Curvature

The curvatures of the curves used to construct the internal diffuser surfaces are the measure by which the surfaces are optimised. The curvature at a particular point on a curve is the rate of change of the direction of the tangent line with respect to arch length, as per equation 4.19 (Pressley 2010):

$$\kappa = \frac{d\alpha}{ds} \tag{4.19}$$

where:

s is the arc length and,

α is the direction of the tangent line measured clockwise from the x-axis

Figure 4.26 is a visual representation of the variables used to compute the curvature at a particular point on a curve.

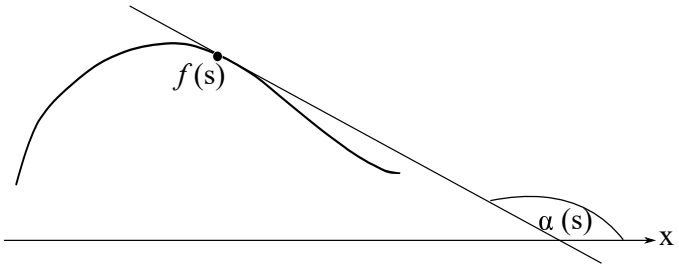


Figure 4.26: The variables used to compute the curvature on a point of a curve

4.4 Design of Experiments

The 2D, external-compression, supersonic inlet design and analysis tool was developed to design inlets with varying geometric features and flight conditions based on user-defined inputs. A sensitivity study was performed to investigate how different user-defined inputs affect the impact of viscous flow phenomena on the supersonic inlet flow fields and performance parameters. The sensitivity was performed using DOE.

The term DOE refers to a branch of applied statistics. It consists of a set of techniques that aim to study the influence of different input (or design) variables on the output (or response) of a controlled laboratory or computer experiment. A functional relationship between the design variables can be estimated to assess the response, providing useful and objective insights. An experiment can be designed using a classical or a modern DOE technique. The use of classical DOE techniques is quite common in designing laboratory experiments. Computational experiments are commonly designed with modern DOE techniques (Giunta, Wojtkiewicz and Eldred 2003).

Classical DOE techniques are formulated on the basis that random error exists in a laboratory experiment. If a laboratory experiment were to be conducted twice with identical design variables, the response produced from each experiment would not be the same. The classical DOE techniques tend to sample points at the extremes of the design space. Sampling in such a manner makes the classical DOE techniques more reliable in extracting trends from non-repeatable experiments (Giunta, Wojtkiewicz and Eldred 2003). On the contrary, randomness does not exist in a simulated response. Multiple runs of a deterministic computer simulation yield the same results given the same design variables. In the modern DOE techniques, the

design variables are changed to extract the trends from sample points placed in the design space interior.

The use of a classical or modern DOE technique depends not only on whether a laboratory or computational experiment is conducted. It also depends on the purpose of the designed experiment and the number of evaluations that the experiment can afford to perform. Classical DOE techniques generally use fewer evaluations. They are more suitable for sensitivity studies that aim to identify the design variables that significantly impact the response of an experiment. Once the significant design variables have been identified, the design variables' effect on the response can also be determined. Modern DOE techniques require a more significant number of evaluations to achieve space-filling sampling over the domain. These techniques are used for applications that extend far beyond a typical sensitivity study to obtain an accurate response surface.

The sensitivity study in the present work makes use of computational data obtained from CFD analyses of supersonic inlets. Even though modern DOE techniques are typically used to design computational experiments, a classical DOE technique was chosen in this particular case. This choice was made because classical DOE techniques will provide global sensitivity information from a more limited number of simulations.

A response surface methodology (RSM) can provide the functional relationship between the design variables and a response. RSM is a set of advanced mathematical and statistical techniques. They are used to understand the relationship between the design variables and the response of an experiment by creating a response surface. A response surface is a mathematical function that describes how the response of a laboratory or computer experiment is affected by the design variables. The use of an RSM is useful in understanding the relationship between the design variables and the response. It is also a valuable tool in optimising responses of interest (Khuri and Mukhopadhyay 2010; Myers, Montgomery and Anderson-Cook 2016).

The central composite design (CCD) technique is a subset of RSM and an established DOE sampling strategy. CCD was of particular interest for the sensitivity study because it generates design variable sample points that evaluate a response over the entire design space using a limited number of evaluations. The CCD sampling method consists of the corner, centre and axial (or star) points (Khuri and Mukhopadhyay 2010; Myers, Montgomery and Anderson-Cook 2016). The corner points define the boundaries of the design space and ensure that data is obtained at the extremes of the design space. Centre points are used to get data from the median values of the design space. Laboratory experiments often have multiple centre points to determine the precision of the experiment. The collective purpose of the

centre and axial points is to acquire data to estimate the curvature of the response. Figure 4.27 is a representation of the CCD sampling of an experiment with two design variables.

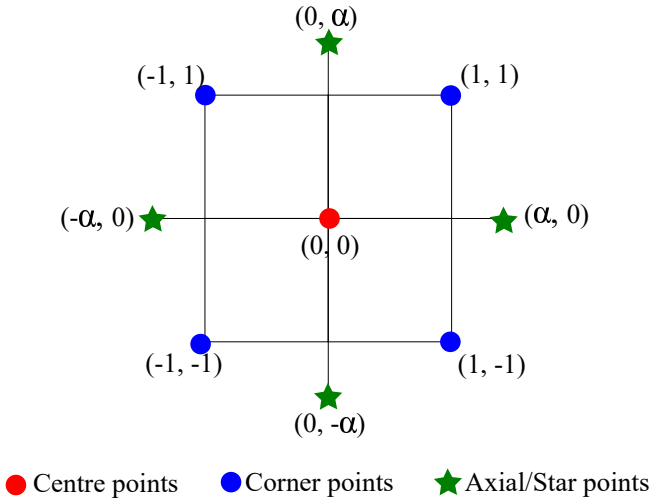


Figure 4.27: CCD sampling for two design variables

There are three prominent types of CCD sampling methods, i.e. circumscribed, inscribed and face centred. For the circumscribed CCD sampling method, the corner points are located at the extremes of the design space. The axial points are a distance α from the centre points. The value of α ensures that the axial and corner points have circular, spherical or hyper-spherical symmetry. As a result, the star points introduce new extreme ranges to the design space. The inscribed CCD sampling method is a scaled-down version of the circumscribed CCD sampling method. It is used when the design variables are limited to specific ranges.

Similarly to the circumscribed CCD sampling method, the corner and axial points have circular, spherical or hyper-spherical symmetry. However, the values of the axial and corner points are scaled down to ensure that the imposed design variable limits are not exceeded. The faced CCD sampling method contains corner points that are located at the extremes of the design space. The axial points are a distance of $\alpha = \pm 1$. Therefore, they are located at the centre of each edge or face (depending on the number of design variables) (Myers, Montgomery and Anderson-Cook 2016).

4.5 Surrogate Modelling

The RSM DOE techniques discussed in section 4.4 generate a map of how to sample the data points required to create a response surface. The response surface is a function that represents the relationship between the design variables and the response. An approximation

function strategy that uses the information obtained from the sampled data points (i.e. the design variables and the response) is needed to create such a response surface.

Surrogate modelling is an approach for constructing approximations for functions. The purpose of surrogate modelling is to apply viscous corrections to the 2D, external-compression, supersonic inlet design and analysis tool. A surrogate model approximates a non-linear function using information from numerous points in the domain of interest. The information is usually limited to zero or first-order information. The advantage of using a surrogate model is that approximating lower-order information of a function at additional points in the domain can be conducted in parallel over multiple cores and computers. This makes it computationally tractable. The main disadvantage of using a surrogate model is associated with the dimensionality of the function (i.e. the number of design variables used in the response surface function). As the dimensionality of the function increases, the design space grows exponentially. Computing exponentially more data readily becomes intractable. This dilemma is referred to as the "curse of dimensionality" (Snyman and Wilke 2018).

There are several surrogate modelling techniques available to approximate functions. These include polynomial response surfaces, radial basis function (RBF), Kriging, neural networks, support vector machines, etc. (Koziel, Ciaurri and Leifsson 2011). The choice of an appropriate surrogate modelling technique is dependant on the true nature of the data used to construct the surrogate model. The true nature of the data used to construct the viscous corrections was not known as a priori. This made it challenging to know which surrogate model would be best suited for the application.

For model development, the RBF surrogate modelling technique was chosen for the present work. Roland Hardy first studied it in the 1970s because he was not satisfied with the results of polynomial interpolation. He found that his method for fitting data handled unevenly distributed data sites with great consistency where polynomials had failed (Hardy 1990). Today, the RBF surrogate modelling technique has many applications in the numerical solution of partial differential equations, machine learning, statistics, etc. (Mongillo 2011). This suggests that it is flexible, which was advantageous for the present work because the true nature of the data used to construct the viscous corrections was not known as a priori.

Furthermore, the RBF surrogate models are easy to construct and scale well with dimensionality. The dimensionality of the viscous correction function depends on the number of user-defined inputs. Eleven user-defined inputs are required by the tool to generate an inlet. Up to eleven input variables could be required to create viscous correction response surfaces. Therefore, a surrogate model that scales well with dimensionality is ideal for the present work. The suitability of other surrogate modelling techniques for constructing viscous correction response surfaces can be explored in future work.

An RBF surrogate model approximates a non-linear function $f(\mathbf{x})$ as a linear combination of P chosen non-linear RBFs $\phi_j(\mathbf{x}, \mathbf{x}_c^j)$, $j = 1, ..., P$, centred around P spatial points x_c^j (Snyman and Wilke 2018). The RBF approximation is expressed as equation 4.20.

$$f(\mathbf{x}) \approx \sum_{j=1}^{P} w_j \phi_j(\mathbf{x}, \mathbf{x}_c^j) = \tilde{f}(\mathbf{x}) \tag{4.20}$$

The variable w_j represents the weight of each RBF. The approximation is linear in the weights. Therefore, they are solved from a linear system of equations. The non-linearity of the function $f(\mathbf{x})$ is represented by the non-linear RBF $\phi_j(\mathbf{x}, \mathbf{x}_c^j)$ (Snyman and Wilke 2018).

Different types of RBFs can be used to approximate a non-linear function. Several RBFs are listed in table 4.3. The RBFs listed in table 4.3 are a function of the shape parameter, denoted by ϵ. The shape parameter determines the radius of the domain over which the RBF has significant influence. The shape parameter is unknown and, therefore, it needs to be determined. It is generally computed using k-fold cross-validation. In k-fold cross-validation, the m sample points used to construct the function approximation are randomly partitioned into k equal-sized subsets. One subset (i.e. the test subset) is removed, and the remaining subsets are used to construct a response surface. The constructed response surface then predicts the responses of the test subset. The actual test subset responses are already known. Therefore, an error is computed between the actual responses and the predicted responses. In this study, the error is calculated as the root mean square error. This process is repeated k times for each subset. All of the errors obtained over the k subsets are averaged to compute the k-fold cross-validation error. The k-fold cross-validation error is then calculated for different shape parameters to find the shape parameter that minimises the k-fold cross-validation error, i.e. ϵ^*. The particular case of making $k = m$ is referred to as leave-one-out cross-validation (Snyman and Wilke 2018).

Table 4.3: Radial basis functions $\phi_j(r_j(\mathbf{x}))$ with $r_j(\mathbf{x}) = \left|\left|\mathbf{x} - \mathbf{x}_c^j\right|\right|$ (Snyman and Wilke 2018)

Name	Equation
Gaussian	$\phi_j(r_j(\mathbf{x})) = e^{-\epsilon r_j(\mathbf{x})^2}$
Exponential	$\phi_j(r_j(\mathbf{x})) = e^{-\epsilon r_j(\mathbf{x})}$
Multiquadric	$\phi_j(r_j(\mathbf{x})) = \sqrt{1 + (\epsilon r_j(\mathbf{x}))^2}$
Inverse quadratic	$\phi_j(r_j(\mathbf{x})) = \frac{1}{1+(\epsilon r_j(\mathbf{x}))^2}$
Inverse multiquadric	$\phi_j(r_j(\mathbf{x})) = \frac{1}{\sqrt{1+(\epsilon r_j(\mathbf{x}))^2}}$

The type of RBF and the shape parameter used in a function approximation significantly impact the accuracy of the RBF model. The selection of an appropriate RBF depends on the type of data available for the approximation and the surface to be approximated. The

process of selecting an appropriate RBF may involve testing different RBFs and selecting the one that yields the least error. This was done by Mongillo (2011) when he performed a study that was focused on choosing basis functions and shape parameters for RBF methods. When surrogate models are used for optimisation applications, a smooth basis function is preferred because it is differentiable everywhere. The Gaussian RBF is often chosen for that purpose (Snyman and Wilke 2018).

DOE and surrogate modelling provide a means to develop a method to apply viscous corrections to the 2D, external-compression, supersonic inlet design and analysis tool developed in the present work. As mentioned previously, the DOE techniques discussed in section 4.4 generate a map of how to sample the data points required to create a response surface. The faced CCD sampling method available in the Python™ PyDOE2 module was chosen for the sensitivity study discussed in section 6.3. This particular CCD sampling method was chosen because classical DOE techniques provide global sensitivity information from a more limited number of sample points. Furthermore, the faced CCD sampling method was also selected to observe the impact of viscous flow phenomena on supersonic inlet flow fields at the extremes of the design space without exceeding the bounds of the design space. The results from the sensitivity study were used as a set of known input variables and responses to construct the viscous correction response surfaces. The viscous correction response surfaces were formulated using the built-in RBF function in the Python™ SciPy module. Based on a trial-and-error approach, the Gaussian RBF function with a shape parameter obtained using the leave-one-out cross-validation method were found to be best suited to construct the RBF viscous correction response surfaces. This combination was found to generate the least amount of error. The development of a method to apply viscous corrections to the 2D, external-compression, supersonic inlet design and analysis tool developed in the present work using DOE and surrogate modelling is discussed in sections 6.3 and 6.4.

Chapter 5 The Development of IADAM

5.1 Introduction

The earliest contributors to the field of supersonic inlet design and analysis developed low-fidelity analytical methods that apply the theory of inviscid compressible flow to design and analyse supersonic inlets (Seddon and Goldsmith 1999; Mahoney 1990). These methods were incorporated into computational tools such as IPAC, the Level II IIP code, NIDA, etc. Therefore, the inviscid compressible flow theory was considered an acceptable starting point in developing a supersonic inlet design and analysis tool.

The current chapter presents a low-fidelity analytical shape optimisation method to design and analyse geometric profiles of 2D, external-compression, supersonic inlets. The method applies the theory of inviscid compressible flow to perform its analyses. Therefore, it will be referred to as inviscid analytical design and analysis method (IADAM).

The current research builds on work previously done by Baloyi (2017). The shape optimisation algorithm developed by Baloyi (2017) was modified and incorporated into IADAM. The details regarding the modifications made to this algorithm are provided in section 5.4.1. Furthermore, additional algorithms were developed to complete the geometric profiles of 2D, external-compression, supersonic inlets by adding internal diffusers to the fore-bodies. Mathematical optimisation theory was incorporated into IADAM to generate optimised geometric profiles for maximum total pressure recovery and mass flow ratio. The inlet drag was taken into consideration. However, minimising the inlet drag was not a key objective.

The 2D, external-compression, supersonic inlet design and analysis tool was developed using the Python™ 3.7.4 programming language from the Anaconda™ 2019.10 distribution. NumPy 1.16.5, SciPy 1.3.1, geomdl 5.3.0 and matplotlib 3.1.1 are the main Python™ modules used by IADAM to automate the design and analysis of supersonic inlets.

5.2 Geometric Structure

The geometric profiles of the 2D, external-compression, supersonic inlets generated by IADAM have the form illustrated in figure 5.1. The inlets consist of a fore-body and an internal diffuser. Figures 5.2 and 5.4 highlight some noteworthy dimensions of the fore-bodies and internal diffusers generated by IADAM, respectively. Some dimensions are user-defined inputs, while others are calculated based on design requirements.

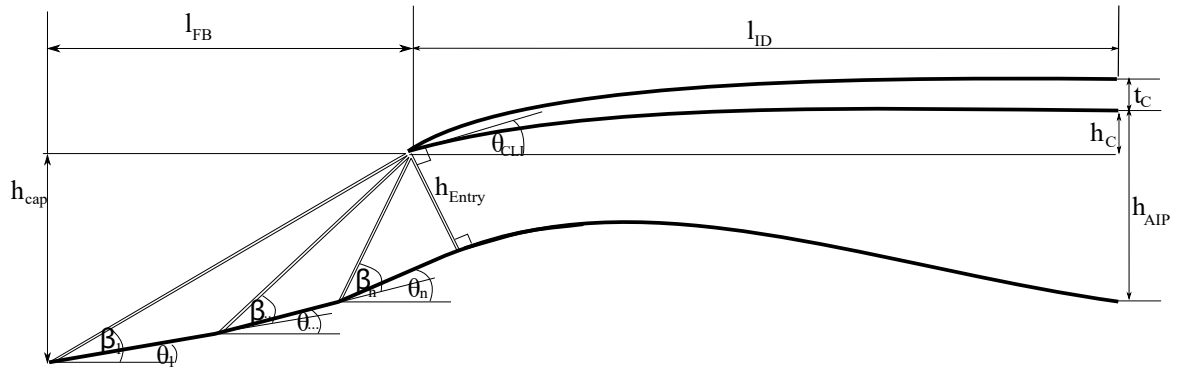


Figure 5.1: The geometric structure of the inlets generated by IADAM

Figure 5.2 provides a close-up of a fore-body generated by IADAM. The fore-body is a structure consisting of a single ramp or a series of ramps. The fore-body ramps have angles denoted by $\boldsymbol{\theta}$. The ramp angles are calculated by executing a mathematical optimisation problem formulated to find the ramp angles that produce a maximum total pressure recovery. This is discussed in more detail in section 5.4.1. The fore-body ramps generate a series of oblique shock waves, denoted by $\boldsymbol{\beta}$. The positioning of the fore-body ramps is such that the oblique shock waves converge at a single point, i.e. the cowl lip. This shock wave structure ensures that the mass flow ratio is maximised.

The capture height (h_{cap}) is a user-defined input. It is the vertical distance from the leading edge of the fore-body to the cowl lip. The length denoted by l_{FB} is a horizontal distance from the leading edge of the fore-body to the cowl lip. It is calculated as a ratio of the capture height to the tangent of the first oblique shock wave angle, as shown in figure 5.2.

The air entering the internal diffuser must be as uniform as possible. IADAM achieves this by ensuring that a straight normal shock wave sits between two parallel surfaces at the internal diffuser entry plane, as illustrated in figure 5.2. Two things are done to ensure that the normal shock wave sits between two parallel surfaces. Firstly, the cowl lip interior angle is made equal to the angle of the last fore-body ramp, denoted by θ_n. Secondly, the last fore-body ramp is extended beyond l_{FB} to the point where the ramp and the normal shock

wave intersect. The length denoted by l^*_{FB} is a horizontal distance from the leading edge of the fore-body to the point of intersection.

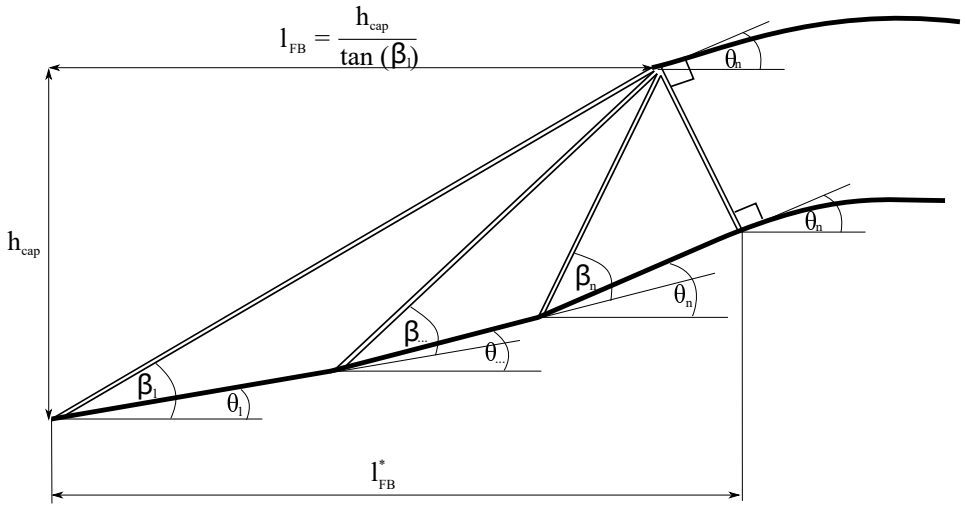
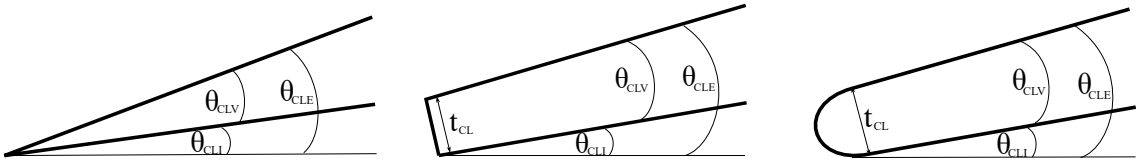


Figure 5.2: Noteworthy fore-body design features and dimensions

The cowl lip is the leading edge of the internal diffuser. The user has a choice between a sharp (Figure 5.3a), rectangular (Figure 5.3b) or a circular (Figure 5.3c) cowl lip profile. The cowl lip interior angle, denoted by θ_{CLI}, is equal to the angle of the last fore-body ramp, denoted by θ_n (Figure 5.2). The cowl lip exterior angle is typically 3° to 5° greater than the interior angle (Slater 2012). The difference between the cowl lip interior and exterior angles is the cowl lip vertex angle, denoted by θ_{CLV}. The cowl lip vertex angle is a user-defined input.



(a) Sharp (b) Rectangular (c) Circular

Figure 5.3: Cowl lip profiles

The internal diffuser generated by IADAM is a diverging duct. Some noteworthy internal diffuser coordinates and dimensions are illustrated in figure 5.4. The x- and y-coordinates with the subscript 'CL' in figure 5.4 represent the location of the cowl lip. The x- and y-coordinates with the subscript 'FB' represent the end of the fore-body. The fore-body ends where a normal shock wave originating from the cowl lip intersects with the last fore-body ramp. The entry height, denoted by h_{Entry}, is the perpendicular distance between the cowl lip (i.e. (x_{CL}, y_{CL})) and the end of the fore-body (i.e. (x_{FB}, y_{FB})). The inlet height at the AIP, denoted by h_{AIP}, is required to isentropically decelerate the air from the Mach number right after the normal shock wave to the user-defined AIP Mach number. The internal diffuser

length, denoted by l_{ID}, is horizontal from the cowl lip to the AIP. The value of l_{ID} is a user-defined input. The internal diffuser length is also measured from the end of the fore-body. This distance is denoted by l^*_{ID}.

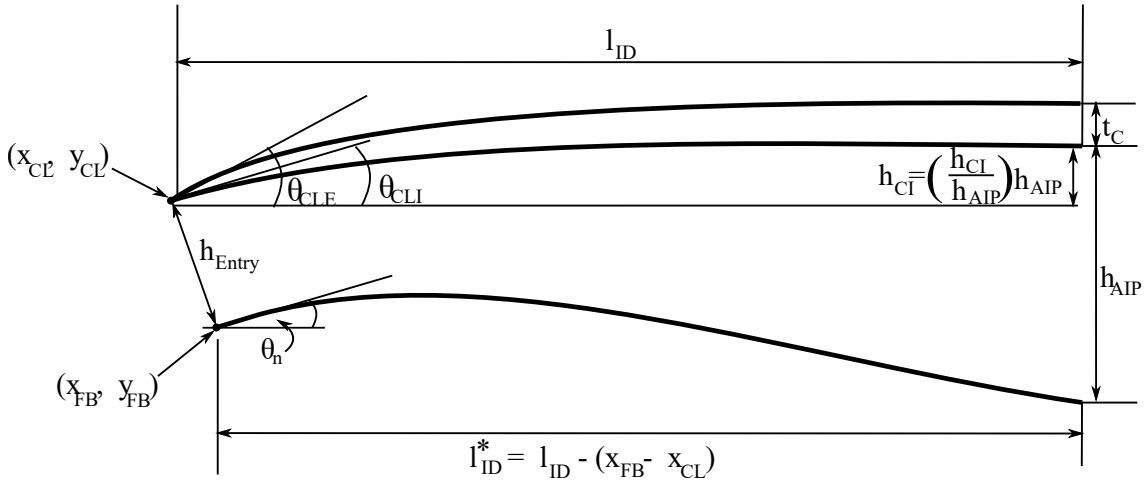


Figure 5.4: Noteworthy internal diffuser coordinates and dimensions

5.3 Flow Analysis

IADAM analyses the air flowing through a 2D, external-compression, supersonic inlet at various stations. The stations at which flow analyses are performed are the same as those described in section 4.1.3.1 and illustrated in figure 4.3. More specifically, flow analyses are performed at free-stream conditions, at the oblique shock waves on the fore-body, at the normal shock wave located at the internal diffuser entry plane and at the AIP.

The fluid properties of the free-stream airflow captured by the inlet are a function of the altitude at which the inlet is operating, as discussed in section 4.1.3.1.2, and the Mach number at which the captured airflow is moving. Altitude and free-stream Mach number are user-defined inputs. The free-stream static temperature and pressure are calculated using equations 4.8 and 4.9, respectively. The free-stream density is calculated using the ideal gas law, i.e. equation 4.1. The free-stream stagnation fluid properties are calculated using the isentropic flow relations presented in section 4.1.3.1.1. More specifically, the stagnation temperature, pressure and density are calculated using equations 4.4, 4.5 and 4.6, respectively.

The fore-body generates a series of oblique shock waves to externally compress the captured airflow from the free-stream supersonic Mach number to a lower supersonic Mach number. The oblique shock wave angles are calculated using equation 4.10. The fluid properties of the air flowing over the fore-body discontinuously change across each oblique shock wave.

Equations B.1 through to B.6 compute the fluid properties of the airflow downstream of each oblique shock wave. These equations are technically used to calculate the fluid properties across normal shock waves. However, a normal shock wave is an oblique shock wave with a deflection angle of 0° and a shock wave angle of 90°. Therefore, these equations can be used to compute the fluid properties of the air downstream of an oblique shock wave provided that the normal component of the oncoming Mach number, i.e. $M \sin \beta$, is used.

The fluid properties just upstream of the normal shock wave are equal to the fluid properties just downstream of the last oblique shock wave. The fluid properties just downstream of the normal shock wave are calculated using equations B.1 through to B.6.

The fluid properties of the airflow at the AIP are a function of the area change between the internal diffuser entry plane and the AIP. The entry height, denoted by h_{Entry}, is the perpendicular distance between the cowl lip (i.e. x_{CL}, y_{CL} in figure 5.4) and the last fore-body ramp (i.e. x_{FB}, y_{FB} in figure 5.4). The inlet height at the AIP, denoted by h_{AIP}, is the height required to isentropically decelerate the air from the Mach number right after the normal shock wave to the user-defined AIP Mach number, denoted by M_{AIP}. The value of h_{AIP} is calculated using the area-Mach number relation presented in equation 4.12. This equation does not calculate h_{AIP} directly. However, based on the assumptions that $A*$ remains constant for isentropic flow and a 2D flow as a unit width, the value of h_{AIP} is the product of $\frac{h_{AIP}}{h^*}$, $\frac{h^*}{h_{Entry}}$ and h_{Entry}.

There are no shock waves inside the internal diffuser. This means that the stagnation fluid properties of the air flowing through the internal diffuser remain constant. Therefore, the stagnation fluid properties downstream of the normal shock wave represent the stagnation fluid properties throughout the internal diffuser, including the AIP. The AIP stagnation fluid properties and the user-defined AIP Mach number are used to calculate the remaining fluid properties of the air at the AIP using equations 4.4, 4.5 and 4.6.

IADAM has been developed to provide the user with the total pressure recoveries and the mass flow ratios of the inlet profiles that it generates. The assumption of inviscid flow implies that total pressure loss only occurs across shock waves. The total pressure ratio across each oblique shock wave is calculated using equation 4.15. The total pressure loss across the normal shock wave is also calculated using equation 4.15, provided a shock wave angle of 90° is used. The overall total pressure recovery of the air flowing through a shock wave system is a product of all the total pressure recoveries across each individual shock wave. IADAM designs inlets to operate at the critical mode of operation. The assumptions of inviscid compressible flow and a critical mode of operation result in no loss in mass. Therefore, the mass flow ratio is always one.

5.4 Shape Optimisation Algorithms

5.4.1 Fore-Body

IADAM's fore-body shape optimisation algorithm was developed to design the fore-body as a structure consisting of a single or several compression ramps. It was initially developed by Baloyi (2017) as a mathematical optimisation problem to compute the fore-body ramp angles that would produce air moving at a specified Mach number downstream of the normal shock wave. The ramp angles were constrained to values that would result in the inlet total pressure recovery falling within a specified range. The benefit of this mathematical formulation is that it works well to ensure that the air delivered to the combustion chamber is below the blow-off limit. Unfortunately, this mathematical formulation sometimes fails because the fore-body ramp angles required to compress the air to the specified Mach number would produce a total pressure recovery outside of the specified range. The addition of an internal diffuser in the present study means that the air downstream of the normal shock wave does not necessarily have to be below the blow-off limit. It can be subsonically decelerated in the internal diffuser via area expansion.

The air flowing through a supersonic inlet must maintain a good total pressure recovery. The total pressure recovery translates directly to the overall engine performance, as explained in sections 4.1.3.1.3 and 4.1.3.4.1. The theory of inviscid compressible flow can only predict the total pressure loss across shock waves. This means that the total pressure recovery across the fore-body represents the overall inlet total pressure recovery computed by IADAM, as discussed in section 5.3. Therefore, the design of the fore-body is critical to ensuring that IADAM generates inlets with good total pressure recoveries.

The updated fore-body shape optimisation algorithm was formulated as a mathematical optimisation problem to compute the fore-body ramp angles, denoted by $\boldsymbol{\theta}$, required to produce a maximum total pressure recovery. Figure 5.5 is a flow chart representing the objective function. The inputs required to calculate the total pressure recovery of the air flowing over a fore-body are the free-stream Mach number (M_∞), the number of fore-body ramps (n) and the fore-body ramp angles ($\boldsymbol{\theta}$). The values of M_∞ and n are user-defined inputs. The array of fore-body ramp angles is the design variable. It consists of $n+1$ points. The first value in the array, θ_0, is the direction of the free-stream flow. The value of θ_0 is fixed. The remaining values are the fore-body ramp angles relative to the x-axis.

The objective function algorithm initialises the overall total pressure recovery, denoted by $P_{_R}$, to a value of one. After that, the algorithm enters a loop that repeats n times for each fore-body ramp. The steps taken during each loop are as follows:

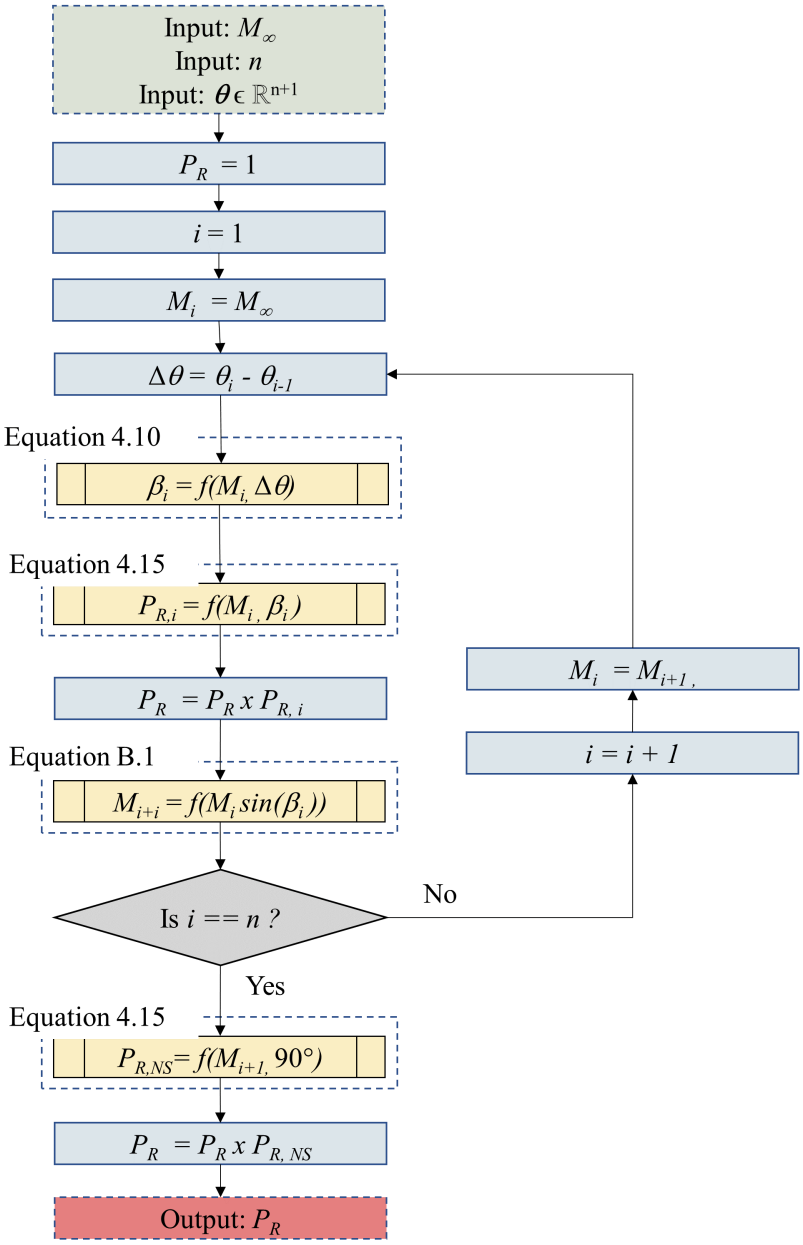


Figure 5.5: Fore-body shape optimisation objective function flow chart

- Calculate the deflection angle, denoted by $\Delta\theta$. This is the angle of the i^{th} ramp relative to the flow direction just upstream of the ramp.
- Solve for the oblique shock wave angle, β_i, using equation 4.10. Equation 4.10 is a function of the Mach number upstream of the ramp (M_i) and the deflection angle ($\Delta\theta$).
- Calculate the total pressure recovery across the i^{th} oblique shock wave using equation 4.15. The equation is a function of the upstream Mach number (M_i) and the oblique shock wave angle (β_i).

- Update the overall total pressure recovery(P_R) by multiplying it with the total pressure recovery across the oblique shock wave ($P_{R,i}$).
- Calculate the Mach number of the airflow just downstream of the oblique shock wave (M_{i+1}) using equation B.1. The equation is a function of the normal component of the upstream Mach number (i.e. $M_i \sin\beta_i$). Equation B.1 calculates the normal component of the Mach number just downstream of the oblique shock wave, i.e. $M_{i+1}\sin(\beta_i - \Delta\theta)$. To obtain the value of M_{i+1}, the calculated value must be divided by the value of $\sin(\beta_i - \Delta\theta)$.

At the end of the loop, the total pressure recovery across a normal shock wave, denoted by $P_{R,NS}$, is calculated. After that, the overall total pressure recovery (P_R) is updated by multiplying it by $P_{R,NS}$.

The fore-body design optimisation problem has constraints that are important to the overall design of the fore-body. The first angle in the design variables array, denoted by θ_0, represents the free-stream direction of the captured airflow. It was assumed that the supersonic inlets generated by the tool operate in an idealised case where the aircraft has an angle of attack of 0° when it is cruising. Therefore, θ_0 has a fixed value of 0°. The fore-body ramp angles may not exceed the maximum deflection angle, denoted by θ_{max}, for the free-stream Mach number of the captured air. This ensures that a detached bow shock wave is avoided on the fore-body. The cowl lip interior angle, denoted by θ_{CLI}, is equal to the last fore-body ramp angle, denoted by θ_n. The cowl lip exterior angle, denoted by θ_{CLE} exceeds the cowl lip interior angle by the cowl lip vertex angle, denoted by θ_{CLV}. To ensure that a detached bow shock wave does not form at the cowl lip, θ_{CLE} must be smaller than θ_{max}. Therefore, the fore-body ramp angles may not exceed the difference between θ_{max} and θ_{CLV}.

Mathematical optimisation problems minimise the objective function. To maximise the objective function, the negative of the objective function is minimised. The fore-body design optimisation problem is presented in equation 5.1:

$$\underset{\text{w.r.t. } \boldsymbol{\theta}}{\text{minimise}} \; -P_R(\boldsymbol{\theta}),\; \boldsymbol{\theta} = [\theta_0, \theta_1, ..., \theta_n]^T \in \mathbb{R}^{n+1} \tag{5.1}$$

subject to constraints:

$$\theta_0 = 0°$$

$$\theta_n - \theta_{max}(M_\infty) + \theta_{CLV} \leq 0$$

The fore-body shape optimisation algorithm solves the above optimisation problem using the built-in Python™ SciPy 1.3.1 optimisation function. For model development, the SLSQP minimisation algorithm was chosen to solve the fore-body design optimisation problem. It

was found to be an acceptable minimisation algorithm for other aerodynamic optimisation problems, as discussed in section 4.2. Therefore, the SLSQP minimisation algorithm was chosen to be an initial driver to construct the fore-body shape optimisation algorithm. In the future, other minimisation algorithms could be used to formulate the shape optimisation algorithms in IADAM.

The design of the fore-body is not only critical to ensuring a maximum total pressure recovery. It is also crucial to ensure a maximum mass flow ratio. Using basic geometry, the fore-body shape optimisation algorithm uses the optimised fore-body ramp angles to position the ramps such that all the oblique shock waves converge at a single point (i.e. the cowl lip). This shock wave structure aims to ensure that the mass flow ratio has a maximum value of one. Furthermore, this shock wave structure minimises the spillage and pre-entry drag, as mentioned in section 4.1.3.4.3.

5.4.2 Internal Diffuser

The internal diffuser shape optimisation algorithms were developed to design the internal diffusers as diverging ducts. The algorithms apply the theory of quasi-1D flow through ducts, discussed in section 4.1.3.1.5, to perform their intended tasks. The incoming airflow is isentropically decelerated to a user-defined AIP Mach number via area expansion (i.e. $A_{AIP}/A_{Entry} > 1$). The air in the internal diffuser is also rotated from the direction of the last fore-body ramp to the direction of the captured free-stream flow before it enters the combustion chamber.

The 2D, external-compression, supersonic inlet design and analysis tool aims to generate inlets with good total pressure recoveries. Real supersonic inlet flow fields experience total pressure loss due to shock waves and viscous effects. Viscous effects cause a loss in total pressure due to the friction between the air and the inlet walls, shock-wave/boundary-layer interactions, and the turbulent mixing caused by boundary layer separation or near separation (Section 4.1.3.4.1). IADAM applies the theory of inviscid compressible flow to generate 2D, external-compression, supersonic inlets. Thus, it is incapable of taking the total pressure losses due to the effects of viscosity into account. However, there are measures taken to try to reduce the total pressure losses caused by viscous effects. These measures are discussed in the following paragraphs.

The internal diffuser shape optimisation algorithms were developed to design the internal diffuser surfaces as smooth surfaces that rotate the incoming airflow gradually and smoothly. The internal diffuser surfaces include the cowl surfaces and the internal diffuser bottom surface

(IDBS). Smooth surfaces are achieved using mathematical optimisation. The objective is to minimise the surface curvature of the internal diffuser surfaces.

The choice to use smooth surfaces was made for several reasons. The use of smooth surfaces reduces the risk of momentum-driven boundary layer separation. Suppose an inlet operates in the super-critical mode of operation (Figure 4.21c). In that case, the smooth surfaces are designed to avoid shock wave reflection at the cowl lip and delay shock wave formation and reflection inside the internal diffuser. Avoiding shock waves inside the internal diffuser reduces the risk of additional total pressure loss caused by the reflected shock waves. Furthermore, the avoidance of shock waves inside the internal diffuser reduces the risk of additional total pressure losses due to shock-wave/boundary-layer interactions occurring inside the internal diffuser when an inlet operates super-critically.

There needs to be a compromise between designing the cowl to turn the airflow smoothly and keeping the cowl wave drag low. The frontal projected height of the cowl required to turn the air gradually and smoothly from the direction of the fore-body back to the direction of free-stream flow can be large. A large cowl frontal projected height causes increased cowl wave drag. The cowl wave drag can be reduced by decreasing the frontal projected height of the cowl. This is achieved by turning the internal diffuser flow field more rapidly.

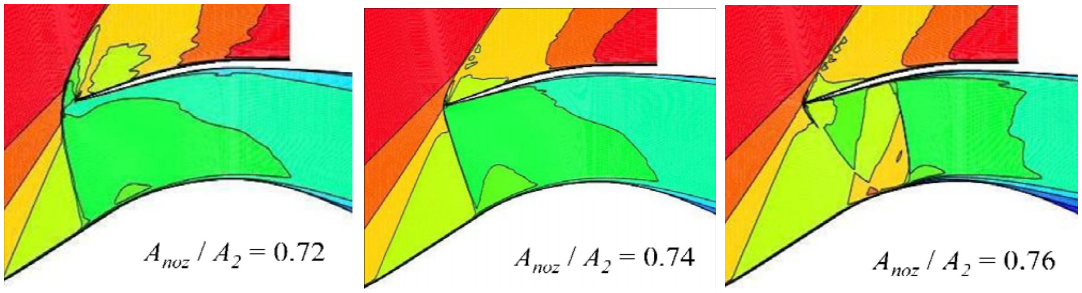
5.4.2.1 Cowl Lip

The cowl lip is the leading edge of the cowl. The user has a choice between a sharp (Figure 5.3a), rectangular (Figure 5.3b) or a circular (Figure 5.3c) cowl lip profile, as discussed in section 5.2. A sharp cowl lip profile minimises pressure drag. Realistically, a sharp lip may be difficult to manufacture. Therefore, the user may provide a small thickness, denoted by t_{CL}, for the rectangular and the circular cowl lip profiles. The advantage of a blunt lip is that it may reduce pre-entry drag by delaying normal shock wave expulsion. (Faro 1965).

The cowl lip design algorithm was developed to ensure that the cowl lip interior angle, denoted by θ_{CLI} (Figure 5.3), is equal to the angle of the last fore-body ramp, denoted by θ_n (Figure 5.2). The cowl lip interior angle would typically not be greater than the last fore-body ramp angle. That would increase the total angle through which the flow must be turned to meet the flow requirements in the combustion chamber and result in an unnecessary increase in cowl wave drag. Having the cowl lip interior angle equal to the last fore-body ramp angle ensures that the air enters the internal diffuser while moving in a uniform direction. In the event that the inlet operates super-critically, having the cowl lip interior angle equal to the last fore-body ramp also reduces the risk of shock wave reflection at the cowl lip.

The cowl lip exterior angle, denoted by θ_{CLE} (Figure 5.3), is typically 3° to 5° greater than the cowl lip interior angle (Slater 2012). The difference between the cowl lip exterior and interior angles is the cowl lip vertex angle, denoted by θ_{CLV} (Figure 5.3). The cowl lip vertex angle is a user-defined input.

If the user provides a cowl lip thickness greater than zero, the cowl lip is assumed to be a small blunt body in a supersonic flow field. There is a possibility of a detached bow shock wave forming upstream of the cowl lip, as discussed in section 4.1.3.1.6. However, the effects of this bow shock wave are assumed to be negligible for an external-compression inlet operating in the critical mode of operation. This assumption is made for two reasons. Firstly, the size of a cowl lip is typically negligible relative to the overall size of a supersonic inlet flow field. Therefore, the effect of this component on the overall supersonic inlet flow field must also be negligible. Secondly, the bow and normal shock waves are located in the same place. The bow shock wave has the characteristics of a normal shock wave, as discussed in section 4.1.3.1.6. The bow and normal shock waves will likely merge into one normal shock wave at the internal diffuser entry plane. Therefore, the effects of the bow shock wave ahead of the cowl lip are already considered in the analysis of the air flowing past the normal shock wave. The CFD results presented in figure 5.6 support the validity of the assumptions made in the current paragraph.



(a) Sub-critical mode (b) Critical mode (c) Super-critical mode

Figure 5.6: Mach number contours of an inlet at different modes of operation (Slater 2012)

Slater (2012) performed a CFD analysis of an external-compression supersonic inlet at various modes of operation. The results are presented in figure 5.6. The cowl lip has a circular profile with a radius of 0.002 ft (approximately 0.0006 m). As a result, a bow shock wave forms just upstream of the cowl lip. The bow shock wave is visible when the inlet operates at the super-critical mode (Figure 5.6c). When the inlet is operating in the critical mode of operation (Figure 5.6b), the normal and bow shock wave appear to be indistinguishable.

As expected, mass spillage occurs around the cowl lip when the inlet operates in the sub-critical mode. This causes the mass flow ratio of the inlet to be approximately 0.935 when operating sub-critically. The bow shock wave at the cowl lip causes mass spillage to occur

when the inlet operates in the critical and the super-critical modes. As a result, the mass flow ratios of the inlet operating in the critical and super-critical modes are approximately 0.970 and 0.973, respectively (Slater 2012). Therefore, using a blunt cowl lip profile causes some mass spillage when the inlet operates in the critical and super-critical modes.

5.4.2.2 Cowl Interior

The cowl interior shape optimisation algorithm designs the cowl interior as a smooth surface defined by a NURBS curve extending from the cowl lip to the AIP. The internal diffuser surfaces may take various forms depending on the flow field requirements specified by the user. NURBS curves provide the flexibility and versatility needed to generate the multiple forms of the internal diffuser surfaces. The choice to use NURBS curves is discussed more extensively in section 4.3.1.

The cowl interior shape optimisation algorithm was formulated as a mathematical optimisation problem that optimises the coordinate points of the NURBS control points such that the overall curvature of the cowl interior surface is minimised. Figure 5.7 is a flow chart representing the objective function. The objective function calculates the coordinate points of the curve representing the cowl interior surface using a built-in Python™ NURBS curve function. The inputs required to generate a NURBS curve are the x- and y-coordinates of the control points (i.e. $\boldsymbol{x_{CP}}$, $\boldsymbol{y_{CP}}$), the weighting of each control point ($\boldsymbol{w_{CP}}$), the degree of the curve and the number of NURBS curve coordinate points that should be generated (k). The cowl interior surface is a third-degree NURBS curve with four control points. The coordinates of the control points are the design variables. To ensure that the NURBS curve function generates enough points to capture the curvature of the cowl interior surface, the value of k is set to a high value of 100.

After computing the cowl interior surface coordinates, the objective function initialises an array that will be populated with the curvatures at particular points on the curve representing the cowl interior surface. After that, the objective function enters a loop that repeats $k-2$ times to calculate the curvature at each coordinate point, excluding the curve endpoints. The curvature at a particular point on a curve is calculated using equation 4.19. The curve has been discretised finely enough to approximate curvature using equation 5.2. At the end of the loop, the overall curvature is calculated as the norm of the curvature array.

$$\kappa \approx \frac{\Delta\alpha}{\Delta s} \tag{5.2}$$

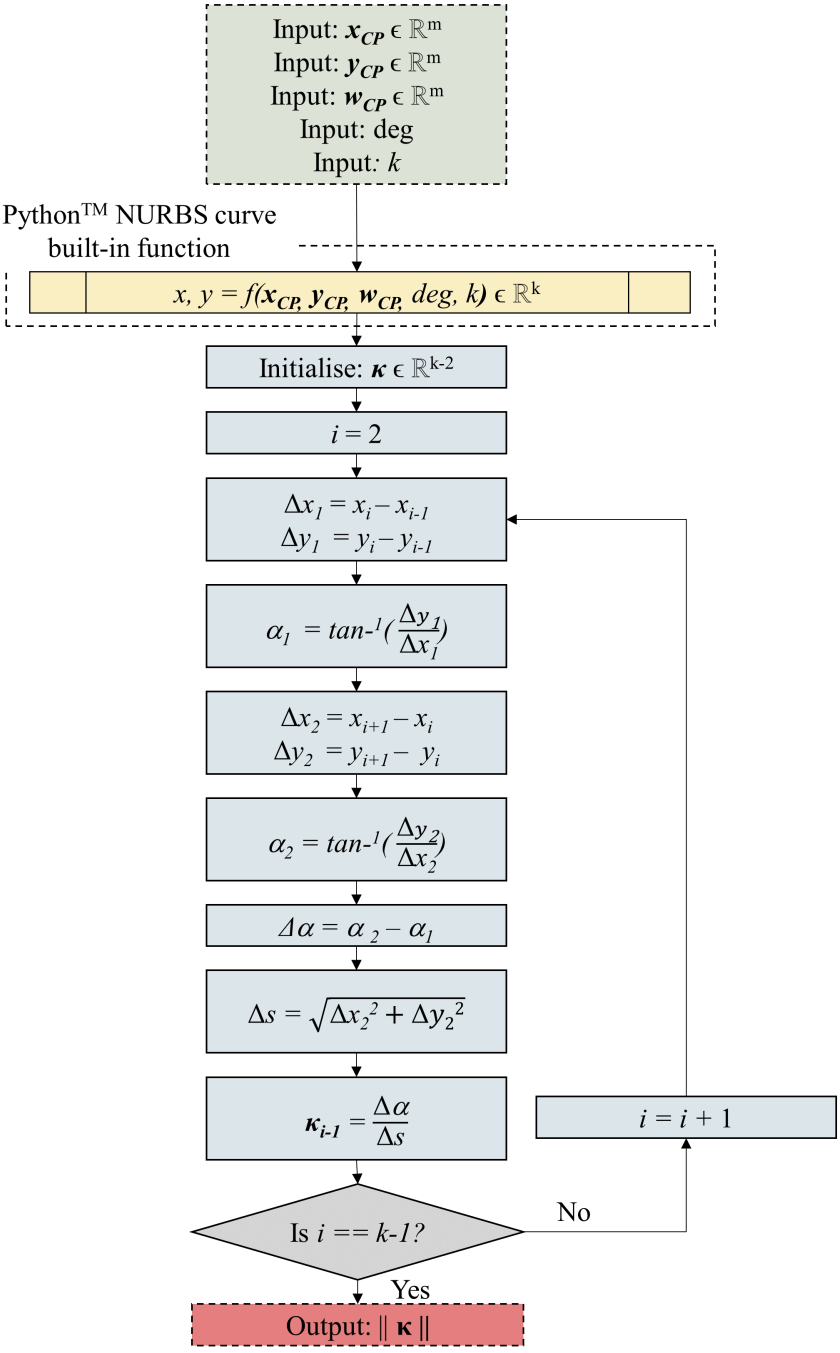


Figure 5.7: Cowl interior shape optimisation objective function flow chart

The NURBS curve representing the cowl interior surface is illustrated in figure 5.8. The NURBS control points are constrained to a particular area, line or point location. The first control point is constrained to the location of the cowl lip. This is the starting point of the cowl interior surface. The second control point is constrained to a line that ensures that the first and second control points make an angle of θ_{CLI} relative to the free-stream direction of flow. This ensures a smooth flow transition at the junction where the cowl lip interior and the cowl interior surfaces meet. The x-coordinate may occupy any location within a

range of $0.00l_{ID}$ to $0.15l_{ID}$ measured horizontally relative to the cowl lip. Due to the angular constraint, the y-coordinate may occupy any location within a range of $0.00l_{ID}\tan(\theta_{CLI})$ to $0.15l_{ID}\tan(\theta_{CLI})$ measured vertically relative to the cowl lip. The limits of $0.15l_{ID}$ and $0.15l_{ID}\tan(\theta_{CLI})$ were chosen for the x- and y-coordinates, respectively, so that the cowl interior turns the flow field in the internal diffuser quickly to contribute towards a small frontal projected height of the cowl.

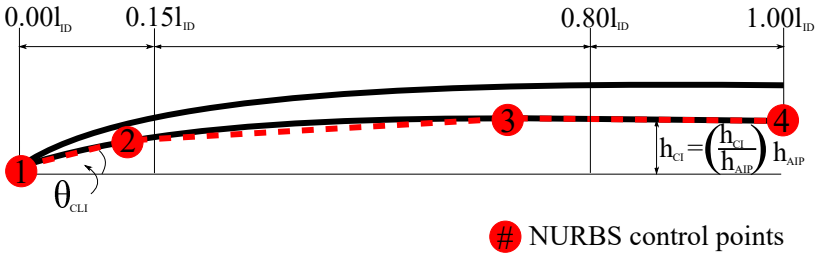


Figure 5.8: Cowl interior design features and dimensions

The third control point is located upstream of the AIP. It forms a horizontal line with the fourth control point. Its purpose is to gradually make the cowl interior surface horizontal towards the AIP. The x-coordinate of the third control point can be located at any position within a range of $0.15l_{ID}$ to $0.80l_{ID}$ measured horizontally relative to the cowl lip location. The y-coordinate is a representation of the height of the cowl interior frontal projected area. This height must be kept small to minimise the cowl wave drag. However, the cowl interior surface is a part of the internal diffuser. Therefore, the cowl interior frontal projected height must contain some proportion of the AIP height. The user can define the proportion of the AIP height that the cowl interior frontal projected height must contain. This user-defined input is denoted as h_{CI}/h_{AIP}. The fourth control point is constrained to a single point. The x-coordinate is located at a distance of l_{ID} measured relative to the cowl lip location. The third and fourth control points make a horizontal line. Therefore, the y-coordinates of these points are equal. The cowl interior surface design optimisation problem is presented in equation 5.3:

$$\underset{\text{w.r.t. } \mathbf{x}}{\text{minimise}} \; ||\kappa(\mathbf{x})||, \quad \mathbf{x} = [x_{CP1}, x_{CP2}, x_{CPm}, y_{CP1}, y_{CP2}, ..., y_{CPm}]^T \in \mathbb{R}^{2m} \tag{5.3}$$

subject to constraints:

Control point 1:

$$x_{CP1} - x_{CL} = 0$$

$$y_{CP1} - y_{CL} = 0$$

Control point 2:

$$\frac{y_{CP2} - y_{CP1}}{x_{CP2} - x_{CP1}} - \tan(\theta_{CLI}) = 0$$
$$x_{CP1} - x_{CP2} \leq 0$$
$$x_{CP2} - x_{CP1} - 0.15 l_{ID} \leq 0$$
$$y_{CP1} - y_{CP2} \leq 0$$
$$y_{CP2} - y_{CP1} - 0.15 l_{ID} \tan(\theta_{CLI}) \leq 0$$

Control point 3:

$$x_{CP1} + 0.15 l_{ID} - x_{CP3} \leq 0$$
$$x_{CP3} - x_{CP1} - 0.80 l_{ID} \leq 0$$
$$y_{CP3} - y_{CP1} - h_{CI} = 0$$

Control point 4:

$$x_{CP4} - x_{CP1} - l_{ID} = 0$$
$$y_{CP4} - y_{CP3} = 0$$

Similarly to the fore-body shape optimisation algorithm, the cowl interior shape optimisation problem solves the above optimisation problem using the built-in Python™ SciPy 1.3.1 optimisation function. For model development, the SLSQP minimisation algorithm was also chosen to solve the cowl interior design optimisation problem. However, other minimisation algorithms could be used in the future to formulate the shape optimisation algorithms in IADAM.

5.4.2.3 Cowl Exterior

The cowl exterior shape optimisation algorithm is almost identical to the cowl interior shape optimisation algorithm. The main difference is that the design of the cowl exterior surface allows a thickness between the cowl interior and exterior surfaces. The maximum cowl thickness, denoted by t_C, is a user-defined input. The NURBS curve representing the cowl exterior surface is illustrated in figure 5.9.

The cowl exterior surface design optimisation problem is presented in equation 5.4. The design optimisation objective function illustrated in figure 5.7 applies to the cowl exterior design optimisation problem.

$$\underset{\text{w.r.t. } \mathbf{x}}{\text{minimise}} \; ||\kappa(\mathbf{x})||, \quad \mathbf{x} = [x_{CP1}, x_{CP2}, x_{CPm}, y_{CP1}, y_{CP2}, ..., y_{CPm}]^T \in \mathbb{R}^{2m} \tag{5.4}$$

subject to constraints:

Control point 1:

$$x_{CP1} - x_{CL} = 0$$

$$y_{CP1} - y_{CL} = 0$$

Control point 2:

$$\frac{y_{CP2} - y_{CP1}}{x_{CP2} - x_{CP1}} - \tan(\theta_{CLE}) = 0$$

$$x_{CP1} - x_{CP2} \leq 0$$

$$x_{CP2} - x_{CP1} - 0.15 l_{ID} \leq 0$$

$$y_{CP1} - y_{CP2} \leq 0$$

$$y_{CP2} - y_{CP1} - 0.15 l_{ID} \tan(\theta_{CLE}) \leq 0$$

Control point 3:

$$x_{CP1} + 0.15 l_{ID} - x_{CP3} \leq 0$$

$$x_{CP3} - x_{CP1} - 0.80 l_{ID} \leq 0$$

$$y_{CP3} - y_{CP1} - h_{CI} - t_C = 0$$

Control point 4:

$$x_{CP4} - x_{CP1} - l_{ID} = 0$$

$$y_{CP4} - y_{CP3} = 0$$

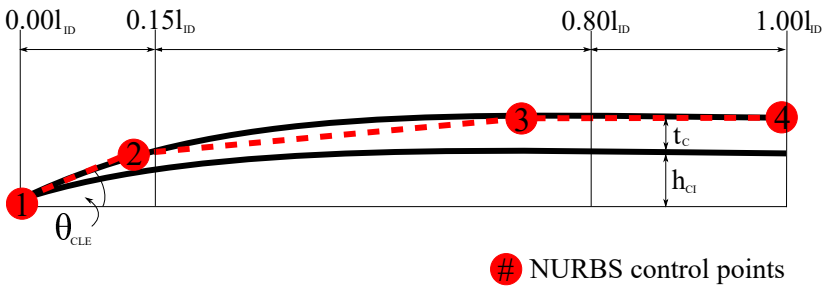


Figure 5.9: Cowl exterior design features and dimensions

The cowl exterior shape optimisation algorithm solves the above optimisation problem using the built-in Python™ SciPy 1.3.1 optimisation function. Similarly to the fore-body and cowl interior shape optimisation algorithms, the cowl exterior shape optimisation algorithm solves

the above optimisation problem using the SLSQP minimisation algorithm. However, other minimisation algorithms could be used in the future to formulate the shape optimisation algorithms in IADAM.

5.4.2.4 Internal Diffuser Bottom Surface

The IDBS shape optimisation algorithm designs the IDBS as a smooth surface defined by a NURBS curve extending from the fore-body to the AIP. The IDBS is a third-degree NURBS curve with four control points. The control points are equally weighted with a weighting of one. The IDBS shape optimisation algorithm was formulated as a mathematical optimisation problem that optimises the control points such that the overall curvature of the IDBS is minimised. The design optimisation objective function illustrated in figure 5.7 applies to the IDBS design optimisation problem. The NURBS curve representing the IDBS is shown in figure 5.10.

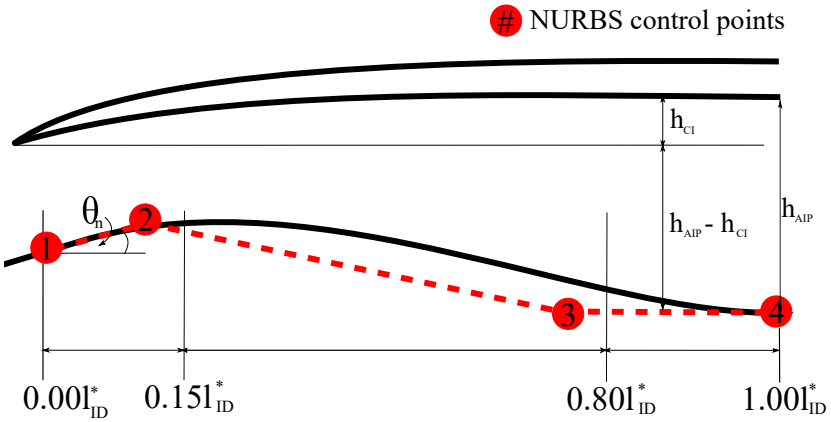


Figure 5.10: IDBS design features and dimensions

The IDBS is an extension of the fore-body. Thus, the first control point is constrained to the point where the fore-body ends. The second control point is constrained to a line that ensures that the first and second control points make an angle of θ_n relative to the free-stream flow. This is done to ensure a smooth flow transition at the junction where the fore-body and the IDBS meet. The x-coordinate of the second control point may occupy any position within a range of $0l^*_{ID}$ to $0.15l^*_{ID}$ measured horizontally relative to the position where the fore-body ends. The constraints applied to the first and second control points of the IDBS are similar to the constraints applied to the corresponding cowl interior control points. This is done to ensure uniformity of the incoming flow as it enters the internal diffuser.

The third control point is located upstream of the AIP. It forms a horizontal line with the fourth control point, ensuring that the curve gradually becomes horizontal as it approaches

the AIP. The x-coordinate can occupy any position within the range of $0.15l^*_{ID}$ to $0.80l^*_{ID}$ measured horizontally relative to the end of the fore-body. The cowl interior supports a proportion of the AIP height. The IDBS must contain the remaining proportion of the AIP height. Therefore, the y-coordinate of the third control point is located at a vertical distance of $h_{AIP} - h_{CI}$ below the cowl lip. The fourth control point is constrained to a single point. The x-coordinate is located at a distance of l^*_{ID} from the end of the fore-body. The y-coordinates of the third and fourth control points are equal. The IDBS design optimisation problem is presented in equation 5.5:

$$\underset{\text{w.r.t. } \mathbf{x}}{\text{minimise}} \; ||\kappa(\mathbf{x})||, \quad \mathbf{x} = [x_{CP1}, x_{CP2}, x_{CPn}, y_{CP1}, y_{CP2}, ..., y_{CPn}]^T \in \mathbb{R}^{2m} \tag{5.5}$$

subject to constraints:

Control point 1:

$$x_{CP1} - x_{FB} = 0$$

$$y_{CP1} - y_{FB} = 0$$

Control point 2:

$$\frac{y_{CP2} - y_{CP1}}{x_{CP2} - x_{CP1}} - \tan(\theta_n) = 0$$

$$x_{CP1} - x_{CP2} \leq 0$$

$$x_{CP2} - x_{CP1} - 0.15l^*_{ID} \leq 0$$

$$y_{CP1} - y_{CP2} \leq 0$$

$$y_{CP2} - y_{CP1} - 0.15l^*_{ID} \tan(\theta_n) \leq 0$$

Control point 3:

$$x_{CP1} + 0.15l^*_{ID} - x_{CP3} \leq 0$$

$$x_{CP3} - x_{CP1} - 0.80l^*_{ID} \leq 0$$

$$y_{CP3} - y_{CL} + (h_{AIP} - h_{CI}) = 0$$

Control point 4:

$$x_{CP4} - x_{CP1} - l^*_{ID} = 0$$

$$y_{CP4} - y_{CP3} = 0$$

The NURBS curve representing the IDBS will not always take the same form. In some instances, the required AIP height will be equal to or slightly larger than the internal diffuser entry height. Thus, the third and fourth control points will be higher than the second control point. In this instance, the IDBS will have a similar form to the cowl interior surface. In other instances, the required AIP height will be much larger than the internal diffuser entry height. Therefore, the IDBS will have the form illustrated in figure 5.10. The form that the IDBS takes is dependent on the AIP height and the cowl interior frontal projected height. The AIP height is a function of the user-defined AIP Mach number. The cowl interior frontal projected height is a function of the user-defined ratio h_{CI}/h_{AIP}. The advantage of defining the IDBS as a NURBS curve is that it provides the flexibility and the versatility needed for the IDBS to take on all these various forms.

The IDBS shape optimisation algorithm solves the above optimisation problem using the built-in Python™ SciPy 1.3.1 optimisation function. For model development, the SLSQP minimisation algorithm was chosen to be an initial driver to construct the IDBS shape optimisation algorithm.

5.5 Multi-Start Optimisation Study

A multi-start optimisation study was performed on the fore-body, cowl interior, cowl exterior and IDBS shape optimisation algorithms. The purpose of the study was to investigate the presence of local minima in the design spaces. If local minima exist, the purpose of the study was also to determine the initial conditions which cause the algorithms to converge to global optimum solutions.

IADAM requires several user-defined inputs to execute the above-mentioned shape optimisation algorithms. The user-defined inputs specified for this particular study are presented in table 5.1. The user-defined inputs presented in table 5.1 will remain constant throughout the study to ensure that any variations in the generated inlet geometry are purely a result of using different initial approximations.

The initial approximations provided to the fore-body, cowl-interior, cowl-exterior and IDBS shape optimisation algorithms were computed at random using the Python™ built-in random number generator. The random initial approximations were generated within the range of constraints specified in section 5.4. For the inlet generated using the user-defined inputs presented in table 5.1, the range of values over which random initial approximations were generated for the fore-body, cowl interior, cowl exterior and IDBS shape optimisation algorithm multi-start optimisation studies are presented in tables 5.2, 5.3, 5.4 and 5.5, respectively.

Table 5.1: The user-defined inputs used by IADAM to generate inlets for the multi-start optimisation study

Altitude (H)	22 860 m
Free-stream Mach number (M_∞)	2
Capture height (h_{cap})	0.1 m
Number of fore-body ramps (n)	3
AIP Mach number (M_{AIP})	0.35
Cowl lip profile	circular
Cowl lip vertex angle (θ_{CLV})	3°
Cowl lip thickness (t_{CL})	$0.001 \times h_{cap}$
Maximum cowl thickness (t_C)	$0.15 \times h_{cap}$
Ratio of h_{CI}/h_{AIP}	0.2
Internal diffuser length (l_{ID})	$6.5 \times h_{cap}$

Table 5.2: The ranges over which random initial approximations were generated for the fore-body shape optimisation algorithm multi-start optimisation study

	Upper bound	Lower bound
θ_0	0°	0°
θ_1 - θ_n	0°	19.97°

Table 5.3: The ranges over which random initial approximations were generated for the cowl interior shape optimisation algorithm multi-start optimisation study

	Upper bound [m]	Lower bound [m]
x_{CP1}	0.14	0.14
y_{CP1}	0.10	0.10
x_{C21}	0.14	0.24
y_{CP2}	0.10	0.12
x_{CP3}	0.24	0.66
y_{CP3}	0.12	0.12
x_{CP4}	0.79	0.79
y_{CP4}	0.12	0.12

Table 5.4: The ranges over which random initial approximations were generated for the cowl exterior shape optimisation algorithm multi-start optimisation study

	Upper bound [m]	Lower bound [m]
x_{CP1}	0.14	0.14
y_{CP1}	0.10	0.10
x_{C21}	0.14	0.24
y_{CP2}	0.10	0.14
x_{CP3}	0.24	0.66
y_{CP3}	0.14	0.14
x_{CP4}	0.79	0.79
y_{CP4}	0.14	0.14

Table 5.5: The ranges over which random initial approximations were generated for the IDBS shape optimisation algorithm multi-start optimisation study

	Upper bound [m]	Lower bound [m]
x_{CP1}	0.16	0.16
y_{CP1}	0.04	0.04
x_{C21}	0.16	0.26
y_{CP2}	0.04	0.07
x_{CP3}	0.26	0.66
y_{CP3}	0.01	0.01
x_{CP4}	0.79	0.79
y_{CP4}	0.01	0.01

Each shape optimisation algorithm was provided with 100 random initial approximations to execute the design of optimised inlet components. Figure 5.11 illustrates the geometric profiles of all the inlets generated during the present study. All 100 geometric profiles were plotted on the same axes to visualise the deviations of the geometric profiles purely as a result of using varying initial approximations.

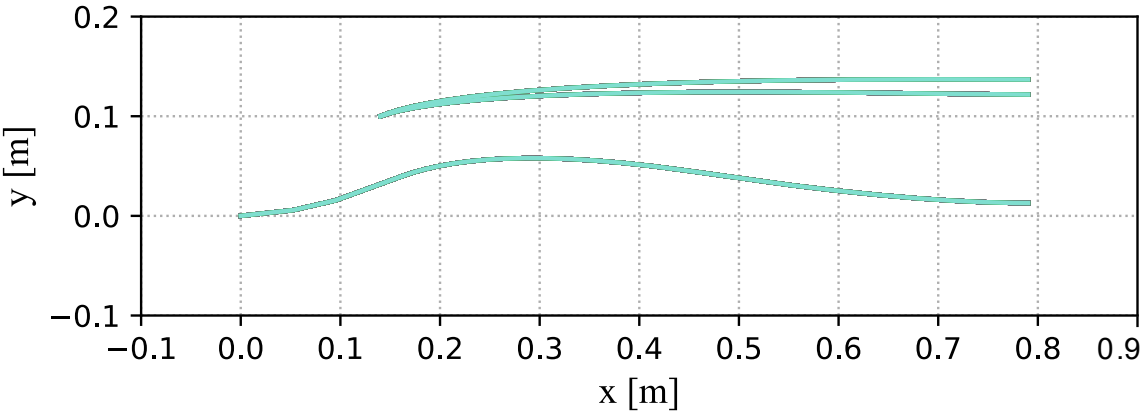


Figure 5.11: The geometric profiles of 100 inlets generated during the multi-start optimisation study

There are 100 plots in figure 5.11. However, the plots are very similar in shape and lie right on top of each other, making it seem like there is only one plot. This suggests that there are little to no deviations in the geometric profiles of the inlets generated IADAM due to varying initial approximations. To investigate this further, the deviations between the geometric profiles in figure 5.11 were quantified by calculating errors between the geometric profiles. The errors relating to specific inlet components were calculated as percentage errors relative to the inlet capture height, denoted by h_{cap}. The errors are root mean square errors between the coordinates of the generated inlet components and a base inlet component. The base inlet components are the inlet components that were generated when the shape optimisation algorithms achieved the smallest objective function values. Figure 5.12 presents histograms of the percentage errors relative to the inlet capture height.

The results presented in figure 5.12 suggest that the geometric profiles presented in figure 5.11 are not identical. The existence of varying errors between the geometric profiles shows slight variations in the geometric profiles. However, these deviations appear to be minor and invisible to the naked eye.

Some statistical data of the errors illustrated in figure 5.12 are presented in table 5.6. The standard deviations are just an order of magnitude greater than a micrometre. Considering the scale of the overall inlet (i.e. h_{cap}), these standard deviations are approximately 0.01-0.06% of the capture height. They are minuscule relative to the scale of the inlet and are

unlikely to have a significant effect on the overall supersonic inlet flow field. Therefore, these standard deviations are not problematic to the overall inlet design. Furthermore, the high level of accuracy required to machine an inlet to the micrometre would be challenging to achieve.

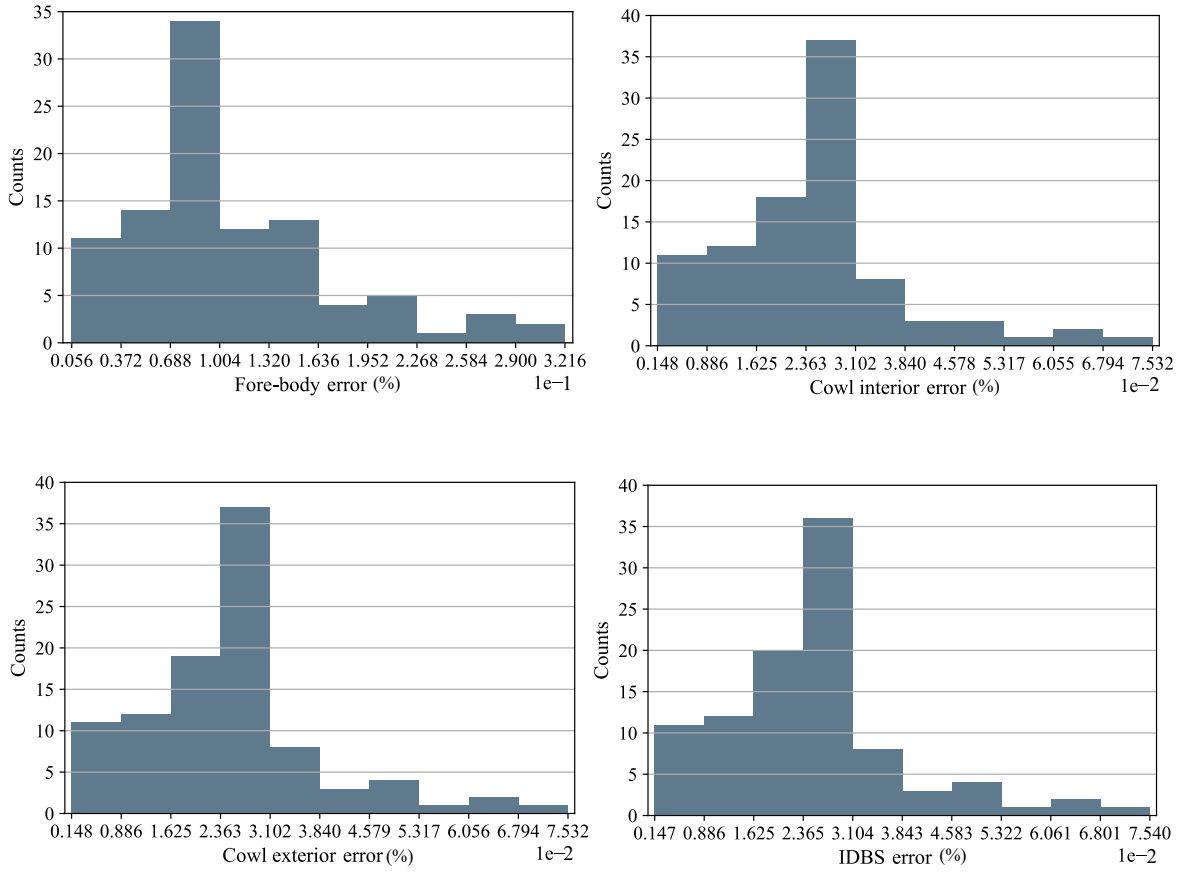


Figure 5.12: The percentage errors relative to h_{cap} for the geometric profiles of the inlets generated during the multi-start optimisation study

Table 5.6: Statistical data of the percentage errors relative to h_cap for the geometric profiles of the inlets generated during the multi-start optimisation study

	Mean	Mode	Median	Standard deviation
Fore-body	1.060e-1%	8.460e-2%	8.664e-2%	6.592e-2%
Cowl interior	2.496e-2%	2.502e-2%	2.503e-2 %	1.357e-2%
Cowl exterior	2.522e-2%	2.517e-2%	2.514e-2%	1.361e-2%
IDBS	2.511e-2%	2.507e-2%	2.499e-2%	1.363e-2%

The means, medians and modes presented in table 5.12 are generally close. This suggests that the datasets have an almost normal distribution. A normal distribution is ideal because the errors presented in figure 5.12 can be mathematically modelled, making it easier to

predict the errors from executing the shape optimisation algorithms using different initial approximations. However, the results illustrated in figure 5.12 suggest that the datasets are not exactly normally distributed. They are slightly skewed to the left. The advantage is that a larger number of the inlets in the multi-start optimisation study generate errors on the lower end of the spectrum. The disadvantage is that these errors can not be easily modelled. Fortunately, the standard deviations are minuscule relative to the scale of the inlet. Therefore, these errors are unlikely to have a significant effect on the overall supersonic inlet flow field.

The multi-start optimisation study showed that different initial approximations result in slight deviations between the geometries generated by the shape optimisation algorithms. These deviations are minuscule, therefore suggesting that the algorithms converge to global optimum solutions. The presence of minor errors between inlet geometries may be a result of truncation errors.

5.6 Conclusion

The current chapter presents the development of an analytical method that applies the theories of inviscid compressible flow and mathematical optimisation to automate the design and analysis of 2D, external-compression, supersonic inlets. The analytical method developed here, i.e. IADAM, designs the overall inlet geometry such that the total pressure recovery and mass flow ratio are maximised. The shape optimisation algorithms in IADAM are solved using the built-in Python™ SciPy 1.3.1 optimisation function. For model development, the SLSQP minimisation algorithm was chosen to be an initial driver to construct the shape optimisation algorithms. A multi-start optimisation study was performed and showed that the use of different initial approximations causes the shape optimisation algorithms to converge to global optimum solutions.

Ignoring the effects of viscosity means that maximising total pressure recovery and mass flow ratio largely depends on the fore-body design. However, IADAM takes steps to reduce the total pressure losses due to viscous effects inside the internal diffuser. These steps involve designing the internal diffuser such that the air is turned smoothly and gradually. Real compressible flows are subjected to the effects of viscosity. Ignoring the effects of viscosity on supersonic inlet flow fields may result in deviations between what IADAM predicts the supersonic inlet flow fields to be and what they are in reality. The effect of viscosity on supersonic inlets must be investigated to determine the impact of viscosity on the overall supersonic inlet performance. This is done in chapter 6.

Chapter 6 Investigation and Implementation of Viscous Effects on IADAM

6.1 Introduction

IADAM (Chapter 5) was developed based on the assumption of inviscid compressible air flowing through the generated inlets. The premise of inviscid flow is not always applicable to real-world compressible flows. Friction between the supersonic inlet surfaces and the air flowing through the supersonic inlets introduces viscosity to the supersonic inlet flow fields. A detailed CFD model was developed on the commercial CFD package STAR-CCM+ to study the viscous flow phenomena in supersonic inlet flow fields. Section 6.2 details the CFD model development. The CFD simulations were submitted to the Centre for High Performance Computing cluster for processing/solving.

IADAM can generate 2D, external-compression, supersonic inlets with different geometric features and operational flight conditions based on user-defined inputs. The impact of viscous flow phenomena on supersonic inlet flow fields may vary for supersonic inlets with different geometric features and flight conditions. The geometric features and flight conditions are a function of the user-defined inputs supplied to IADAM. Section 6.3 investigates how different user-defined inputs impact viscous flow phenomena on supersonic inlet flow fields.

The data obtained from the sensitivity study were used to develop a method to apply viscous corrections to IADAM. The application of viscous corrections provides an improved approximation of the performance parameters of the inlets generated by IADAM. Furthermore, viscous corrections also provide the user with an improved understanding of the quality of the air that the inlet supplies to the combustion chamber. Further details of how viscous corrections were applied to IADAM are presented in section 6.4.

6.2 Computational Fluid Dynamics

The development of a CFD model to investigate viscous effects in supersonic inlet flow fields is demonstrated with an inlet generated by IADAM. IADAM requires a set of user-defined inputs to create an inlet. The user-defined inputs presented in table 5.1 in the multi-start optimisation study (Section 5.5) were used to generate the inlet used in the CFD model development. The generated inlet geometry is presented in figure 6.1.

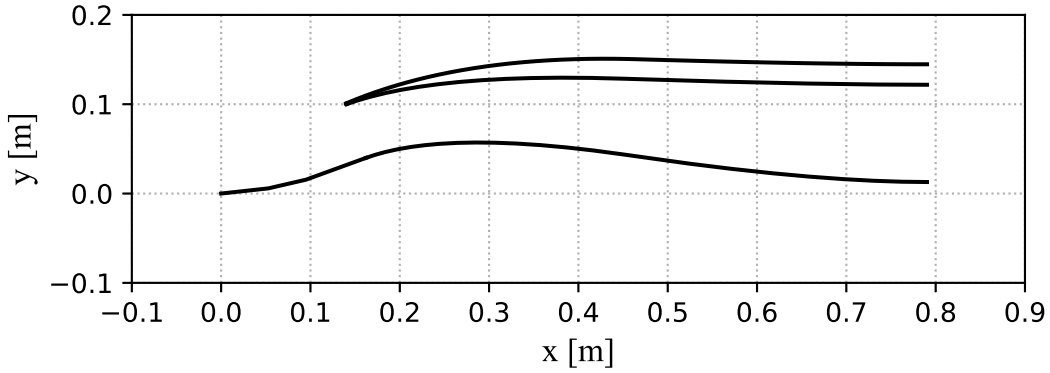


Figure 6.1: A 2D, external-compression, supersonic inlet generated by IADAM

6.2.1 Domain Specification

The CFD model was developed in both the 2D and 3D space. A validation study was performed to determine how closely the 2D and 3D CFD model results compare to each other and to published experimental data obtained from a paper titled "Mesoflap and Bleed Flow Control for a Mach 2 Inlet" (Loth et al. 2004). The validation study is discussed in more detail in section 6.2.8 and appendix C. The validation study showed that the 2D CFD model sufficiently approximates the 2D, external-compression, supersonic inlet flow field and captures the essential flow features. However, the 3D CFD model produced quantitative results that were in better agreement with the published experimental data than the results produced by the 2D CFD model. This is because the flow field in 2D, external compression, supersonic inlets is inherently 3D in nature. The accuracy of the 3D CFD model has a high computational cost. It would not have been practical to use the 3D CFD model in a sensitivity study (Section 6.3) where several CFD analyses had to be conducted. The computational cost is significantly reduced in the 2D CFD model. The 2D CFD model can capture the essential flow features in a 2D, external-compression, supersonic inlet flow field and provides reasonable approximations of the flow field. Therefore, the 2D CFD model was used in the present work. The qualitative and quantitative results used to justify only using the 2D CFD model are provided in greater detail in section 6.2.8 and appendix C.

Figure 6.2 depicts the CFD fluid domain and the associated boundary conditions. The domain was modelled using SolidWorks 2018. The free-stream inflow was modelled with a free-stream boundary condition placed upstream of the inlet geometry. The horizontal distance between the free-stream inflow boundary and the leading edge of the fore-body is equal to the user-defined capture height. The free-stream outflow was modelled with a pressure outlet boundary condition. All the internal diffuser surfaces were modelled with the wall boundary condition. The airflow exiting the internal diffuser was modelled with a pressure outlet boundary condition.

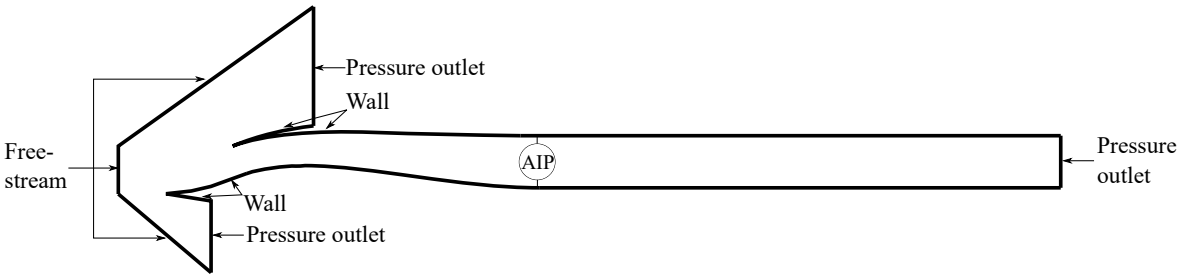


Figure 6.2: The 2D CFD model domain with boundary conditions

Initially, the pressure outlet boundary condition representing the airflow exiting the internal diffuser was located at the AIP. The resulting CFD simulation was characterised by a normal shock wave oscillating back and forth at the internal diffuser entry plane. This occurred because the pressure outlet boundary condition tends to be highly reflective. Pressure disturbances in the flow reflect off the boundary and work their way upstream in subsonic flow. The pressure wave changes the flow conditions downstream of the normal shock wave, resulting in unsteady movement of the normal shock wave. Ekermo (2018) performed CFD analyses of a supersonic inlet and placed the pressure outlet boundary condition well enough downstream of the AIP to reduce the potential of pressure disturbances reflecting off the boundary. This was accomplished by adding a constant-area duct downstream of the AIP. This allowed the flow to be more uniform before the pressure outlet boundary condition.

An additional constant-area duct was added to the domain downstream of the AIP, as illustrated in figure 6.2. The pressure outlet boundary condition was placed at the end of the additional duct. The duct has the same height as the internal diffuser at the AIP. It also has a length ten times the height of the internal diffuser at the AIP. The appropriate length of the constant-area duct was decided upon based on a trial-and-error process.

6.2.2 Mesh Specification

The computational mesh was generated using the STAR-CCM+ parts-based meshing strategy. The polyhedral and prism layer meshers were used to generate the mesh. The mesh was refined in the regions where shock wave formation and boundary layer separation are expected.

A mesh independence study was performed for a similar inlet in the CFD validation study (Appendix C) to ensure that the solution is independent of the mesh resolution. The base cell sizes tested were $0.030h_{cap}$, $0.025h_{cap}$, $0.020h_{cap}$, $0.015h_{cap}$ and $0.010h_{cap}$. Mesh independence was evaluated based on the total pressure recovery distributions at the AIP for the various mesh cell sizes. Figure 6.3 presents the total pressure recovery distribution at the AIP for the various mesh cell sizes. The root mean square errors between the plots in figure 6.3 are presented in table 6.1. Although the results appeared to be very close, the root mean square errors between the total pressure recovery distributions indicate no significant differences in total pressure recovery for base cell sizes smaller than $0.015h_{cap}$. This is the base cell size used to generate the mesh.

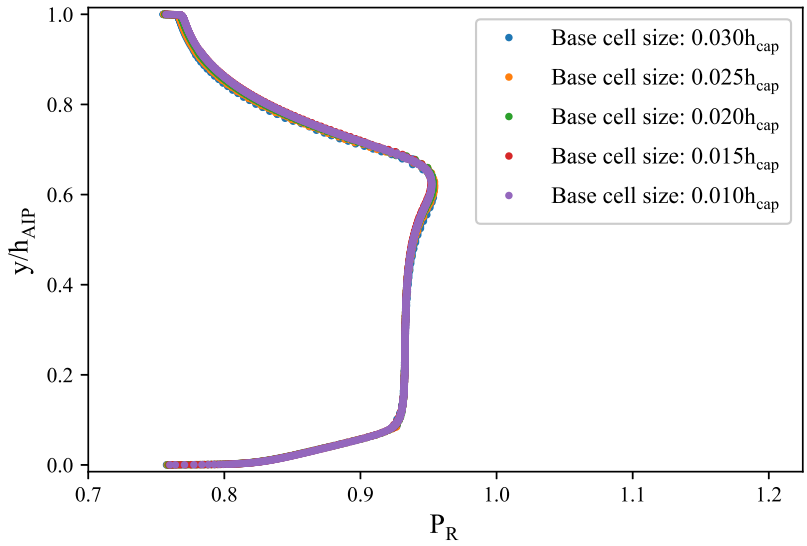


Figure 6.3: The P_R distribution at the AIP for various 2D mesh cell sizes

The computational mesh is illustrated in figure 6.4. The mesh in the constant-area duct is not included in figure 6.4 to provide a close up of the mesh illustrating mesh refinement in the regions where shock wave formation and boundary layer separation are expected. The size of the mesh is presented in table 6.2.

Table 6.1: The errors between P_R distribution curves for various 2D mesh cell sizes

Computational Mesh 1	Computational Mesh 2	P_R Error
Base cell size: $0.030h_{cap}$	Base cell size: $0.025h_{cap}$	0.015
Base cell size: $0.025h_{cap}$	Base cell size: $0.020h_{cap}$	0.008
Base cell size: $0.020h_{cap}$	Base cell size: $0.015h_{cap}$	0.003
Base cell size: $0.015h_{cap}$	Base cell size: $0.010h_{cap}$	0.000



Figure 6.4: The 2D CFD model computational mesh

Table 6.2: The size of the 2D CFD model computational mesh

Number of cells	1 873 162
Number of polyhedral layers	100

The mesh metrics that measure the cell quality of a 2D mesh in STAR-CCM+ are face validity, volume change, cell skewness angle, chevron quality indicator and least-squares quality (Siemens Digital Software 2020). The mesh quality metrics of the computational mesh illustrated in figure 6.4 are presented in figure 6.5.

The face validity of a particular cell is an area-weighted calculation of how correct the directions of the face normals are relative to the location of the cell centroid (Siemens Digital Software 2020). The mesh in question is a 2D mesh. Therefore, the edges of the cells are considered. A good quality 2D cell has edge normals that are directed outward and away from the cell centroid. Such a cell has a face validity of one. Cells with a face validity less

than 0.5 are negative cells, which should be avoided. Based on figure 6.5, all the cells in generated mesh have a face validity of one. There are no negative cells in the mesh.

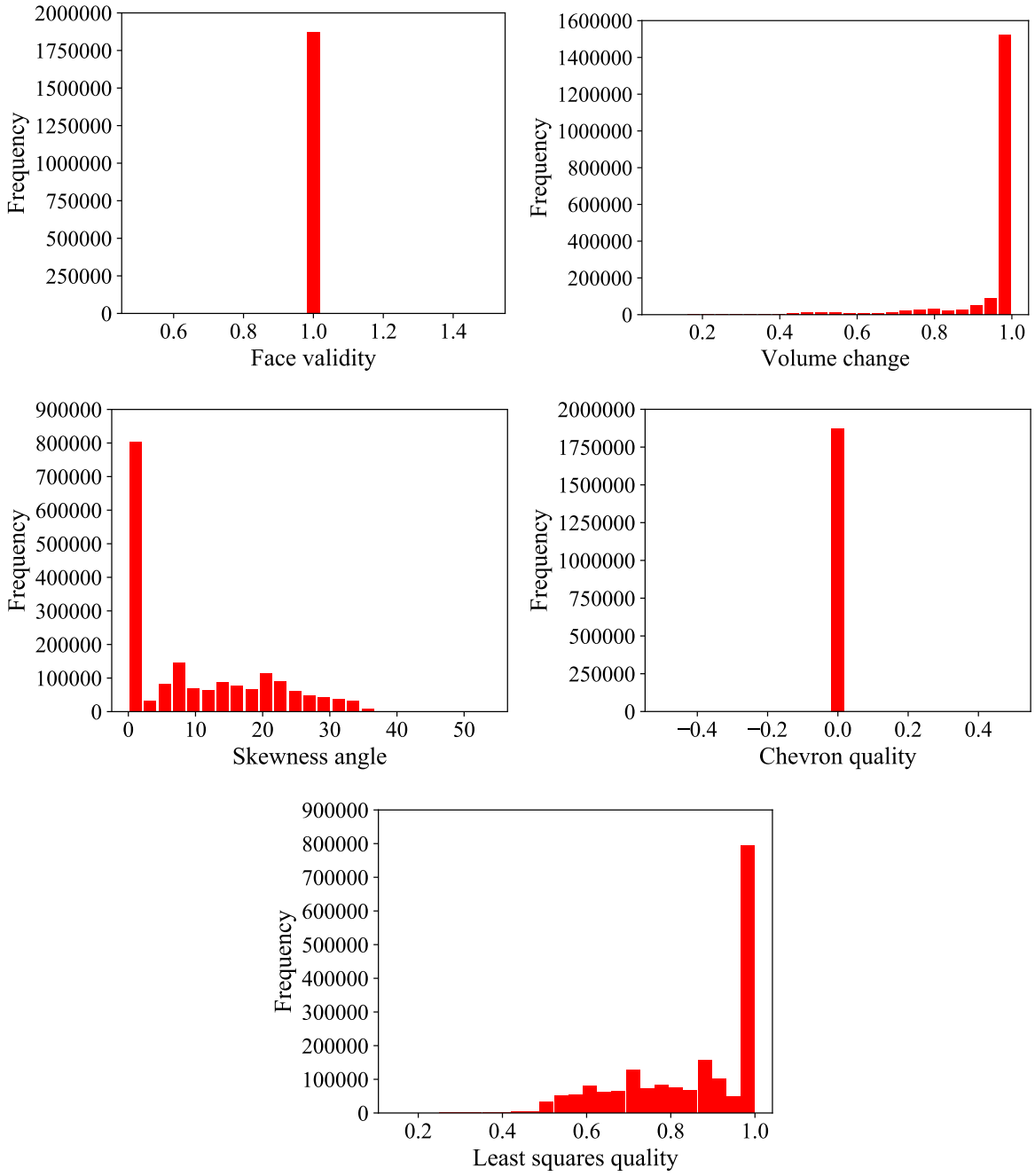


Figure 6.5: The mesh metrics of the 2D CFD model computational mesh

Volume change indicates the volume of a particular cell relative to the volume of its biggest neighbouring cell (Siemens Digital Software 2020). The generated mesh (Figure 6.4) is 2D. Therefore, the volume change is calculated based on the areas of the cells. Cells with an area equal to or larger than their neighbours have a volume change of one. Bad quality cells have a volume change of 0.01 or less. The results presented in figure 6.5 indicate that a large

proportion of the cells in the generated mesh have a volume change close to one. None of the cells in the generated mesh have a volume change of 0.01 or less.

Considering two neighbouring 2D cells, the cell skewness angle is the angle between the orthogonal vector of the common edge between the cells and the line that connects the centroids of the cells. The cell skewness angle must be kept lower than 85° to avoid bad equality cells (Siemens Digital Software 2020). The results presented in figure 6.5 show that the highest skewness angle of the cells in the generated mesh is approximately 53°.

Chevron cells are bad quality cells that should be avoided in a mesh. They are defined as two neighbouring slender cells that meet at an angle in such a way that the line joining the cell centroids does not pass through the face (3D)/edge (2D) that the cells share (Siemens Digital Software 2020). Figure 6.5 indicates that the mesh has no chevron cells.

The least-squares quality measures the quality of a particular cell based on the location of its cell centroid relative to the location of the centroids of the neighbouring cells that it shares common faces (3D)/edges (2D) with. A least-squares quality of one is an indicator of a good quality cell. Bad quality cells have a least-squares quality of 10^{-3} or lower (Siemens Digital Software 2020). Based on figure 6.5, approximately 800 000 cells ($\approx 42\%$ of total cells) have a least-squares quality of one. There are no cells that have a least-squares quality less than 10^{-3}.

6.2.3 Physics Models

All the physics models used in the CFD simulation are tabulated in table 6.3. The CFD model was developed in the 2D space. The air flowing through the inlet was assumed to be an ideal gas. The compressibility of a gas cannot be ignored. Therefore, the density-based solver (i.e. coupled flow) was selected. The CFD model was developed to compute a steady-state solution.

The $\kappa-\epsilon$ turbulence model was used to model viscous effects on the supersonic inlet flow field. The decision to use this model was influenced by the work done by Mizukami and Saunders (1995). Mizukami and Saunders (1995) performed a study to investigate three turbulence models to analyse the flow in a Mach 2.68, bifurcated, rectangular, mixed-compression inlet. The turbulence models investigated were the $\kappa-\epsilon$, Baldwin-Barth, and Baldwin-Lomax turbulence models. They found that the $\kappa-\epsilon$ turbulence model compared well with experimental data. Furthermore, they found that it applies to a wide range of flows, and it is expected to simulate 3D flows more accurately than 2D flows. Therefore, they recommend this turbulence model for the analysis of supersonic inlet flow fields. Loth et al. (2004),

Bourdeau et al. (1999), and Aziz, Elbanna and Abdelrahman (2010), just to name a few, also performed CFD analyses of supersonic inlet flow fields using the $\kappa - \epsilon$ turbulence model. Therefore, the $\kappa - \epsilon$ appears to be an acceptable turbulence model for this application.

Table 6.3: The 2D CFD model physics models

Group box	Model
Space	Two-dimensional
Time	Steady
Material	Gas
Flow	Coupled flow
Equation of state	Ideal gas
Energy	Coupled energy
Gradient metrics	Gradients
Viscous regime	Turbulent
Turbulence	Reynolds-averaged Navier-Stokes
Reynolds-averaged turbulence	$\kappa - \epsilon$ turbulence
$\kappa - \epsilon$ turbulence model	Realisable $\kappa - \epsilon$ two-layer
Wall distance	Exact wall distance
$\kappa - \epsilon$ two-layer wall treatment	Two-layer all-y+ wall treatment

There are several $\kappa - \epsilon$ turbulence models available in STAR-CCM+. However, the realisable $\kappa - \epsilon$ turbulence model was specifically chosen for this application. The realisable $\kappa - \epsilon$ turbulence model was developed by Shih et al. (1994). It was used to model various types of flow. These include duct and flat plate boundary layer flows. The flow simulations were performed with and without pressure gradients. The analyses conducted by Shih et al. (1994) showed that the realisable $\kappa - \epsilon$ turbulence model performed better than the standard $\kappa - \epsilon$ turbulence model in most cases.

In addition, the two-layer approach has the added flexibility of an all-y+ wall treatment. This means that the turbulence model can model viscous boundary layer flows for prism layer meshes of varying degrees of coarseness or fineness. This is advantageous to the current study because the cells in the computational mesh are not the same size. The mesh is refined in regions where shock waves and boundary layer separation are expected. The flow field in the supersonic inlet also has varying velocity scales due to the shock waves and area compression occurring in the inlet. Therefore, this makes it difficult to achieve a pure high-y+ or low-y+ mesh.

6.2.4 Boundary Conditions

The fluid properties applied to the free-stream boundary conditions in table 6.4 were derived from the user-defined inputs. The air was assumed to be moving in a horizontal direction. The free-stream Mach number is a user-defined input. The static temperature and pressure were calculated using the user-defined altitude and the standard atmosphere model.

Table 6.4: The 2D CFD model free-stream boundary conditions

Flow direction	$[1.0, 0.0, 0.0]$
Mach number	2
Static pressure	3 542.68 Pa
Static temperature	219.43 K
Turbulence intensity	0.01
Turbulent viscosity ratio	10

The turbulence intensity in table 6.4 was left as the default STAR-CCM+ value. According to the STAR-CCM+ user manual, external free-stream flows are considered to be a low turbulence case. Low turbulence cases generally have turbulence intensities of 1% or lower (Siemens Digital Software 2020; ANSYS Inc 2009). Ideally, the best estimate of turbulence intensity would be obtained from empirical data. However, there was no empirical data available for the current study. Therefore, the default turbulence intensity of 1% was considered an acceptable approximation for the present work. This may be revisited in future work.

The turbulent viscosity ratio in table 6.4 was also left as the default STAR-CCM+ value. It is typically set as a small value within the range of 1 and 10 for external free-stream flows (ANSYS Inc 2009). However, STAR-CCM+ does not apply the set value in table 6.4 during the simulation when a realisable $\kappa - \epsilon$ model is used. It applies a turbulent viscosity ratio that it calculates during the simulation. The turbulent viscosity ratio is calculated based on the boundary condition and parameters that are unknown before the simulation runs (Siemens Digital Software 2020). There is a method that can be applied to hard-code a desired turbulent viscosity ratio. This may be especially useful when a good estimate of the turbulent viscosity ratio is known from empirical data. However, there was no empirical data available for the current study. Therefore, the turbulent viscosity ratio calculated by STAR-CCM+ during the simulation was considered an acceptable approximation for the present work. This may be revisited in future work.

The fluid properties applied to the pressure outlet boundary condition located downstream of the AIP are presented in table 6.5. An inviscid flow analysis of the supersonic inlet flow

field was used to compute the static temperature based on the desired user-defined AIP Mach number. The applied pressure was adjusted to a value that ensured the normal shock wave was located at the internal diffuser entry plane. This process does not resemble the process that occurs in a real ramjet during the flight. A real ramjet would not adjust the back pressure during flight until it finds a value that ensures the normal shock wave is located at the internal diffuser entry plane. This approach simulates an idealised case where the normal shock wave is located at the internal diffuser entry plane. The back pressure required to simulate this idealised case was not known. Therefore, it had to be adjusted until it could be determined.

Table 6.5: The 2D CFD model pressure outlet boundary condition

Static pressure	23 000 Pa
Static temperature	385.52 K
Turbulence intensity	0.01
Turbulent viscosity ratio	10

The turbulence intensity in table 6.5 was left as the default STAR-CCM+ value. The turbulence intensity inside the internal diffuser is not known. However, an estimation can be made using equation 6.1 (ANSYS Inc 2009).

$$I = 0.16(Re_{D_H})^{-1/8} \tag{6.1}$$

Technically, equation 6.1 is used to calculate the turbulence intensity at the core of a fully developed duct flow (ANSYS Inc 2009). The geometry of a supersonic inlet does not look exactly like a regular duct. Furthermore, boundary layers are expected in supersonic inlet flow fields. However, supersonic inlet flow fields are not typically fully developed. The results from this estimation were seen as a limiting case.

For this estimation, the supersonic inlet was approximated as a regular duct. The Reynolds number, denoted by Re_{D_H}, was calculated using equation 6.2 (Anderson 2010). It was calculated based on the free-stream properties of the captured air. These represent the fluid properties of the flow entering the duct.

$$Re_{D_H} = \frac{\rho v D_H}{\mu} \tag{6.2}$$

Width and height were required to calculate the hydraulic diameter of the captured stream-tube of air. The value for h_{cap} represents the height of the captured stream-tube of air. The 2D CFD model assumes the domain has a unit width. For this estimation, the hydraulic diameter was calculated for a rectangular duct with a height equivalent to h_{cap} and a unit width. Based on this estimation, the flow entering the inlet had a Reynolds number of approximately 422 713. The resultant turbulence intensity was approximately 0.032.

The default STAR-CCM+ turbulence intensity is lower than the calculated turbulence intensity. The calculated turbulence intensity is an estimation based on fully developed duct flow. Supersonic inlet flow fields are not typically fully developed. Therefore, the turbulence intensity in a supersonic inlet flow field is expected to be lower than the turbulence intensity of a fully developed duct flow. The default STAR-CCM+ value was assumed to be a fair selection for this purpose. This assumption may be revisited in future work.

The turbulent viscosity ratio in table 6.5 was also left as the default STAR-CCM+ value. As previously mentioned, STAR-CCM+ does not apply the set value in table 6.5 during the simulation when a realisable $\kappa - \epsilon$ model is used. It applies a turbulent viscosity ratio that it calculates during the simulation. The turbulent viscosity ratio is calculated based on the boundary condition and parameters that are unknown before the simulation runs (Siemens Digital Software 2020). The turbulent viscosity ratio calculated by STAR-CCM+ during the simulation is an acceptable approximation for the present work. This may be revisited in future work

6.2.5 Reference Values and Initial Conditions

The reference values are tabulated in table 6.6. The reference pressure is 0.0 Pa to ensure the use of absolute pressures. The minimum allowable wall distance is left as the default STAR-CCM+ value of $1e^{-6}$ m. This value is acceptable to the CFD model because turbulence models require a non-zero value for wall distance (i.e. y+). The algorithm calculating wall distance has been developed to produce a positive value for almost all cell shapes. However, the algorithm can compute negative values for badly shaped cells. The default minimum allowable wall distance prevents this from happening. Furthermore, an all-y+ wall treatment was selected. The default minimum allowable wall distance is small enough for the solver to model the turbulent flows with low-y+ meshes.

Table 6.6: The 2D CFD model reference values

Reference pressure	0.0 Pa
Minimum allowable wall distance	$1e^{-6}$ m
Minimum allowable absolute pressure	1 000 Pa
Maximum allowable absolute pressure	$1e^{8}$ Pa
Minimum allowable temperature	100.0 K
Maximum allowable temperature	5 000.0 K

The minimum and maximum allowable absolute pressures in table 6.6 were left as the default STAR-CCM+ values of 1 000 Pa and $1e^{8}$ Pa, respectively. The purpose of a supersonic

inlet is to compress air from the atmospheric free-stream pressure to a higher pressure at the AIP. Therefore, the free-stream pressure (Table 6.4) is expected to be the lowest pressure in the flow field. The highest pressure in the flow field is expected to be the AIP pressure (Table 6.5). The expected minimum and maximum pressures are 3 542.68 Pa and 23 000 Pa, respectively. These fall within the default STAR-CCM+ allowable absolute pressure range. Therefore, the default minimum and maximum allowable absolute pressures were considered acceptable.

The minimum and maximum allowable temperatures in table 6.6 were left as the default STAR-CCM+ values of 100 K and 5 000 K, respectively. When air is compressed, the temperature of the air increases. Therefore, the lowest and highest temperatures in the flow field are expected to occur at the free-stream and AIP, respectively. The boundary conditions presented in tables 6.4 and 6.5 indicate that the expected minimum and maximum flow field temperatures are 219.43 K and 385.52 K, respectively. These values fall within the default STAR-CCM+ allowable temperature range. Therefore, the default temperature range was considered acceptable for the CFD model.

The initial conditions applied to the entire domain are tabulated in table 6.7. They are the fluid properties downstream of a normal shock wave, whereby the upstream fluid properties are the properties of the captured free-stream airflow (Table 6.4). The initial pressure, temperature and velocity were calculated using ideal gas calculations. Through trial-and-error, it was established that this initial condition was a sensible place to start the CFD analysis.

Table 6.7: The 2D CFD model initial conditions

Static pressure	15740.07 Pa
Static temperature	370.42 K
Turbulence intensity	0.01
Turbulence specification	Intensity + Viscosity ratio
Turbulent velocity scale	222.76 m/s
Turbulent viscosity ratio	10.0
Velocity	$[222.76, 0.0, 0.0]$ m/s

According to Siemens Digital Software (2020), the turbulent velocity scale is typically set to a value equal to the initial velocity. The turbulent viscosity ratio in table 6.7 is left as the default STAR-CCM+ value. STAR-CCM+ does not apply this value during the initialisation of the simulation when a realisable $\kappa - \epsilon$ model is used. It applies a turbulent viscosity ratio that it calculates based on parameters that are unknown before the simulation is initialised (Siemens Digital Software 2020). The turbulent viscosity ratio calculated by STAR-CCM+

during the initialisation is an acceptable approximation for the present work. This may be revisited in future work

6.2.6 Solver

The CFD model uses a second-order coupled implicit solver because it is well suited to compressible flows. The second-order coupled implicit solver has a grid sequencing expert initialisation feature. This feature performs a normal initialisation of the flow field. After that, it rapidly computes an approximate inviscid solution of the flow field. Obtaining an inviscid solution first made the viscous CFD simulation converge faster.

6.2.7 Results and Discussion

The CFD model developed here investigated the effects of viscosity on the air flowing through a supersonic inlet. The flow field in the constant-area duct is not included in this discussion because it is not essential to the investigation. The Mach number contour plot (Figure 6.6) provides qualitative and quantitative information about the supersonic inlet flow field. The captured airflow is compressed from a supersonic free-stream Mach number of Mach 2 to a lower supersonic Mach number of approximately Mach 1.3 by a series of oblique shock waves. After that, the airflow is compressed to a subsonic Mach number by the normal shock wave located at the internal diffuser entry plane. The system of oblique shock waves and the normal shock wave all converge at a single point, as per the fore-body design specifications outlined in section 5.4.1. The subsonic air entering the internal diffuser is compressed even further to a lower subsonic Mach number at the AIP.

There is a difference between the user-defined AIP Mach number and the AIP Mach number computed by the CFD model. This difference is illustrated in figure 6.7. The user-defined AIP Mach number has a single and constant value. However, the CFD model calculates an AIP Mach number that varies in the direction perpendicular to the airflow.

The airflow can be treated as if composed of two independent components, i.e. a non-viscous potential flow region and a viscous flow region adjacent to the internal diffuser surfaces. Based on figure 6.6, the viscous flow regions at the AIP are boundary layers that have separated from the cowl interior surface and the IDBS. The air within the viscous flow regions is retarded by friction between the flow and the internal diffuser surfaces. This causes the Mach number of the air within the viscous flow region to be zero at the internal diffuser surfaces and increase to the Mach number of the airflow in the potential flow region. Furthermore, the viscous flow region alters the effective internal diffuser surfaces. This decreases the effective internal

diffuser expansion ratio. A reduction in the expansion ratio reduces the amount by which the air in the potential flow region is compressed. This causes the air within this region to have a higher Mach number at the AIP relative to the user-defined M_{AIP}.

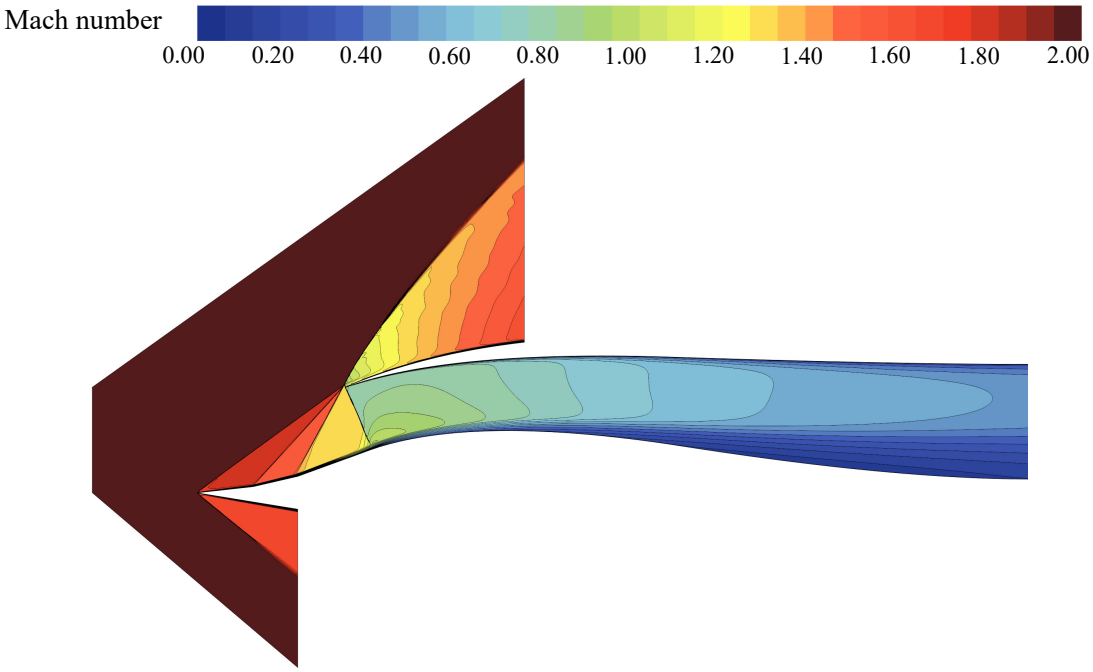


Figure 6.6: A Mach number contour plot of the supersonic inlet flow field

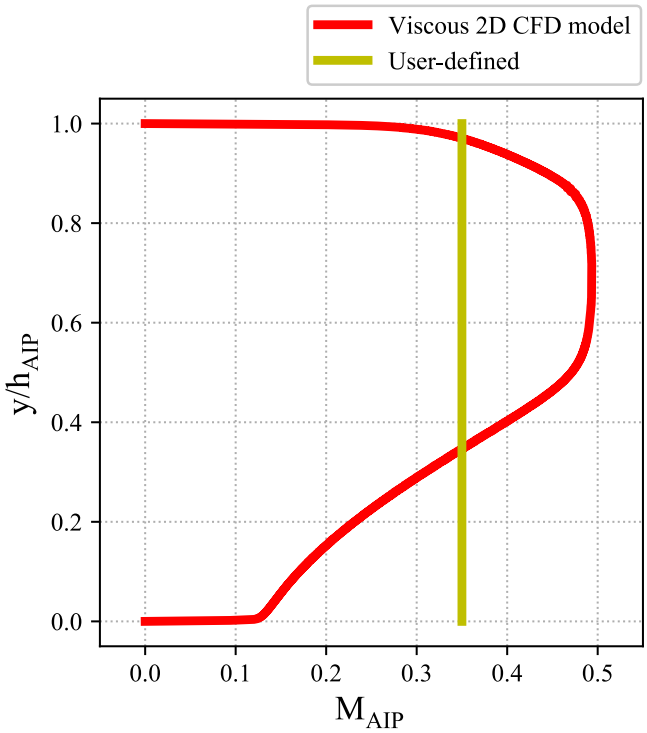


Figure 6.7: The M_{AIP} distribution

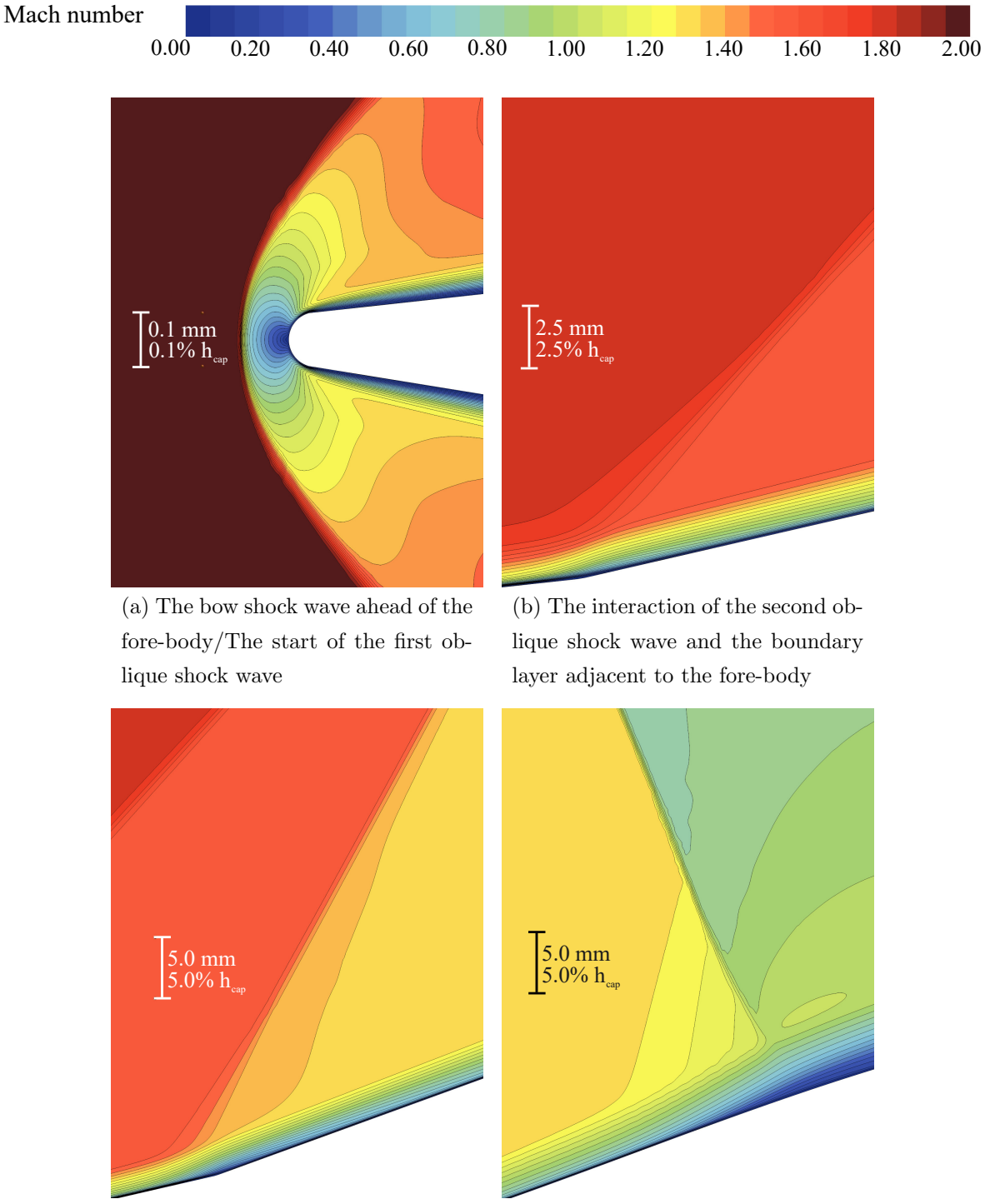
The viscous flow phenomena that exist in the supersonic inlet flow field are illustrated in figure 6.6. Complex shock wave patterns result from the shock-wave/boundary-layer interactions. The images in figure 6.8 take a closer look at the complex shock wave patterns occurring in the viscous flow adjacent to the fore-body surface.

The leading edge of the fore-body is a small blunt body with a thickness of 0.0001 m, which is 0.1% of the capture height. As discussed in section 4.1.3.1.6, a blunt body moving through a supersonic flow generates a curved, detached bow shock wave. Figure 6.8a is an illustration of the bow shock wave that has formed ahead of the fore-body. The bow shock wave rapidly transforms into the first oblique shock wave in the oblique shock wave system generated by the fore-body. There is no shock-wave/boundary-layer interaction associated with this particular shock wave.

The second oblique shock wave appears to be diffused at the base, as illustrated in figure 6.8b. The interaction of the second oblique shock wave and the boundary layer causes the boundary layer ahead of the compression ramp to thicken. The thickened boundary layer makes the sharp compression ramp corner appear smoother to the air flowing over the corner. A series of compression waves form over the apparently smooth ramp and converge with the second oblique shock wave above the surface. The compression waves give the oblique shock wave a diffused look at the base.

The boundary layer ahead of the third compression ramp thickens faster than the boundary layer ahead of the second oblique shock wave. It separates from the surface upstream of the compression ramp corner and subsequently turns back and reattaches to the surface at a location downstream of the corner (Figure 6.8c). The separation bubble is too small to cause the shock wave structure consisting of a leading and rear shock wave, as illustrated in figure 4.16. However, it does contribute towards the boundary layer smoothing out the compression ramp corner. As a result, the base of the third oblique shock wave appears diffused. The degree of diffusion at the third oblique shock wave base is more significant than the second oblique shock wave.

The interaction of the normal shock wave and the boundary layer causes the boundary layer ahead of the normal shock wave to thicken. The boundary layer separates from the surface and does not subsequently reattach (Figure 6.8d). The point of boundary layer separation is slightly ahead of the normal shock wave. The high pressure behind the normal shock wave feeds upstream through the subsonic portion of the boundary layer and pushes the separation point ahead of the normal shock wave. This causes a lambda foot to occur at the base of the normal shock wave, as illustrated in figure 6.8d.



(a) The bow shock wave ahead of the fore-body/The start of the first oblique shock wave

(b) The interaction of the second oblique shock wave and the boundary layer adjacent to the fore-body

(c) The interaction of the third oblique shock wave and the boundary layer adjacent to the fore-body

(d) The interaction of the normal shock wave and the boundary layer adjacent to the fore-body

Figure 6.8: The complex shock wave patterns occurring in the viscous flow adjacent to the fore-body surface

The boundary layer that has separated from the fore-body surface enters the internal diffuser. Therefore, a separated flow is supplied to the combustion chamber. Supplying separated air

to the combustion chamber will negatively affect the performance of the combustion chamber and, consequently, the engine performance as a whole. This is because the separated flow is characterised by high levels of distortion and total pressure loss.

The cowl lip has a circular profile similar to the leading edge of the fore-body. The cowl lip thickness is 0.0001 m, which is 0.1% of the capture height. A curved, detached bow shock wave forms ahead of the cowl lip (Figure 6.9). As predicted in section 5.4.2.1, the bow shock rapidly transforms into the normal shock wave located at the inlet entry plane. The bow shock wave is ahead of the cowl interior surface. Therefore, it does not interact with the boundary layer adjacent to the cowl surfaces.

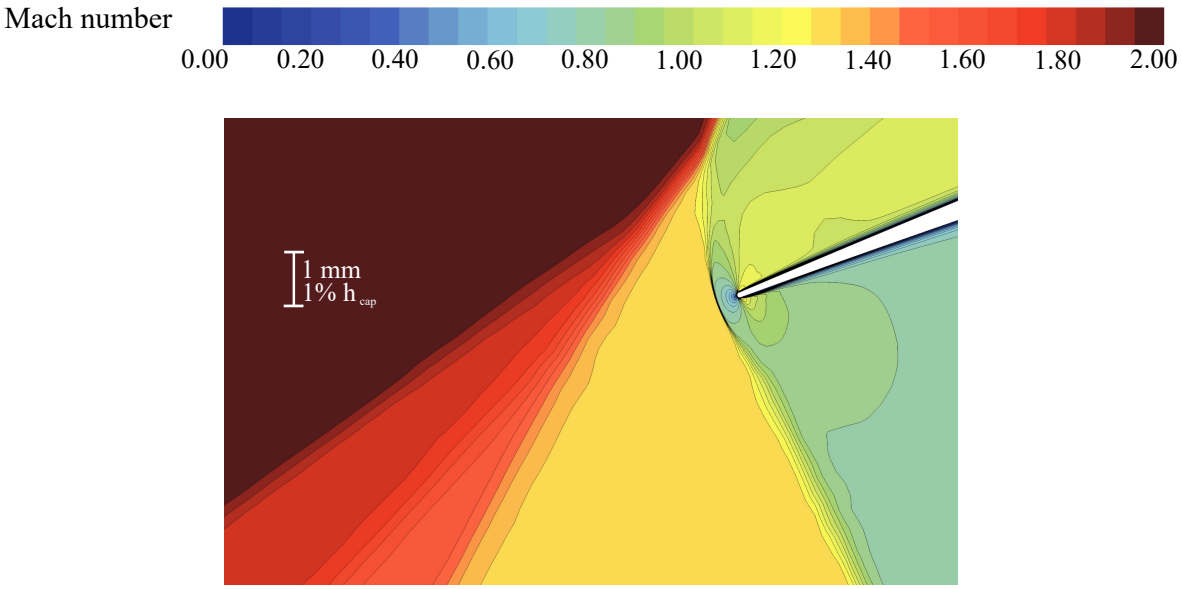


Figure 6.9: The bow shock wave ahead of the cowl lip

The boundary layer forming on the cowl interior surface is subjected to an adverse pressure gradient in the internal diffuser. As illustrated in figure 6.6, it travels far enough against this adverse pressure gradient to separate from the cowl interior surface. The height of the separated flow region is approximately 20% of the total AIP height. The region of separated flow adjacent to the IDBS is approximately 60% of the total AIP height. Therefore, the AIP region of separated flow adjacent to the cowl interior surface is approximately three times smaller than the AIP region of separated flow adjacent to the IDBS.

The viscous flow phenomena that have been discussed here cause a difference between the inviscid supersonic inlet flow field calculated by IADAM and the viscous supersonic inlet flow field calculated by the CFD model. This affects the performance parameters maximised by IADAM, i.e. the total pressure recovery and mass flow ratio. How these performance parameters are affected is discussed next.

The inviscid analysis of the air flowing through the supersonic inlet computes a maximum mass flow ratio of one. The mass flow ratio obtained from the viscous CFD analysis is reduced to 0.9854. This is primarily due to the velocity deficit within the boundary layers adjacent to the supersonic inlet surfaces. The velocity deficit within the boundary layers reduces the mass carrying capability of the flow within the boundary layer. The boundary layer cannot carry its full share of the captured airflow. Therefore, this causes a mass flow rate deficit to occur.

Furthermore, figure 6.9 shows that the oblique shock waves converge slightly above the cowl lip. The boundary layer on the fore-body surface alters the effective surface. The fore-body ramp angles appear larger to the air flowing over them than they are in reality. Consequently, the generated oblique shock waves have larger angles relative to the direction of free-stream flow than those computed using inviscid flow calculations. As a result, the generated oblique shock waves converge slightly above the cowl lip. The bow shock wave at the cowl lip also occurs upstream of the cowl lip. The position of the shock waves relative to the cowl lip causes mass spillage to occur around the cowl lip, contributing to the reduced mass flow ratio. The reduction in mass flow ratio in this particular case is 1.48%. There is, however, a potential for it to be higher in supersonic inlets that have thicker boundary layers relative to the size of the overall inlet flow field.

The total pressure recovery of the air delivered to the combustion chamber translates directly to the overall engine thrust. Therefore, it is vital to ensure that the total pressure losses of the air flowing through a supersonic inlet are minimal. IADAM generates inlets that have been optimised for maximum total pressure recovery. The assumption of inviscid flow means that IADAM can only consider the total pressure losses across the system of oblique and normal shock waves. IADAM cannot compute the total pressure losses associated with the viscous flow phenomena in real supersonic inlet flow fields. Figure 6.10 compares the AIP total pressure recovery distribution produced by IADAM and the viscous CFD model.

IADAM assumes that every captured air particle experiences the same total pressure loss across the oblique and normal shock wave system. Therefore, it predicts that the air flowing through the inlet will have a uniform total pressure distribution at the AIP, as illustrated in figure 6.10. The CFD model computes an AIP total pressure distribution that varies in the direction perpendicular to the airflow due to the viscous flow regions adjacent to the internal diffuser surfaces. There is a small uniform flow region whereby the total pressure recovery calculated by the CFD model equals the total pressure recovery computed by IADAM. The airflow within this region corresponds to a flow that is not severely affected by the effects of viscosity, as discussed in section 4.1.3.2.1. Above and below the uniform flow region, the airflow corresponds to the viscous flow regions adjacent to the internal diffuser surfaces. The airflow within the viscous flow regions experiences additional losses in total pressure due to

the friction between the flow field and the internal diffuser surfaces, shock-wave/boundary-layer interaction and turbulent mixing due to boundary layer separation or near separation. The root mean square error between the two curves in figure 6.10 is approximately 0.075.

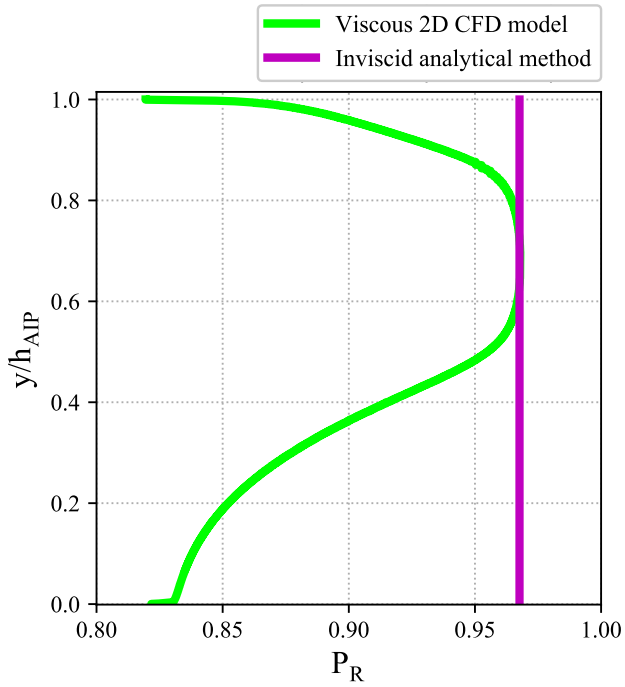


Figure 6.10: The P_R distribution at the AIP

6.2.8 Validation

6.2.8.1 Validation Study Introduction

The study presented in appendix C is a validation of the developed CFD model. The CFD model was validated against published experimental data obtained from a paper titled "Meso-flap and Bleed Flow Control for a Mach 2 Inlet" (Loth et al. 2004). Both 2D and 3D CFD models were investigated to determine how closely the results compare to the published experimental data and to each other. The photograph presented in figure 6.11 illustrates the experimental set-up of the inlet installed in the wind tunnel.

The 2D CFD model for the validation inlet is developed identically to the CFD model developed in the current section. Further details are outlined in appendix C. The orientation of the inlet presented by Loth et al. (2004) differs from the orientation used in the present study. More specifically, the orientation is such that the inlet appears to have been flipped over the x-axis. The inlet orientation is a function of the inlet installation location (i.e. fuselage-, side-, nose-, or top-mounted etc.).

The 3D CFD domain is very similar to the 2D CFD domain. The main differences are that the 3D inlet flow field has a finite span, and the inlet geometry contains side walls. The inlet has a rectangular cross-section throughout, and it is symmetric about the x-y plane. Therefore, only half the actual domain was used for the CFD analysis. A symmetry plane boundary condition was used to account for the other half of the domain.

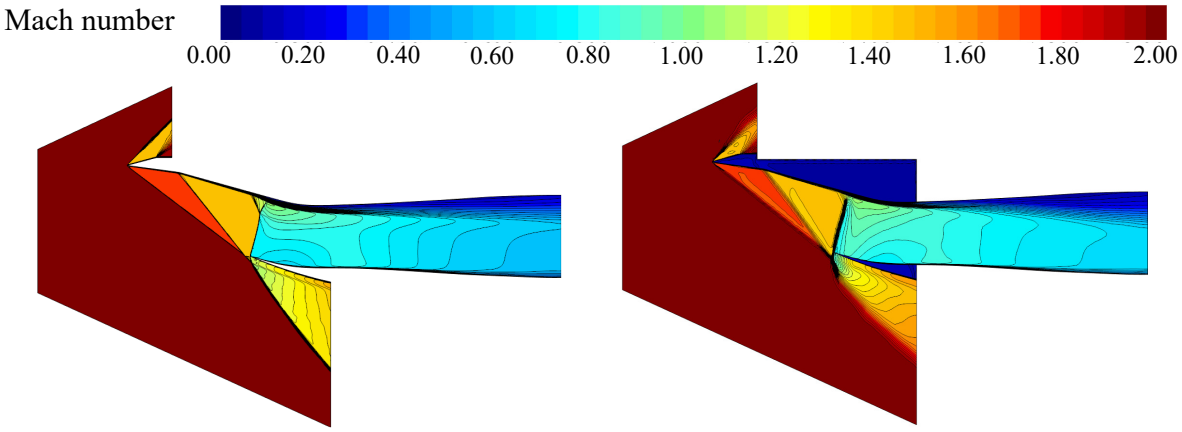


Figure 6.11: A photograph of the validation inlet installed in a wind tunnel (Loth et al. 2004)

6.2.8.2 Validation Study Results and Discussion

The 2D and 3D CFD models generated the Mach number contour plots illustrated in figure 6.12. The 3D CFD model Mach number contour plot (Figure 6.12b) is specifically obtained from the centreline, where the symmetry plane boundary condition is located. There is a blue block in figure 6.12b, which is not apparent in figure 6.12a. This blue block represents the external part of the inlet side-wall. The presence of the side-wall in the 3D CFD domain is more clearly illustrated in figure C.11, which is located in appendix C.

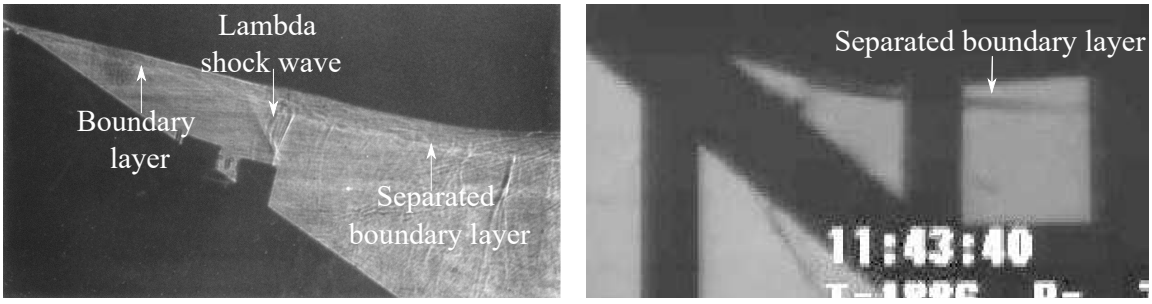
The Mach number contour plots appear to be quite similar. They both show a flow field whereby the fore-body generates a system of two oblique shock waves and a normal shock wave located at the internal diffuser entry plane. The captured airflow is compressed from a supersonic free-stream Mach number of Mach 2 to a lower supersonic Mach number of approximately Mach 1.45 by the oblique shock wave system. The airflow is compressed further to a subsonic Mach number by the normal shock wave. After that, the subsonic airflow enters the internal diffuser, and it is compressed even further to a lower subsonic Mach number at the AIP. All the oblique shock waves and the normal shock wave converge at a single point near the cowl lip.



(a) 2D CFD (b) 3D CFD

Figure 6.12: The Mach number contour plots of the air flowing through the validation inlet

The Mach number contour plots (Figure 6.12) also illustrate complex shock wave patterns in the supersonic inlet flow field. These are a result of the shock-wave/boundary-layer interactions occurring on the fore-body. The adverse pressure gradient across the normal shock wave causes the upstream boundary layer to thicken and separate from the fore-body surface. The normal shock wave develops a lambda foot as a result of the boundary layer separation. Separated flow enters the internal diffuser. These observations correlate with the observations made during the experiment (Figure 6.13).



(a) A wind tunnel shadowgraph (b) An image captured from video Schlieren

Figure 6.13: Flow visualisation images of the shock/boundary-layer interaction documented during the wind-tunnel experiment performed by Loth et al. (2004)

Figure 6.13 is an illustration of the flow visualisation images obtained during the experiment. The wind tunnel shadowgraph presented in figure 6.13a is a close-up of the normal shock-wave/boundary-layer interaction on the fore-body surface. "The block-like shapes are reference marks taped to the inlet window to bracket the design location of the normal shock"(Loth et al. 2004). Based on figure 6.13a, the boundary layer appears to thicken as it passes through the normal shock wave. The normal shock wave develops an upside-down

lambda foot due to its interaction with the boundary layer. The video Schlieren image presented in figure 6.13b is a close-up of the throat section of the inlet. It shows that the boundary layer separates from the fore-body surface, and separated flow enters the internal diffuser. Loth et al. (2004) stated that this flow feature appeared in all the Schlieren videos.

The similarities between the 2D and 3D CFD Mach number contour plots with the flow visualisation images presented in figure 6.13 shows that both CFD models capture the essential flow features in a 2D, external-compression, supersonic inlet flow field, and provide good qualitative information about the overall supersonic inlet flow field.

Figure 6.14 provides a comparison of the static pressure distributions on the inlet surfaces. Loth et al. (2004) present the supersonic inlet orientation differently from the orientation used in the present study. For the validation study, the fore-body and its extension into the internal diffuser are referred to as the fore-body and top interior surface (FTIS). The cowl interior is simply referred to as the cowl interior surface (CIS).

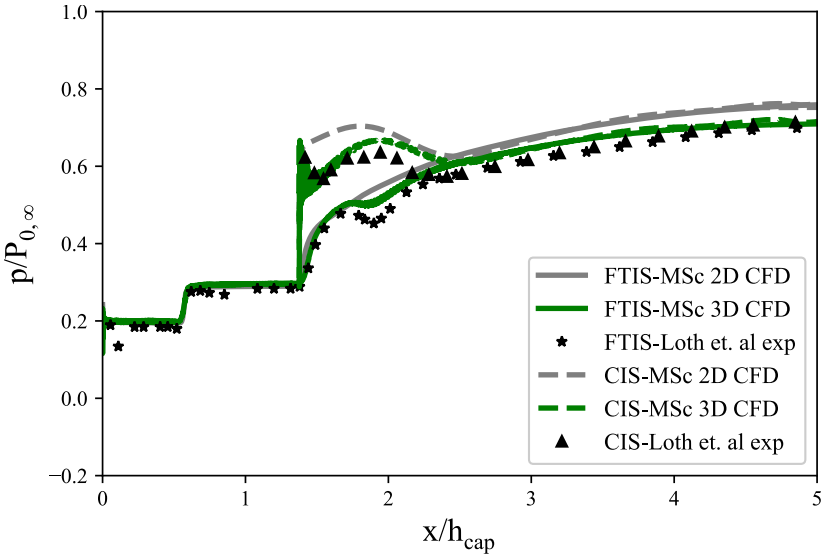


Figure 6.14: A comparison of the static pressure distributions produced by the 2D CFD model, the 3D CFD model and the experiments performed by Loth et al. (2004)

The static pressure distributions produced by the 2D and 3D CFD models appear to follow a similar trend to the static pressure distribution obtained from the experimental data. Based on figure 6.14, the location of the pressure jumps on the FTIS correlate well. The correlation of the magnitudes of the static pressures on the compression ramps was determined using root mean square errors between the experimental data points and the curves produced by the 2D and 3D CFD models. The root mean square errors between the experimental and 2D CFD model static pressures on the first and second compression ramps are approximately 0.05 and 0.02, respectively. The root mean square errors between the experimental and 3D

CFD model static pressures on the first and second compression ramps are approximately 0.05 and 0.004, respectively. Based on the calculated errors, the compression ramp static pressures calculated by the 2D and 3D CFD models produce static pressures that correlate well with the experimental data and to each other.

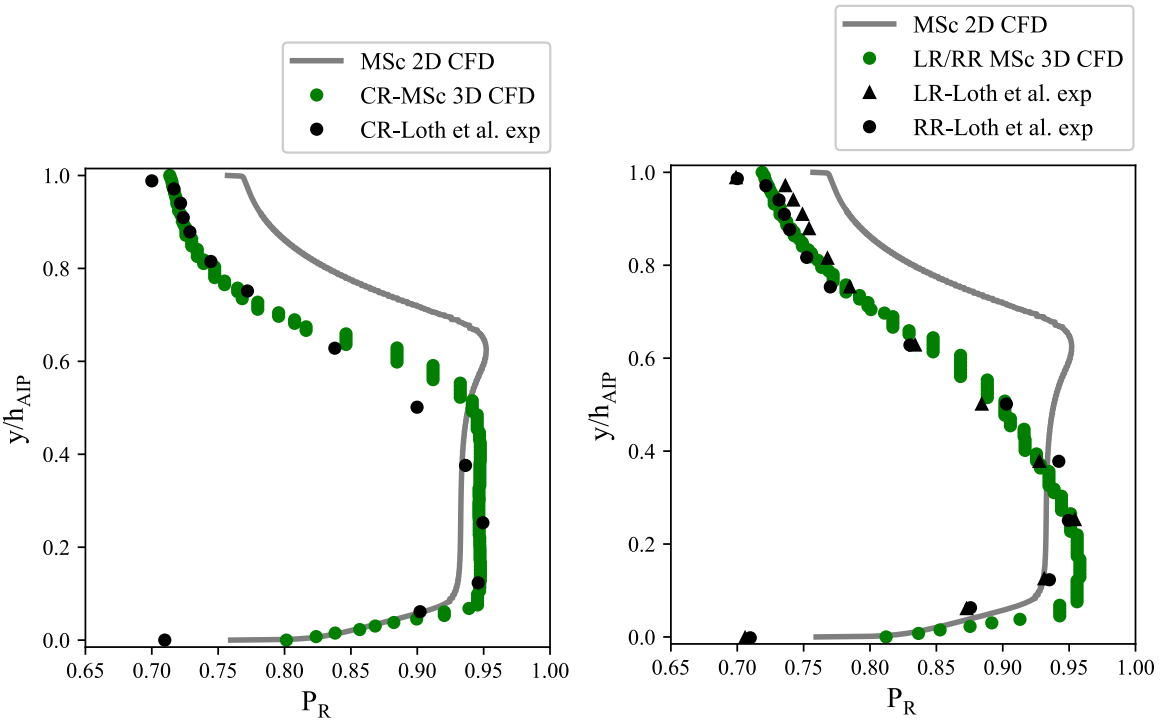
The experimental data indicates that the airflow downstream of the normal shock wave accelerates as it flows through the curved throat. This is evident from the slight pressure decrease observed in this region on both the FTIS and the CIS. This is a result of the airflow turning through the constant-height throat. This flow feature is apparent in the 3D CFD model results. However, the static pressure distributions obtained from the 2D CFD model do not appear to detect this flow feature.

All three sets of results demonstrate a similar gradual rise in static pressure on the internal diffuser surfaces. For the normal shock wave to be positioned at the internal diffuser entry plane, the 3D CFD model requires an AIP pressure almost identical to the back pressure applied during the experiment. However, the 2D CFD model requires a pressure that is 11.34% higher than the experimental AIP pressure. This is because the pressure rise within the internal diffuser depends on the cross-sectional area expansion ratio. Boundary layers alter the effective inlet surfaces. This decreases the effective internal diffuser cross-sectional areas. The effective expansion ratio observed by the flow in the 2D CFD model only takes the boundary layer development on the FTIS and CIS into account. In reality, there is an additional boundary layer developing on the inlet side walls. This boundary layer decreases the effective expansion ratio even further. The 3D CFD model models this boundary layer. As a result, the pressure rise modelled by the 3D CFD model is similar to that of the experiment. The root mean square errors between the experimental and the 3D CFD model static pressures on the FTIS and CIS are approximately 0.03 and 0.04, respectively. The 2D CFD model does not model the boundary layer on the side walls. This causes the root mean square errors between the experimental and 2D CFD model static pressures on the FTIS and CIS to be approximately 0.17 and 0.14, respectively.

The images in figure 6.15 compare the AIP total pressure recovery distributions obtained from the 2D CFD model, the 3D CFD model, and the experiments performed by Loth et al. (2004). During the experiment, total pressure was measured with a three-element total pressure rake. The total pressure rake elements are referred to as the left rake (LR), centre rake (CR) and right rake (RR).

All three sets of results illustrated in figure 6.15 show a similar trend. The total pressure recoveries are lower in the regions near the surfaces and increase as the distance between the airflow and the surfaces increases. The reduced total pressure recovery near the CIS is due to the friction between the supersonic inlet flow field and the CIS. The total pressure

recovery reduction near the FTIS is due to the turbulent mixing associated with boundary layer separation.



(a) Center rake

(b) Left and right rake

Figure 6.15: A comparison of the P_R distribution at the AIP produced by the 2D CFD model, the 3D CFD model and the experiment performed by Loth et al. (2004)

The AIP total pressure recovery distribution at the position of the CR is presented in figure 6.15a. Based on figure 6.15a, the shapes of the curves produced by the 3D CFD model and the experiment appear to be similar. The root mean square error between the experimental and the 3D CFD model total pressure recovery distribution is approximately 0.03. The source of the error is mostly attributed to the differences in the total pressure recoveries in the core flow. The 3D CFD model results detect a small region of uniform flow. There is no evidence of a small region of uniform flow in the experimental results.

Figure 6.15b presents the AIP total pressure recovery distribution at the position of the LR and RR. The geometry of the inlet was assumed to be symmetric about the x-y plane. Only half the actual domain was used for the CFD analysis. Therefore, the AIP total pressure recovery distribution produced at the LR and RR are treated as the same. Similarly to figure 6.15a, the shapes of the experimental and 3D CFD model curves appear quite similar. Although the 3D CFD model does not predict a uniform flow region at the position of the LR and RR, the root mean square errors between the 3D CFD model and the experimental total pressure recoveries at the LR and RR are approximately 0.03 and 0.03, respectively.

This error is identical to the error calculated at the CR. The source of this error is largely a result of the differences in total pressure recovery near the CIS.

The 3D CFD computational mesh is coarse relative to the 2D computational mesh. It was difficult to use a smaller base cell size due to how large the simulation file was and how long the simulation took to run. There is a possibility that the coarseness of the mesh is a source of error between the total pressure recoveries produced by the experiment and the 3D CFD model. A mesh independence study would have to be performed to determine if the simulation results are independent of mesh cell size. However, such a study will not be performed in the present work due to the imposed time constraints.

Another source of the error between the total pressure recoveries produced by the experiment and the 3D CFD model could be the selected turbulence model. The $\kappa - \epsilon$ turbulence model was selected because it was recommended in several studies investigating the flow field in supersonic inlets. However, there could be turbulence models that perform better than the $\kappa - \epsilon$ turbulence model. A study to investigate turbulence models to analyse the flow in 2D, external-compression, supersonic inlets is beyond the scope of this work.

The turbulence parameters used in the CFD model could also be the source of the error between the total pressure recoveries produced by the experiment and the 3D CFD model. Ideally, the best estimate of turbulence parameters would be obtained from empirical data. However, there was no empirical data available for the current study. Therefore, approximations had to be made.

The differences between the CR and LR/RR AIP total pressure recovery distributions computed by the 3D CFD model are due to the proximity of the rake to the side walls. The side walls introduce viscous flow phenomena to the inlet flow field. This causes a variation in the supersonic inlet flow field in the span-wise direction. The total pressure rakes closest to the side walls (i.e. LR and RR) are the most affected by the viscous flow phenomena introduced by the side walls. Conversely, the total pressure rake furthest from the side walls (i.e. CR) is the least affected by the viscous flow phenomena introduced by the side walls. This is evident from the presence of a small region of uniform flow illustrated in figure 6.15a and the absence of such a flow in figure 6.15b.

Based on figure 6.15, the shape of the AIP total pressure recovery produced by the 2D CFD model differs from its experimental counterpart. The 2D CFD model computes a wide region of uniform flow in the region away from the surfaces. This region corresponds to the flow region where the effects of viscosity are assumed to be negligible. There is no evidence of a region of uniform flow in the AIP total pressure recovery distribution obtained from the experimental data. The 2D CFD model only computes the total pressure losses associated

with viscous flow phenomena in the airflow adjacent to the FTIS and CIS. Side walls on real 2D supersonic inlets introduce additional viscous flow phenomena that vary the inlet flow field in the span-wise direction. The 2D CFD model assumes the inlet flow field is constant in the span-wise direction and ignores the presence of side walls. As a result, it predicts a larger region of uniform flow.

Furthermore, the total pressure recoveries of the flow adjacent to the CIS are quite similar. However, the 2D CFD model predicts larger total pressure recoveries for the flow adjacent to the FTIS. All of the factors mentioned above cause the root mean square errors between the 2D CFD model and the experimental total pressure recoveries at the CR, LR and RR to be approximately 0.07, 0.07 and 0.07, respectively. These errors are more than double the errors generated by the 3D CFD model.

The shape of the total pressure recovery distribution curve calculated by the 2D CFD model does not look the same as the shape of the curve measured during the experiment. However, it captures the essential flow features such as boundary layers and regions of separated flow. Furthermore, the average total pressure recoveries obtained from the 2D CFD model are similar to those obtained from the experimental data. The 2D CFD model calculates an average total pressure recovery of 0.86. The average experimental total pressure recoveries at the CR, LR and RR are approximately 0.81, 0.81 and 0.81, respectively. The average total pressure recovery errors at the CR, LR and RR are approximately 6.17%, 6.17% and 6.17%, respectively. Therefore, the 2D CFD model provides a reasonable approximation of the average total pressure recovery at the AIP.

6.2.8.3 Validation Study Conclusion

The validation study showed that the 2D CFD model sufficiently approximates the 2D, external-compression, supersonic inlet flow field and captures the essential flow features. However, the 3D CFD model produced results that were in better agreement with experimental data than the results produced by the 2D CFD model. This is because 2D, external compression, supersonic inlets have side walls to contain the airflow. The friction between the side walls and the airflow introduces viscous flow phenomena that vary the supersonic inlet flow field in the span-wise direction. The 3D CFD model models this span-wise flow variation. However, the 2D CFD model assumes that the flow field is constant in the span-wise direction.

The accuracy of the 3D CFD model has a high computational cost and requires a lot of time to design, mesh, and run a simulation. The CFD model developed in the present section was used in a sensitivity study (section 6.3) where several CFD analyses had to be conducted.

Running all of these analyses using a 3D CFD analysis would not be possible within the time constraints imposed on the present study. The computational cost is significantly reduced in the 2D CFD model. Therefore, the 2D CFD model was used in the present work to analyse the air flowing through the generated supersonic inlets.

6.3 Sensitivity Study

The results obtained from the CFD model developed in section 6.2 have demonstrated the significant effect of viscous flow phenomena on a supersonic inlet flow field. However, they are unique to a particular supersonic inlet geometry with specific flight conditions. The impact of viscous flow phenomena on supersonic inlet flow fields may vary for supersonic inlets with different geometric features and flight conditions. The geometric features and flight conditions of a particular inlet are a function of the user-defined inputs required by IADAM to generate the inlet. The sensitivity study in the current section is an investigation of how the impact of viscous flow phenomena varies for inlets designed with different user-defined inputs. Special attention was given to total pressure recovery and mass flow ratio because these are important performance parameters that IADAM aims to maximise.

6.3.1 Sensitivity Study Design Space

The user-defined inputs required by IADAM to generate an inlet geometry and define its operational flight conditions are:

1. altitude (H),
2. free-stream Mach number (M_∞),
3. inlet capture height (h_{cap}),
4. number of fore-body ramps (n),
5. cowl lip profile,
6. cowl lip thickness ($t_{_{CL}}$),
7. cowl lip vertex angle ($\theta_{_{CLV}}$),
8. maximum cowl thickness ($t_{_C}$),
9. desired AIP Mach number ($M_{_{AIP}}$),
10. ratio of cowl interior frontal projected height to the internal diffuser height at the AIP ($h_{_{CI}}/h_{_{AIP}}$) and,
11. internal diffuser length ($l_{_{ID}}$).

The time constraints imposed on the study made it challenging to investigate all eleven user-defined inputs. Therefore, the sensitivity study design space was reduced to five user-defined inputs, i.e. H, M_∞, h_{cap}, n and M_{AIP}. These user-defined inputs were believed to significantly influence the impact of viscous flow phenomena on supersonic inlet flow fields. The design space is defined by the lower and upper bounds tabulated in table 6.8.

Table 6.8: Sensitivity study design space

User-defined input	Lower bound	Upper bound	Unit
H	9 144	36 576	m
M_∞	1.5	2.5	-
h_{cap}	0.01	1	m
n	1	5	-
M_{AIP}	0.2	0.5	-

The chosen lower and upper bounds for altitude include realistic ranges at which various types of aircraft fly, as discussed in section 4.1.3.1.2. The selected lower and upper bounds for the desired AIP Mach number were selected as per the combustion chamber blow-off limits mentioned in section 4.1.2.

The lower and upper bounds for free-stream Mach number were selected based on the typical operational flight conditions of a 2D, external-compression, supersonic inlet. The lower bound is Mach 1.5 because there is no need for external staged compression below this limit. An inlet with a single normal/bow shock wave can provide the necessary compression without significant total pressure losses. The upper bound is Mach 2.5. An external-compression inlet designed to operate at a Mach number above this limit may experience considerable cowl wave drag due to the large frontal projected height of the cowl required to turn the air from the direction of the last fore-body ramp to the combustion chamber directional requirements. The arguments made to support these lower and upper bounds are discussed in sections 4.1.3.1.3 and 4.1.3.4.3, respectively.

The capture height influences the size of the entire supersonic inlet geometry. The size of an inlet depends on the size of the engine to which it is fitted. The engine size is dependent on the size of the aircraft that the engine propels. It was challenging to find accurate supersonic inlet geometries because supersonic inlets are typically used for military applications. Appendix F provides some pictures of supersonic inlets and the aircraft to which they are fitted. The photographs in appendix F were used to approximate an appropriate capture height range for the sensitivity study.

The Meteor is a small ramjet-propelled missile. The capture heights of the supersonic inlets on the Meteor (Figure F.1) are unknown. However, a rough estimation was made based on

the diameter of the Meteor and how the diameter relates to the inlet capture heights. The Meteor has a diameter of 0.178 m (SAAB 2021). The inlets on the sides of the Meteor appear to have capture heights that are roughly a quarter of the missile diameter, i.e. 0.04 m. The GQM-163 Coyote, illustrated in figure F.2, is an example of a larger ramjet-propelled missile. The capture heights of the inlets on the GQM-163 Coyote are unknown. However, a rough estimation was made based on the missile diameter. The missile has a diameter of 0.3555 m (Orbital Sciences Corporation 2004). Based on figure F.2, the capture heights of the inlets on the sides of the missile are roughly a quarter of the capture height, i.e. 0.09 m. The Boeing F-15 is a large aircraft with two 2D inlets fitted onto the wings, as illustrated in figure F.4. The aircraft has a height of 5.65 m (Boeing 2021). Based on figure F.4, the inlet capture heights are roughly a quarter of the aircraft height, i.e. 1.4 m.

Supersonic inlets that are fitted to different-sized aircraft can have capture heights that differ by orders of magnitude. Considering the inlets fitted to the above-mentioned missiles and aircraft, the inlet on a small, medium and large aircraft can have capture heights with orders of magnitudes of -2, -1 and 0, respectively. Therefore, the lower and upper bounds for inlet capture height were set to 0.01 m and 1.00 m, respectively.

An external-compression inlet can have any number of ramps from one to infinity (i.e. a smoothly contoured fore-body). An increase in the number of ramps reduces the total pressure loss across the fore-body due to the shock wave system (as discussed in section 4.1.3.1.3). Increasing the number of fore-body ramps also increases the complexity of the design of a fore-body. Smoothly contoured fore-bodies are very difficult to design accurately and even more challenging to manufacture. The number of fore-body ramps was limited to five for the sensitivity study.

The remaining user-defined inputs which were not investigated during the sensitivity study are the cowl lip profile, t_{CL}, θ_{CLV}, t_C, h_{CI}/h_{AIP} and l_{ID}. IADAM still requires these inputs to generate inlets. Therefore, the inputs tabulated in table 6.9 were used to generate the inlets for the sensitivity study.

Table 6.9: The remaining user-defined inputs which were not investigated during the sensitivity study but are still required to generate inlets

cowl lip profile	circular
t_{CL}	$0.001 \times h_{cap}$
θ_{CLV}	3°
t_C	$0.15 \times h_{cap}$
h_{CI}/h_{AIP}	0.2
l_{ID}	$6.5 \times h_{cap}$

A circular cowl lip profile was selected for the sensitivity study. External-compression inlets are designed to operate in the critical mode of operation, as discussed in section 4.1.3.3. Suppose the inlet experiences a disturbance during flight. In that case, the position of the normal shock wave makes it easier for it to be expelled from the inlet. The blunt circular cowl lip profile has the added advantage of delaying shock wave expulsion (Faro 1965).

The cowl lip thickness was defined relative to h_{cap}. This was done to scale the cowl lip thickness with the different values of h_{cap} used in the sensitivity study. The cowl lip thickness was specifically defined as $0.001 \times h_{cap}$. The purpose of this definition was to ensure that the cowl lip is negligible in size compared to the overall size of the supersonic inlet. Therefore, making the effect of this component on the overall supersonic inlet flow field insignificant.

According to Slater (2012), θ_{CLV} should be within the range of 3° to 5°. A value of 3° was chosen for the sensitivity study because it lies within this range. The cowl exterior is not fully modelled in the CFD model. This is because it does not directly impact the interior fluid flow of a supersonic inlet. The value of t_C does not impact the interior fluid flow of a supersonic inlet. However, it is required by IADAM. Therefore, a value of $0.15 \times h_{cap}$ was supplied to IADAM for the sensitivity study.

A survey of 2D, external-compression, supersonic inlets was performed to determine suitable values of h_{CI}/h_{AIP} and l_{ID} for the sensitivity study. The survey is presented in appendix D. A survey of this nature was challenging to perform because most studies in supersonic inlet design provide limited data about the inlet geometries. This is because these inlets are typically used for military applications.

The inlets used in the survey (Appendix D) have cowls that vary in shape and form. The ratios of h_{CI}/h_{AIP} range from 0.00 to 0.27. The internal diffusers of inlets with h_{CI}/h_{AIP} of 0.00 do not have straight horizontal cowls. The internal diffusers are s-shaped. For the sensitivity study, a value of 0.2 was chosen. This value lies within the range of 0.00 and 0.27. Furthermore, it is considerate of the compromise between designing the cowl to turn the airflow smoothly and keeping the frontal projected height as small as possible.

The geometries of the inlets used in the survey (Appendix D) have different scales and orders of magnitude. Therefore, the values of l_{ID} were measured relative to h_{cap}. Based on data obtained from the survey, there is no strict industry standard pertaining to the ratio l_{ID}/h_{cap}. The ratio l_{ID}/h_{cap} varies from 3.52 to 8.11 for the inlets used in the survey. A value of 6.5 was chosen for the sensitivity study because it lies within this range. Therefore, the inlets used in the sensitivity study have an internal diffuser length of $6.5 \times h_{cap}$. The internal diffuser length was defined relative to h_{cap} to ensure that it scales with the different values of h_{cap} used in the sensitivity study.

6.3.2 Sensitivity Study Execution

The sensitivity study sample points were selected using the faced CCD sampling method available in the Python™ PyDOE2 module. This particular sampling method was chosen because classical DOE techniques provide global sensitivity information from a more limited number of sample points. Furthermore, the faced CCD sampling method was also selected to observe the impact of viscous flow phenomena on supersonic inlet flow fields at the extremes of the design space without exceeding the bounds of the design space (Table 6.8). Table 6.10 is a list of the generated sample points.

Table 6.10: Sensitivity study sample points

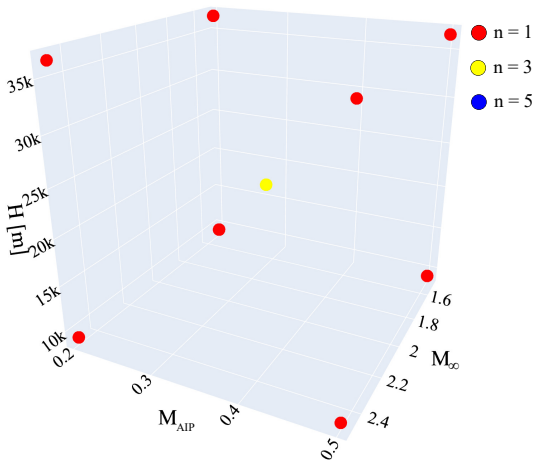
Inlet model	H	M_∞	h_{cap}	n_{ramps}	M_{AIP}
1	9 144 m	1.5	0.01 m	1	0.20
2	9 144 m	1.5	0.01 m	1	0.50
3	9 144 m	1.5	0.01 m	5	0.20
4	9 144 m	1.5	0.01 m	5	0.50
5	9 144 m	1.5	1.00 m	1	0.20
6	9 144 m	1.5	1.00 m	1	0.50
7	9 144 m	1.5	1.00 m	5	0.20
8	9 144 m	1.5	1.00 m	5	0.50
9	9 144 m	2.0	0.10 m	3	0.35
10	9 144 m	2.5	0.01 m	1	0.20
11	9 144 m	2.5	0.01 m	1	0.50
12	9 144 m	2.5	0.01 m	5	0.20
13	9 144 m	2.5	0.01 m	5	0.50
14	9 144 m	2.5	1.00 m	1	0.20
15	9 144 m	2.5	1.00 m	1	0.50
16	9 144 m	2.5	1.00 m	5	0.20
17	9 144 m	2.5	1.00 m	5	0.50
18	22 860 m	1.5	0.10 m	3	0.35
19	22 860 m	2.0	0.01 m	3	0.35
20	22 860 m	2.0	0.10 m	1	0.35
21	22 860 m	2.0	0.10 m	3	0.20
22	22 860 m	2.0	0.10 m	3	0.35
23	22 860 m	2.0	0.10 m	3	0.50
24	22 860 m	2.0	0.10 m	5	0.35
25	22 860 m	2.0	1.00 m	3	0.35
26	22 860 m	2.5	0.10 m	3	0.35

Table 6.10 Sensitivity study sample points (continued)

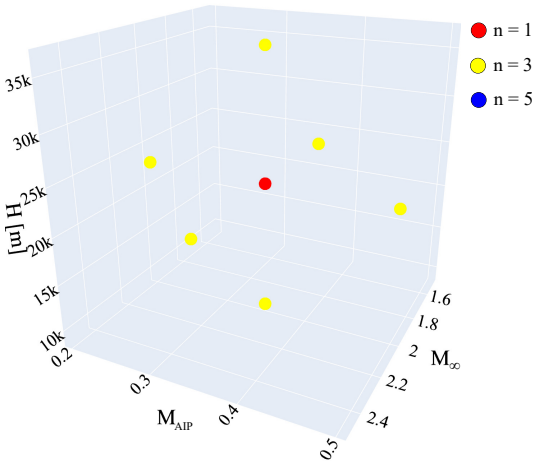
Inlet model	H	M_∞	h_{cap}	n_{ramps}	M_{AIP}
27	36 576 m	1.5	0.01 m	1	0.20
28	36 576 m	1.5	0.01 m	1	0.50
29	36 576 m	1.5	0.01 m	5	0.20
30	36 576 m	1.5	0.01 m	5	0.50
31	36 576 m	1.5	1.00 m	1	0.20
32	36 576 m	1.5	1.00 m	1	0.50
33	36 576 m	1.5	1.00 m	5	0.20
34	36 576 m	1.5	1.00 m	5	0.50
35	36 576 m	2.0	0.10 m	3	0.35
36	36 576 m	2.5	0.01 m	1	0.20
37	36 576 m	2.5	0.01 m	1	0.50
38	36 576 m	2.5	0.01 m	5	0.20
39	36 576 m	2.5	0.01 m	5	0.50
40	36 576 m	2.5	1.00 m	1	0.20
41	36 576 m	2.5	1.00 m	1	0.50
42	36 576 m	2.5	1.00 m	5	0.20
43	36 576 m	2.5	1.00 m	5	0.50

The sample points in table 6.10 are graphically illustrated in figure 6.16. Considering figures 6.16a and 6.16c, it appears as if there are no blue sample points, i.e. sample points for five ramps. However, for every inlet model with one ramp, there is a corresponding inlet with five ramps. Therefore, the blue sample points are not visible because the red sample points overlap them. Furthermore, the red sample point in figure 6.16b overlaps two sample points. One is yellow, and the other is blue.

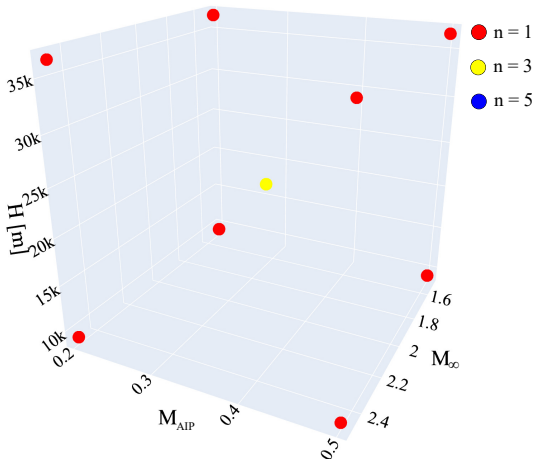
The sample points in table 6.10 and figure 6.16 were supplied to IADAM to generate 43 inlet models. A CFD analysis of each inlet model was carried out using the CFD model developed in section 6.2.



(a) $h_{cap} = 0.01\ m$



(b) $h_{cap} = 0.1\ m$



(c) $h_{cap} = 1\ m$

Figure 6.16: Sensitivity study sample points

6.3.3 Results and Discussion

The discussion is focused on understanding how different user-defined inputs affect the impact of viscous flow phenomena on the supersonic inlet performance parameters (i.e. the total pressure recovery and mass flow ratio) of the inlets generated by IADAM. The performance parameters help the user to understand the generated inlet capability and efficiency. Therefore, focussing on the supersonic inlet performance parameters creates a more realistic understanding of the performances of the inlets generated by IADAM.

The results obtained from the CFD analyses of all 43 inlet models (Table 6.10) are in appendix E. The results show differences between the performance parameters computed by IADAM and the viscous CFD model. The differences between the performance parameters obtained from inviscid and viscous calculations will be referred to as total pressure recovery and mass flow ratio errors, denoted by E_{P_R} and E_{m_R}, respectively. The values of E_{P_R} and E_{m_R} are root mean square errors.

6.3.3.1 The Variation of E_{P_R}, with changes in H, M_∞, M_{AIP}, n and h_{cap}

The bubble plots presented in figure 6.18 are a graphical representation of how E_{P_R} varies with changes in H, M_∞, M_{AIP}, n and h_{cap}. The size of the bubbles represents the magnitudes of the root mean square errors. The largest and smallest E_{P_R} have a value of 0.3683 and 0.0274, respectively. They are related to inlet models 33 and 2, respectively. The most significant errors in figure 6.18 are observed in all the inlet models that have been designed with the combination of free-stream and AIP Mach numbers of 1.5 and 0.2, respectively. In the sensitivity study, these are inlet models 1, 3, 5, 7, 27, 29, 31 and 33. An example of such an inlet is illustrated in figure 6.17.

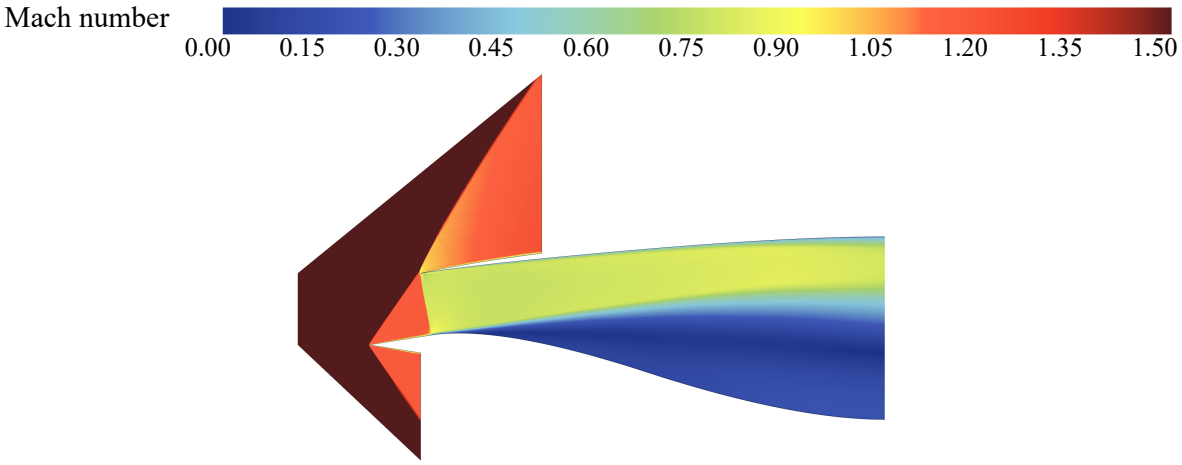
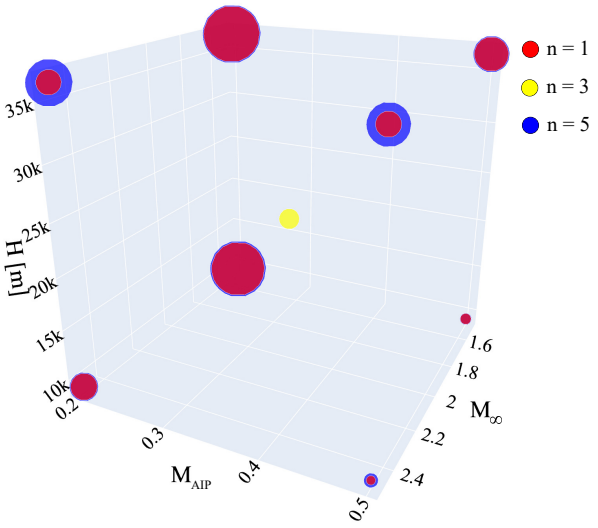
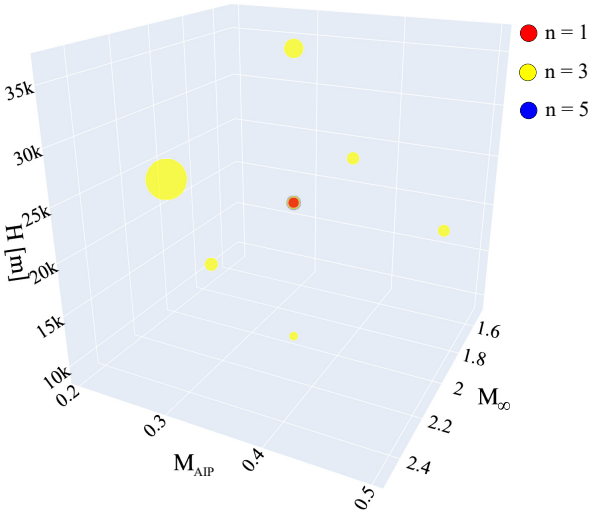


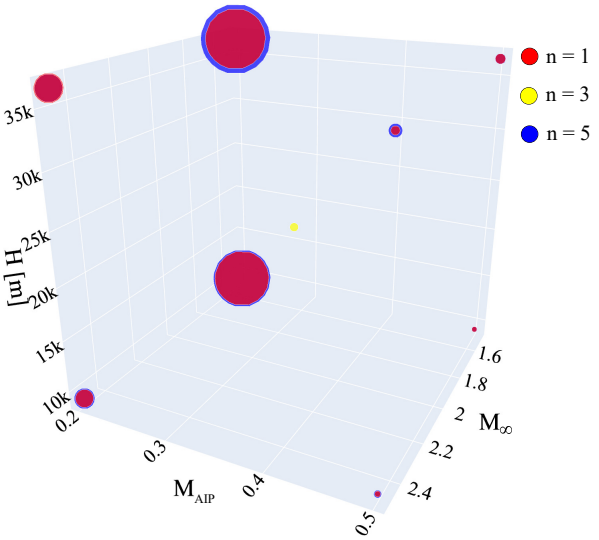
Figure 6.17: The Mach number contour plot of inlet model 1



(a) $h_{cap} = 0.01\ m$



(b) $h_{cap} = 0.1\ m$



(c) $h_{cap} = 1\ m$

Figure 6.18: The variation of E_{P_R}, with changes in H, M_∞, M_{AIP}, n and h_{cap}

The large values of E_{P_R} observed in inlet models 1, 3, 5, 7, 27, 29, 31 and 33 are primarily due to the momentum-induced boundary layer separation that occurs on the IDBS. The separation of the boundary layer results in a large region of boundary layer separated flow. Based on figure 6.19, the height of the region of flow where there is a loss in total pressure due to viscous effects is approximately 90% of the total AIP height. The large volume of air within the viscous separated flow region is subjected to a loss in total pressure due to turbulent mixing. This results in high values of E_{P_R}.

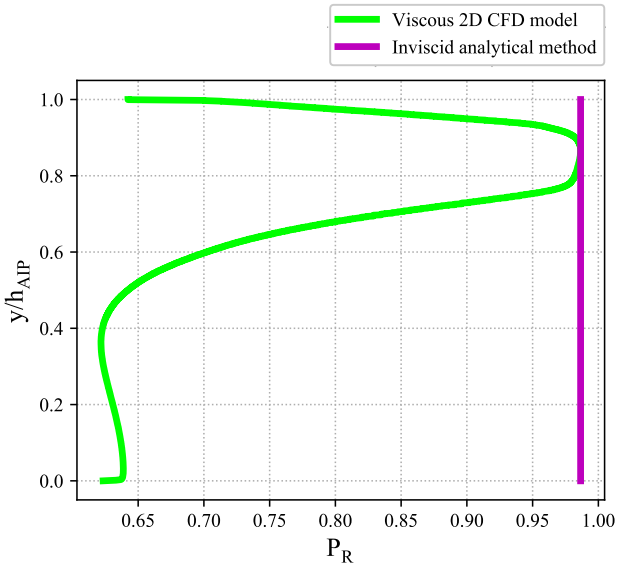
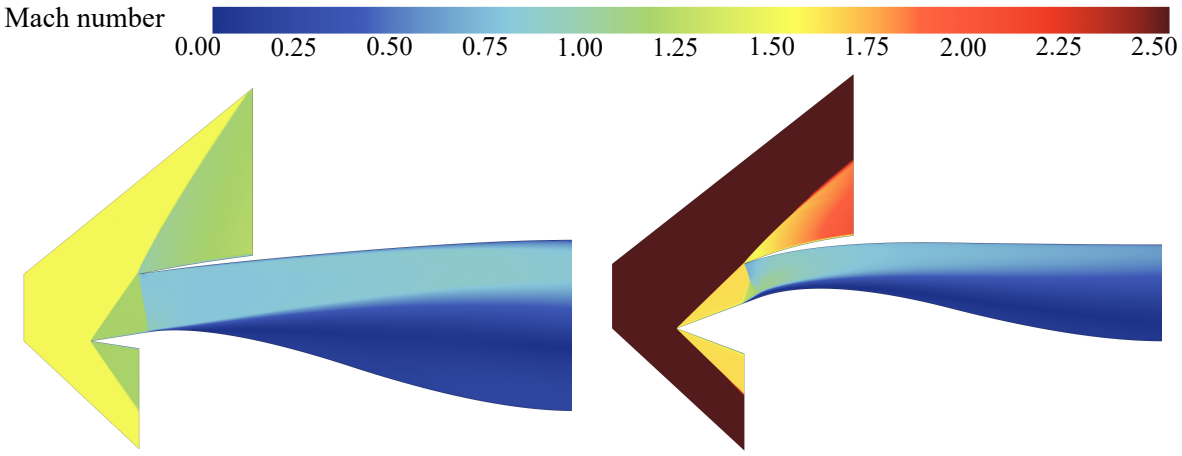


Figure 6.19: The P_R distribution for inlet model 1 at the AIP

The large curvatures of the IDBS cause momentum-induced boundary layer separation to occur. IADAM designs the inlets such that the values of M_∞, M_{AIP} and h_{CI}/h_{AIP} greatly influence the shape of an inlet and all its surfaces. The free-stream Mach number influences the angles of the fore-body ramps. Considering figure 6.20, inlet models 1 and 10 were designed to capture air moving at free-stream Mach numbers of Mach 1.5 and 2.5, respectively. All the other user-defined inputs used to generate inlet models 1 and 10 are identical. The inlet model designed to capture a lower free-stream Mach number airflow (inlet model 1) has a relatively flatter fore-body compared to the inlet model designed to capture a higher free-stream Mach number airflow (inlet model 10). This is because the higher free-stream Mach number airflow needs compression ramps with larger angles to generate oblique shock waves that decelerate the airflow to an appropriate Mach number before the normal shock wave.

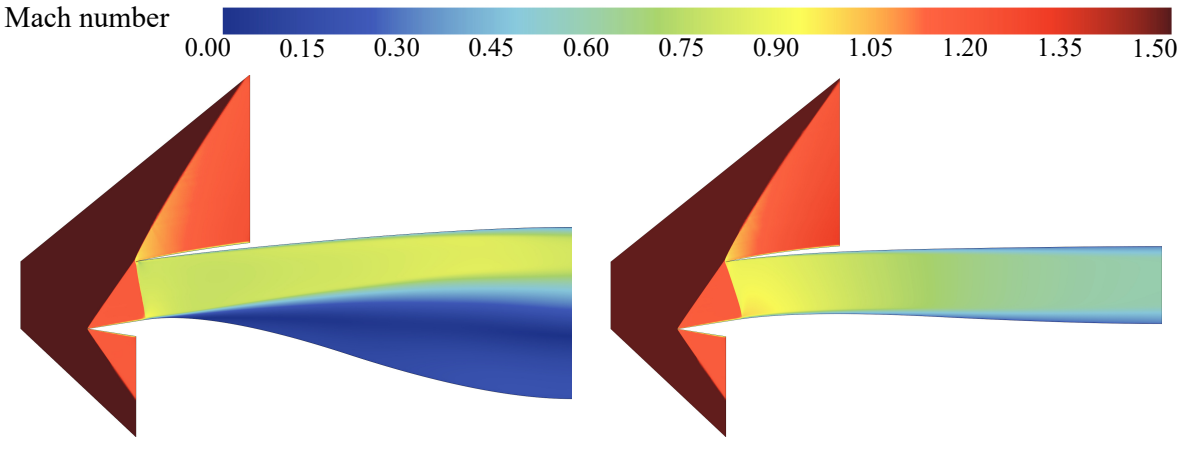
The internal diffuser geometry is dependant on the values of M_{AIP}, h_{CI}/h_{AIP} and the generated fore-body geometry. The internal diffuser subsonically decelerates the air downstream of the normal shock wave to the desired AIP Mach number via area expansion. Considering figure 6.21, inlet models 1 and 2 were designed to compress the captured air to AIP Mach

numbers of 0.2 and 0.5, respectively. All the other user-defined inputs used to generate inlet models 1 and 2 are identical. The fore-body geometries of these inlet models are identical. However, the internal diffusers differ because the area expansion ratio required by inlet model 1 to decelerate the incoming airflow to Mach 0.2 is approximately 2.2 times larger than the expansion ratio required by inlet model 2 to decelerate the incoming airflow to Mach 0.5.



(a) Inlet model 1 ($M_\infty = 1.5$) (b) Inlet model 10 ($M_\infty = 2.5$)

Figure 6.20: The Mach number contour plots of inlet models 1 and 10



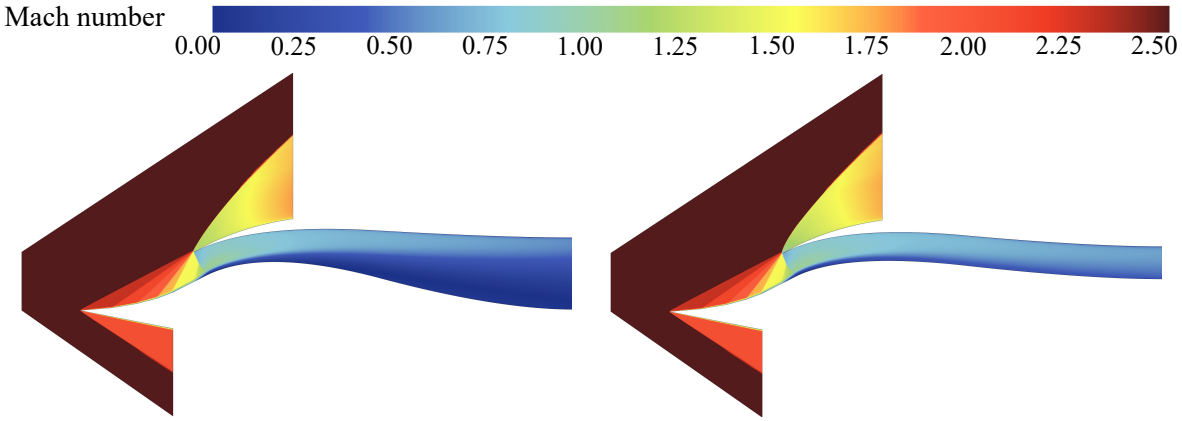
(a) Inlet model 1 ($M_{AIP} = 0.2$) (b) Inlet model 2 ($M_{AIP} = 0.5$)

Figure 6.21: The Mach number contour plots of inlet models 1 and 2

The cowl projected height cannot be too high because this can result in high levels of cowl wave drag. For this sensitivity study, h_{CI} is 20% of the height of the inlet at the AIP. This has an adverse effect on the curvature of the IDBS when the internal diffuser expansion ratio is large. The combination of a flat fore-body when the M_∞ is low (i.e. Mach 1.5), a large expansion ratio when M_{AIP} is low (i.e. Mach 0.2), and a low h_{CI} causes IADAM to generate inlet models that have IDBS with large curvatures. The curvature of the IDBS causes momentum-induced boundary layer separation to occur. The height of the flow region

where there is a loss in total pressure due to viscous effects is approximately 90% of the total AIP height. Therefore, this results in high values of E_{P_R} for inlet models which were designed using the combination of free-stream and AIP Mach numbers of 1.5 and 0.2, respectively.

The results illustrated in figure 6.18 show that E_{P_R} significantly increases with a decrease M_{AIP}. This generally applies to all the inlet models generated by IADAM and is a major contributing factor towards the high values of E_{P_R}. Inlet models 12 and 13 are another example of inlet models that demonstrate the effect that varying the desired AIP Mach number has on the viscous flow phenomena in supersonic inlet flow fields. The area expansion ratio required by inlet model 12 to decelerate the airflow to an AIP Mach number of 0.2 is 2.2 times greater than the expansion ratio required by inlet model 13 to decelerate the airflow to an AIP Mach number of 0.5. The larger the area change across the internal diffuser, the larger the region of separated flow. This increases the volume of air within the separated flow region subjected to a loss in total pressure due to turbulent mixing.



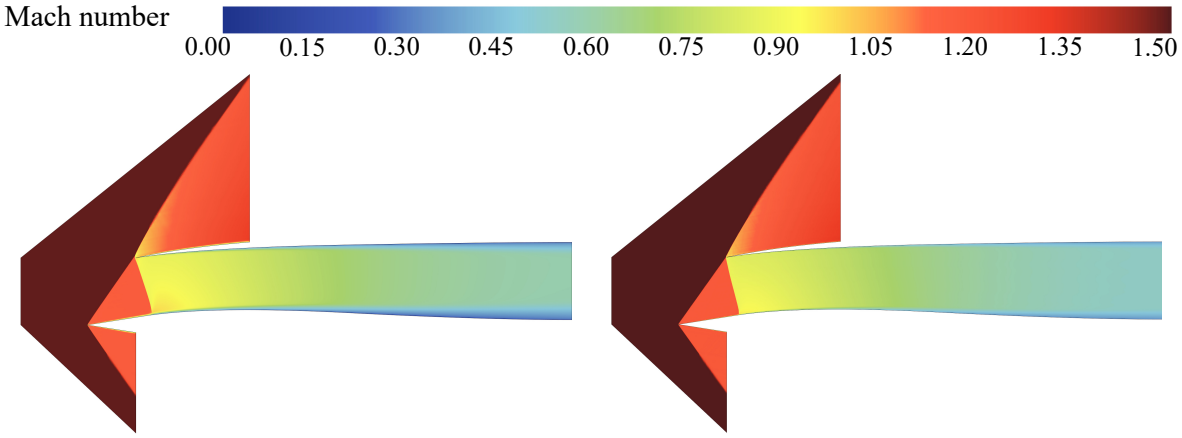
(a) Inlet model 12 ($M_{AIP} = 0.2$)

(b) Inlet model 13 ($M_{AIP} = 0.5$)

Figure 6.22: The Mach number contour plots of inlet models 12 and 13

The results illustrated in figure 6.18 also show that h_{cap} significantly affects the values of E_{P_R}. The values of E_{P_R} significantly increase with decreasing h_{cap}. For the sensitivity study, the user-defined inputs that define the dimensions of specific inlet components were defined relative to the capture height (Table 6.9). Therefore, inlet models presented in table 6.10 have been created by IADAM such that the capture height scales the entire inlet geometry. Consider the inlet models shown in figure 6.23. The user-defined inputs used to generate inlet models 2 and 6 are identical, except for the capture height. More specifically, inlet models 2 and 6 have capture heights of 0.01 m and 1 m, respectively. Therefore, inlet model 2 is a scaled-down version of inlet model 6.

The thickness of a boundary layer is a function of: the distance from the leading edge of the surface; the pressure gradient across the surface; any heat transfer between the fluid and



(a) Inlet model 2 ($h_{cap} = 0.01\ m$)

(b) Inlet model 6 ($h_{cap} = 1\ m$)

Figure 6.23: The Mach number contour plots of inlet models 2 and 6

the surface; surface roughness; and the Reynolds number of the flow. Inlet model 2 may be a geometrically scaled-down version of inlet model 6. However, the boundary layers on the supersonic inlet surfaces do not scale down with the size of the supersonic inlet.

The capture height can be considered a possible characteristic length for the inlet, similar to hydraulic diameter. Based on equation 6.2, an increase in the capture height would increase the Reynolds number. Reynolds number and boundary layer thickness are related as per equation 6.3 (Anderson 2010).

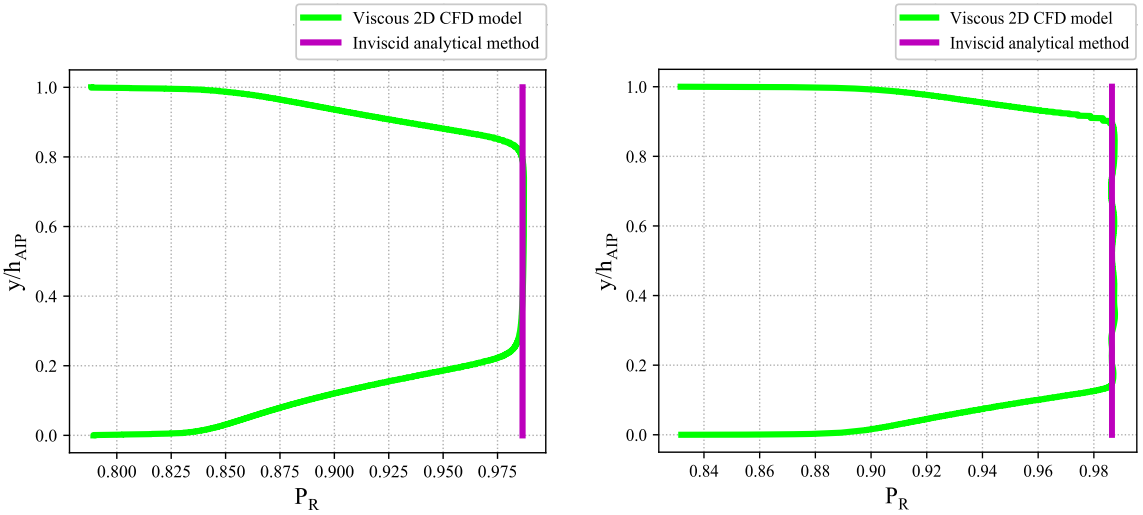
$$\delta \propto \frac{1}{R_e^m} \tag{6.3}$$

where:

δ is the boundary layer thickness,
R_e is the Reynolds number and,
m is some positive parameter.

Based on equation 6.3, an increase in the Reynolds number would decrease the boundary layer thickness. Therefore, the boundary layer thickness increases with a decrease in the inlet capture height. This corresponds with the observation made from the total pressure recovery distributions in figure 6.24.

The volume of air within a boundary layer experiences a loss in total pressure. Therefore, the distribution of P_R can be used to approximate boundary layer thickness at the AIP relative to the AIP height. Based on the total pressure recovery distributions in figure 6.24, the total height of the boundary layer flow regions at the AIPs of inlet models 2 and 6 are approximately 49% and 26% of the AIP height, respectively. Therefore, the inlet model with the smaller capture height (i.e. inlet model 2) has thicker boundary layers relative to the AIP height compared to the inlet model with the larger capture height (i.e. inlet model 6).



(a) Inlet model 2 ($h_{cap} = 0.01\ m$)

(b) Inlet model 6 ($h_{cap} = 1\ m$)

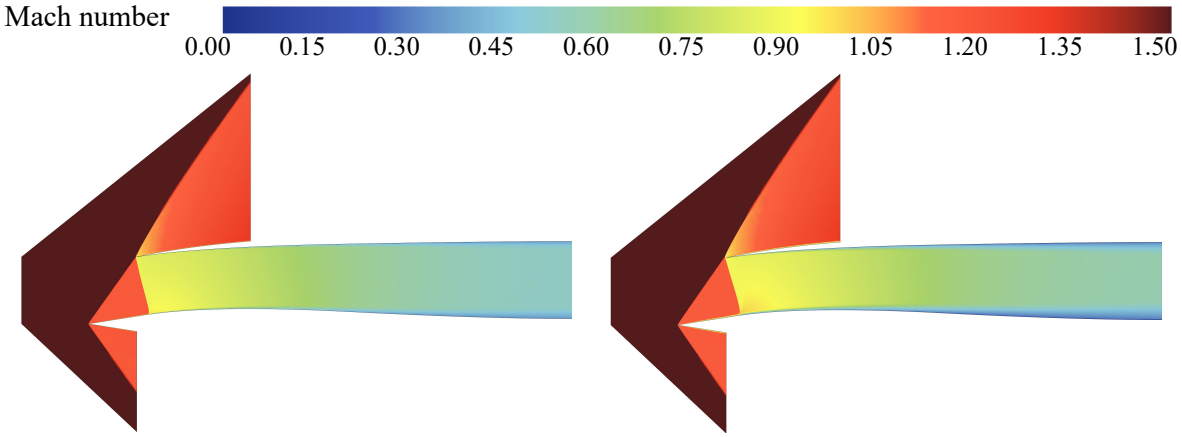
Figure 6.24: The P_R distribution for inlet models 2 and 6 at the AIP

An inlet with thicker boundary layers relative to the AIP height is associated with larger values of E_{P_R} compared to an inlet with thinner boundary layers relative to the AIP height. This occurs for two main reasons. Firstly, the friction between the supersonic inlet surfaces and the supersonic inlet flow field causes a loss in total pressure within the boundary layers. The thicker the boundary layers are relative to the AIP height, the larger the fraction of air subjected to total pressure losses. Therefore, the total pressure losses within the boundary layer have a more dominant effect on the overall total pressure recovery. As a result, the overall total pressure recovery error increases with increasing boundary layer thickness. The Mach number contour plots and total pressure recovery distributions in figures 6.23 and 6.24, respectively, show that the boundary layer thickness relative to AIP height increases with decreasing capture height. Therefore, the E_{P_R} increases with decreasing h_{cap}.

Secondly, boundary layers alter the effective fore-body surfaces. The thicker the boundary layers are relative to AIP height, the more the effective fore-body surface deviates from the actual fore-body surface. Consequently, the generated oblique shock waves have larger shock wave angles relative to the direction of free-stream flow compared to those predicted by inviscid flow calculations. As a result, the difference between the total pressure recoveries obtained from inviscid flow calculations and the viscous CFD model, i.e E_{P_R}, increases with an increase in the relative thickness of the boundary layers. The relative boundary layer thickness increases with decreasing capture height. Therefore, the E_{P_R} increases with decreasing h_{cap}.

Based on figure 6.18, there is a variation in E_{P_R} with altitude. The values of E_{P_R} increase with an increase in altitude. However, the significance of this relationship differs for inlets with different capture heights. The increase in E_{P_R} with an increase in altitude is smaller for inlets with large capture heights compared to inlets with small capture heights.

Consider inlet models 6 and 32, illustrated in figure 6.25. All but one of the user-defined inputs used by IADAM to generate inlet models 6 and 32 are identical. The differing user-defined input is the altitude at which the inlets operate. Altitude does not have a direct effect on the geometry of the generated inlet. It mainly affects the flight conditions under which the inlets operate. Therefore, inlet models 6 and 32 are geometrically identical. However, they operate at flight altitudes of 9 144 m and 36 576 m, respectively.



(a) Inlet model 6 ($H = 9\ 144\ m$)

(b) Inlet model 32 ($H = 36\ 576\ m$)

Figure 6.25: The Mach number contour plots of inlet models 6 and 32

The altitude at which the inlets operate affects the thickness of the boundary layers developing on the inlet surfaces. This is because the thickness of a boundary layer is dependent on the Reynolds number of the airflow. Reynolds number is a function of the atmospheric fluid properties that vary with altitude, as discussed in section 4.1.3.1.2. The variation of Reynolds number with altitude, specifically within the bounds presented in table 6.8, is illustrated in figure 6.26. Based on equation 6.3 and figure 6.26, the thickness of a boundary layer increases with an increase in altitude.

Based on the Mach number contour plots of inlet models 6 and 32 presented in figure 6.25, the inlet model operating at a higher altitude (i.e. inlet model 32) has thicker boundary layers relative to the AIP height compared to the inlet model operating at a lower altitude (i.e. inlet model 6). The images in figure 6.27 confirm this. The total height of the boundary layer flow regions at the AIPs of inlet models 6 and 32 are approximately 26% and 43% of the AIP height, respectively. The larger the region of boundary layer flow at the AIP relative to the AIP height, the larger the total pressure recovery error. The reasons for this were previously mentioned in the discussion about capture height. Therefore, inlet models that operate at higher altitudes have larger values for E_{P_R} than inlet models that operate at lower altitudes.

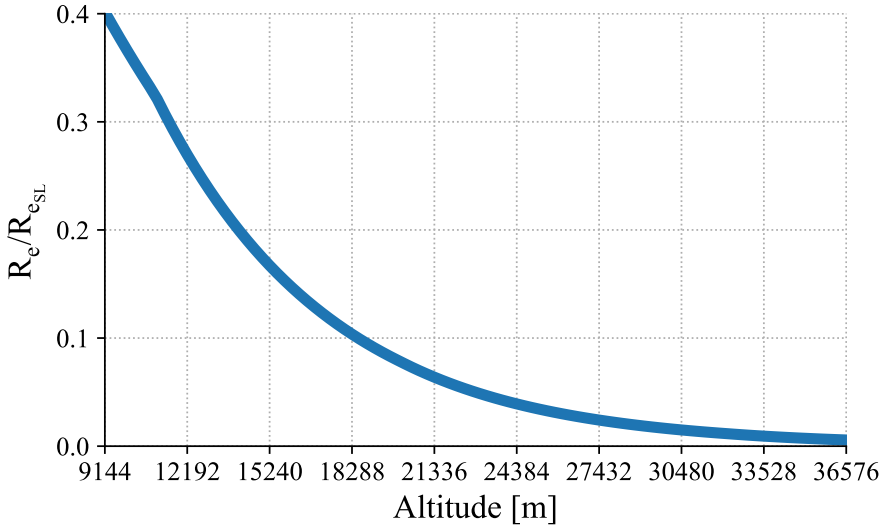
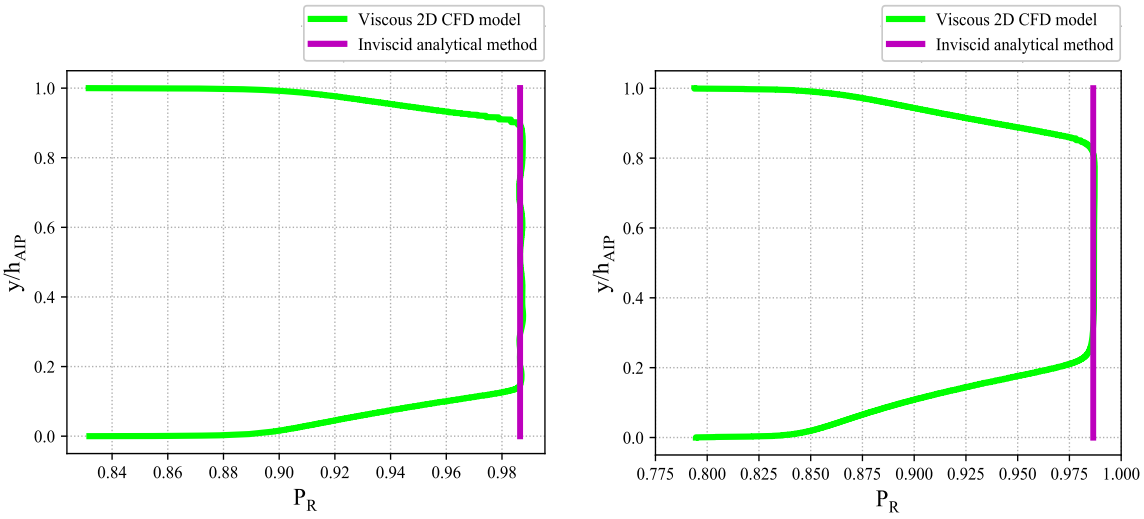


Figure 6.26: The relationship between altitude and the ratio of the Reynolds number at a specific altitude to the Reynolds number at sea level



(a) Inlet model 6 ($H = 9\ 144\ m$)

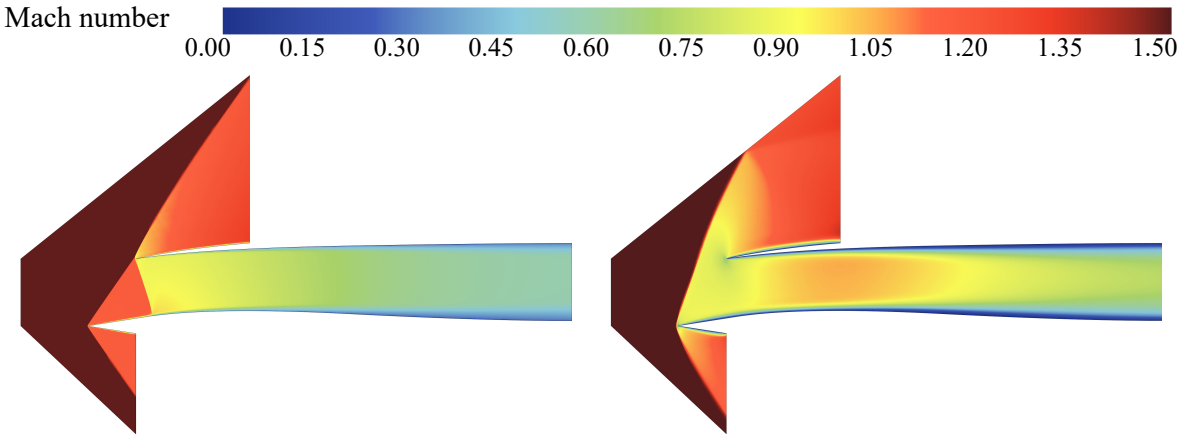
(b) Inlet model 32 ($H = 36\ 576\ m$)

Figure 6.27: The P_R distribution for inlet models 6 and 32 at the AIP

As previously mentioned, the significance of the relationship between E_{P_R} and H differs for inlets with different capture heights. Inlet models 6 and 32 have capture heights of 1 m. Consider the inlet models 2 and 28, presented in figure 6.28. These inlet models are scaled-down versions of inlet models 6 and 32, respectively. Inlet models 2 and 28 have capture heights of 0.01 m.

The significance of the relationship between E_{P_R} and H differs for inlets with different capture heights because the cumulative effect of an increase in altitude and a decrease in capture height is an increase in the boundary layer thickening. The sensitivity study has revealed

extreme cases whereby the supersonic inlet models are designed to operate at the maximum altitude of 36 576 m and are scaled down to the minimum capture height of 0.01 m. The boundary layers that develop on the inlet surfaces are very thick relative to the AIP height and severely alter the effective internal diffuser surfaces. Consequently, the effective internal diffusers are converging-diverging ducts whereby the Kantrowitz criterion (i.e. equation 4.13) is not met. This causes the terminating normal shock waves to be expelled from the inlets, as illustrated in figure 6.28b. The viscous corrections applied to IADAM must warn the user that certain user-defined input combinations may result in normal shock wave expulsion.



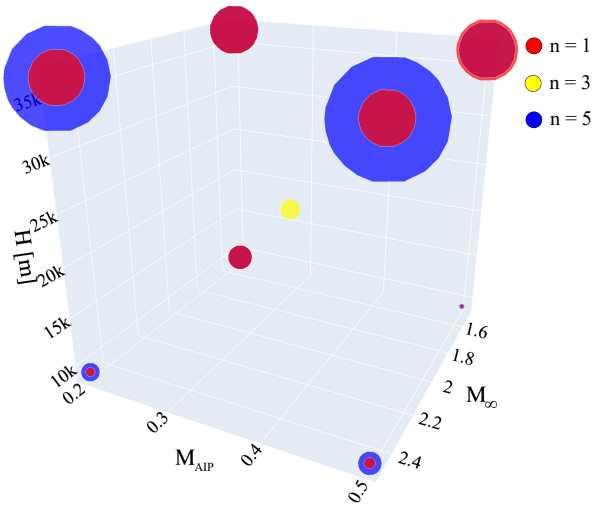
(a) Inlet model 2 ($H = 9\ 144\ m$, $h_{cap} = 0.01\ m$) (b) Inlet model 28 ($H = 36\ 576\ m$, $h_{cap} = 0.01\ m$)

Figure 6.28: The Mach number contour plots of inlet models 2 and 28

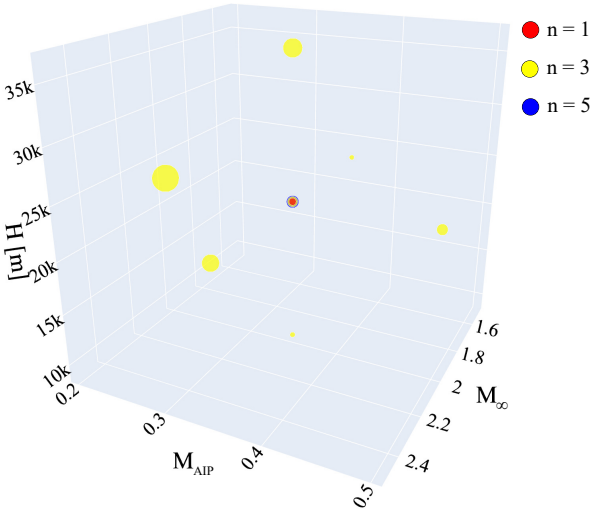
The variations of E_{P_R} with M_∞ and n do not appear to be significant relative to how E_{P_R} varies with M_{AIP}, h_{cap} and H (Figure 6.18). Therefore, these relationships are not discussed in detail. In most cases, the inlets with more fore-body ramps have slightly larger E_{P_R} relative to those with fewer ramps. However, there are four inlet models in figure 6.18a, where the inlet models with more ramps have a significantly larger E_{P_R} than the inlet models with fewer ramps. These particular inlet models, i.e. inlet models 27, 28, 29, 30, are inlet models characterised by normal shock wave expulsion.

6.3.3.2 The Variation of E_{m_R}, with changes in H, M_∞, M_{AIP}, n and h_{cap}

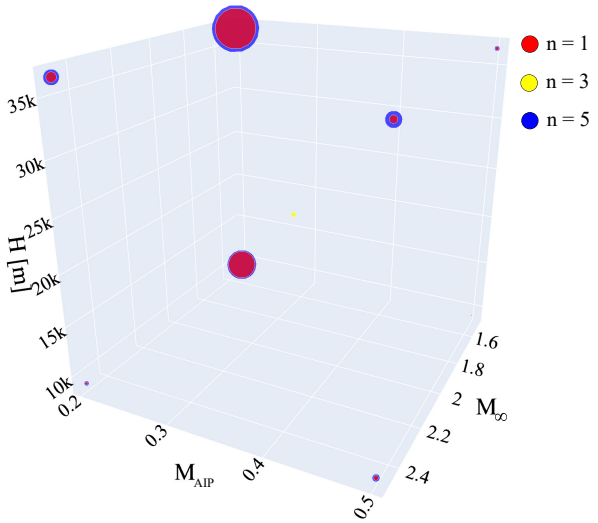
The bubble plots presented in figure 6.29 represent how E_{m_R} varies with changes in H, M_∞, M_{AIP}, n and h_{cap}. The size of the bubbles in figure 6.29 represent the magnitudes of the root mean square errors. The largest and smallest E_{m_R} have a value of 0.1890 and 0.0013, respectively. They are related to inlet models 37 and 2, respectively. Based on figure 6.29, the user-defined inputs that significantly and consistently affect the value of E_{m_R} are altitude and capture height. The magnitude of E_{m_R} increases with an increase in H and a decrease in h_{cap}.



(a) $h_{cap} = 0.01\ m$



(b) $h_{cap} = 0.1\ m$



(c) $h_{cap} = 1\ m$

Figure 6.29: The variation of E_{m_R}, with changes in H, M_∞, M_{AIP}, n and h_{cap}

The presence of boundary layers in the CFD modelled supersonic inlet flow fields cause the mass flow rate of the air flowing through the inlet to be lower than the mass flow rate computed by inviscid flow calculations. This is primarily because inviscid flow calculations assume that the velocity profile over a surface is flat and has a value equal to the mainstream flow velocity. In reality, the friction between the airflow and the inlet surfaces causes boundary layers to form. The fluid velocity within the boundary layers is zero on the inlet surfaces and increases to the velocity of the mainstream flow in the direction perpendicular to the inlet surfaces. As a result, the mass carrying capability of the airflow within the boundary layer region is reduced. Consequently, this causes a momentum and mass flow rate deficit within the boundary layer relative to the fluid momentum and mass flow rate computed by inviscid flow calculations.

The inlet capture area, or the inlet capture height in the case of 2D flow fields, limits the maximum mass flow rate that an inlet can support. The thicker the boundary layer is relative to the inlet capture height, the greater the airflow proportion subjected to a mass flow rate deficit. Therefore, E_{m_R} increases with an increase in the boundary layer thickness relative to the inlet capture height. The thickness of a boundary layer relative to inlet capture height increases with increasing H and decreasing h_{cap}. The reasons for this were discussed in section 6.3.3.1. As a result, E_{m_R} increases with an increase in H and a decrease in h_{cap}.

Furthermore, IADAM uses inviscid flow calculations to ensure that the oblique shock wave system converges at the cowl lip. The boundary layer developing on a fore-body alters the effective fore-body surface. This causes the oblique shock waves to converge away from the cowl lip. A small bow shock wave also occurs just upstream of the cowl lip. The position of the shock waves relative to the cowl lip causes mass spillage to occur around the cowl lip, contributing to the reduced mass flow ratio. The thicker the boundary layer is relative to the inlet capture height, the farther away the point of convergence is from the cowl lip. This causes a greater quantity of mass spillage to occur around the cowl lip. As a result, the error in mass flow ratio is higher when the boundary layer is thicker relative to the inlet capture height. Thicker boundary layers measured relative to the inlet capture height are observed at high altitudes and small capture heights. Therefore, the E_{m_R} increases with an increase in H and a decrease in h_{cap}.

The variations of E_{m_R} with M_∞, n and M_{AIP} do not appear to be consistent or significant relative to how E_{m_R} varies with h_{cap} and H (Figure 6.29). Therefore, these relationships are not discussed in detail. It should be noted that in most cases, the inlets with a greater number of fore-body ramps have slighter larger E_{m_R} relative to those with fewer fore-body ramps. However, there are four inlet models in figure 6.29a where the inlet models with a greater number of ramps have a significantly larger E_{m_R} than the inlet models with fewer ramps.

These particular inlet models, i.e. inlet models 27, 28, 29, 30, are inlet models characterised by normal shock wave expulsion.

6.4 Viscous Corrections

Ideally, the work done in the present chapter would be used to apply viscous corrections to the shape optimisation of the geometric profiles generated by the tool. However, performing a shape optimisation of a particular inlet while taking viscous effects into account would require several iterations of adjusting the calculated geometry to accommodate boundary layer effects and performing CFD analyses of the adjusted inlet geometry. A CFD analysis would have to be performed for every geometric adjustment to evaluate the flow field, and to determine if any further adjustments to the geometric profile are required.

The results presented in section 6.3 demonstrated how varying the user-defined inputs required by IADAM to generate an inlet changes the impact of viscous flow phenomena on the generated inlet performance parameters. Therefore, the process of performing several geometric adjustments and CFD analyses would have to be performed for several inlet geometries generated with varying user-defined inputs to be able to apply viscous corrections to all the possible inlet geometries that a user may require the tool to generate. This is a very complex and time-consuming process. As such, it is beyond the scope of this study but may be explored in future work.

Although applying viscous corrections to the geometric profiles of the inlets generated by the tool may not have been attainable at the time of the study, viscous corrections were applied to the performance parameters of the inlets generated by IADAM. IADAM computes the performance parameters using inviscid flow calculations. Applying viscous corrections to the supersonic inlet performance parameters ensures that the user is provided with a computationally efficient but improved approximation of the performance parameters of the inlets generated by IADAM. This also provides the user with an improved understanding of the quality of the air that the inlet supplies to the combustion chamber. The present section presents the development of a mathematical function that applies viscous corrections to the total pressure recovery and mass flow ratio of the inlets generated by IADAM.

6.4.1 Viscous Correction Response Surface Formulation

The performance parameters of the 2D, external-compression, supersonic inlets generated by IADAM were corrected for viscous flow. This was done to provide the user with a more

accurate representation of how well the inlets perform. Viscous corrections to the AIP Mach number were also performed to help the user see how the AIP Mach number corrected for viscous flow compares to the desired AIP Mach number. The user will make this comparison with a graph consisting of the user-defined and the viscous corrected AIP Mach number distributions. With this information, the user will also determine whether the AIP Mach number corrected for viscous flow exceeds the combustions chamber blow-off limit.

The viscous corrections were achieved using the CFD data obtained from the sensitivity study to create response surfaces of the supersonic inlet performance parameters. The response surfaces are formulated using the RBF surrogate modelling technique. RBF was specifically chosen because it is flexible, scales well with dimensionality, and is easy to construct. The choice to use RBF is explained in more detail in section 4.5.

6.4.2 Total Pressure Recovery Response Surface Formulation

The total pressure recovery of a supersonic inlet varies in the direction perpendicular to the airflow. The 2D, external-compression, supersonic inlet design and analysis tool provides the user with a graph of the total pressure recovery distribution at the AIP for each inlet that it generates. This graph gives the user a better understanding of the quality of air supplied to the combustion chamber. For instance, it helps the user visualise the presence of boundary layers at the AIP and helps them identify regions of separated boundary layer flow.

The generation of an AIP total pressure recovery distribution graph was achieved using several RBF response surfaces, one for each point on the AIP. There are a total of 100 points. Each point is a function of the user-defined inputs investigated during the sensitivity study, i.e. H, M_∞, h_{cap}, n and M_{AIP}. Figure 6.30 is a visual representation of how this was achieved.

The built-in RBF function in the Python™ SciPy module generates the total pressure recovery response surfaces. The Python™ RBF function requires a set of known input variables and the associated responses to construct the response surfaces. The user-defined inputs and the total pressure recoveries of the inlet models listed in table 6.10 were used for this purpose. Furthermore, the Python™ RBF function requires a suitable RBF function (i.e. table 4.3) and an appropriate shape parameter. A trial-and-error approach revealed that the Gaussian RBF function with a shape parameter obtained using the leave-one-out cross-validation method (Section 4.5) are best suited for the present response surface formulations. This combination generates total pressure recovery graphs with the least error. As a result, the graphs obtained closely resemble the expected CFD results. This is shown in the verification study presented in section 7.

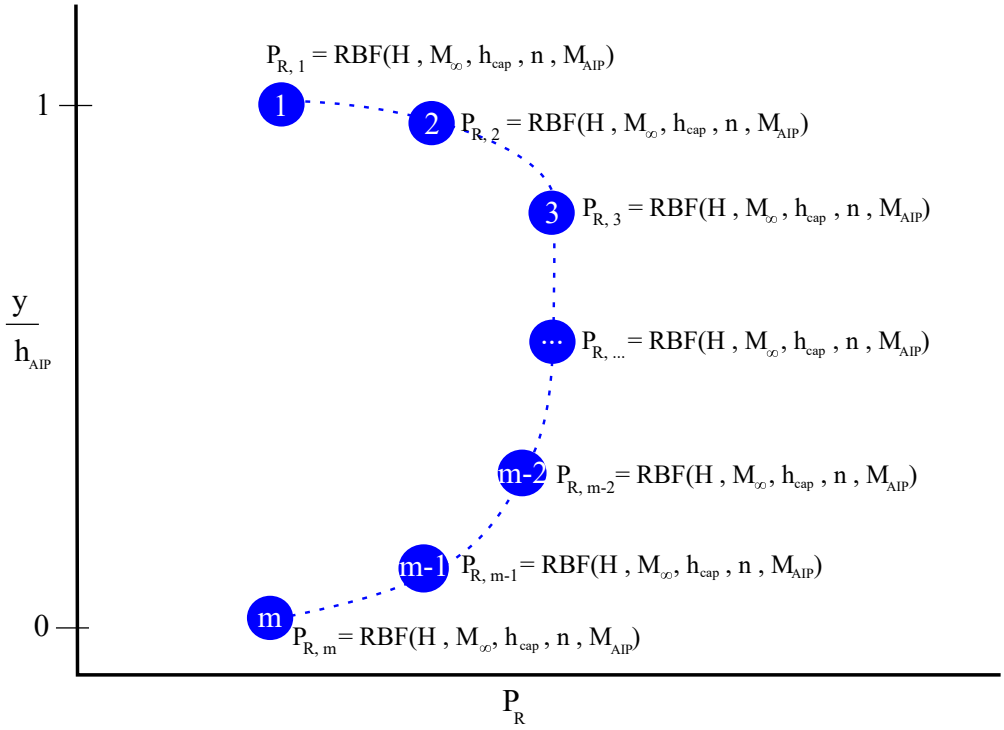


Figure 6.30: A visual representation of the response surfaces representing the P_R at a specific point on the AIP

6.4.3 Mass Flow Ratio Response Surface Formulation

The mass flow ratio of a supersonic inlet is a single value. Therefore, the mass flow ratio response surface was formulated using a single RBF function. The built-in Python™ RBF function was used to construct the mass flow ratio response surface. The user-defined inputs and the CFD computed mass flow ratios of the inlet models listed in table 6.10 were provided to the Python™ RBF function as the set of known input variables and responses. The response surface was formulated using the Gaussian RBF function with a shape parameter obtained using the leave-one-out cross-validation method (Section 4.5). This combination generates mass flow ratios with the least amount of error.

6.4.4 AIP Mach Number Response Surface Formulation

The Mach number of the airflow at the AIP varies in the direction perpendicular to the airflow. Therefore, the 2D, external-compression, supersonic inlet design and analysis tool provides the user with a graph of the AIP Mach number distribution at the AIP for each supersonic inlet that it generates. This was achieved following the same procedure as the total pressure recovery distribution (Section 6.4.2), as illustrated in figure 6.31.

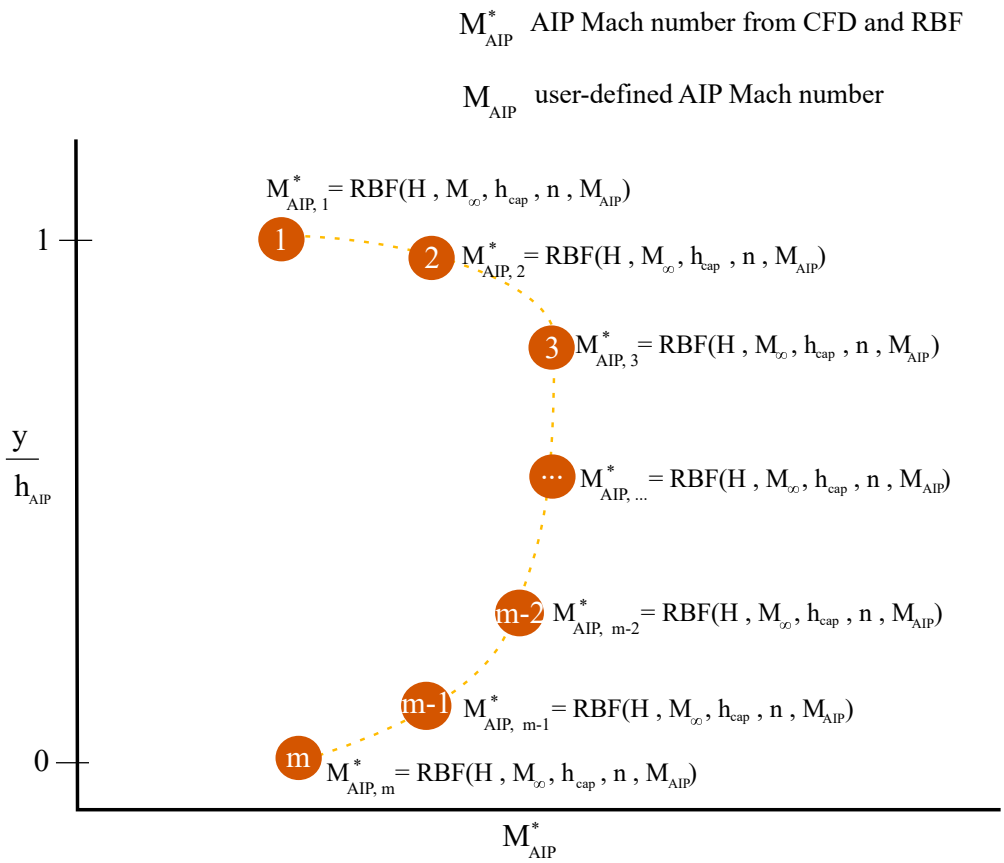


Figure 6.31: A visual representation of the response surfaces representing the M_{AIP} at a specific point on the AIP

The AIP Mach number distribution graph provided to the user also contains a plot of the AIP Mach number initially defined by the user. The user will visualise how the desired AIP Mach number compares to the AIP Mach number corrected for viscous flow. The user will also determine whether the AIP Mach number corrected for viscous flow exceeds the combustion chamber blow-off limit.

6.4.5 Mach Number Contour Plot

Suppose the user wants the tool to generate one of the inlet models listed in table 6.10. In that case, the tool provides the user with a Mach number contour plot of the supersonic inlet flow field. The Mach number contour plots were obtained from the CFD analyses performed during the sensitivity study. They provide the user with a visual representation of the supersonic inlet flow fields computed by a detailed viscous CFD analysis. Note that the Mach number contour plots are only provided to the user if they provide the tool with the combination of inputs used to generate any one of the inlet models listed in table 6.10.

6.5 Conclusion

IADAM (Chapter 5) was developed based on the assumption of inviscid compressible air flowing through the generated inlets. The CFD model developed in the current chapter demonstrated the significant effects of viscosity on the supersonic inlet flow fields. The viscous flow phenomena observed in the supersonic inlet flow field include boundary layer development, shock-wave/boundary-layer interaction, and boundary layer separation. The inability of IADAM to take the viscous effects into account causes a deviation between the flow fields computed by IADAM and the viscous CFD model. Special attention was given to the mass flow ratio and the total pressure recovery because these are important performance parameters that IADAM aims to maximise. The results presented in the current chapter highlight the deviations in these performance parameters.

The sensitivity study established that the impact of viscous flow phenomena on the supersonic inlet performance parameters vary for supersonic inlets generated with different user-defined inputs. The user-defined inputs that most significantly vary the magnitude of E_{P_R} are M_{AIP}, h_{cap} and H. The values of E_{P_R} increase as H increases and as M_{AIP} and h_{cap} decrease. The user-defined inputs that most significantly vary the magnitude of E_{m_R} are h_{cap} and H. The values of E_{m_R} increase as H increases and as h_{cap} decreases. The results from the sensitivity study were used to apply viscous corrections to the performance parameters of supersonic inlets that were generated with IADAM. The viscous corrections were formulated as response surfaces using RBF. The results from the sensitivity study in section 6.3 served as a set of known inputs and responses that were used to construct the response surfaces. Response surfaces were formulated for the supersonic inlet total pressure recovery distribution, mass flow ratio and AIP Mach number distribution. This information is useful to the user because it provides them with information about the generated supersonic inlet's overall performance and the quality of the air delivered to the combustion chamber. The viscous corrections applied to IADAM are verified in chapter 7.

Chapter 7 Viscous Correction Verification

7.1 Introduction

The total pressure recovery, mass flow ratio and AIP Mach number response surfaces developed in section 6.4 were verified against the CFD model developed in section 6.2. The response surfaces were developed using RBF. The accuracy of an RBF approximation is dependant on the distance between the unknown data point that is being evaluated and the known data points used to construct the RBF function. The farther away the unknown data point is from the known data points, the less accurate the RBF approximation. Therefore, the total pressure recovery, mass flow ratio and AIP Mach number response surfaces developed in the current chapter were believed to yield reasonable results for inlets generated with user-defined inputs within the bounds of the sensitivity study design space. However, the response surfaces were not believed to yield adequate results for inlets generated with user-defined inputs outside the bounds of the sensitivity study design space. The validity of these beliefs was investigated in the present chapter.

7.2 Methodology

The viscous correction response surface verification was achieved with two inlets generated by IADAM. The first verification inlet was generated with user-defined inputs within the bounds of the sensitivity study design space. The second verification inlet was generated with user-defined inputs outside the bounds of the sensitivity study design space. This was done to determine how well the RBF response surfaces model the performance parameters of inlets generated with user-defined inputs both inside and outside the sensitivity study design space. The user-defined inputs used to generate the supersonic inlets for the current verification study are presented in table 7.1.

Note that the user-defined AIP Mach number of verification inlet 2 is within the sensitivity study design space. Inlets generated with an AIP Mach numbers below Mach 0.2 have

an internal diffuser with an unrealistically large area expansion ratio. The inlets appear deformed. Furthermore, many inlets designed for an AIP Mach number greater than Mach 0.5 have contracting internal diffusers. Under certain conditions, the boundary layers could alter the effective contracting internal diffuser surfaces to the extent that the Kantrowitz criterion is not met (equation 4.13), causing the expulsion of the normal shock wave. Even though the user-defined AIP Mach number of verification inlet 2 is within the sensitivity study design space, all the other user-defined inputs are outside the sensitivity study design space. Therefore, the overall data point is outside the sensitivity study design space.

Table 7.1: The user-defined inputs used to generate verification inlets 1 and 2

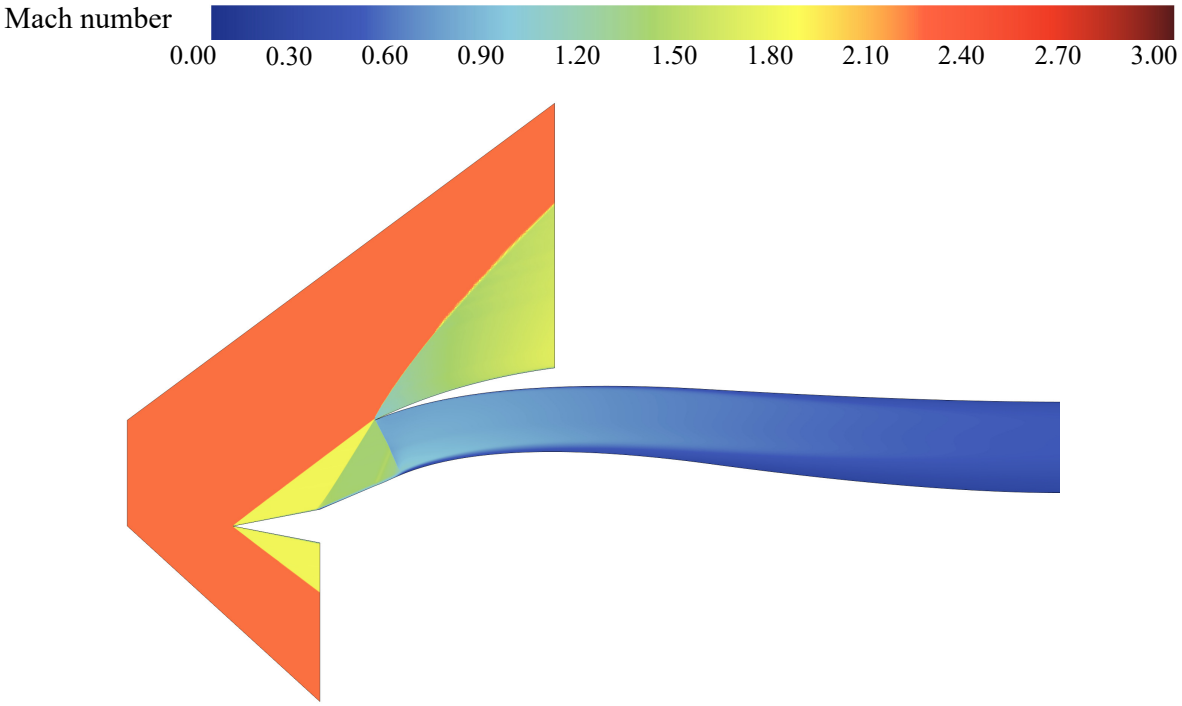
User-defined input	Verification inlet 1	Verification inlet 2
H	18 288	40 000 m
M_∞	2.20	3.00
h_{cap}	0.25 m	2.00 .
n	2	10
Cowl lip profile	circular	circular
t_{CL}	$0.001 \times h_{cap}$	$0.001 \times h_{cap}$
θ_{CLV}	3°	3°
t_C	$0.15 \times h_{cap}$	$0.15 \times h_{cap}$
M_{AIP}	0.40	0.25
h_{CI}/h_{AIP}	0.20	0.20
l_{ID}	$6.5 \times h_{cap}$	$6.5 \times h_{cap}$

CFD analyses of the verification inlets in table 7.1 were performed using the 2D CFD model presented in section 6.2. The results from the CFD analyses were compared to the results generated by the RBF response surface to evaluate the performance of the RBF response surfaces.

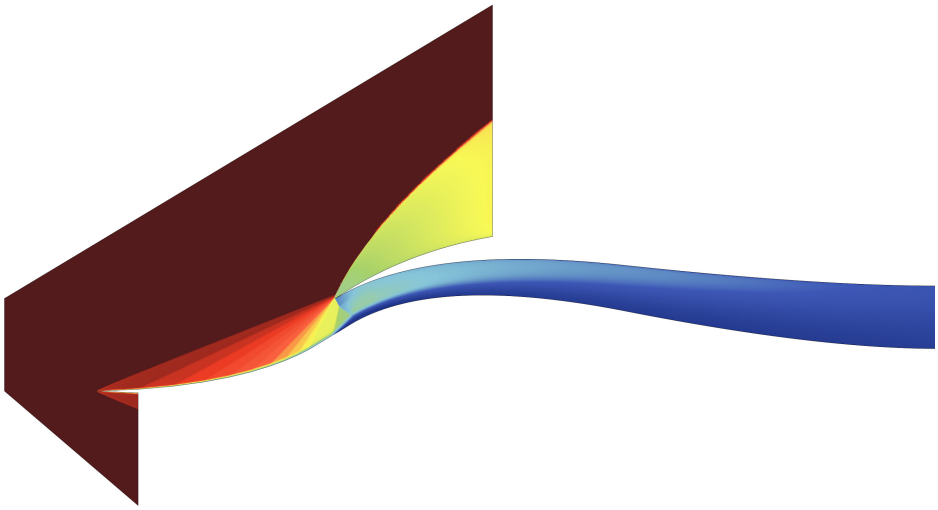
7.3 Results and Discussion

The Mach number contour plots in figures 7.1a and 7.1b are a visual representation of the CFD generated supersonic inlet flow fields in verification inlets 1 and 2, respectively.

Figure 7.2 compares the total pressure recovery distributions obtained from the CFD analyses and the RBF response surfaces. The total pressure recovery response surfaces of verification inlet 1 (Figure 7.2a) appear to generate results that correlate well with those obtained from the CFD analysis. The root mean square error between the CFD and RBF plots is approximately 0.05.



(a) Verification inlet 1

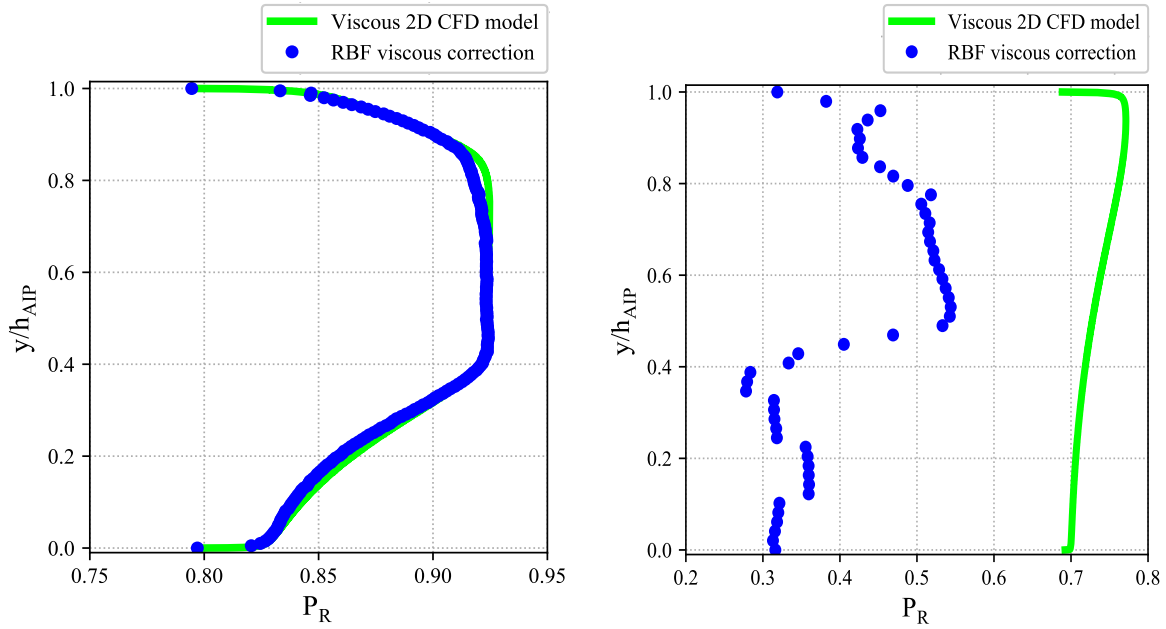


(b) Verification inlet 2

Figure 7.1: The Mach number contour plots of verification inlet 1 and 2

The error between the CFD and RBF plots in figure 7.2a results from slight differences within the ranges of $0.05 \leq y/h_{AIP} \leq 0.30$ and $0.70 \leq y/h_{AIP} \leq 0.85$. The source of the error could be the DOE sampling method chosen for the sensitivity study. A classical DOE method was selected for the sensitivity study. More specifically, the faced CCD sampling method. This choice was made because classical DOE techniques provide global sensitivity information from a more limited number of sample points. The number of sample points used in the sensitivity study had to be limited due to the time constraints imposed on the

present work. The choice of a classical DOE sampling method may have been sufficient for a sensitivity study. However, it may not have been the best choice to formulate accurate response surfaces. Accurate response surfaces are typically formulated with a modern DOE technique. Modern DOE techniques require a more significant number of sample points to achieve space-filling sampling over the domain. These techniques are used for applications that extend far beyond a typical sensitivity study to obtain an accurate response surface.



(a) Verification inlet 1

(b) Verification inlet 2

Figure 7.2: A comparison of the P_R distributions obtained from CFD and RBF

The choice of a classical DOE, which generates a limited number of sample points, may have introduced the 'curse of dimensionality' to the total pressure recovery response surfaces. The 'curse of dimensionality' is a dilemma observed when the dimensionality of a function increases. As the dimensionality of the function increases, the design space grows exponentially. Therefore, the amount of data required to model the function output accurately also grows exponentially. The total pressure recovery response surfaces have five inputs. There were 43 sets of known data used to construct the RBF response surfaces. The source of the error between the total pressure recovery distributions obtained from the CFD analyses and the RBF response surfaces could be that there were not enough data points to model the entire total pressure recovery distribution accurately. More data points could be used to increase the accuracy of this model.

There may be some error between the total pressure recovery distributions obtained from the CFD analyses and the RBF response surfaces of verification inlet 1. However, the RBF response surfaces provide a graph that correlates well with the CFD data in a fraction of the

time. It can take up to a week to design, mesh, and run the 2D CFD simulations of one supersonic inlet. Multiple simulations have to be performed to find the AIP back pressure that ensures that the normal shock wave is located at the internal diffuser entry plane. The RBF response surfaces provide the AIP total pressure recovery distribution within 10-25 minutes.

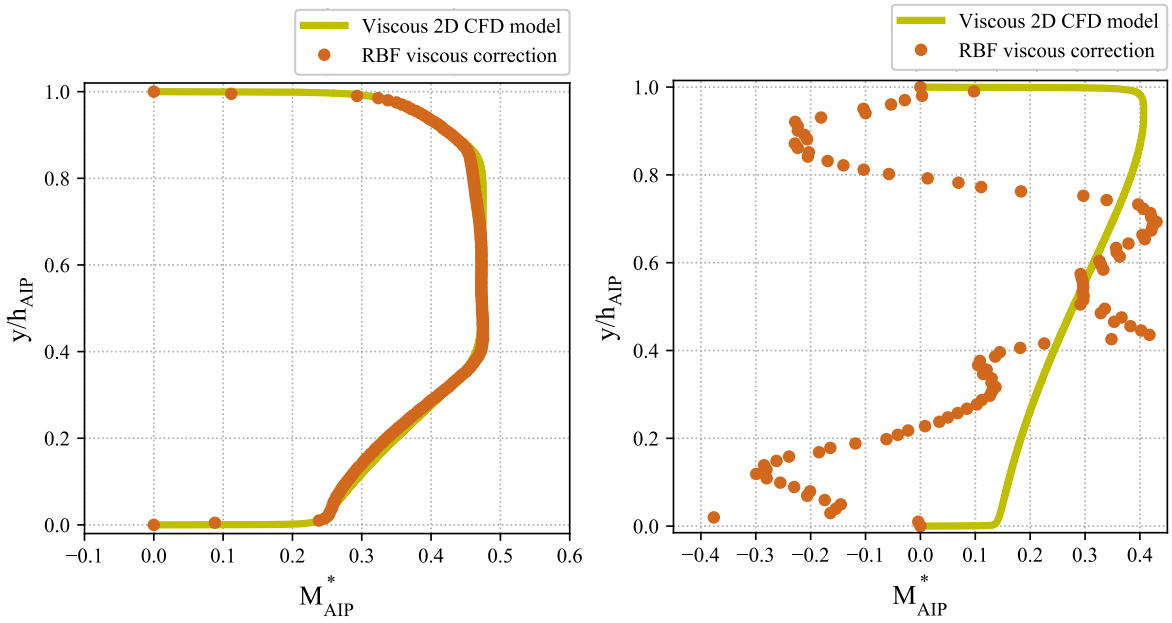
There is no correlation between the total pressure recovery distributions obtained from the CFD analyses and the RBF response surfaces of verification inlet 2 (Figure 7.2b). The root mean square error between the CFD and RBF plots in figure 7.2b is approximately 2.51. This error is 50 times greater than the average error observed for verification inlet 1. RBF approximations provide reasonable function approximations within the bounds of the design space. That is, within the bounds defined by the known set of input variables and responses used to construct the RBF. The RBF response surfaces do not make accurate predictions outside of the design space.

The mass flow ratios obtained from the CFD analysis and the RBF response surface are shown in table 7.2. Considering verification inlet 1, the mass flow ratio obtained from the RBF response surface correlates well with the value obtained from CFD. The error between the CFD and RBF mass flow ratios is approximately 0.29%. Although this error is quite small, the error sources are attributed to the DOE sampling method chosen for the sensitivity study and the 'curse of dimensionality', as discussed for the total pressure recovery response surfaces. In verifying inlet 2, the CFD and RBF mass flow ratio error is approximately 10.26%. The large error associated with verification inlet 2 is because the user-defined inputs used to generate the inlet are outside the bounds of the sensitivity study design space.

Table 7.2: A comparison between the mass flow ratios obtained from CFD and RBF

Verification inlet	RBF viscous correction	Viscous 2D CFD model
1	0.9948	0.9919
2	0.8500	0.9472

Figure 7.3 compares the AIP Mach number distributions obtained from the CFD analyses and the RBF response surfaces. The results in figure 7.3 are similar to those related to total pressure recovery (Figure 7.2). The AIP Mach number response surfaces of verification inlet 1 (Figure 7.3a) appear to generate results that correlate well with those obtained from the CFD analysis. The root mean square error between the CFD and RBF plots is approximately 0.05. The error between the CFD and RBF plots in figure 7.3a results from slight differences that exist in the same places as the differences observed in the total pressure recovery plots, namely within the ranges of $0.05 \leq y/h_{AIP} \leq 0.30$ and $0.70 \leq y/h_{AIP} \leq 0.85$. The sources of this error are attributed to the DOE sampling method chosen for the sensitivity study and the 'curse of dimensionality', as discussed previously.



(a) Verification inlet 1

(b) Verification inlet 2

Figure 7.3: A comparison of the M_{AIP} distributions obtained from CFD and RBF

In the case of verification inlet 2 (Figure 7.3b), there is no correlation between the AIP Mach number distributions obtained from the CFD analyses and the RBF response surfaces. The root mean square error between the CFD and RBF plots in figure 7.3b is approximately 2.02. This is because the user-defined inputs used to generate verification inlet 2 are outside the bounds of the sensitivity study design space, as discussed previously.

7.4 Conclusion

The response surfaces correlate well with the data obtained from CFD analyses when the user-defined inputs used to generate inlets are within the bounds of the sensitivity study design space. When the user-defined inputs used to generate inlets are outside the bounds of the sensitivity study design space, the response surfaces fail to yield reasonable approximations of the performance parameters. Therefore, the viscous corrections developed in section 6.4 are only applied when the user specifies inputs within the sensitivity study design space.

Chapter 8 Summary and Conclusion

The work presented documents the first iteration of a shape optimisation tool for 2D, external-compression, supersonic inlet design and analysis. The development of the tool was motivated by the desire of the CSIR to remain competitive in the field of commercial supersonic flight. The tool developed in the present research automates the design and analysis of optimised 2D, external-compression, supersonic inlets based on user-defined inputs. The user is provided with an inlet geometry in the form of coordinates. Furthermore, they are provided with the performance parameters of the generated inlet (i.e. total pressure recovery and mass flow ratio) and the Mach number at the AIP to ensure that it does not exceed the combustion chamber blow-off limit. The total pressure recovery, mass flow ratio and AIP Mach number provided to the user indicate the inlet performance when operating in the critical mode of operation.

The development of IADAM was the starting point in developing the tool. IADAM is a collection of shape optimisation algorithms that apply the theories of inviscid compressible flow and mathematical optimisation to generate geometric profiles of inlets that are optimised for maximum total pressure recovery. The inlets are also designed such that the mass flow ratio is maximised. The shape optimisation algorithms in IADAM were formulated using the built-in Python™ SciPy 1.3.1 optimisation function. The SLSQP minimisation algorithm was chosen to be an initial driver to construct the shape optimisation algorithms in IADAM. It was proven to generate global optimum solutions in a multi-start optimisation study consistently. Therefore, it is considered to perform satisfactorily for this application. However, other minimisation algorithms could be used to formulate the shape optimisation algorithms in IADAM in the future. For IADAM to generate the geometric profile of an inlet, eleven user-defined inputs are required, i.e. H, M_∞, h_{cap}, n, cowl lip profile, t_{CL}, θ_{CLV}, t_C, M_{AIP}, h_{CI}/h_{AIP} and l_{ID}.

The inviscid flow analyses performed by IADAM suggest that the implications of viscous effects on the generated inlet flow fields have not been considered. A detailed CFD model was developed to understand the implications of viscous effects on supersonic inlet flow fields. The CFD model was developed in both the 2D and 3D space. The 3D CFD model was proven

to be more accurate than the 2D CFD model. However, the 3D CFD model has a higher computational cost relative to the 2D CFD model. Even though the accuracy of the 2D model is less than the 3D model, it was considered acceptable to the study because the 2D model does capture the essential flow features of a 2D, external-compression, supersonic inlet flow field. Both the 2D and 3D CFD analyses showed that viscous flow phenomena, such as boundary layer development, shock-wave/boundary-layer interactions, and boundary layer separation, significantly affect supersonic inlet flow fields. Viscous effects cause a difference between the ideal flow fields computed by IADAM and the more realistic flow fields obtained from the CFD analyses.

The results obtained from the CFD model demonstrated the significant effect of viscous flow phenomena on a supersonic inlet flow field. However, they are unique to a particular supersonic inlet geometry with specific flight conditions. The present work aims to develop a tool that generates inlets of various shapes, sizes, and operating conditions based on user-defined inputs. Therefore, a sensitivity study was performed to investigate how the impact of viscous flow phenomena varies for inlets designed with different user-defined inputs. The sensitivity study was conducted using DOE techniques and the 2D CFD model. Special attention was given to the impact of viscous effects on the performance parameters (i.e. total pressure recovery and mass flow ratio) as these are the variables the tool aims to optimise.

The results obtained from the sensitivity study were used to develop a method to apply viscous corrections to IADAM. This was achieved through surrogate modelling. Ideally, viscous corrections would be directly applied to the shape optimisation algorithms in IADAM. However, this process would require several iterations of CFD analyses and geometry adjustments per inlet geometry. As such, it is beyond the scope of this study but may be explored in future work. In the present work, viscous corrections were applied to the supersonic inlet performance parameters. The viscous corrections provide the user with an improved approximation of the performance parameters of a generated inlet relative to the performance parameters initially computed by IADAM. They also help the user identify boundary layers and separated boundary layer flow at the AIP. This provides the user with an understanding of the quality of the air that the inlet supplies to the combustion chamber.

As mentioned previously, the work presented in the present research is the first iteration of a shape optimisation tool for 2D, external-compression, supersonic inlet design and analysis. Further developments and verifications of the tool are required to improve its capabilities. Potential refinements and improvements to the tool are discussed in the recommendations chapter (Chapter 9).

Chapter 9 Recommendations

The work presented documents the first iteration of a shape optimisation tool for 2D, external-compression, supersonic inlet design and analysis. Further developments and verifications of the tool are required to improve its capabilities. These present opportunities for future work, which can be explored from what was completed with the recommendations listed below:

- The shape optimisation algorithms in IADAM were formulated using the SLSQP minimisation algorithm. SLSQP was chosen as an initial driver to construct the shape optimisation algorithms because it was proven to work well in other studies similar to the present study. Furthermore, it is readily available in Python™, as discussed in section 4.2. It worked well for model development. However, a study could be performed to investigate the performance of other minimisation algorithms. This could include minimisation algorithms available in Python™, those that aren't available in Python™, a hybrid minimisation algorithm (i.e. an algorithm that combines two or more existing algorithms), or a newly developed minimisation algorithm. A study of this nature would ensure that the tool utilises the best-suited optimisation algorithms.

- The internal diffuser surfaces were constructed using the NURBS model mainly due to its flexibility and wide range of uses. The use of NURBS curves is justified in more detail in section 4.3.1. Although the NURBS model performed well in generating the required surfaces, a study could be conducted to investigate the applicability of other curve fitting methods. These could include both implicit and explicit curve fitting methods.

- The manner in which the NURBS curves were utilised to generate internal diffuser surfaces is very specific. For instance, a certain number of control points were used, and each of these control points was constrained to a particular point, line or region. This method performed well in generating a first iteration of the internal diffuser shape optimisation algorithms. However, a study could be conducted to investigate how changing the number of control points, the constraints of the control points, and the degree of the NURBS curves affects the optimisation of internal diffuser surfaces.

- Similarly to the NURBS curve model, the RBF surrogate modelling technique was selected to form response surfaces of the supersonic inlet performance parameters using CFD data. RBF was specifically chosen because it is flexible, scales well with dimensionality, and is easy to construct. The choice to use RBF is explained in more detail in section 4.5. RBF worked well to generate the required response surfaces, as discussed in chapter 7. However, a study could be performed to investigate the performance of different surrogate modelling techniques in constructing these response surfaces. Potential surrogate modelling techniques could include polynomial response surfaces, Kriging, neural networks, support vector machines, etc.

- Viscous flow phenomena such as boundary layer development, shock-wave/boundary-layer interaction and boundary layer separation are frequently occurring phenomena in supersonic inlet flow fields. The adverse effects of viscous flow on the overall performance of an inlet can be reduced by equipping the tool with the capability of adding a boundary layer diverter or bleed to the inlet designs. The purpose of these components would be to prevent the boundary layer from a forward external surface from entering the internal diffuser. Forward external surfaces include the fore-body, the fuselage, wing, etc. Boundary layer diverters and bleeds are discussed in section 4.1.2.

- The shape optimisation algorithms currently perform their analyses based on the assumption of an inviscid flow field. A study can be conducted to develop a method that applies viscous corrections directly to the shape optimisation algorithms, as briefly discussed in section 6.4. This ensures that the adverse effects of viscous flow are taken into account during the shape optimisation process. Performing the shape optimisation of a particular inlet while taking viscous effects into account will require several iterations of adjusting the calculated geometry to accommodate boundary layer effects and performing CFD analyses of the adjusted inlet. A CFD analysis will have to be performed for every geometric adjustment to evaluate the flow field and determine if any further adjustments to the geometric profile are required.

- The CFD model was developed in both the 2D and the 3D space. The 3D CFD model produced results that were in better agreement with experimental data than the results produced by the 2D CFD model. However, due to the high computational cost of the 3D CFD model, the computational mesh was coarse relative to the 2D CFD model. A mesh refinement study to ensure that the 3D CFD model solution is independent of mesh resolution could not be performed. With the development of powerful computers, a mesh refinement study could be conducted in future work to find a computational mesh that generates a solution independent of mesh resolution. This could improve the accuracy of the 3D CFD model.

- The turbulence parameters used in the CFD model were left as the default STAR-CCM+ values. The reasons why the default STAR-CCM+ values were considered to be acceptable are documented in section 6.2. Ideally, the best estimate of turbulence parameters would be obtained from empirical data. Therefore, wind-tunnel experiments of 2D, external-compression, supersonic inlets could be performed to evaluate the turbulence parameters at the boundary conditions and compare them against the default STAR-CCM+ values.

- The sensitivity study made use of data obtained from a 2D CFD model. The 3D CFD model produced results that were in better agreement with experimental data compared to the results produced by the 2D CFD model. To improve the accuracy of the sensitivity study results, a 3D CFD model could be used to acquire the required data. A 3D supersonic inlet flow field has a finite width. The width could be a user-defined input. Therefore, the sensitivity study could also investigate how different widths affect the impact of viscous flow phenomena on supersonic inlet flow fields. The images of inlets in appendix F indicate that the aspect ratios (i.e. ratio of width to capture height) range from approximately 0.5 to 1. These aspect ratios could be used for the sensitivity study design space. The addition of width to the five user-defined inputs investigated in the sensitivity study will require the CFD analyses of 77 inlet models using the faced CCD sampling method. After that, the sensitivity study results could be incorporated into the offline viscous correction functions (Section 6.4).

- Due to the time limitations imposed on the present work, only five user-defined inputs were investigated during the sensitivity study, i.e. H, M_{∞}, h_{cap}, n and M_{AIP}. Another study could be conducted to investigate how a variation in all eleven user-defined inputs affects the impact of viscous flow phenomena on the performance parameters of the generated inlets. Analysing all eleven user-defined inputs will require CFD analyses of 2071 inlet models using the faced CCD sampling method. Suppose the width is also added to the sensitivity study. In that case, 4121 inlet models will need to be analysed using CFD. The number of CFD analyses required is large for a single study. However, the sensitivity study could be broken down into several studies.

- Currently, the tool provides the user with the performance parameters when operating in the critical mode, as discussed in chapter 4.1.3.3. This is an ideal condition. However, a supersonic inlet could operate in the sub-critical or super-critical modes of operation in off-design conditions. The tool can be improved by providing the user with a performance characteristic curve (i.e. figure 4.24) to provide the user with the inlet performance parameters when operating in off-design conditions. This could be achieved by performing several CFD analyses with different AIP pressures that vary from a value that positions the normal shock wave upstream of the AIP to a value that expels the normal shock wave.

Bibliography

Ames Research Staff (1953). *Report 1135: Equations, Tables, and Charts for Compressible Flow*. Tech. rep. Ames Aeronautical Laboratory, Moffett Field, California, USA: National Advisory Committee for Aeronautics, pp. 613–680.

Anderson, J. D. (2010). *Fundamentals of Aerodynamics*. 5th. New York, New York, USA: McGraw-Hill Education. ISBN: 978-0-07-339810-5.

ANSYS Inc (2009). *ANSYS FLUENT. User's Guide*. Version 12.0.

Aziz, M., H. M. Elbanna and M. M. Abdelrahman (2010). 'Design Optimization of a Three Dimension Supersonic Intake Using the CFD-RC Package'. In: *Proceedings of ICFD 10: Tenth International Congress of Fluid Dynamics*. Ain Soukhna, Red Sea, Egypt: International Congress of Fluid Dynamics (ICFD).

BAE Systems (2021). *BAC Concorde - Luxury at Twice as Fast as the Speed of Sound*. URL: https://www.baesystems.com/en/heritage/bac-concorde (visited on 2021).

Baloyi, B. T. C. (2017). 'A Computational Tool for Supersonic Inlet Design and Analysis'. Honours Degree Research. Pretoria, Gauteng, South Africa: University of Pretoria.

Barnhart, P. J. (1997). *IPAC - Inlet Performance Analysis Code*. Tech. rep. Brook Park, Ohio, USA: NYMA Incorporation.

Beals, N. E. and B. Govindarajan (2021). 'Trim Strategies for Over-Actuated Vehicle Configurations During Conceptual Design'. In: *AIAA AVIATION 2021 FORUM*, p. 2460. DOI: 10.2514/6.2021-2460.

Boeing (2021). *F-15*. URL: https://www.boeing.com/defense/f-15/#/video/advanced-f-15-survivability (visited on 2021).

Bordbar, M. and Y. F. Yao (2015). 'Analysis of 2D Shock-Wave/Boundary-Layer Intraction Phenomena'. In: *29th International Symposium on Shock Waves 2*. Ed. by R. Bonazza and D. Ranjan. Madison, Wisconsin, USA: Springer, pp. 1205–1210. ISBN: 978-3-319-16837-1. DOI: 10.1007/978-3-319-16838-8_66.

Bourdeau, C. et al. (1999). 'Three Dimensional Optimization of Supersonic Inlets'. In: *35st AIAA/ASME/SAE/ASEE Joint Propulsion Conference and Exhibit*. Los Angeles, California, USA: American Institute of Aeronautics and Astronautics. DOI: 10.2514/6.1999-2108.

Carrier, G. et al. (2001). 'Multi-Criteria Design Optimization of Two-Dimensional Supersonic Inlet'. In: *39th Aerospace Sciences Meeting and Exhibit*. Reno, Nevada, USA, p. 1064. DOI: 10.2514/6.2001-1064.

Collard, D. (1991). 'Concorde Airframe Design and Development'. In: *Aerospace Technology Conference and Exposition*. SAE Technical Paper Series. DOI: 10.4271/912162.

Corriveau, D. and R. Pimentel (2009). *Wind Tunnel Tests on Two-Dimensional Air Intakes at DRDC Valcartier*. Tech. rep. Quebec, Canada: Defence Research and Development Canada - Valcartier.

Crickmore, P. F. (2015). *SR-71 Blackbird*. Great Britain: Osprey Publishing. ISBN: 9781472804921.

Dunbar, B. (2014). *NASA Armstrong Fact Sheet: XB-70 Valkyrie*. URL: https://www.nasa.gov/centers/armstrong/news/FactSheets/FS-084-DFRC.html (visited on 2021).

Ekermo, J. (2018). 'Validation and Parametric Study of Supersonic Air Intake'. Masters Degree Research. Gothenburg, Sweden: Chalmers University of Technology.

Engelund, W. C. et al. (2001). 'Aerodynamic Database Development for the Hyper-X Airframe-Integrated Scramjet Propulsion Experiments'. In: *Journal of Spacecraft and Rockets* 38.6, pp. 803–810. DOI: 10.2514/2.3768.

Eshel, T. (2017). *British F-35B to Carry Meteor Missiles from 2024*. URL: https://defense-update.com/20170421_f35_meteor.html (visited on 2021).

Esterhuyse, J. C. (1997). 'Aerodynamic Drag of a Two-Dimensional External Compression Inlet at Supersonic Speed'. PhD thesis. Cape Technikon.

Faro, I. D. V. (1965). *Supersonic Inlets*. Tech. rep. North Atlantic Treaty Organization, Advisory Group for Aerospace Research and Development.

Fayez, K. et al. (2021). 'Conceptual Design for Long-Endurance Convertible Unmanned Aerial System'. In: *AIAA Scitech 2021 Forum*, p. 1059. DOI: 10.2514/6.2021-1059.

Giunta, A. A., S. F. Wojtkiewicz and M. S. Eldred (2003). 'Overview of Modern Design of Experiments Methods for Computational Simulations'. In: *41st AIAA Aerospace Sciences Meeting and Exhibit*. Reno, Nevada, USA: American Institute of Aeronautics and Astronautics, p. 649. DOI: 10.2514/6.2003-649.

Haas, M., R. A. Elmquist and D. R. Sobel (1993). 'The NIDA Code: A New Tool for Supersonic Inlet Design and Analysis'. In: *JANNAF Propulsion Meeting*. Monterey, California, USA: Chemical Propulsion Information Agency.

Hardy, R. L. (1990). 'Theory and Applications of the Multiquadric-Biharmonic Method 20 years of Discovery 1968–1988'. In: *Computers & Mathematics with Applications* 19.8-9, pp. 163–208.

Hastie, T., R. Tibshirani and J. Friedman (2009). *The Elements of Statistical Learning*. 2nd. New York, New York, USA: Springer-Verlag. ISBN: 978-0-387-84857-0. DOI: 10.1007/978-0-387-84858-7.

Houghton, E. L. and P. W. Carpenter (2003). *Aerodynamics for Engineering Students*. 5th. Oxford, England: Butterworth-Heinemann. ISBN: 9780080493855.

Incropera, F. P. et al. (2007). *Fundamentals of Heat and Mass Transfer*. 6th. Hoboken, New Jersey, USA: John Wiley & Sons, pp. 359–361. ISBN: 978-0-471-45728-2.

Kantrowitz, A. and C. Donaldson (1945). *Preliminary Investigation of Supersonic Diffusers*. Tech. rep. Hampton, Virginia, USA: National Advisory Committee for Aeronautics (NACA).

Khuri, A. I. and S. Mukhopadhyay (2010). 'Response Surface Methodology'. In: *Wiley Interdisciplinary Reviews: Computational Statistics* 2.2, pp. 128–149. DOI: 10.1002/wics.73.

Koziel, S., D. E. Ciaurri and L. Leifsson (2011). 'Surrogate-Based Methods'. In: *Computational Optimization, Methods and Algorithms*. Ed. by S. Koziel and X.-S. Yang. Berlin, Heidelberg: Springer Berlin Heidelberg, pp. 33–59. ISBN: 978-3-642-20859-1. DOI: 10.1007/978-3-642-20859-1_3.

Kraft, D. (1988). *A Software Package for Sequential Quadratic Programming*. Tech. rep. Obersfaffeuhofen, Germany: Deutsche Forschungs- und Versuchsanstalt für Luft- und Raumfahrt.

Lalee, M., J. Nocedal and T. Plantenga (1998). 'On the Implementation of an Algorithm for Large-Scale Equality Constrained Optimization'. In: *SIAM Journal on Optimization* 8.3, pp. 682–706. DOI: 10.1137/S1052623493262993.

LIU, J. et al. (2017). 'Unsteady Supercritical/Critical Dual Flowpath Inlet Flow and its Control Methods'. In: *Chinese Journal of Aeronautics* 30.6, pp. 1877–1884. ISSN: 1000-9361. DOI: 10.1016/j.cja.2017.10.007.

Loth, E. et al. (2004). 'Mesoflap and Bleed Flow Control for a Mach 2 Inlet'. In: *42nd AIAA Aerospace Sciences Meeting and Exhibit*. Reno, Nevada, USA: American Institute of Aeronautics and Astronautics, pp. 9586–9609. DOI: 10.2514/6.2004-855.

Mahoney, J. (1990). *Inlets for Supersonic Missiles*. 1st. Washington, DC, USA: American Institute of Aeronautics and Astronautics. ISBN: 978-0-930403-79-9. DOI: 10.2514/4.403799.

Mizukami, M. and J. D. Saunders (1995). 'Parametrics on 2D Navier-Stokes Analysis of a Mach 2.68 Bifurcated Rectangular Mixed-Compression Inlet'. In: *31st Joint Propulsion Conference and Exhibit*. San Diego, California, USA: American Institute of Aeronautics and Astronautics (AIAA). DOI: 10.2514/6.1995-2755.

Mongillo, M. (2011). 'Choosing Basis Functions and Shape Parameters for Radial Basis Function Methods'. In: *SIAM Undergraduate Research Online* 4, pp. 190–209. DOI: 10.1137/11s010840.

Myers, R. H., D. C. Montgomery and C. M. Anderson-Cook (2016). *Response Surface Methodology: Process and Product Optimization Using Designed Experiments*. 4th. Hoboken, New Jersey, USA: John Wiley & Sons. ISBN: 978-1-118-91603-2.

Orbital Sciences Corporation (2004). *Orbital's 'Coyote' Supersonic Sea-Skimming Target Missile Successfully Launched for U.S. Navy*. URL: https://news.northropgrumman.com/news/releases/orbital-s-coyote-supersonic-sea-skimming-target-missile-successfully-launched-for-u-s-navy (visited on 2021).

Parsch, A. (2007). *Orbital Sciences GQM-163 Coyote*. URL: http://www.designation-systems.net/dusrm/m-163.html (visited on 2021).

Phillips, W. F. (2010). *Mechanics of Flight*. 2nd. Hoboken, New Jersey, USA: John Wiley & Sons. ISBN: 978-0-470-53975-0.

Piegl, L. and W. Tiller (1997). *The NURBS Book*. 2nd. Berlin, Heidelberg: Springer-Verlag. ISBN: 978-3-540-61545-3. DOI: 10.1007/978-3-642-59223-2.

Plotkin, K. J. (1989). 'Review of Sonic Boom Theory'. In: *12th Aeroacoustic Conference*. San Antonio, Texas, USA: American Institute of Aeronautics and Astronautics (AIAA). DOI: 10.2514/6.1989-1105.

Powell, M. J. (1994). 'A Direct Search Optimization Method That Models the Objective and Constraint Functions by Linear Interpolation'. In: *Advances in Optimization and Numerical Analysis*, pp. 51–67. DOI: https://doi.org/10.1007/978-94-015-8330-5_4.

Pressley, A. N. (2010). *Elementary Differential Geometry*. 2nd. Springer Science & Business Media. ISBN: 978-1-84882-890-2. DOI: 10.1007/978-1-84882-891-9.

Rathakrishnan, E. (2010). *Applied Gas Dynamics*. 1st. Singapore: John Wiley & Sons (Asia). ISBN: 978-0-470-82576-1.

SAAB (2021). *Meteor*. URL: https://www.saab.com/products/meteor (visited on 2021).

Seddon, J. (1966). *Boundary-Layer Interaction Effects in Intakes with Particular Reference to those Designed for Dual Subsonic and Supersonic Performance*. Tech. rep. London, England: Aeronautical Research Council.

Seddon, J. and E. L. Goldsmith (1999). *Intake Aerodynamics*. 2nd. Boston, Massachusetts, USA: Blackwell Science. ISBN: 978-1-56-347361-6.

Shih, T. H. et al. (1994). 'A New $\kappa - \epsilon$ Eddy Viscosity Model for High Reynolds Number Turbulent Flows-Model Development and Validation'. In: *Computers and Fluids* 24.3, pp. 227–238. ISSN: 0045-7930. DOI: 10.1016/0045-7930(94)00032-T.

Siemens Digital Software (2020). *Simcenter STAR-CCM+. Product Overview*. Version 15.02.

Skinner, S. N. and H. Zare-Behtash (2018). 'State-of-the-Art in Aerodynamic Shape Optimisation Methods'. In: *Applied Soft Computing* 62, pp. 933–962.

Slater, J. W. (2012). 'Design and Analysis Tool for External-Compression Supersonic Inlets'. In: *50th AIAA Aerospace Sciences Meeting Including the New Horizons Forum and Aerospace Exposition*. Cleveland, Ohio, USA: National Aeronautics and Space Administration. DOI: 10.2514/6.2012-16.

Snyman, J. A. and D. N. Wilke (2018). *Practical Mathematical Optimization*. 2nd. Cham, Switzerland: Springer International Publishing AG. ISBN: 978-3-319-77585-2. DOI: 10.1007/978-3-319-77586-9.

Sorensen, V. L. (1965). *Computer Program for Calculating Flow Fields in Supersonic Inlets*. Tech. rep. Moffett Field, California, USA: National Aeronautics and Space Administration.

Storm, R. et al. (2007). *Pushing the Envelope: A NASA Guide to Engines*. Tech. rep. Cleveland, Ohio, USA: NASA Glenn Research Center Office of Educational Programs, pp. 1–23.

Tindell, R. and G. Tamplin (1983). 'An Inlet System Installed Performance Prediction Program Using Simplified Modeling'. In: *19th Joint Propulsion Specialists Conference*. Seattle, Washington, USA: American Institute of Aeronautics and Astronautics. DOI: 10.2514/6.1983-1167.

Van Staden, P. A. (1990). 'Supersonic, Four Shock, Ramp Type Intake Design, with Internal Boundary Layer Bleed'. Masters Degree Research. Stellenbosch, Western Cape, South Africa: University of Stellenbosch.

Vos, R. and S. Farokhi (2015). 'Method of Characteristics'. In: *Introduction to Transonic Aerodynamics. Fluid Mechanics and Its Applications*. Vol. 110. Springer, Dordrecht, pp. 211–273. DOI: 10.1007/978-94-017-9747-4_5.

Walsh, K. R. et al. (1997). *Inlet Distortion for an F/A-18A Aircraft During Steady Aerodynamic Conditions up to 60 deg Angle of Attack. NASA Technical Memorandum 104329*. Tech. rep. Edwards, California, USA: Dryden Flight Research Center.

Wendorff, A., E. Botero and J. J. Alonso (2016). 'Comparing Different Off-the-Shelf Optimizers' Performance in Conceptual Aircraft Design'. In: *17th AIAA/ISSMO Multidisciplinary Analysis and Optimization Conference*, p. 3362. DOI: 10.2514/6.2016-3362.

Zha, G. C. et al. (1996). 'High Performance Supersonic Missile Inlet Design Using Automated Optimization'. In: *6th AIAA/NASA/ISSMO Symposium on Multidisciplinary Analysis & Optimization*. Bellevue, Washington, USA: American Institute of Aeronautics and Astronautics, pp. 1355–1371. DOI: 10.2514/6.1996-4142.

Zhang, J. et al. (2020). 'Experiment and Numerical Investigation of Flow Control on a Supersonic Inlet Diffuser'. In: *Aerospace Science and Technology* 106, p. 106182. ISSN: 1270-9638. DOI: 10.1016/j.ast.2020.106182.

Appendix A The Two-Dimensional, External-Compression, Supersonic Inlet Design and Analysis Tool

A digital appendix was created to present data that is too large to insert directly within the PDF version of this document. It is available at the shared Google Drive here. The URL used to access this digital appendix by users not using the electronic version of this document is https://drive.google.com/drive/folders/1o3jQh1bKuyJbsDgVDYk7GNTrMGS-8d32?usp=sharing.

The digital appendix contains the computational tool for two-dimensional, external-compression, supersonic inlet design and analysis. To download the tool, follow this hyperlink. There is a user guide available in this hyperlink to assist the users using the tool.

Appendix B Oblique and Normal Shock Wave Theory Equations

The theory of oblique and normal shock waves (Section 4.1.3.1.3) plays an instrumental role in the development of IADAM. The continuity, momentum and energy equations have been used to derive equations for calculating the changes in the fluid properties across a normal shock wave as a function of the oncoming Mach number M_1. Equations B.1 through to B.6 present the relationships between upstream and downstream Mach number, static pressure, static density, static temperature, stagnation pressure and stagnation temperature, respectively. The fluid properties upstream and downstream of the normal shock wave are represented by subscripts '1' and '2', respectively. (Anderson 2010).

$$M_2^2 = \frac{1 + \frac{\gamma-1}{2} M_1^2}{\gamma M_1^2 - \frac{\gamma-1}{2}} \tag{B.1}$$

$$\frac{p_2}{p_1} = 1 + \frac{2\gamma}{\gamma+1}(M_1^2 - 1) \tag{B.2}$$

$$\frac{\rho_2}{\rho_1} = \frac{(\gamma+1)M_1^2}{2 + (\gamma-1)M_1^2} \tag{B.3}$$

$$\frac{T_2}{T_1} = \left[1 + \frac{2\gamma}{\gamma+1}(M_1^2 - 1)\right] \frac{2 + (\gamma-1)M_1^2}{(\gamma+1)M_1^2} \tag{B.4}$$

$$\frac{p_{0,2}}{p_{0,1}} = \left[\frac{(\gamma+1)M_1^2}{(\gamma-1)M_1^2 + 2}\right]^{\frac{\gamma}{\gamma-1}} \left[\frac{\gamma+1}{2\gamma M_1^2 - (\gamma-1)}\right]^{\frac{1}{\gamma-1}} \tag{B.5}$$

$$T_{0,2} = T_{0,1} \tag{B.6}$$

The equations used to calculate changes across oblique shock waves have a similar form to those used to calculate the change in the fluid properties across a normal shock wave. However, the upstream Mach number M_1 is replaced with the normal component of the oncoming Mach number (i.e. $M \sin \beta$). Therefore, the equations that govern the properties of a normal shock wave (i.e. equation B.1 though to B.6) can be used to compute the fluid properties of the air downstream of an oblique shock wave provided that the normal

component of the oncoming Mach number is used (Anderson 2010). In the case of Mach number, equation B.1 calculates the normal component of the Mach number just downstream of the oblique shock wave, i.e. $M_2 \sin(\beta - \theta)$. To obtain the value of M_2, the calculated value must be divided by the value of $\sin(\beta - \theta)$.

Appendix C CFD Validation

C.1 Introduction

The CFD model presented in chapter 6.2 was validated against published experimental data obtained from a paper titled 'Mesoflap and Bleed Flow Control for a Mach 2 Inlet' by Loth et al. (2004). The published paper documents wind tunnel experiments that were performed on a 2D, external-compression, supersonic inlet. The photograph presented in figure C.1 illustrates the experimental set-up of the inlet installed in the wind tunnel. Both 2D and 3D CFD models were investigated to determine how closely the results compare to the experimental data and to each other.



Figure C.1: A photograph of the inlet installed in the wind tunnel (Loth et al. 2004)

C.2 2D CFD Simulation of the Supersonic Inlet Flow Field

C.2.1 Domain Specification

The 2D, external-compression, supersonic inlet tested in the wind tunnel experiments performed by Loth et al. (2004) is presented in figure C.2. It consists of a fore-body with two compression ramps. The compression ramps have angles of 7° and 15°, respectively. The inlet also consists of an internal diffuser with a rectangular cross-section throughout. The inlet dimensions are presented in terms of capture height (h_{cap}). The orientation of the inlet differs from the orientation used in this study. More specifically, the orientation is such that the inlet arrears to have been flipped over the x-axis. The inlet orientation is a function of the inlet installation location (i.e. fuselage-, side-, nose-, or top-mounted etc.).

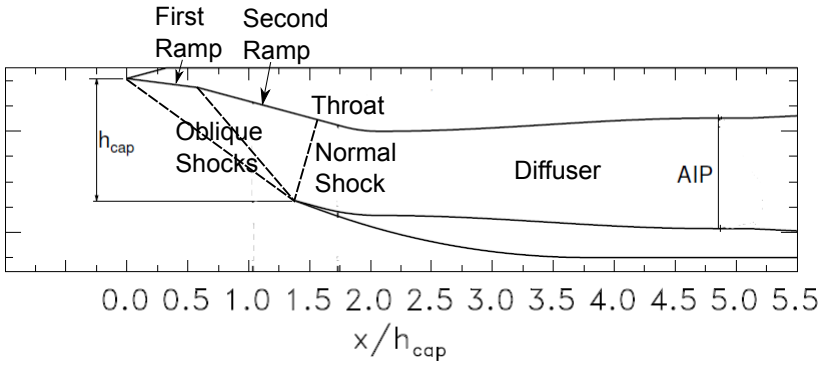


Figure C.2: The geometry of a 2D, external-compression, supersonic inlet (Loth et al. 2004)

Figure C.3 depicts the CFD fluid domain and the associated boundary conditions. The domain was modelled using SolidWorks 2018. The free-stream inflow was modelled with a free-stream boundary condition placed upstream of the inlet geometry. The horizontal distance between the free-stream inflow boundary and the leading edge of the fore-body is equal to the capture height. The free-stream outflow was modelled with a pressure outlet boundary condition. All the internal diffuser surfaces were modelled with the wall boundary condition. The airflow exiting the internal diffuser was modelled with a pressure outlet boundary condition.

Initially, the pressure outlet boundary condition representing the airflow exiting the internal diffuser was located at the AIP. The resulting CFD simulation was characterised by a normal shock wave that would oscillate back and fourth at the internal diffuser entry plane. This occurred because the pressure outlet boundary condition tends to be highly reflective in that pressure disturbances in the flow will reflect off the boundary and work their way upstream in subsonic flow. The pressure wave may change the flow conditions downstream of the normal

shock wave, therefore, resulting in unsteady movement of the normal shock wave. To reduce the potential of pressure disturbances reflecting off the boundary, Ekermo (2018) performed CFD analyses of a supersonic inlet and placed the pressure outlet boundary condition well-enough downstream of the AIP. This was accomplished by adding an additional constant-area duct downstream of the AIP. This allowed the flow to be more uniform before the pressure outlet boundary condition.

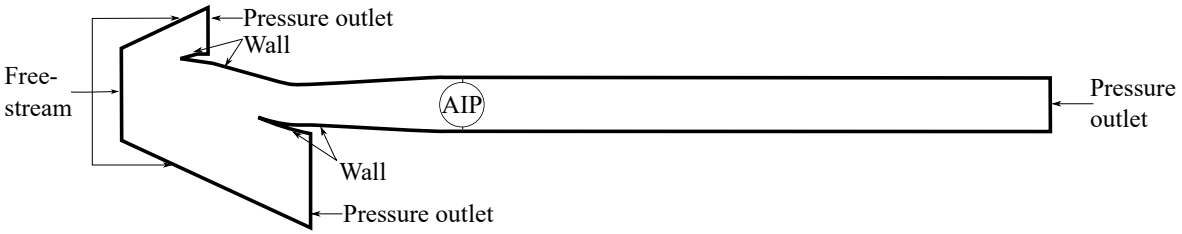


Figure C.3: The 2D CFD domain with boundary conditions

An additional constant-area duct was added to the domain downstream of the AIP, as illustrated in figure C.3. The pressure outlet boundary condition was placed at the end of the additional duct. The duct has the same height as the internal diffuser at the AIP. It also has a length ten times the height of the internal diffuser at the AIP. The length of the constant-area duct was decided upon based on a trial-and-error process.

C.2.2 Mesh Specification

The computational mesh was generated using the STAR-CCM+ parts-based meshing strategy. The polyhedral and prism layer meshers were used to generate the mesh. The mesh was refined in the regions where shock wave formation and boundary layer separation are expected to occur.

A mesh independence study was done to ensure that the solution is independent of the mesh resolution. The base cell sizes tested were $0.030h_{cap}$, $0.025h_{cap}$, $0.020h_{cap}$, $0.015h_{cap}$ and $0.010h_{cap}$. Figure C.4 presents the total pressure recovery distribution at the AIP for the various mesh cell sizes. The root mean square errors between the plots in figure C.4 are presented in table C.1. Although the results appear very close in figure C.4, the results presented in table C.1 indicate that there is no significant differences in total pressure recovery for base cell sizes smaller than $0.015h_{cap}$.

The final computational mesh is presented in figure C.5. The mesh in the constant-area duct is not included in figure C.5 in order to provide a close up of the mesh illustrating mesh

refinement in the regions where shock wave formation and boundary layer separation are expected to occur. The size of the mesh is presented in table C.2.

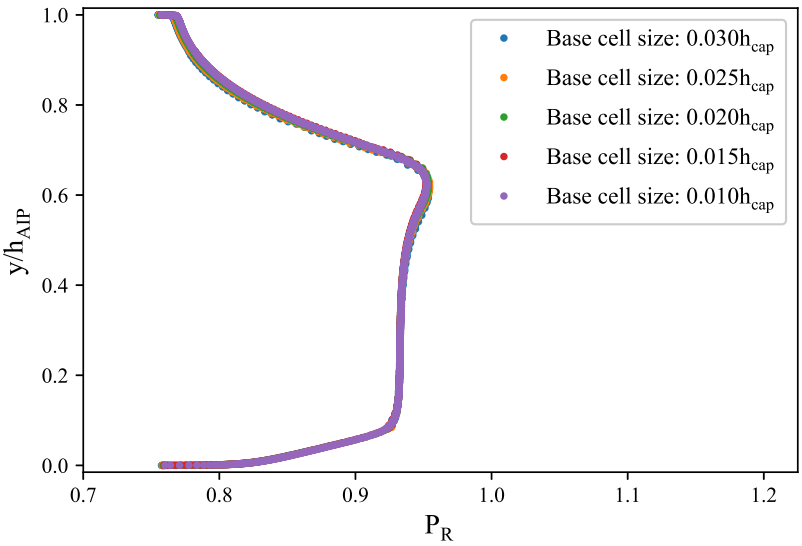


Figure C.4: The P_R distribution at the AIP for various 2D mesh cell sizes

Table C.1: The errors between P_R distribution curves for various 2D mesh cell sizes

Computational Mesh 1	Computational Mesh 2	P_R Error
Base cell size: $0.030h_{cap}$	Base cell size: $0.025h_{cap}$	0.015
Base cell size: $0.025h_{cap}$	Base cell size: $0.020h_{cap}$	0.008
Base cell size: $0.020h_{cap}$	Base cell size: $0.015h_{cap}$	0.003
Base cell size: $0.015h_{cap}$	Base cell size: $0.010h_{cap}$	0.000

Table C.2: The size of the 2D CFD computational mesh

Number of cells	932 468
Number of polyhedral layers	100

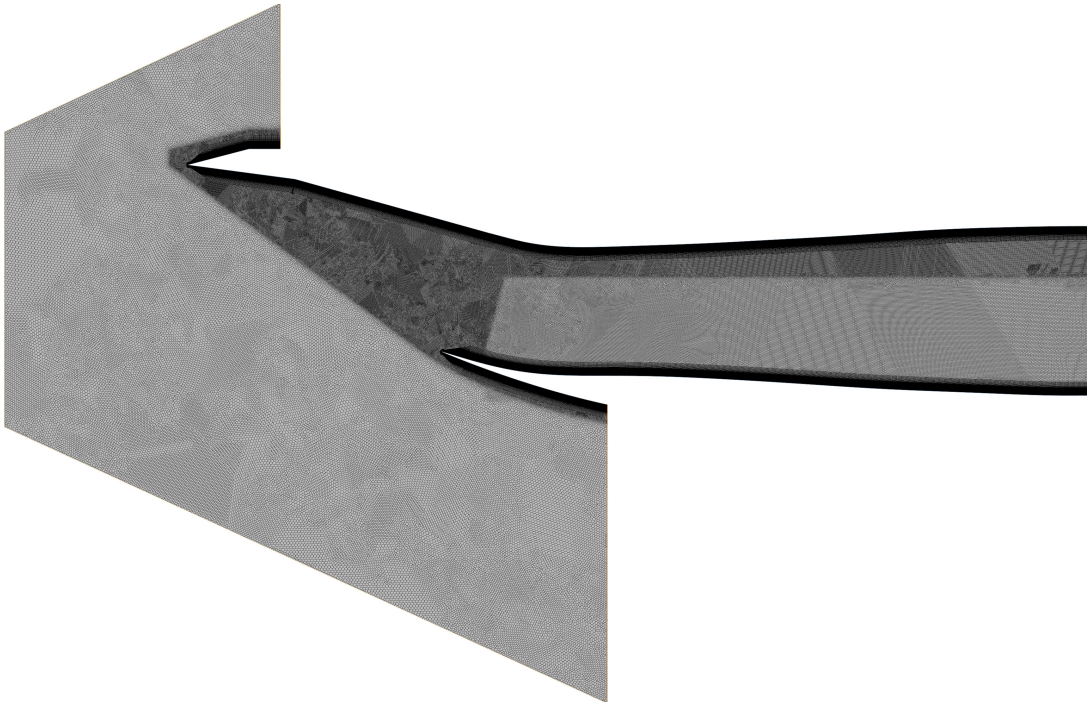


Figure C.5: The 2D CFD computational mesh

The mesh metrics that measure the cell quality of a 2D mesh in STAR-CCM+ are face validity, volume change, cell skewness angle, chevron quality indicator and least-squares quality (Siemens Digital Software 2020). The mesh quality metrics of the computational mesh illustrated in figure C.5 are presented in figure C.6.

The face validity of a particular cell is an area-weighted calculation of how correct the directions of the face normals are relative to the location of the cell centroid (Siemens Digital Software 2020). The mesh in question is a 2D mesh. Therefore, the edges of the cells are considered. A good quality 2D cell has edge normals that are directed outward and away from the cell centroid. Such a cell has a face validity of one. Cells with a face validity less than 0.5 are negative cells, which should be avoided. Based on figure C.6, all the cells in generated mesh have a face validity of one. There are no negative cells in the mesh.

Volume change is an indication of the volume of a particular cell relative to the volume of its biggest neighbouring cell (Siemens Digital Software 2020). The generated mesh (Figure C.5) is 2D. Therefore, volume change is calculated based on the areas of the cells. Cells with an area that is equal to or larger than their neighbours have a volume change of one. Bad quality cells have a volume change of 0.01 or less. The results presented in figure C.6 indicate that a large proportion of the cells in the generated mesh have a volume change that is close to one. None of the cells in the generated mesh have a volume change of 0.01 or less.

Considering two neighbouring 2D cells, the cell skewness angle is the angle between the orthogonal vector of the common edge between the cells and the line that connects the centroids of the cells. The cell skewness angle must be kept lower than 85° to avoid bad equality cells (Siemens Digital Software 2020). The results presented in figure C.6 show that the highest skewness angle of the cells in the generated mesh is approximately 53°.

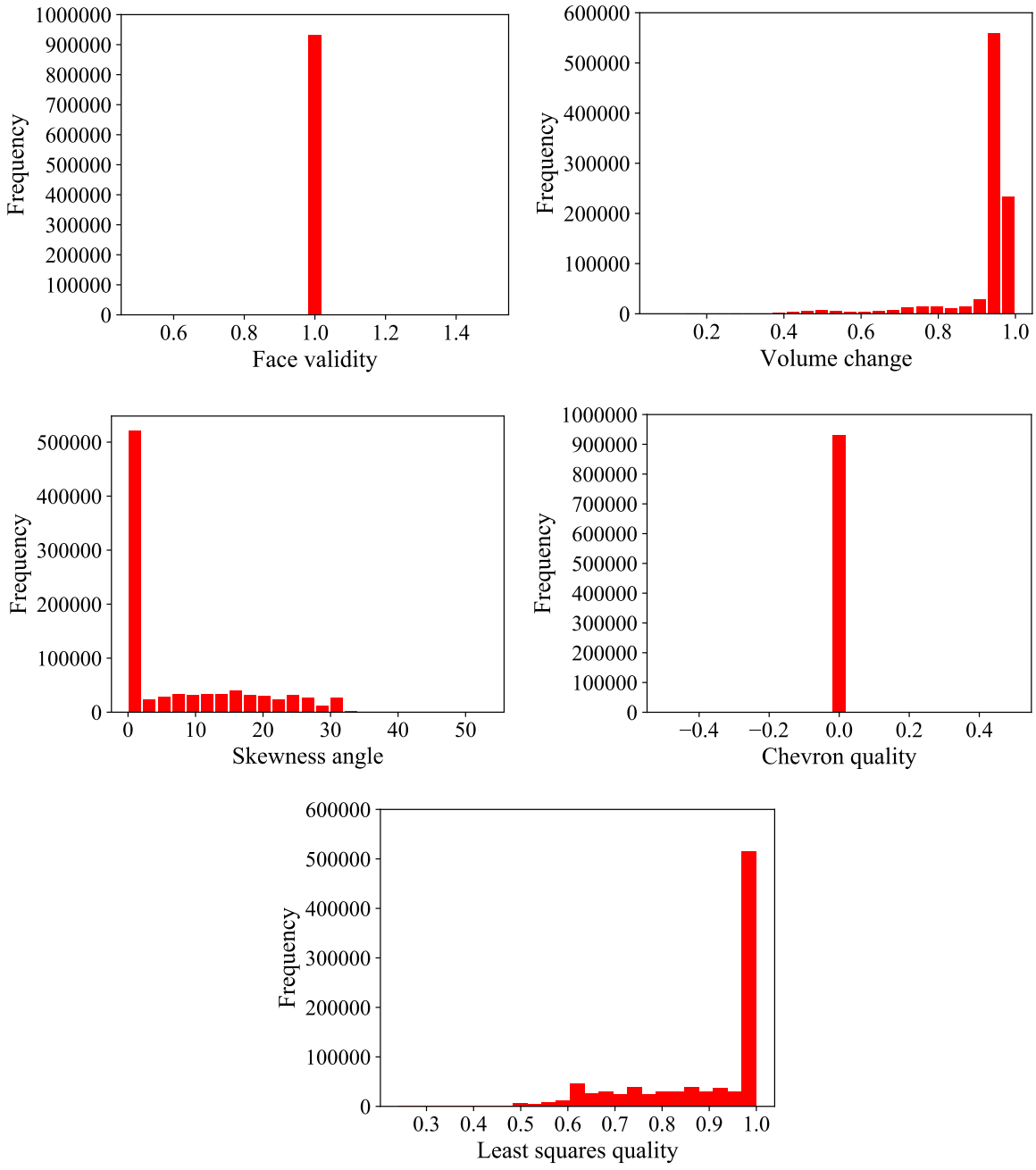


Figure C.6: The mesh metrics of the 2D CFD model computational mesh

Chevron cells are bad quality cells that should be avoided in a mesh. They are defined as two neighbouring slender cells that meet at an angle in such a way that the line joining the cell centroids does not pass through the face (3D)/edge (2D) that the cells share (Siemens

Digital Software 2020). Figure C.6 indicates that there are no chevron cells in the generated mesh (Figure C.5).

The least-squares quality is measure of the quality of a particular cell based on the location of the cell centroid relative to the location of the centroids of the neighbouring cells that it shares common faces (3D)/edges (2D) with. A least-squares quality of one is an indicator of a good quality cell. Bad quality cells have a least-squares quality of 10^{-3} or lower. Based on figure C.6, approximately 500 000 cells ($\approx 54\%$ of total cells) have a least-squares quality of one. There are no cells that have a least-squares quality less than 10^{-3}.

C.2.3 Physics Models

All the physics models used in the CFD simulation are tabulated in table C.3. The CFD model was developed in the 2D space. The air flowing through the inlet was assumed to be an ideal gas. The compressibility of a gas cannot be ignored. Therefore, the density-based solver (i.e. coupled flow) was selected. The CFD model was developed to compute a steady-state solution.

Table C.3: The physics models

Group box	Model
Space	Two-dimensional
Time	Steady
Material	Gas
Flow	Coupled flow
Equation of state	Ideal gas
Energy	Coupled energy
Gradient metrics	Gradients
Viscous regime	Turbulent
Turbulence	Reynolds-averaged Navier-Stokes
Reynolds-averaged turbulence	$\kappa - \epsilon$ turbulence
$\kappa - \epsilon$ turbulence model	Realisable $\kappa - \epsilon$ two-layer
Wall distance	Exact wall distance
$\kappa - \epsilon$ two-layer wall treatment	Two-layer all-y+ wall treatment

The $\kappa - \epsilon$ turbulence model was used to model the effects of viscosity on the supersonic inlet flow field. The decision to use this model was influenced by the work done by Mizukami and Saunders (1995). Mizukami and Saunders (1995) performed a study to investigate three turbulence models to analyse the flow in a Mach 2.68, bifurcated, rectangular, mixed-compression

inlet. The turbulence models investigated were the $\kappa-\epsilon$, Baldwin-Barth, and Baldwin-Lomax turbulence models. They found that the $\kappa-\epsilon$ turbulence model compared well with experimental data. Furthermore, it is applicable to a wide range of flows and it is expected to simulate 3D flows more accurately than 2D flows. Therefore, they recommend this turbulence model for the analysis of supersonic inlet flow fields. Loth et al. (2004), Bourdeau et al. (1999), and Aziz, Elbanna and Abdelrahman (2010), just to name a few, also performed CFD analyses of supersonic inlet flow fields using the $\kappa-\epsilon$ turbulence model. Therefore, the $\kappa-\epsilon$ appears to be an acceptable turbulence model for this application.

There are several $\kappa-\epsilon$ turbulence models available on STAR-CCM+. However, the realisable $\kappa-\epsilon$ turbulence model was specifically chosen for this application. The realisable $\kappa-\epsilon$ turbulence model was developed by Shih et al. (1994). It was used to model various types of flow. These include duct and flat plate boundary layer flows. The flow simulations were performed with and without pressure gradients. The analyses conducted by Shih et al. (1994) showed that the realisable $\kappa-\epsilon$ turbulence model performed better than the standard $\kappa-\epsilon$ turbulence model in most cases.

In addition, the two-layer approach has the added flexibility of an all-y+ wall treatment. This means that the turbulence model has the ability to model viscous boundary layer flows for prism layer meshes of varying degrees of coarseness or fineness. This is advantageous to the current study because the cells in the computational mesh are not the same size. The mesh is refined in regions where shock waves and boundary layer separation are expected to occur. The flow field in the supersonic inlet also has varying velocity scales as a result of the shock wave and area compression occurring in the inlet. Therefore, this makes it difficult to achieve a pure high-y+ or low-y+ mesh.

C.2.4 Boundary Conditions

According to Loth et al. (2004), the captured free-stream airflow has a free-stream Mach number of Mach 2, a stagnation pressure of 61.7 kPa and a stagnation temperature of 339 K. The free-stream boundary condition in STAR-CCM+ requires the flow direction, Mach number, static pressure, static temperature, turbulence intensity and turbulent viscosity ratio as inputs (Table C.4). The static pressure and static temperature were computed using isentropic flow relations presented in equations 4.5 and 4.4, respectively.

The turbulence intensity in table C.4 was left as the default STAR-CCM+ value. According to the STAR-CCM+ user manual, external free-stream flows are considered to be a low turbulence case. Low turbulence cases generally have turbulence intensities of 1% or lower (Siemens Digital Software 2020; ANSYS Inc 2009). Ideally, the best estimate of turbulence

Table C.4: The free-stream boundary conditions

Flow direction	$[1.0, 0.0, 0.0]$
Mach number	2
Static pressure	7885.5 Pa
Static temperature	188.3 K
Turbulence intensity	0.01
Turbulent viscosity ratio	10

intensity would be obtained from empirical data. However, there was no empirical data available to the current study. Therefore, the default turbulence intensity of 1% was considered to be an acceptable approximation for the present work. This may be revisited in future work.

The turbulent viscosity ratio in table C.4 was also left as the default STAR-CCM+ value. It is typically set as a small value within the range of 1 and 10 for external free-stream flows (ANSYS Inc 2009). However, STAR-CCM+ does not apply the set value in table C.4 during the simulation when a realisable $\kappa - \epsilon$ model is used. It applies a turbulent viscosity ratio that it calculates during the simulation. The turbulent viscosity ratio is calculated based on the boundary condition and parameters that are unknown before the simulation runs (Siemens Digital Software 2020). There is a method that can be applied to hard-code a desired turbulent viscosity ratio. This may be especially useful when a good estimate of turbulent viscosity ratio is known from empirical data. However, there was no empirical data available to the current study. Therefore, the turbulent viscosity ratio that is calculated by STAR-CCM+ during the simulation was considered to be an acceptable approximation for the present work. This may be revisited in future work.

The fluid properties applied to the pressure outlet boundary condition located downstream of the AIP are presented in table C.5. According to Loth et al. (2004), the flow should reach a Mach number of about 0.45 at the AIP. This desired AIP Mach number was used to compute the static temperature using isentropic flow relations. The applied pressure was adjusted to a value that placed the normal shock wave at the internal diffuser entry plane. This process does not resemble the process that occurs in a real ramjet during flight. A real ramjet would not adjust the back pressure during flight until it finds a value that ensures that the normal shock wave is located at the internal diffuser entry plane. This approach aims to simulate an idealised case where the normal shock wave is located at the internal diffuser entry plane. The back pressure required to simulate this idealised case was not known. Therefore, it had to be adjusted until it could be determined.

Table C.5: The pressure outlet boundary conditions

Static pressure	47200 Pa
Static temperature	326.7 K
Turbulence intensity	0.01
Turbulent viscosity ratio	10

The turbulence intensity in table C.5 was left as the default STAR-CCM+ value. The turbulence intensity inside the internal diffuser is not known. However, an estimation can be made using equation C.1 (ANSYS Inc 2009).

$$I = 0.16(Re_{D_H})^{-1/8} \tag{C.1}$$

Technically, equation C.1 is used to calculate the turbulence intensity at the core of a fully developed duct flow (ANSYS Inc 2009). The geometry of a supersonic inlet does not look exactly like a regular duct. Furthermore, boundary layers are expected in supersonic inlet flow fields. However, supersonic inlet flow fields are not typically fully developed. The results from this estimation were seen as a limiting case.

For this estimation, the supersonic inlet was approximated as a regular duct. The Reynolds number, denoted by Re_{D_H}, was calculated using equation C.2 (Anderson 2010). It was calculated based on the free-stream properties of the captured air. These represent the fluid properties of the flow entering the duct.

$$Re_{D_H} = \frac{\rho v D_H}{\mu} \tag{C.2}$$

A width and height were required to calculate the hydraulic diameter of the captured stream-tube of air. The value for h_{cap} represents the height of the captured stream-tube of air. The 2D CFD model assumes the domain has a unit width. For this estimation, hydraulic diameter was calculated for a rectangular duct that has a height equivalent to h_{cap} and a unit width. Based on this estimation, the flow entering the inlet had a Reynolds number of approximately 1 323 008. The resultant turbulence intensity was approximately 0.027.

The default STAR-CCM+ turbulence intensity is lower than the calculated turbulence intensity. The calculated turbulence intensity is an estimation based on fully developed duct flow. Supersonic inlet flow fields are not typically fully developed. Therefore, the turbulence intensity in a supersonic inlet flow field is expected to be lower than the turbulence intensity of a fully developed duct flow. The default STAR-CCM+ was assumed to be a fair selection for this purpose. This assumption may be revisited in future work.

The turbulent viscosity ratio in table C.5 was also left as the default STAR-CCM+ value. As previously mentioned, STAR-CCM+ does not apply the set value in table C.5 during the

simulation when a realisable $\kappa - \epsilon$ model is used. It applies a turbulent viscosity ratio that it calculates during the simulation. The turbulent viscosity ratio is calculated based on the boundary condition and parameters that are unknown before the simulation runs (Siemens Digital Software 2020). The turbulent viscosity ratio calculated by STAR-CCM+ during the simulation was considered to be an acceptable approximation for the present work. This may be revisited in future work

C.2.5 Reference Values and Initial Conditions

The reference values are tabulated in table C.6. The reference pressure is 0.0 Pa to ensure the use of absolute pressures. The minimum allowable wall distance is left as the default STAR-CCM+ value of $1e^{-6}$ m. This value is acceptable to the CFD model because turbulence models require a non-zero value for wall distance (i.e. y+). The algorithm calculating wall distance has been developed to produce a positive value for almost all cell shapes. However, it is possible for the algorithm to compute a negative value for cells that are badly shaped. The default minimum allowable wall distance prevents this from happening. Furthermore, an all-y+ wall treatment was selected. The default minimum allowable wall distance is small enough to allow the solver to model the turbulent flows with low-y+ meshes.

Table C.6: The reference values

Reference pressure	0.0 Pa
Minimum allowable wall distance	$1e^{-6}$ m
Minimum allowable absolute pressure	1 000 Pa
Maximum allowable absolute pressure	$1e^{8}$ Pa
Minimum allowable temperature	100.0 K
Maximum allowable temperature	5000.0 K

The minimum and maximum allowable absolute pressures in table C.6 were left as the default STAR-CCM+ values of 1 000 Pa and $1e^{8}$ Pa, respectively. The purpose of a supersonic inlet is to compress air from the atmospheric free-stream pressure to a higher pressure at the AIP. Therefore, the free-stream pressure (Table C.4) is expected to be the lowest pressure in the flow field. The highest pressure in the flow field is expected to be the AIP pressure (Table C.5). The expected minimum and maximum pressures are 7 885.50 Pa and 47 200.00 Pa, respectively. These fall within the default STAR-CCM+ allowable absolute pressure range. Therefore, the default minimum and maximum allowable absolute pressures were considered to be acceptable for the CFD model.

The minimum and maximum allowable temperatures in table 6.6 were left as the default STAR-CCM+ values of 100 K and 5 000 K, respectively. When air is compressed, the temperature of the air increases. Therefore, the lowest and highest temperatures in the flow-field are expected to occur at the free-stream and AIP, respectively. The boundary conditions presented in tables C.4 and C.5 indicate that the expected minimum and maximum flow field temperatures are 188.30 K and 326.70 K, respectively. These values fall within the default STAR-CCM+ allowable temperature range. Therefore, the default temperature range was considered acceptable for the CFD model.

The initial conditions applied to the entire domain are tabulated in table C.7. The initial conditions are the fluid properties downstream of a normal shock wave whereby the upstream fluid properties are the properties of the captured free-stream flow presented in table C.4. Through trial-and-error, it was established that this initial condition was an sensible place to start the CFD analysis.

According to Siemens Digital Software (2020), the turbulent velocity scale is typically set to a value that is equal to the initial velocity. The turbulent viscosity ratio in table C.7 is left as the default STAR-CCM+ value. STAR-CCM+ does not apply this value during the initialisation of the simulation when a realisable $\kappa - \epsilon$ model is used. It applies a turbulent viscosity ratio that it calculates based on parameters that are unknown before the simulation is initialised (Siemens Digital Software 2020). The turbulent viscosity ratio calculated by STAR-CCM+ during the initialisation was considered to be an acceptable approximation for the present work. This may be revisited in future work

Table C.7: The initial conditions

Static pressure	35484.9 Pa
Static temperature	317.8 K
Turbulence intensity	0.01
Turbulence specification	Intensity + Viscosity ratio
Turbulent velocity scale	206.3 m/s
Turbulent viscosity ratio	10.0
Velocity	[206.3, 0.0, 0.0] m/s

C.2.6 Solver

The CFD model uses a second-order coupled implicit solver because it is well suited to compressible flows. The second-order coupled implicit solver has a grid sequencing expert

initialisation feature. This feature performs a normal initialisation of the flow field. Thereafter, it rapidly computes an approximate inviscid solution of the flow field. Obtaining an inviscid solution first made the viscous CFD simulation converge faster.

C.2.7 Results and Discussion

The Mach number contour plot illustrated in figure C.7 is a product of the 2D CFD model. It provides both qualitative and quantitative information about the supersonic inlet flow field. The fore-body generates a system of two oblique shock waves. The terminating normal shock wave is located at the internal diffuser entry plane, as per the design specification. The captured airflow is compressed from a supersonic free-stream Mach number of Mach 2 to a lower supersonic Mach number of approximately Mach 1.45 by the oblique shock wave system. The airflow is compressed further to a subsonic Mach number by the terminating normal shock wave. After that, the subsonic airflow enters the internal diffuser, and it is compressed even further to a lower subsonic Mach number at the AIP. All the oblique shock waves and the normal shock wave converge at a single point near the cowl lip. This shock wave structure maximises the mass flow ratio and minimises the spillage drag.

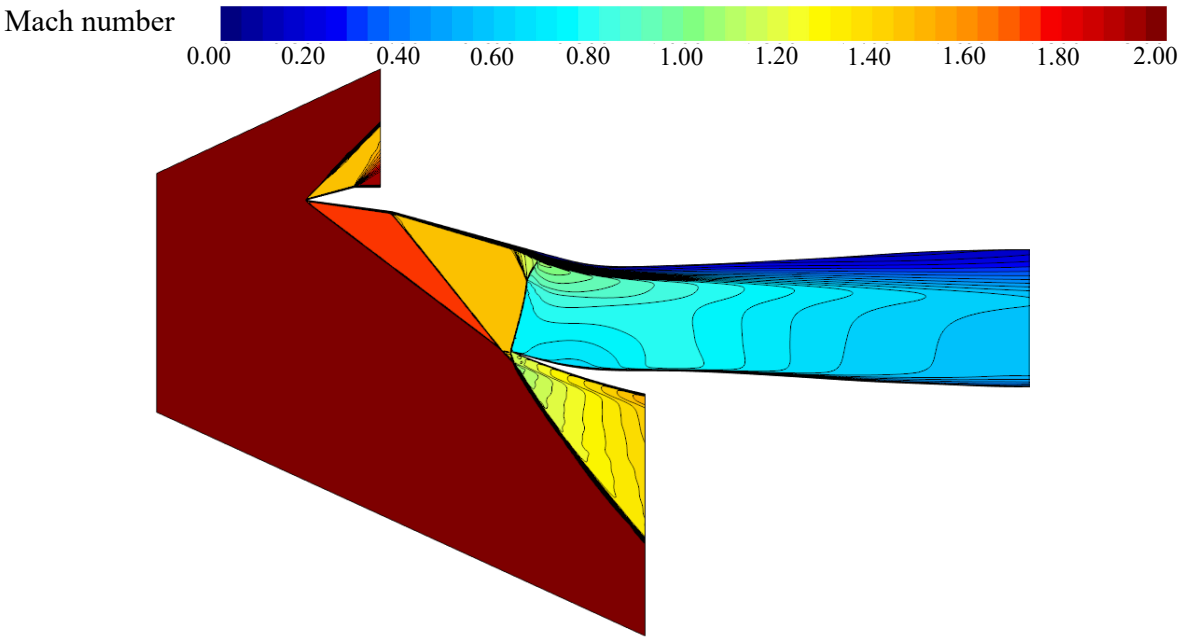
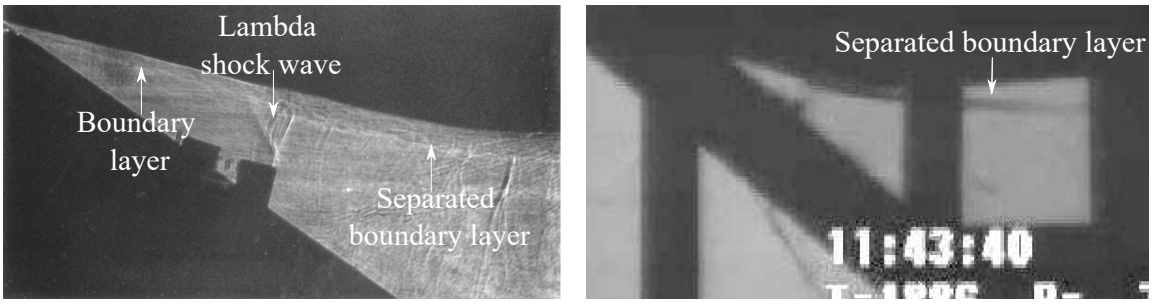


Figure C.7: The 2D CFD validation Mach number contour plot

Figure C.7 illustrates the occurrence of complex shock wave patterns in the supersonic inlet flow field. These are a result of the shock-wave/boundary-layer interactions occurring on the fore-body. The first oblique shock wave is generated at the leading edge of the fore-body. The leading edge is a small blunt body. A blunt body moving through a supersonic flow generates

a curved, detached bow shock wave. The bow shock wave rapidly transforms into the first oblique shock wave. There is no shock-wave/boundary-layer interaction associated with this particular shock wave. The boundary layer adjacent to the fore-body surfaces experiences a local thickening as it passes through the second oblique shock wave. The thickened boundary layer makes the sharp compression ramp corners appear smoother to the air flowing over the ramp. A series of compression waves form over the apparently smooth ramp and converge with the oblique shock wave at some distance above the surface. The compression waves give the oblique shock wave a slightly diffused look at the base. The adverse pressure gradient across the normal shock wave causes the upstream boundary layer to thicken and subsequently separate from the fore-body surface. The normal shock wave develops a lambda foot as a result of the boundary layer separation. Separated boundary layer flow enters the internal diffuser, as illustrated in figure C.7.

Figure C.8 is an illustration of the flow visualisation images obtained during the experiment. The wind tunnel shadowgraph presented in figure C.8a is a close-up of the normal shock-wave/boundary-layer interaction on the fore-body surface. "The block-like shapes are reference marks taped to the inlet window to bracket the design location of the normal shock"(Loth et al. 2004). Based in figure C.8a, the boundary layer appears to thicken as it passes through the normal shock wave. The normal shock wave develops an upside-down lambda foot as a result of its interaction with the boundary layer. The video Schlieren image presented in figure C.8b is a close-up of the throat section of the inlet. It shows that the boundary layer separates from the fore-body surface and separated flow enters the internal diffuser. Loth et al. (2004) stated that this flow feature appeared in all the Schlieren videos.



(a) A wind tunnel shadowgraph (b) An image captured from video Schlieren

Figure C.8: Flow visualisation images of the shock/boundary-layer interaction documented during the wind-tunnel experiment performed by Loth et al. (2004)

The similarities between the 2D CFD Mach number contour plots and the flow visualisation images presented in figure C.8 show that the CFD model captures the essential flow features in a 2D, external-compression, supersonic inlet flow field and provide good qualitative information about the overall supersonic inlet flow field.

Figure C.9 provides a comparison of the static pressure distributions on the inlet surfaces. Loth et al. (2004) present the supersonic inlet in a different orientation from the orientation used in this study. For this validation study, the fore-body and its extension into the internal diffuser are referred to as the fore-body and top interior surface (FTIS). The cowl interior is referred to as the cowl interior surface (CIS).

The static pressure distributions produced by the 2D CFD model follow a similar trend to the static pressure distribution obtained from the experimental results produced by Loth et al. (2004). Based on figure C.9, the location and magnitude of the pressure jumps on the FTIS correlate well. The correlation of the magnitudes of the static pressures on the compression ramps was determined using root mean square errors between the experimental data points and the curves produced by the 2D CFD model. The root mean square errors between the experimental and 2D CFD model static pressures on the first and second compression ramps are approximately 0.05 and 0.02, respectively.

The experimental data indicates that the airflow downstream of the normal shock wave accelerates as it flows through the curved throat. This is evident from the slight pressure decrease observed in this region on both the FTIS and the CIS. This is a result of the airflow turning through the constant-height throat. The static pressure distributions obtained from the 2D CFD model do not appear to detect this feature.

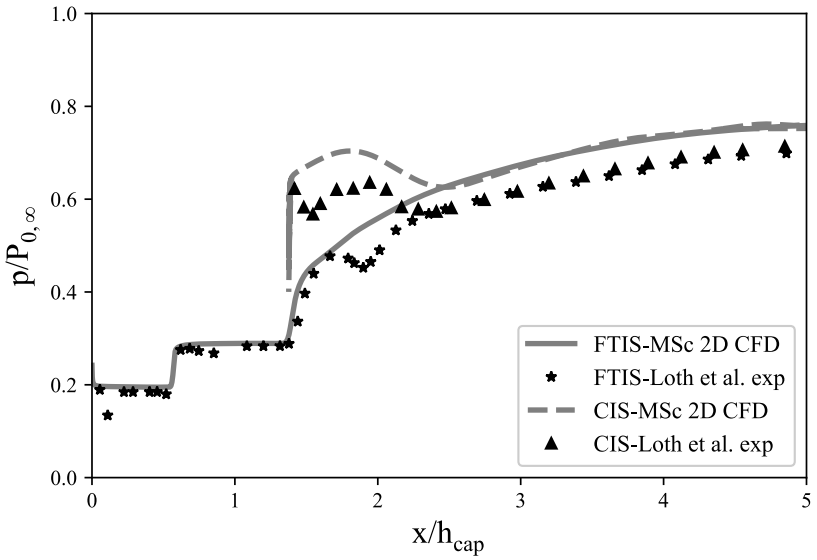


Figure C.9: A comparison of the static pressure distributions produced by the 2D CFD model and the experiments performed by Loth et al. (2004)

Both sets of results demonstrate a similar gradual rise in static pressure on the internal diffuser surfaces. However, the 2D CFD model requires an AIP pressure that is 11.34% higher than the experimental AIP pressure. This is because the pressure rise within the internal diffuser

is a function of the cross-sectional area expansion ratio. Boundary layers alter the effective inlet surfaces. This decreases the effective internal diffuser cross-sectional areas. The effective expansion ratio observed by the flow in the 2D CFD model only takes the boundary layer development on the FTIS and CIS into account. In reality, there is an additional boundary layer developing on the inlet side walls. This boundary layer decreases the effective expansion ratio even further. The 2D CFD model does not model the boundary layer on the side walls. Therefore, the AIP pressure required by the 2D CFD model to position the normal shock wave at the internal diffuser entry plane is 11.34% higher than the experimental AIP pressure. This causes the root mean square errors between the experimental and 2D CFD model static pressures on the FTIS and CIS to be approximately 0.17 and 0.14, respectively.

Figure C.10 presents a comparison between the 2D CFD model results of the AIP total pressure recovery distribution and the experimental results produced by Loth et al. (2004). During the experiment, total pressure was measured with a three-element total pressure rake. The results illustrated in figure C.10 represent the total pressure recovery distributions measured by each total pressure rake element. The total pressure rake elements are referred to as the left rake (LR), centre rake (CR) and right rake (RR).

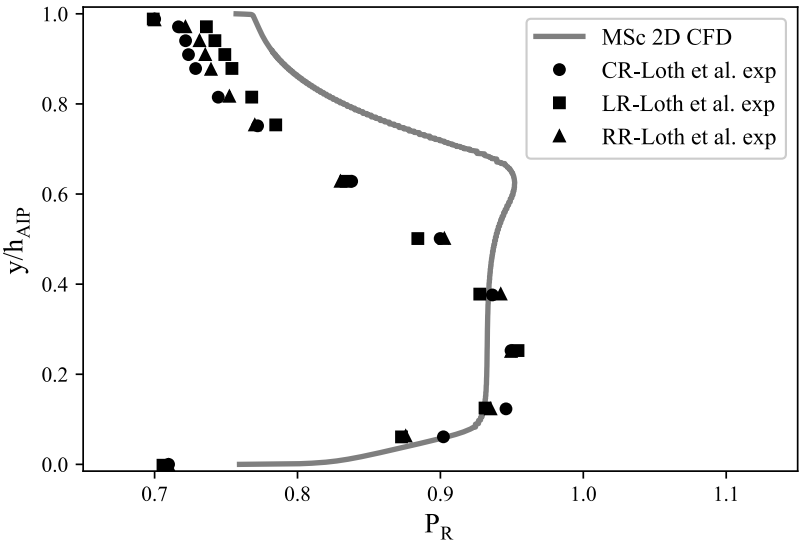


Figure C.10: A comparison of the total pressure recovery distribution at the AIP produced by the 2D CFD model and the experiments performed by Loth et al. (2004)

The results illustrated in figure C.10 show a similar trend for the AIP total pressure recoveries obtain from the 2D CFD model and the experimental data. The total pressure recoveries are lower in the regions near the surfaces and increase as the distance between the airflow and the surfaces increases. The reduced total pressure recovery near the CIS is due to the friction between the supersonic inlet flow field and the CIS. The total pressure recovery reduction near the FTIS is due to the turbulent mixing associated with boundary layer separation.

Based on figure C.10, the shape of the AIP total pressure recovery produced by the 2D CFD model differs from its experimental counterpart. The 2D CFD model computes a wide region of uniform flow in the region away from the surfaces. This region corresponds to the flow region where the effects of viscosity are assumed to be negligible. There is no evidence of a region of uniform flow in the AIP total pressure recovery distribution obtained from the experimental data. The 2D CFD model only computes the total pressure losses that are associated with viscous flow phenomena in the airflow adjacent to the FTIS and CIS. The presence of side walls on real 2D supersonic inlets introduces additional viscous flow phenomena that vary the inlet flow field in the span-wise direction. The 2D CFD model assumes the inlet flow field is constant in the span-wise direction and ignores the presence of side walls. As a result, it predicts a larger region of uniform flow. Furthermore, the total pressure recoveries of the flow adjacent to the CIS are quite similar. However, the 2D CFD model predicts larger total pressure recoveries for the flow adjacent to the FTIS. All of factors mentioned above cause the root mean square errors between the 2D CFD model and the experimental total pressure recoveries at the CR, LR and RR to be approximately 0.07, 0.07 and 0.07, respectively.

The shape of the total pressure recovery distribution curve calculated by the 2D CFD model does not look the same as the shape of the curve measured during the experiment. However, it does capture the essential flow features such as the presence boundary layers and regions of separated flow. Furthermore, the average total pressure recoveries obtained from the 2D CFD model are similar to those obtained from the experimental data. The 2D CFD model calculates an average total pressure recovery of 0.86. The average experimental total pressure recoveries at the CR, LR and RR are approximately 0.81, 0.81 and 0.81, respectively. The average total pressure recovery errors at the CR, LR and RR are approximately 6.17%, 6.17% and 6.17%, respectively. Therefore, the 2D CFD model provides a reasonable approximation of the average total pressure recovery at the AIP.

C.3 3D CFD Simulation of the Supersonic Inlet Flow Field

C.3.1 Domain Specification

The 3D CFD domain is similar to the 2D CFD domain. The only differences are that the inlet flow field has a finite span and the inlet geometry contains side walls. The inlet has a rectangular cross-section throughout, and it is symmetric about the x-y plane. Therefore, only half the actual domain was used for the CFD analysis. The final 3D CFD domain and associated boundary conditions are illustrated in figure C.11.

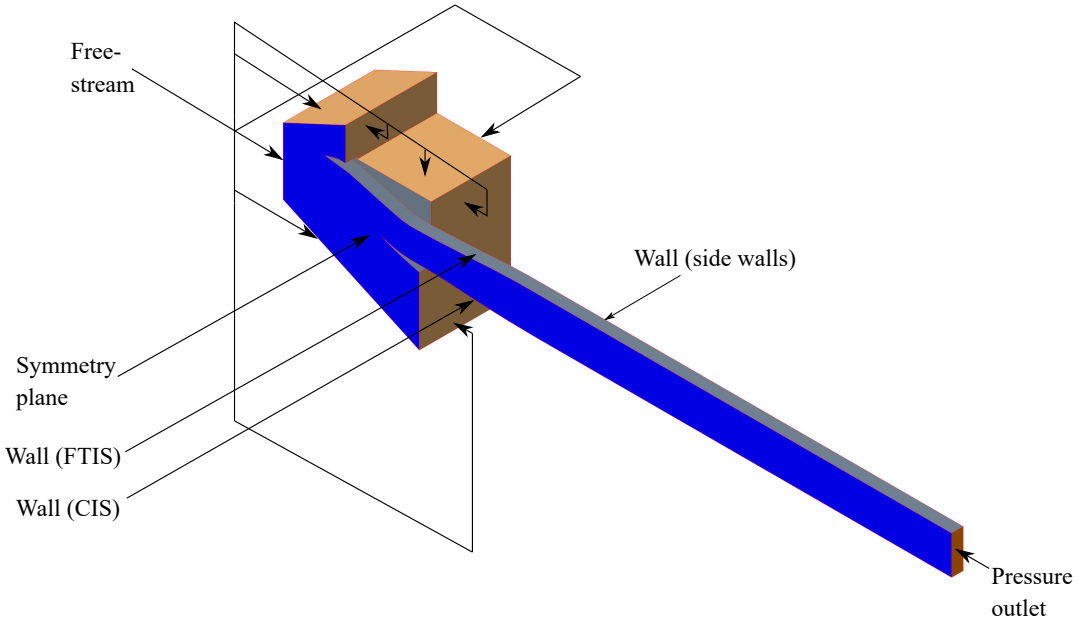


Figure C.11: The 3D CFD domain with boundary conditions

C.3.2 Mesh Specification

The computational mesh presented in figure C.12 was generated using the region-based meshing strategy along with the surface remesher, polyhedral volume mesher and the prism layer mesher. The mesh was refined in the regions where the air is known to experience shock wave formation and boundary layer separation. The 3D CFD computational mesh is coarse relative to the 2D computational mesh. It has a base cell size of $0.1h_{cap}$. It was difficult to use a smaller base cell size due to how computationally expensive the simulation file was. The time constraints imposed on the present study made it challenging to perform a mesh independence study using base cell sizes smaller than $0.1h_{cap}$. Therefore, a mesh independence study could not be performed for the 3D CFD model. There is a possibility that the results generated by the coarse mesh may not be independent of mesh cell size. However, the results explain how the increment of flow dimensions affects the flow analysis. The size of the mesh is presented in table C.8.

Table C.8: The size of the 3D CFD model computational mesh

Number of cells	47 004 380
Number of polyhedral layers	25

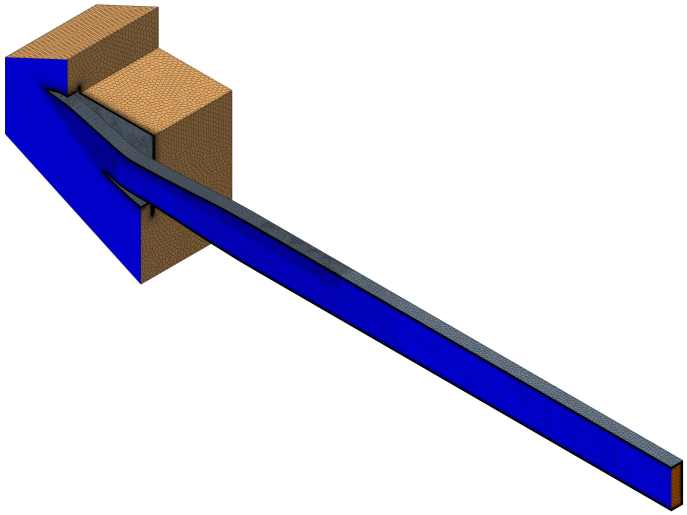


Figure C.12: The 3D CFD computational mesh

The mesh metrics that measure the cell quality of a 3D mesh in STAR-CCM+ are face validity, cell quality, volume change, cell skewness angle, chevron quality indicator, least-squares quality and cell warpage quality. The mesh metrics of the computational mesh in figure C.12 are illustrated in figure C.13. Face validity, volume change, cell skewness angle, chevron quality indicator and least-squares quality were explained in section C.2.2. Cell quality and warpage are explained in the paragraphs that follow.

Cell quality is metric that evaluates how the cell centroids of the face neighbouring cells are geometrically distributed. It also evaluates how the cell faces are oriented. A cell with bad cell quality has a flat shape and highly non-orthogonal faces. Good quality cells have a cell quality of one. Bad cells quality have a face quality of $1.0e^{-5}$ or less.

The presence of thin and warped cells in a computational mesh are identified by the cell warpage quality. Such cells are undesirable because they can cause issues with the CFD solver. The value of cell warpage quality ranges from 0 to 1. A cell with a cell warpage quality of 0 has the worst warpage. Conversely, a cell with a cell warpage quality of 1 has no warpage. Bad cells have a cell warpage quality of 0.15 or lower.

Based on the mesh metric definitions provided in sections C.2.2 and C.3.2, the generated mesh is of an acceptable quality.

C.3.3 Physics Models

The physics models used in the 3D CFD model are almost identical to those used in the 2D CFD model. The space category in table C.3 was, however, changed from 2D to 3D.

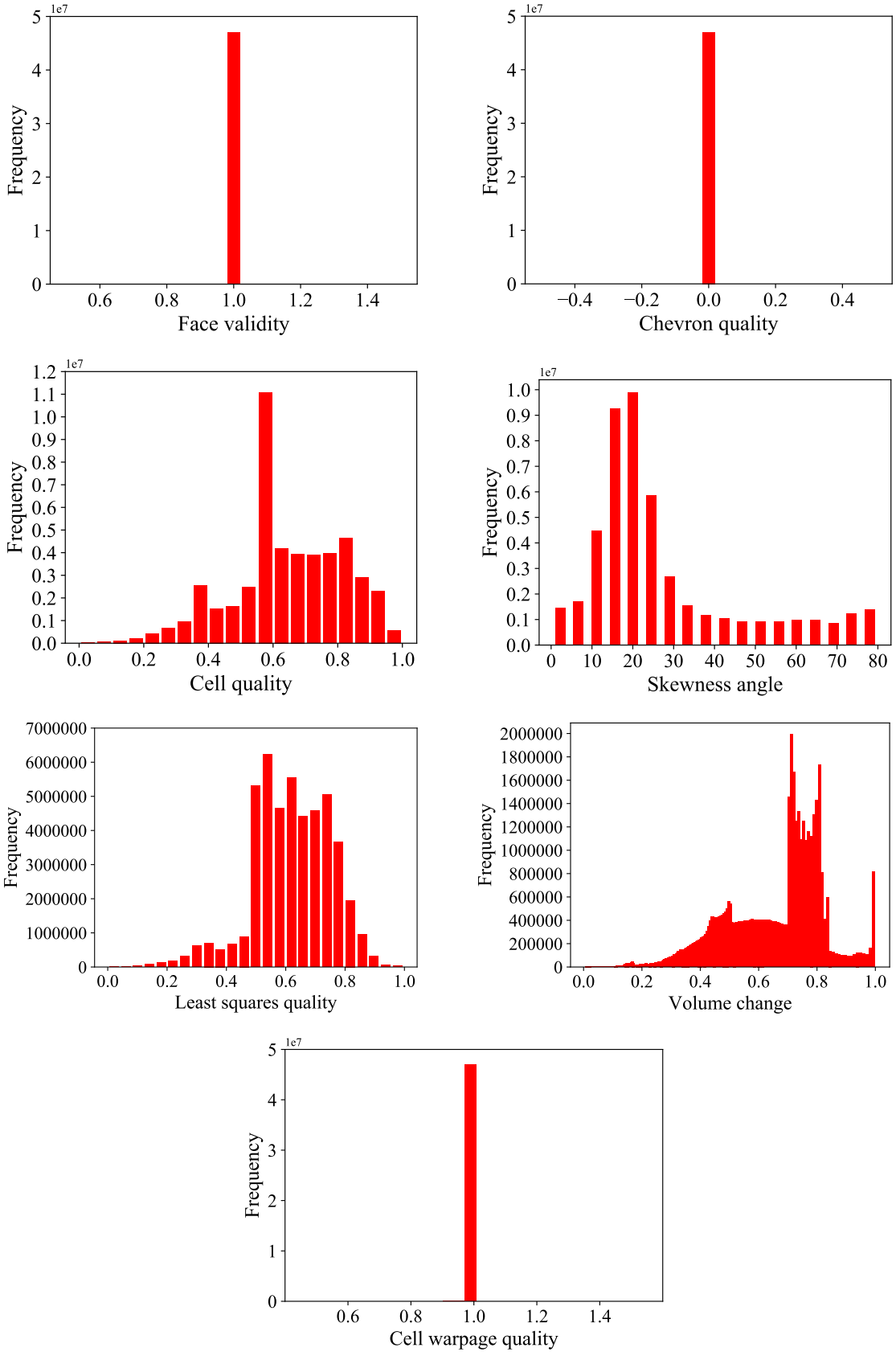


Figure C.13: The mesh metrics of the 3D CFD model computational mesh

C.3.4 Boundary Conditions

The fluid properties applied to the free-stream boundary condition are identical to those presented in table C.4. To ensure that the normal shock wave was located at the internal diffuser entry plane, the pressure applied to the pressure outlet was adjusted to a value of 43 275 Pa. The remaining pressure outlet boundary conditions are identical to those presented in table C.5.

C.3.5 Reference Values and Initial Conditions

The reference values and initial conditions that were used in the 3D CFD model are identical to those presented in section C.2.5.

C.3.6 Solver

The solver specifications that were used for the 3D CFD model are the same as those presented in section C.2.6.

C.3.7 Results and Discussion

The 3D CFD model produced the Mach number contour plot presented in figure C.14 at the centreline, where the symmetry plane boundary condition is located. There is a blue block in figure C.14, which is not apparent in figure C.7. This blue block represents the external part of the inlet side-wall. The 3D CFD flow field presented in figure C.14 appears to be similar to the 2D CFD flow field presented in figure C.7. The airflow is compressed from the free-stream supersonic Mach number to a subsonic Mach number at the AIP in an almost identical way. Similarly, the viscous flow phenomena and the resultant complex shock wave patterns are almost identical to those observed in the 2D CFD Mach number contour plot (Figure C.7) and the flow visualisation images (Figure C.8).

The results presented in figure C.15 compare the static pressure distribution on the FTIS and CIS produced by the 3D CFD model and the experiment. Based on figure C.15, the location and magnitude of the pressure jumps on the FTIS tightly correlate. The root mean square errors between the experimental and 3D CFD model static pressures on the first and second compression ramps are approximately 0.05 and 0.004, respectively.

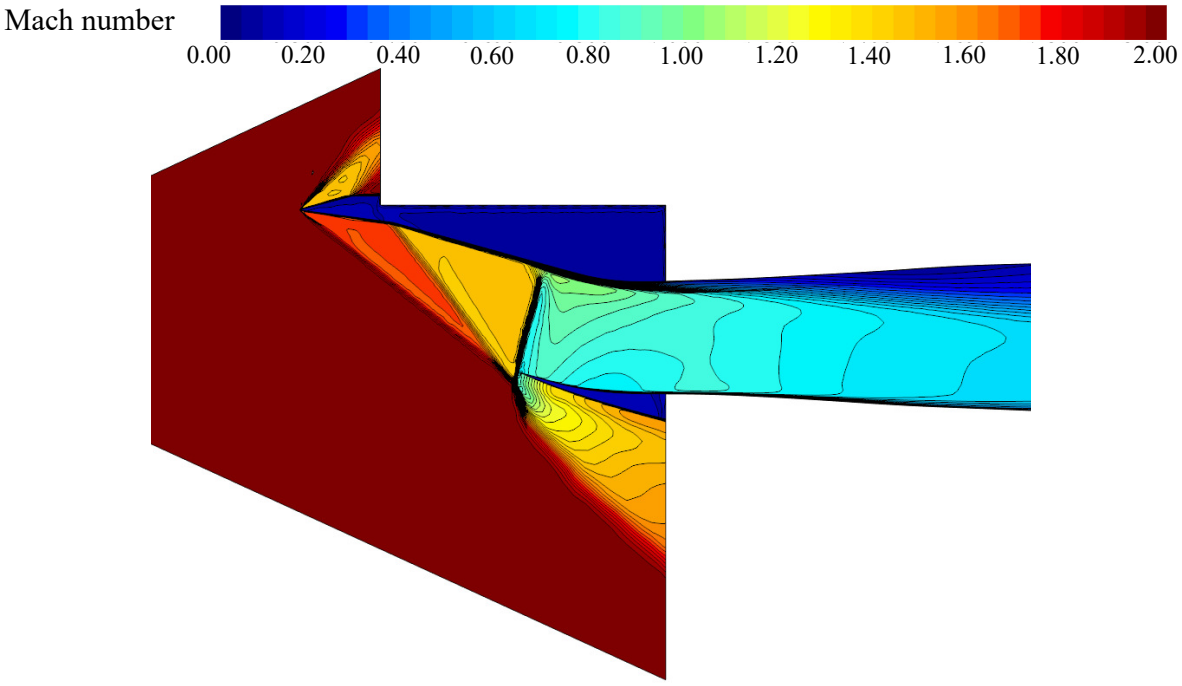


Figure C.14: The 3D CFD validation Mach number contour plot

The experimental results detect a slight pressure decrease just after the normal shock wave. This is assumed to be a result of the air accelerating as it passes through the curved, constant-area throat. The 2D CFD model results do not show this feature. However, it is apparent in the 3D CFD model results.

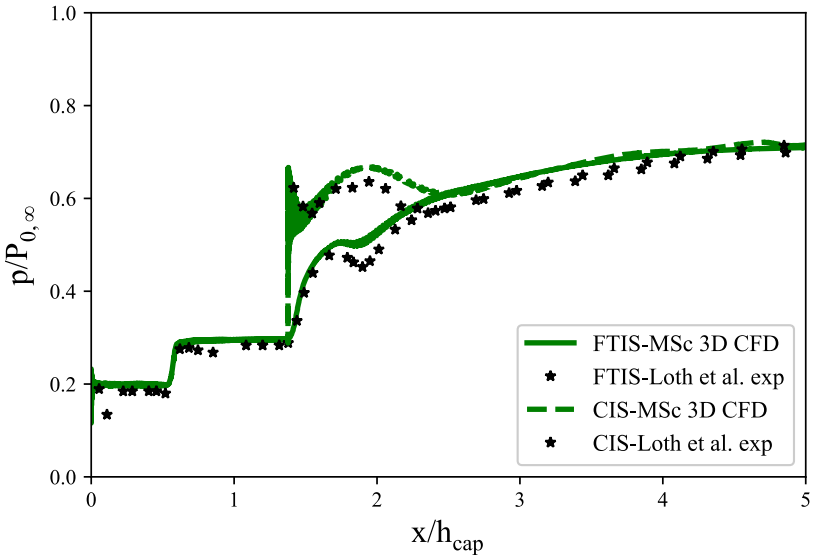


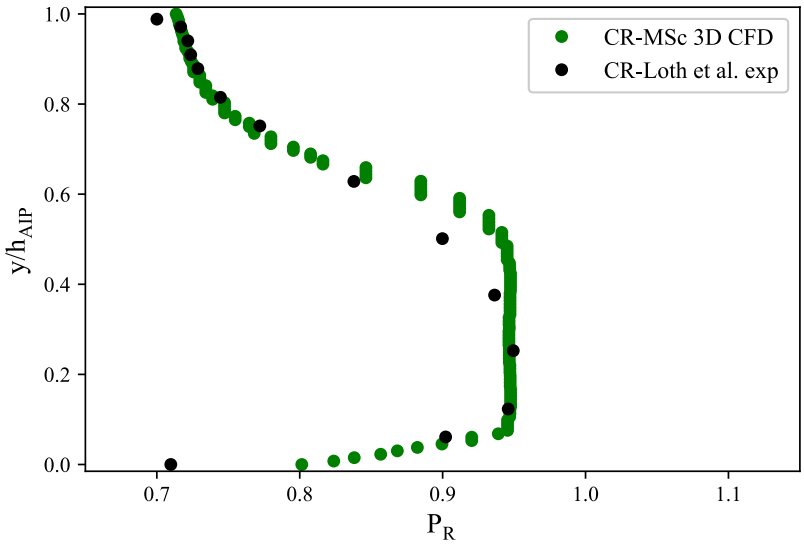
Figure C.15: A comparison of the static pressure distributions produced by the 3D CFD model and the experiments performed by Loth et al. (2004)

The 3D CFD model requires an AIP pressure that is almost identical to the back pressure applied during the experiment for the normal shock wave to be positioned at the internal diffuser entry plane. Therefore, 3D CFD model computes a more gradual pressure rise in the internal diffuser compared to the 2D CFD model. This is because, the 3D CFD model models the boundary layer developing on the inlet side walls. As a result, the pressure rise modelled by the 3D CFD model is similar to that of the experiment. The root mean square error between the experiment and 3D CFD model static pressures on the FTIS and CIS are approximately 0.03 and 0.04, respectively. The root mean square errors related to the FTIS and CIS are approximately 5.7 and 3.5 times smaller than their 2D counterparts, respectively. The 3D CFD static pressure distribution in the internal diffuser correlates better with the experimental results than the 2D CFD model results.

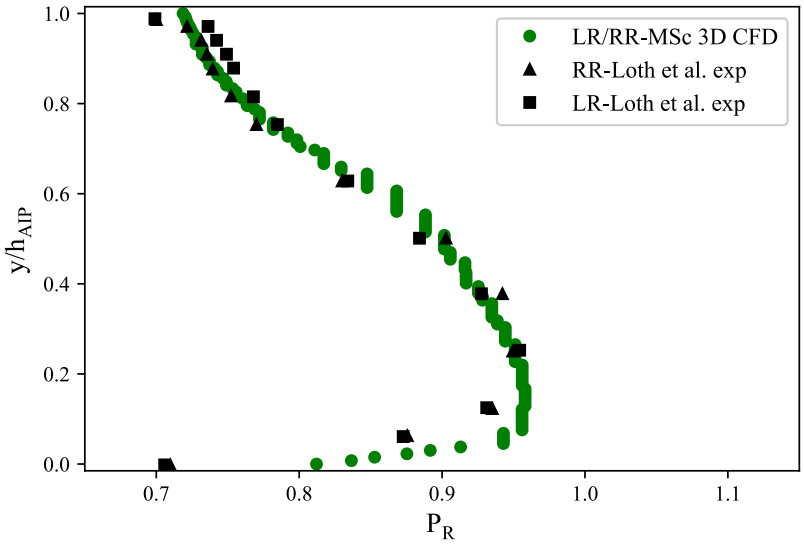
The images in figure C.16 present a comparison between the AIP total pressure recovery distributions at the AIP obtained from the 3D CFD model and the experiments performed by Loth et al. (2004). The results illustrated in figure C.16 show a similar trend. The total pressure recoveries are lower in the regions near the surfaces and increase as the distance between the airflow and the surfaces increases. The reduced total pressure recovery near the CIS is due to the friction between the supersonic inlet flow field and the CIS. The total pressure recovery reduction near the FTIS is due to the turbulent mixing associated with boundary layer separation.

The AIP total pressure recovery distribution at the position of the CR is presented in figure C.16a. Based in this figure, the shapes of the curves produced by the 3D CFD model and the experiment appear to be similar. The root mean square error between the experiment and the 3D CFD model total pressure recovery distribution is approximately 0.03. This error is approximately 2.33 times smaller than its 2D counterpart. The source of the error is mostly attributed to the differences in the total pressure recoveries in the core flow. The 3D CFD model results detect a small region of uniform flow. There is no evidence of a small region of uniform flow in the experimental results.

Figure C.16b presents the AIP total pressure recovery distribution at the position of the LR and RR. The geometry of the inlet was assumed to be symmetric about the x-y plane. Only half the actual domain was used for the CFD analysis. Therefore, the AIP total pressure recovery distribution produced at the LR and RR are treated as the same. Similarly to figure C.16a, the shapes of the experimental and 3D CFD model curves appear quite similar. The root mean square errors between the 3D CFD model and the experimental total pressure recoveries at the LR and RR are approximately 0.03 and 0.03, respectively. Despite the fact that the 3D CFD model does not predict a uniform flow region at the position of the LR and



(a) Center rake



(b) Left and right rake

Figure C.16: A comparison of the total pressure recovery distribution at the AIP produced by the 3D CFD model and the experiments performed by Loth et al. (2004)

RR, these errors are identical to the error calculated at the CR. The source of this error is largely a result of the differences in total pressure recovery near the CIS.

The 3D CFD computational mesh is coarse relative to the 2D CFD computational mesh. It was difficult to use a smaller base cell size due to how large the simulation file was and how long the simulation took to run. There is a possibility that the coarseness of the mesh is a source of error between the total pressure recoveries produced by the experiment and the 3D CFD model. A mesh independence study would have to be performed to determine if the simulation results are independent of mesh cell size. However, such a study will not be performed in the present work due to the imposed time constraints.

Another source of the error between the total pressure recoveries produced by the experiment and the 3D CFD model could be the selected turbulence model. The $\kappa - \epsilon$ turbulence model was selected because it was recommended in several studies investigating the flow field in supersonic inlets. However, there could be turbulence models that perform better than the $\kappa - \epsilon$ turbulence model. A study to investigate turbulence models to analyse the flow in 2D, external-compression, supersonic inlets is beyond the scope of this work.

The turbulence parameters used in the CFD model could also be the source of the error between the total pressure recoveries produced by the experiment and the 3D CFD model. Ideally, the best estimate of turbulence parameters would be obtained from empirical data. However, there was no empirical data available to the current study. Therefore, approximations had to be made.

The differences between the CR and the LR/RR AIP total pressure recovery distributions computed by the 3D CFD model are due to the proximity of the rake to the side walls. The side walls introduce viscous flow phenomena to the inlet flow field. This causes a variation in the supersonic inlet flow field in the span-wise direction. The total pressure rakes closest to the side walls (i.e. LR and RR) are the most affected by the viscous flow phenomena introduced by the side walls. Conversely, the total pressure rake that is furthest from the side walls (i.e. CR) is the least affected by the viscous flow phenomena introduced by the side walls. This is evident from the presence of a small region of uniform flow illustrated in figure C.16a and the absence of such a flow in figure C.16b.

C.4 Conclusion

The validation study showed that the 2D CFD model provides reasonable approximations of the 2D, external-compression, supersonic inlet flow field and captures the essential flow features. However, the 3D CFD model produced results that were in better agreement with experimental data compared to the results that were produced by the 2D CFD model. This is because 2D, external compression, supersonic inlets have side walls to contain the airflow. The friction between the side walls and the airflow introduces viscous flow phenomena that vary the supersonic inlet flow field in the span-wise direction. The 3D CFD model models this span-wise flow variation. However, 2D CFD model assumes that the flow field is constant in the span-wise direction.

The accuracy of the 3D CFD model has a high computational cost and requires a lot of time to design, mesh, and run a simulation. The CFD model developed in this chapter was used in a sensitivity study (Chapter 6.3) where several CFD analyses had to be conducted.

Running all of these analyses using a 3D CFD analysis would not be possible within the time constraints imposed on the present study. The computational cost is greatly reduced in the 2D CFD model. Therefore, the 2D CFD model was used in the present work to analyse the air flowing through the generated supersonic inlets.

Appendix D A Survey of Two-Dimensional, External-Compression, Supersonic Inlet Geometries

A survey of 2D, external-compression, supersonic inlets was performed. The purpose of the survey was to supply the tool with suitable default values of l_{ID} and h_{CI}/h_{AIP} for the sensitivity study (Chapter 6.3). The values obtained from the survey ensure that the dimensions of the inlet components generated by the tool are in line with industry standards. A survey of this nature was challenging to perform because most studies in the field of supersonic inlet design provide limited data about the inlet geometries. This is because these inlets are typically used for military applications.

Five inlets were used for this survey. The geometries of the inlets are illustrated in figures D.1, D.2, D.3, D.4 and D.5. These inlets were obtained from several studies. The geometries of the inlets used in the survey have different scales and orders of magnitude. Therefore, the values of l_{ID} are measured relative to h_{cap}. The approximate values of l_{ID}/h_{cap} and h_{CI}/h_{AIP} for each inlet are tabulated in table D.1.

Table D.1: The dimensions of 2D, external-compression, supersonic inlets from several studies

Survey model	l_{ID}/h_{cap}	h_{CI}/h_{AIP}
1. Zhang et al. (2020)	4.01	0.00
2. LIU et al. (2017)	5.13	0.00
3. Corriveau and Pimentel (2009)	8.11	0.22
4. Van Staden (1990)	4.00	0.11
5. Loth et al. (2004)	3.52	0.27

Based on the data in table D.1, there is no strict industry standard pertaining to relative dimensions of inlet components. The values of l_{ID}/h_{cap} vary from 3.52 to 8.11. Similarly, the values of h_{CI}/h_{AIP} vary from 0.00 to 0.27. It should be noted that the inlet models with a ratio of h_{CI}/h_{AIP} equal to zero have s-shaped internal diffusers (i.e. figures D.1 and D.2).

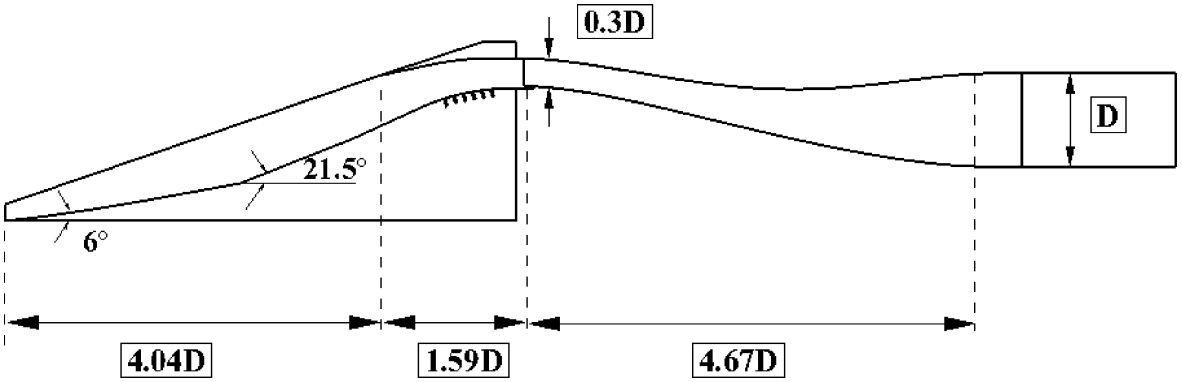


Figure D.1: Survey Model 1 (Zhang et al. 2020)

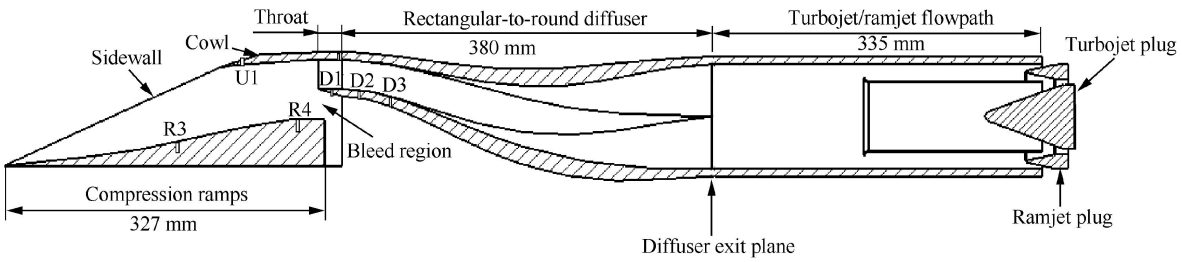


Figure D.2: Survey Model 2 (LIU et al. 2017)

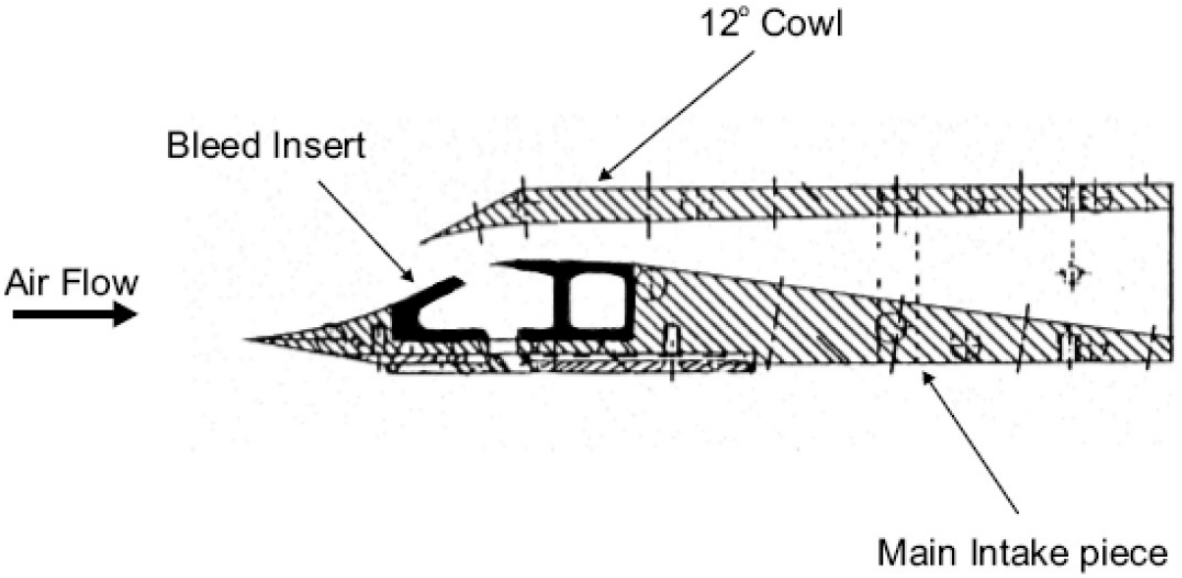


Figure D.3: Survey Model 3 (Corriveau and Pimentel 2009)

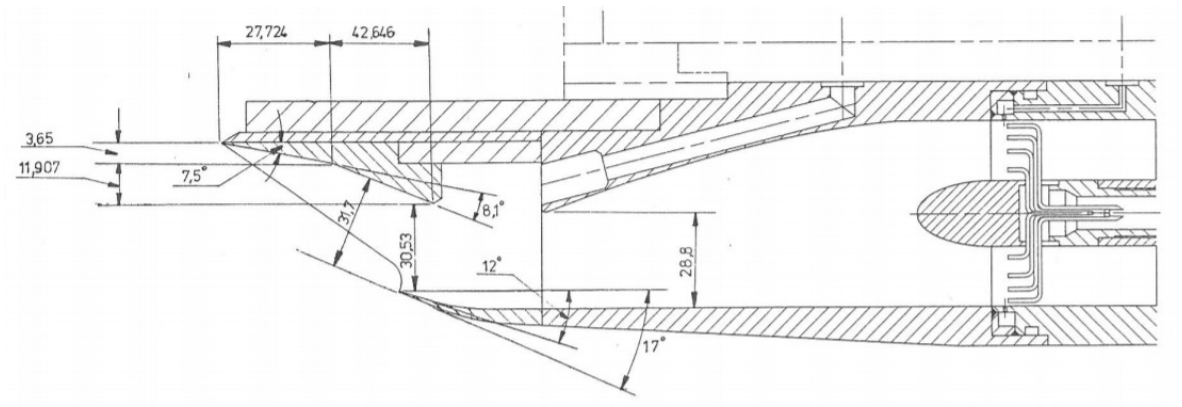


Figure D.4: Survey Model 4 (Van Staden 1990)

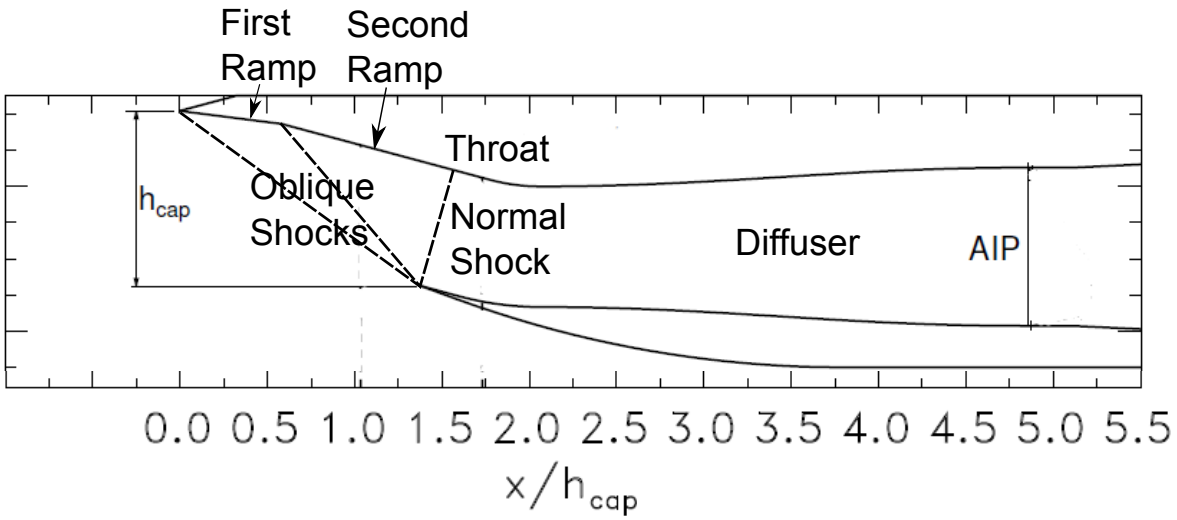


Figure D.5: Survey model 5 (Loth et al. 2004)

Appendix E Sensitivity Study Digital Appendix

The sensitivity study presented in chapter 6.3 investigates how different user-defined inputs affect the impact of viscous flow phenomena on supersonic inlet flow fields. The results obtained from the sensitivity study are available in the digital appendix mentioned in chapter A. The results show differences between the performance parameters computed by IADAM (Chapter 5) and the viscous CFD model (Chapter 6.2). This hyperlink can be used to access the sensitivity study results.

The sensitivity study digital appendix contains 43 folders. Each folder contains the following data for a specific inlet model in the sensitivity study (Table 6.10):

- A file titled '01_User_Defined_Inputs.txt'. As the name suggests, this file outlines the user-defined inputs used to generate that specific inlet model.
- A file titled '02__Geometry.pdf'. This file contains an image of the generated inlet geometry.
- A file titled '03_Mach_Number_Contour_Plot.pdf. As the name suggests, the file contains an image of the Mach number contour plot of the flow field in the generated inlet when it is operating in the critical mode.
- A file titled '04_Total_Pressure_Recovery.pdf' which contains a graph of the AIP total pressure distribution obtained from IADAM and the viscous CFD analysis.
- A file titled '05_Mass_Flow_Ratio.txt'. The file contains the mass flow ratios obtained from IADAM and the viscous CFD analysis.
- A file titled '06_AIP_Mach_Number.pdf'. As the name suggests, the file contains a graph of the AIP Mach number distribution obtained from IADAM and the viscous CFD analysis.

The hyperlinks required to access specific items in the sensitivity study digital appendix are presented in table E.1.

Table E.1: Sensitivity study results

Inlet model	Inputs	Geometry	Flow field	P_R	m_R	M_{AIP}
1	download	download	download	download	download	download
2	download	download	download	download	download	download
3	download	download	download	download	download	download
4	download	download	download	download	download	download
5	download	download	download	download	download	download
6	download	download	download	download	download	download
7	download	download	download	download	download	download
8	download	download	download	download	download	download
9	download	download	download	download	download	download
10	download	download	download	download	download	download
11	download	download	download	download	download	download
12	download	download	download	download	download	download
13	download	download	download	download	download	download
14	download	download	download	download	download	download
15	download	download	download	download	download	download
16	download	download	download	download	download	download
17	download	download	download	download	download	download
18	download	download	download	download	download	download
19	download	download	download	download	download	download
20	download	download	download	download	download	download
21	download	download	download	download	download	download
22	download	download	download	download	download	download
23	download	download	download	download	download	download
24	download	download	download	download	download	download
25	download	download	download	download	download	download
26	download	download	download	download	download	download
27	download	download	download	download	download	download
28	download	download	download	download	download	download
29	download	download	download	download	download	download
30	download	download	download	download	download	download
31	download	download	download	download	download	download
32	download	download	download	download	download	download
33	download	download	download	download	download	download
34	download	download	download	download	download	download

Table E.1 Sensitivity study results (continued)

Inlet model	Inputs	Geometry	Flow field	P_R	m_R	M_{AIP}
35	download	download	download	download	download	download
36	download	download	download	download	download	download
37	download	download	download	download	download	download
38	download	download	download	download	download	download
39	download	download	download	download	download	download
40	download	download	download	download	download	download
41	download	download	download	download	download	download
42	download	download	download	download	download	download
43	download	download	download	download	download	download

Appendix F Images of Two-Dimensional, External-Compression, Supersonic Inlets on Aircraft



Figure F.1: The Meteor Missile (Eshel 2017)



Figure F.2: The GQM-163 Coyote Missile (Parsch 2007)



Figure F.3: The XB-70 Valkyrie (Dunbar 2014)



Figure F.4: The Boeing F-15 (Boeing 2021)



Figure F.5: The Concord (BAE Systems 2021)